Molecular simulations in microporous materials:
adsorption and separation

PROEFSCHRIFT

ter verkrijging van de graad van doctor
aan de Technische Universiteit Delft,
op gezag van de Rector Magnificus Prof. ir. K.C.A.M. Luyben,
voorzitter van het College voor Promoties,
in het openbaar te verdedigen
op maandag 7 juni 2010 om 10:00 uur
door

Juan Manuel CASTILLO SANCHEZ
Diplom–Fysica; Master of Philosophy (University of Granada)
geboren te Puertollano (Spain).

Dit proefschrift is goedgekeurd door de promotoren:

Prof. dr. S Calero
Prof. dr. ing. J. Gross

Copromotor: Dr. ir. T.J.H Vlugt

Samenstelling promotiecommissie:

Rector Magnificus	voorzitter
Prof. dr. S. Calero	Universidad Pablo de Olavide, Promotor
Prof. dr. Ing. J. Gross	Technische Universiteit Delft, Promotor
Dr. ir. T.J.H Vlugt	Technische Universiteit Delft, Copromotor
Prof. dr. F. Kapteijn	Technische Universiteit Delft
Prof. dr. G.J. Witkamp	Technische Universiteit Delft
Prof. dr. ir. B. Smit	University of California at Berkeley
Dr. J.M. Simon	Université de Bourgogne

Cover image: Drop of water in microgravity – NASA. Available at http://commons.wikimedia.org/
Back cover images: Equipotential energy surfaces of zeolite STW (top) and MOF Lin (bottom). These and other figures in this thesis were generated using the Visual Molecular Dynamics (VMD) package, available at http://www.ks.uiuc.edu/research/vmd.

The author can be contacted by email: jmcassan@upo.es

Contents

Introduction

1.1. Zeolites

The name "zeolite" originated from the Greek words $\zeta\acute{\varepsilon}\omega$, "to boil" and $\lambda\acute{\iota}\theta o\varsigma$, "stone", and it can be translated as "stone that boils"[1]. This term was originally introduced by the Swedish mineralogist Axel Fredrik Cronstedt in the 18th century when he realized that certain minerals, when swiftly heated, expulsed water in the form of vapour[1]. The materials studied by Cronstedt were crystalline, aluminosilicate minerals formed in nature when volcanic rocks and ash layers react with alkaline ground water. As it will be discussed later, zeolites have a wide range of industrial and commercial applications nowadays. There are 48 different types of natural zeolites[2], and they are rarely found in a pure form but mixed with other zeolites or minerals such as quartz. For this reason, synthetic zeolites rather than natural are preferred for most commercial applications, although natural zeolites are usually cheaper to obtain. The number of known framework structures to date is close to two hundred[3].

The zeolite structure is formed by tetrahedral units (primary building units), with one oxygen atom at every vertex and one T atom at the centre, see Figure 1.1. The T atom is usually a silica or alumina atom, although some structures have been synthesized in which some of the T-atoms are replaced by other atom types like Ge, P, Mg, Mn, Co or Zn[4,5]. The generally accepted Löwenstein rule states that Al-O-Al sequences are energetically forbidden, although structures that violate this rule have been recently synthesized at high temperatures[6]. Due to the constraints imposed by the bond lengths and angles within the tetrahedral building blocks, only a limited number of primary building unit association geometries are available. In Figure 1.2, the secondary building units (SBUs), or different arrangement of tetrahedral units, that have been found in zeolites are shown. Zeolites can be completely described by the asymmetric unit cell of the particular zeolite and its space group, from which every atom position of the symmetric unit cell can be generated. A perfect, infinite zeolite crystal is obtained by copying the symmetric unit cell in all three directions in space. In reality, perfect zeolite crystals do not exist. Zeolite crystals often consist of complex inter-grown structures with internal grain boundaries and varying pore orientation[7]. One

common defect in zeolites is the rupture of one of the Si-O-Si bonds to form silanol groups Si-O-H, altering the crystal structure and the hydrophobic character of the zeolite[8].

Zeolite structures contain microporous in one or more dimensions, with diameters between 5 and 10 Å[3]. These microporous are responsible for most of their interesting properties. According to their pore arrangement, zeolites are usually classified in three different categories: straight channels, intersecting channels, and cages. Some typical examples are shown in Figure 1.3.

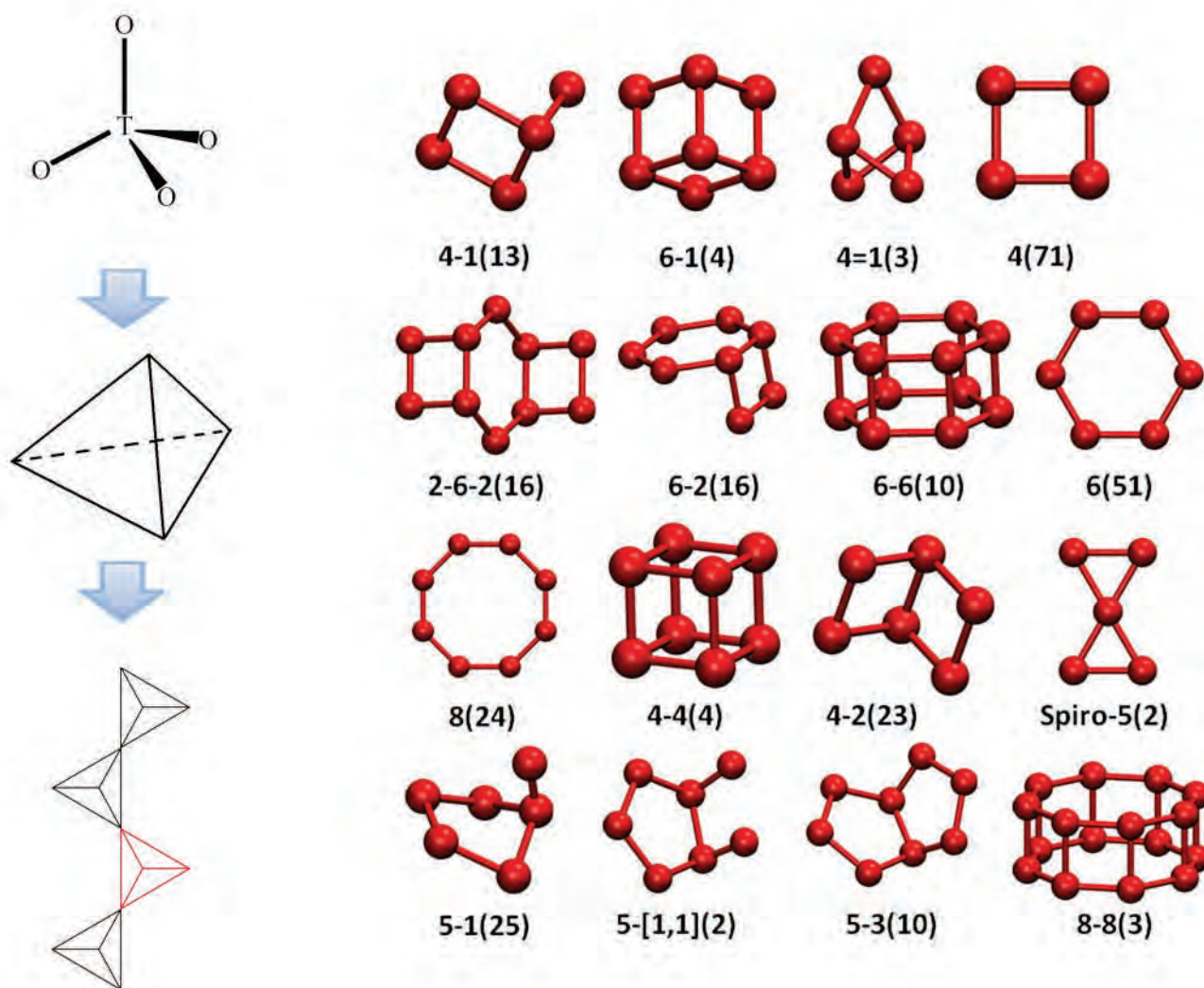**Figure 1.1**. *Primary building units (PBUs) in zeolites, and an example of linking.*

Figure 1.2. *Some examples of secondary building units (SBUs) present in zeolites. T atoms are represented by beads. The oxygen atoms are located approximately at the middle each line joining T atoms. The first numbers are the description code of the SBU, and the number in parenthesis the frequency of occurrence in zeolites[9].*

In pure siliceous zeolites, the number of oxygen atoms is twice as large as the number of silica atoms, and the electrostatic charge is perfectly balanced so that the zeolite is charge neutral. In the cases where framework silica atoms are substituted by alumina, the alumina atoms introduce a net negative charge. This is due to the different charge of aluminium (3^+) and silicon (4^+) ions. Therefore, this net negative charge has to be counter balanced by non-framework cations present in the zeolite pores. One important property of zeolites is the easy exchange of non-framework cations from solution[10]. This property makes zeolites ideal candidates for water purification and softening[11]. The selectivity of a zeolite for one specific cation depends on several factors such as temperature, pH, size and charge of the cation, the concentration of the cations in the solution, and the particular structure of the zeolite[12].
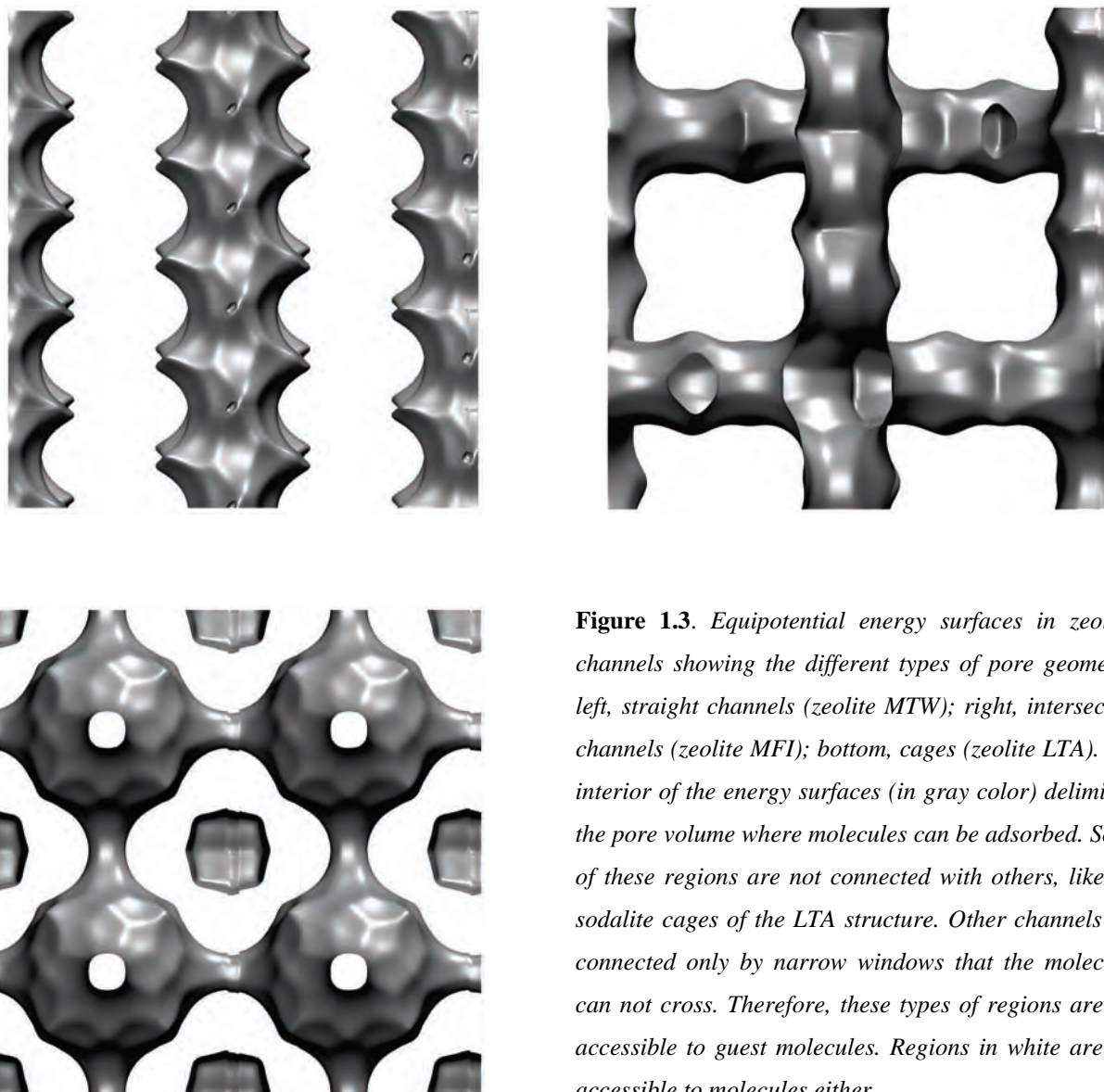
Figure 1.3. *Equipotential energy surfaces in zeolites channels showing the different types of pore geometry: left, straight channels (zeolite MTW); right, intersecting channels (zeolite MFI); bottom, cages (zeolite LTA). The interior of the energy surfaces (in gray color) delimitate the pore volume where molecules can be adsorbed. Some of these regions are not connected with others, like the sodalite cages of the LTA structure. Other channels are connected only by narrow windows that the molecules can not cross. Therefore, these types of regions are not accessible to guest molecules. Regions in white are not accessible to molecules either.*

The large surface area of zeolites, as well as their excellent thermal and chemical stability, makes zeolites suitable materials for a large number of applications, apart from the previously mentioned. Specific zeolites have to be chosen for a particular use depending on their particular characteristics such as hydrophilic character, pore volume, surface area, pore size, non-framework cations present in the structure, and cost:

- Zeolites are used as molecular sieves to separate gasses for different applications. For example, zeolites are used to produce highly purified medical oxygen or to remove water, carbon dioxide, and sulphur compounds from natural gas streams[13,14].

- Zeolites are widely used in petrochemical industry. Proton exchanged zeolites are powerful solid state Lewis acids that can act as catalysts for isomerisation, alkylation, and cracking reactions[15]. Their particular shape can be exploited to concentrate reactants at a particular active site, or to separate hydrocarbons[16].

- Zeolites are resistant to radiation[17]. They are able to efficiently trap many fission products and remove them from nuclear waste. Afterwards, the zeolite can be pressed into an extremely durable ceramic form, closing the pores and permanently trapping the waste in a solid stone block.

- The natural zeolite clinoptilolite (CLI) is used as a soil treatment, as it is a source of slowly released potassium or ammonium[18]. It also can retain water and release it depending on the plant demands, preventing root rot and moderating mild draught cycles[19].

- Even in low concentrations, zeolites are able to remove animal odors in animal sands[20].

- Zeolites can be used as energy storage materials for solar thermal collectors, due to their reversible adsorption of water[21].

- Zeolites are added to concrete to reduce its manufacture and laying temperature, providing easier compaction and improving break strength[22].

1.2. Metal-organic frameworks (MOFs)

MOFs are a relatively new type of materials, which were discovered in the search of porous materials with larger surface area and larger pores than existing materials, or the capability of tailor design. The first MOFs were synthesized in the early 1990's[23,24]. These structures are formed by molecular assemblies constructed by coordination bonds, where the main building units are metal complexes linked by organic

polydentate molecules[25]. Due to the large number of choices for both the metal complex and the organic linker, the number of potential structures that can be synthesized is enormous. The number of MOFs types synthesized to date is larger than two thousand[26]. Some of the most used organic ligands are shown in Figure 1.4.

Due to the large variety in chemical compositions available for MOFs, their properties can be quite different. In many cases MOFs have a well defined porous structure, with pores of different shape that range between very narrow openings that do not allow the adsorption of molecules[27] to pores with size close to mesopores (25-30 Å)[28]. Due to the particular way they are built (metal centers linked by large organic molecules), MOFs usually have a low density and a large pore volume. In general, MOFs are quite unstable, as upon heating or upon template removal they easily lose their crystal structure and decompose[29]. There are some cases where water can attack the metal centers and destroy the crystalline framework structure[30-32]. Other MOFs are stable upon the removal of the template, but these are often very flexible, changing their structure in the presence of some types of molecules[33,34]. The number of newly synthesized, stable MOFs with potential industrial and commercial applications grows at a fast pace. Figure 1.5 shows some examples of MOFs with different properties.
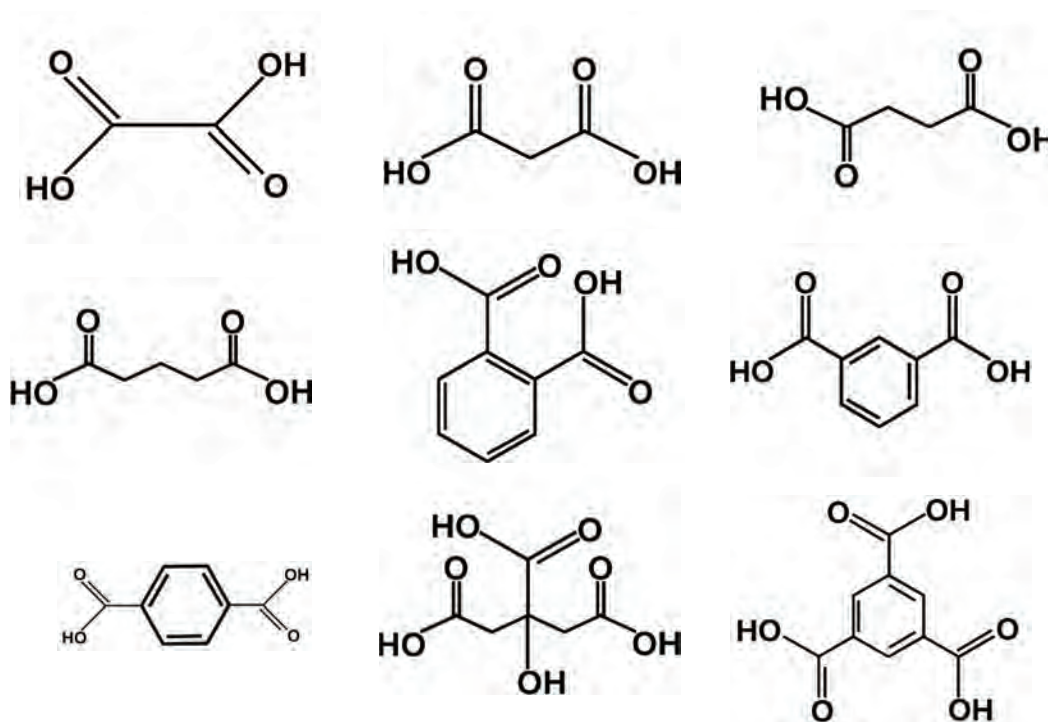
Figure 1.4. *Examples of often used organic linkers in Metal-Organic Frameworks. From left to right and top to bottom: oxalic acid, malonic acid, succinic acid, glutaric acid, phthalic acid, isophtalic acid, terephthalic acid, citric acid, and trimesic acid.*
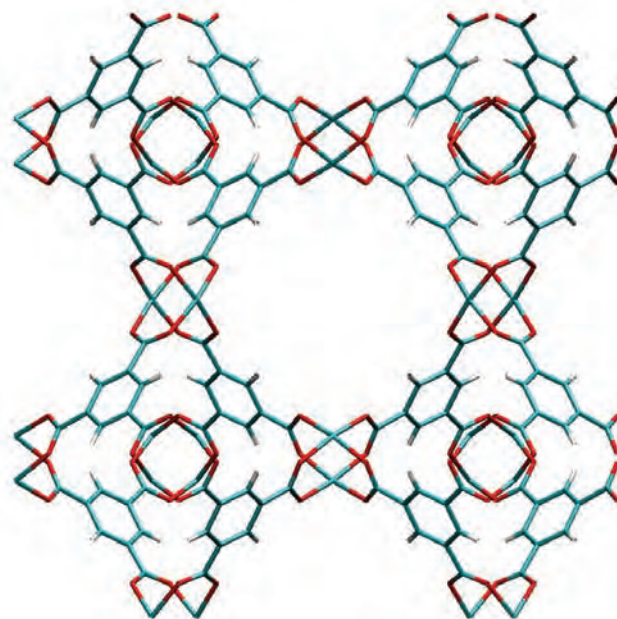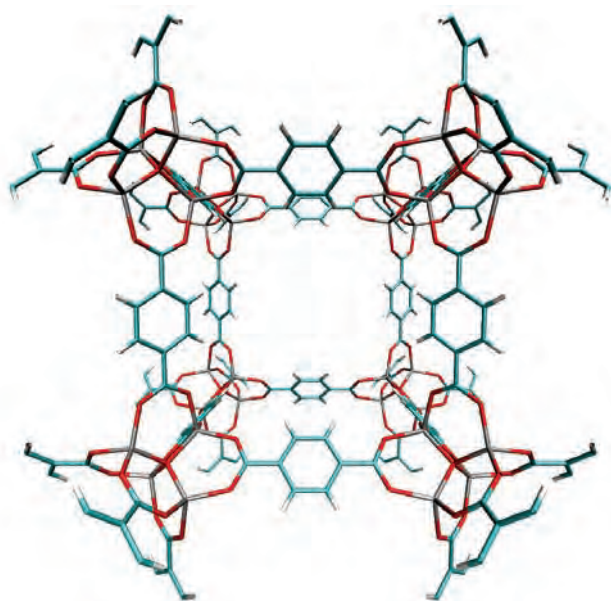
Figure 1.5. *Examples of MOFs structures. Left, IRMOF-1, a MOF with a very large pore volume[35]. Its metal center is Zn_4O and its linker molecule benzene dicarboxylate (BDC). a=b=c=25.832 Å. α=β=γ=90°. IRMOF-1 is quite flexible and decomposes in the presence of water. Right, Cu-BTC, another MOF with large pores, but with a more complicated structure consisting in large central pores and small side pockets[36]. It is formed by Cu atoms and benzene-1,3,5-tricarboxylate (BTC). a=b=c=26.343 Å. α=β=γ=90°. Cu-BTC is quite rigid and stable in the presence of water at ambient temperature. Bottom, Cu-5Fpymo, a stable structure with very small channels that can only adsorb very small molecules such as water[27]. It is formed by Cu atoms and 4-hydroxypyrimidine as linker molecule. a=b=20.4891 Å, c=10.1033 Å. α=β=γ=90°.*
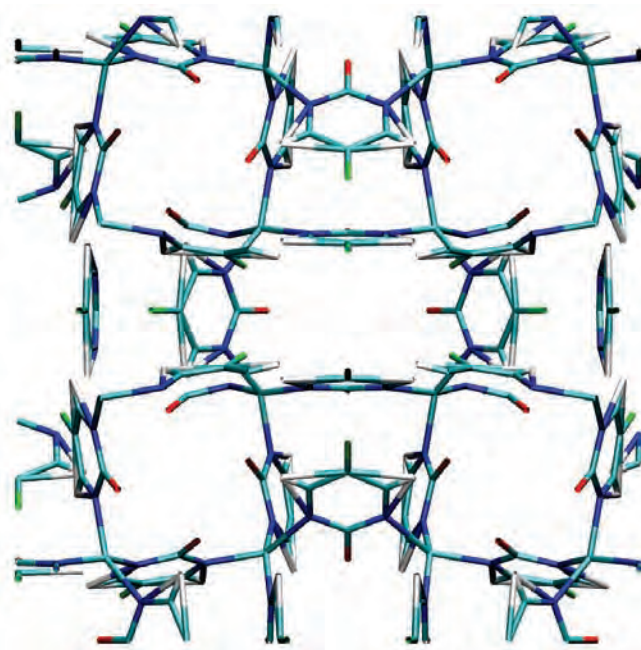
MOFs are not widely used in many real life applications yet. Nevertheless, some of these materials have shown to be effective in the separation of gasses, for example the different components of natural gas[37]. Future prospects are pressure swing separation of rare gasses and storage of hydrogen for its use as a fuel[38]. MOFs can also be easily modified to become active catalysts[38]. There are several studies on their possible use as drug delivery materials and other pharmaceutical applications[39]. Interestingly, a small number of MOFs is already commercially available, for example Cu-BTC, Fe-BTC and the alumina form of MIL-53[40].

1.3. Models and methods

In the previous section we gave a general description of zeolites and MOFs. In the following sections, we will describe the computational approach we will follow to study the adsorption and diffusion of guest molecules in these structures.

A classical, molecular model of a system needs to describe the geometry of the system, i.e. the arrangement of the atoms forming molecules, and the way every atom/molecule interacts with each other. Both geometry and interactions will generally depend on the chemical nature of every atom. Such model is generally called *force field*. It is necessary to choose a force field that is appropriate to study the properties of interest. The force field will generally be more complex as more realistic calculations are required. For reducing the calculation time, it is convenient to use the simplest model suitable to study the property of interest with the desired accuracy. Many different force fields exist, such as AMBER[41,42], widely used for modeling proteins and DNA, or CHARMM[43] and CVFF[44], used for macromolecules and proteins. In this work we use force fields specially designed for the description of molecules in microporous systems[45].

In this chapter we describe the force fields used to study the adsorption of water and other guest molecules in microporous materials. The precise values of the force field parameters for every specific calculation are given in sections 2.2, 3.3, 4.2, 5.3, 6.2, and 7.2.

The total energy of the system U^{total} is separated in two parts, bonded interactions between linked atoms, and non-bonded interactions between non-linked atoms:

$$U^{total} = U^{bonded} + U^{non-bonded}$$

(1.1)

Non-bonded interactions are also considered between atoms belonging to the same molecule, if they are separated more than three atomic bonds. The non-bonded potential consists of two parts, a contribution of electrostatic origin and another contribution corresponding to the dispersive interactions between molecules:

$$U^{\,non\text{-}bonded} = U^{\,Coulomb} + U^{\,dispersive} \tag{1.2}$$

In this study, dispersive interactions are modelled with a Lennard-Jones pair potential:

$$U^{\,dispersive} = \sum_{j=1}^{N}\sum_{i<j}^{N} U^{\,LJ}(r_{ij}) \tag{1.3}$$

with

$$U^{\,LJ}(r_{ij}) = 4\varepsilon\left[\left(\frac{\sigma}{r_{ij}}\right)^{12} - \left(\frac{\sigma}{r_{ij}}\right)^{6}\right] \tag{1.4}$$

where r_{ij} is the distance between the interacting particles i and j, N the number of particles, σ the size parameter of the potential and ε the energy parameter. The summation in Eq. (1.3) is carried out for all particle pairs. This potential is repulsive at short distances, and has a minimum at $r_{min} = 2^{1/6}\sigma$ with $U^{LJ}(r_{min}) = -\varepsilon$. As the potential rapidly vanishes for large distances, it is usually *truncated and shifted* at a certain *cutoff radius* r_{cutoff}.

$$U^{\,LJ}_{shift}(r_{ij}) = \begin{cases} U^{\,LJ}(r_{ij}) - U^{\,LJ}(r_{cutoff}) & r_{ij} < r_{cutoff} \\ 0 & r_{ij} > r_{cutoff} \end{cases} \tag{1.5}$$

The electrostatic term is calculated from the Coulombic interaction between point charges:

$$U^{\,Coulomb} = \sum_{j=1}^{N}\sum_{i<j}^{N} \frac{1}{4\pi\varepsilon_0}\frac{q_i q_j}{r_{ij}} \tag{1.6}$$

where ε_o is the electric constant of vacuum ($8.85\cdot10^{-12}$ C^2 s^2 kg^{-1} m^{-3}) and q_i, q_j the charges of particles i and j. We do not include polarization effects.

With molecular simulations we can only describe a limited number of atoms, usually in the order of a few thousands, within the limit of a reasonable simulation time. This is a serious limitation in the size of the system we can describe with classical molecular simulations, as real systems usually have a number of

atoms or molecules of the order of Avogadro's number ($N_{AV}=6.022 \cdot 10^{23}$ molecules/mol). Furthermore, for a system with a few thousand atoms the ratio of the total area and the volume is quite large compared to bulk systems (i.e. systems with of the order of N_{AV} molecules). Therefore, surface effects have a large influence on the properties we compute. To avoid these inconveniences, we use *periodic boundary conditions*. With this method, the volume containing the system is infinitely replicated in each direction of space depending on the dimensionality of the problem (see Figure 1.6). For calculating the interaction energy U_i of a single particle we need to consider the total interaction with all the periodic images. This leads to:

$$U_i = \sum_{j=1, j \neq i}^{N} U(r_{ij}) + \sum_{n>1} \sum_{j=1}^{N} U\left(\left| r_{ij} + n\mathbf{L} \right| \right) \qquad (1.7)$$
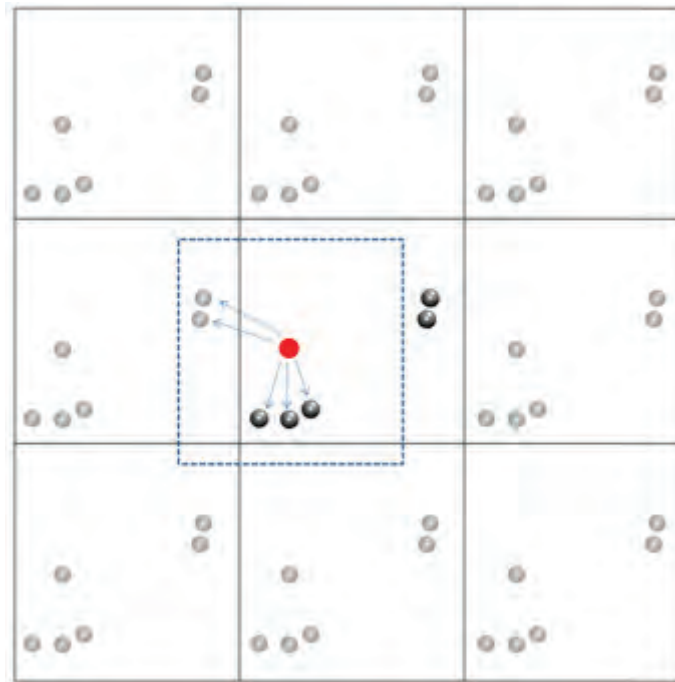

Figure 1.6. *Periodic boundary conditions and the nearest image convention. For the highlighted particle, the only interactions that have to be calculated using the nearest image convention are indicated with an arrow.*

In the case of truncated interactions, it is only necessary to consider the particles j whose distance to the interaction center i is less than the cutoff radius r_{cutoff}. If the condition $r_{cutoff} < \boldsymbol{L}/2$ is satisfied (being $\boldsymbol{L}$ a vector whose components are the box lengths a b c), it is only necessary to consider the nearest periodic image of j to i (see dotted box in Figure 1.6). This is called the *nearest image convention*[46,47]. For calculating the interactions due to the Coulombic, long range potential of Eq. (1.6), special methods are needed, which will be discussed in section 1.3.3.d.

1.3.1. Modeling porous materials

The International Zeolite Association classifies the different types of zeolites according to their framework type[9]. Structures with the same geometry but with different chemical composition are considered to be the same framework, as it is the case of zeolites with different degree of alumina substitution[9]. In the present work we will only consider zeolites in their pure siliceous form. The former classification has been extended to MOFs, with some exceptions. For example, the metal center of MIL-53 can be alumina, iron, chromium or indium, while the vanadium form of this MOF is called MIL-47. The reason for classifying the same framework type by two different names arises from their different properties. While MIL-53 is a very flexible structure that adapts its geometry to guest molecules, MIL-47 is very rigid[48]. These particular structures are a good example where framework flexibility can be vital in the description of the system[49].

1.3.1.a. Models for rigid frameworks

Both zeolites and MOFs are crystalline structures, and therefore they are completely described in terms of their unit cell and their space group. Their atomic structures can be resolved from different diffraction techniques (X-ray diffraction, electron diffraction, neutron diffraction, small angle X-ray scattering (SAXS), etc), absorption techniques (extended X-ray absorption fine structure (EXAFS), X-ray absorption near edge structure (XANES)) or nuclear magnetic resonance (NMR), provided that large enough crystals can be synthesized[50]. X-ray diffraction is the most common technique to resolve atomic positions. Bombarding a large crystal with X-rays produces a diffraction pattern of regularly spaced dots known as *reflections*[50]. The two dimensional images obtained at different angles of incident radiation, combined with chemical data known for the sample, are converted in a three-dimensional model of the density of electrons within the crystal using a Fourier transform method[50].

Atom Type	Site Multiplicity	X	Y	Z
T_1	24	0.0000	0.1823	0.3684
O1	12	0.0000	0.2122	0.5000
O2	24	0.1103	0.1103	0.3384
O3	12	0.0000	0.2967	0.2967

Table 1.1. *Coordinates of LTA-atoms in the cubic space group Pm 3m (group number 221). The cell parameters are: a = b = c = 11.919 Å   α = β = γ = 90°* [9]. *With this data, the unit cell of the framework structure LTA is completely described.*

To describe a rigid framework structure in our simulations, we simply place the appropriate framework atoms at their crystallographic positions. As an example, in Table 1.1, we provide the spatial group and location of the atoms in the asymmetric unit cell of the zeolite LTA[3]. The location of all atoms in the unit cell can be found from this information.

Apart from the atomic positions, we need to describe the interactions of each atom with another. If atomic positions are fixed, there is no need to consider interactions between framework atoms, but only interactions with adsorbents and non-framework atoms. According to Eq. (1.2), non-bonded interactions consist of dispersive and electrostatic interactions. The dispersive interactions are usually described by Lennard-Jones terms Eq. (1.4). Lennard-Jones interactions between different atom types are often computed using the Lorentz-Berthelot mixing rules[46]:

$$\varepsilon_{ij} = \sqrt{\varepsilon_{ii} \cdot \varepsilon_{jj}} \tag{1.8}$$

$$\sigma_{ij} = \frac{1}{2}\left(\sigma_{ii} + \sigma_{jj}\right) \tag{1.9}$$

in which ε_{ii} and σ_{ii} are the Lennard-Jones parameters for the interaction between particles of type *i*. For a better characterization of the system, the dispersive interaction between the framework and the adsorbents is usually fitted to experimental data[51]. In the case of zeolites, every silicon or aluminum atom is surrounded by four oxygen atoms. Therefore, the oxygen atoms are dominating the dispersive forces between guest molecules and the zeolite[52-54]. For this reason, only effective dispersive interactions with framework oxygen atoms are taken into account.

Electrostatic interactions are taken into account by assigning partial charges to every atom of the zeolite. These charges can be estimated using quantum chemistry calculations. However, there is not an

unambiguous way to do this. In principle, they can also be fitted to reproduce experimental data, assuming that their values are physically consistent. We show an example of this procedure in section 4.3.

1.3.1.b. Models for flexible frameworks

In some cases, taking into account framework flexibility is important to correctly describe properties of the system. For example, the diffusion of molecules in zeolites may depend strongly on framework flexibility[55], while for adsorption of alkanes flexibility is not important[56]. In our study we only consider rigid MOF structures, as the particular MOFs we model are quite rigid upon the adsorption of molecules. Although some flexible models have been proposed for some types of MOFs[49,57], developing such models is very time consuming and is beyond the scope of this work.

We use the Nicholas model[58] to describe flexible zeolite frameworks. This model is in principle able to describe any type of flexible zeolite. It consists on different bonded potentials between the atoms of the framework, as well as dispersive and electrostatic interactions between all atoms of the framework separated by more than three bonds. The crystallographic atomic positions of the zeolite approximately describe the minimum energy configuration of the framework. The different bonded potentials considered in this model are:

• **Bond stretching**. The Si-O bond is modeled with a harmonic potential

$$U^{bond}(r) = \frac{k_r}{2}\left(r - r_{eq}\right)^2 \tag{1.10}$$

where $k_r/k_B = 300724.776635821$ K is the energy constant of the potential (k_B is the Boltzmann constant) and r_{eq} the equilibrium distance between atoms, taken from the crystallographic structure of the particular zeolite.

• **Bond bending**. The O-Si-O angle bend is also modeled with a harmonic potential

$$U^{bend}_{O-Si-O}(\theta) = \frac{k_\theta}{2}\left(\theta - \theta_{eq}\right)^2 \tag{1.11}$$

while the Si-O-Si angle bend is fitted to ab-initio data with a fourth order expression

$$U^{bend}_{Si-O-Si}(\theta) = \frac{k_{\theta_1}}{2}\left(\theta - \theta_{eq}\right)^2 - \frac{k_{\theta_2}}{2}\left(\theta - \theta_{eq}\right)^3 + \frac{k_{\theta_3}}{2}\left(\theta - \theta_{eq}\right)^4 \qquad (1.12)$$

$k_\theta/k_B = 69537.4441655052$ K, $k_{\theta1}/k_B = 5462.50556903947$ K, $k_{\theta2}/k_B = -17157.8055108631$ K and $k_{\theta3}/k_B = 13351.6725982421$ K are constants and θ_{eq} the equilibrium bend angle, taken from the crystallographic structure of the particular zeolite.

• **Bond-bend coupling**. It has been observed experimentally that the Si-O bond stretches when the Si-O-Si angle becomes smaller. A Urey-Bradley term is included to take this effect into account:

$$U^{U-B}(r) = \frac{k_s}{2}\left(r_{Si-Si} - r_{eq}\right)^2 \qquad (1.13)$$

in which r_{Si-Si} is the Si-Si distance in a Si-O-Si bend sequence and $k_s/k_B = 27488.7377022631$ K the energy parameter of the potential. Note that r_{eq} in Eq. (1.13) and Eq. (1.10) are different in general.

• **Torsion**. It is taken into account with a torsion potential between four linked atoms A-B-C-D:

$$U^{tors}(\varphi) = \frac{k_\varphi}{2}(1 + \cos(3\varphi)) \qquad (1.14)$$

with $k_\varphi/k_B = -176.209857065789$ K the energy parameter of the potential and φ the torsion angle. The torsion angle is the dihedral angle between the two planes defined by the groups of three linked atoms A-B-C and B-C-D.

• **Switching function**. An empirical switching function is coupled to the torsion potential to avoid discontinuities in the torsion energy when the bond-bending angle approaches 180°.

For details about the switching function and the value of the equilibrium parameters of the force field, the reader is referred to the original publication[55,58]. In this work we change the original point charges of the framework atoms to adapt them to our needs. This is consistent with the fact that the flexibility of the zeolite is mainly determined by the bonded potentials.

1.3.2. Models for adsorbed guest molecules

In this work we only use atomistic, classical models of atoms and molecules. In these models, one atom or set of atoms is represented by a single interaction center called *pseudo atom*. Pseudo atoms are the center of dispersive interaction and may carry a partial charge. In Molecular Dynamic simulations, described in section 1.3.3.3, the masses of the pseudo atoms need to be known. Pseudo atoms are linked by rigid or flexible bonds in such a way that their geometry resembles the geometry of the molecule. In some cases, models may include pseudo atoms that do not correspond to actual atoms in order to better describe some properties of the real molecules, such as their quadrupole moment. The bonded interactions are easily fitted from quantum chemistry calculations. The non-bonded interactions between guest molecules are fitted to reproduce specific properties, such as the vapor-liquid equilibrium curve (VLE), the liquid density, or the location of the triple point. For this reason, the further we use the model from the particular fitting conditions the worse the model will account for the properties of the molecule.

1.3.2.a. Water models

Due to the extensive use of molecular simulations for studying water containing systems, the number of water models available in the literature is huge[59]. Although many different water models have been developed, there is not any that fully captures the complex behavior of this molecule[59]. Force fields have been designed to describe water at specific conditions, such as bulk water at different temperature, pressure and phase. There are also force fields to describe the interaction of water with macromolecules and proteins, or to reproduce specific properties such as critical parameters, the heat of vaporization, the microscopic structure or the dielectric constant[59].

Most molecular models of water can be classified in one of the categories depicted in Figure 1.7. Many of these models use a wider bend angle and longer O-H bond length than the ones found experimentally in the gas and liquid phase. This is to increase the hydrogen bonding capacity of the force field, which is necessary to reproduce experimental properties of water[59]. Another common practice is displacing the negative partial charge of the oxygen atom closer to the hydrogen atoms, in order to obtain a larger dipole moment than the gas phase value necessary to reproduce many liquid state properties[59]. Other models introduce additional pseudo atoms to give the molecule the tetrahedral geometry that is found in the liquid and solid phases of water[60]. Finally, the more refined models include flexibility and polarization, or complex interaction potentials fitted from ab-initio calculations[61,62].
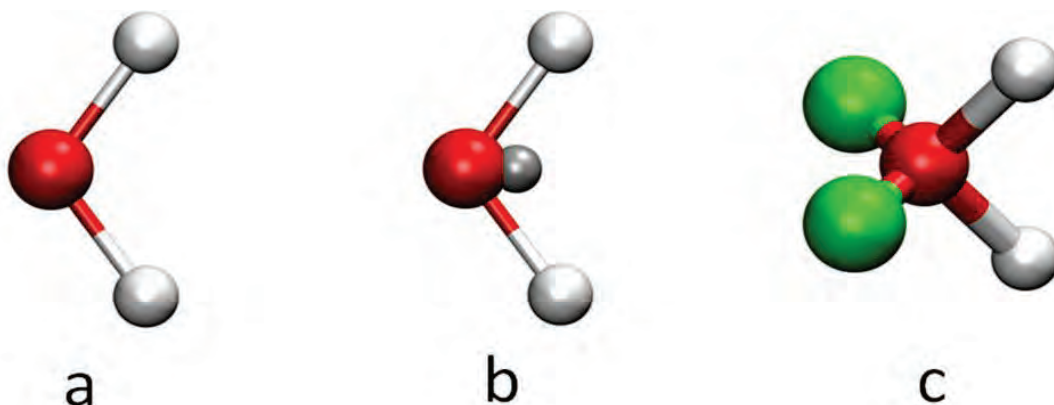
Figure 1.7. *Common types of water models. a) One pseudo atom at the location of each atom (SPC[63], SPC/E[64], SPC/Fw[65], Tip3p[66], Tip3p/Fw[65], F3C[67]); b) One extra pseudo atom is added to change the internal charge distribution (Tip4p[68], Tip4pEw[69], Tip4p-FQ[70], Tip4p-Ice[71], Tip4p/2005[72]); c) Two extra pseudo atoms are added to generate a tetrahedral structure (ST2[73], Tip5p[60], Tip5p-Ew[74]).*

In this work, all calculations will be based on the Tip5pEw model[74], which is a five-site model with a rigid, tetrahedral geometry (see Figure 1.7.c). It has a single dispersive center at the oxygen atom, and point charges located at the hydrogen and two pseudo atoms, the latter accounting for the negative partial charge of the oxygen atom, which does not carry any charge. For a discussion on the selection of this particular model, the reader is referred to section 2.3.

1.3.2.b. Alkane model

Contrarily to the case of water, alkanes can be easily modeled to reproduce their most important physical properties. The main difference with water is the fact that the electrostatic energy can be neglected, as dispersive interactions are dominating. Nevertheless, hydrocarbons are quite flexible molecules, especially when the chain length is large. For this reason we will model hydrocarbons using the flexible, united-atom, TraPPE model[75,76]. In this model, every CH_x group in the molecule is represented by a single pseudo atom. This pseudo atom, which does not possess any partial charge, is the center of the dispersive interaction. Pseudo atoms are linked together by bonded potentials, as shown in Figure 1.8. The bond length between two atoms is fixed, while three consecutive atoms interact with the harmonic bending potential of Eq. (1.11). The torsion potential of four consecutive atoms is of the OPLS type[77]:

$$U^{tors}(\varphi) = c_0 + c_1[1 + \cos\varphi] + c_2[1 - \cos(2\varphi)] + c_3[1 + \cos(3\varphi)] \qquad (1.15)$$

were c_o, c_1, c_2 and c_3 are energy parameters of the potential and φ the torsion angle. For the values of the different parameters of the potentials, the reader is referred to the original publications[75,76].
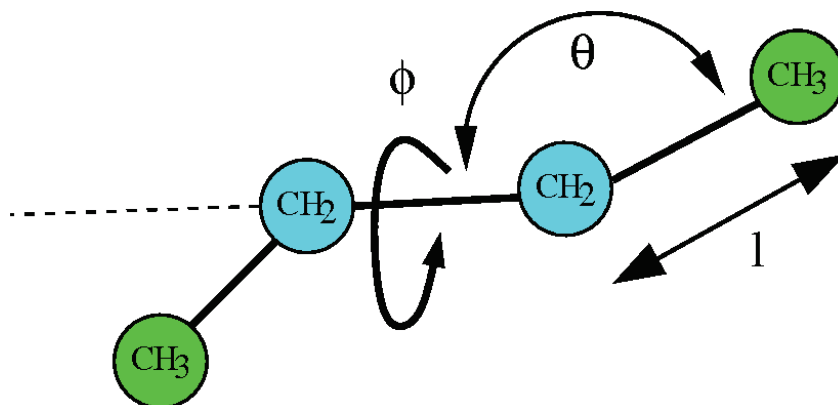
Figure 1.8. *Schematic representation of an alkane molecule using a united-atom model. l is the bond length, θ the bend angle and φ the torsion angle.*

1.3.2.c. CO₂ model

CO_2 is a linear molecule with a large quadrupole moment, see Figure 1.9. We will use the rigid model of Harris[78] to characterize this molecule. It consists of three pseudo atoms, each of them being the center of a dispersive potential and carrying a partial charge.
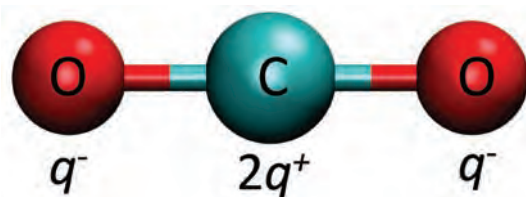
Figure 1.9. *Rigid model of a CO₂ molecule. The experimental quadrupole of this molecule is reproduced assigning partial charges to each pseudo-atom (q^+ = 0.3256 e). The bond length (1.149 Å) is taken from experiments[79].*

1.3.3. Simulation methods

1.3.3.a. Introduction to statistical mechanics

The aim of molecular simulations is to describe a system using a molecular model in order to predict its properties. For example, with molecular simulations we would easily observe the orientation and arrangement of molecules inside a zeolite. To connect the simulation with the real world and make useful predictions, it is crucial to compare the result of the calculations with macroscopic properties of the system which can be measured experimentally, such as temperature, pressure or diffusion coefficients. This connection between the microscopic and macroscopic view of the system can be achieved using *statistical mechanics*. In particular, we will use the classical statistical mechanics theory[80].

Let's consider a very large system of N classical particles (not relativistic, no quantum effects). This system is dynamically described by 3N spatial coordinates $\boldsymbol{q}$, and 3N velocity (or linear momentum) coordinates $\boldsymbol{v}$. This means that every *microstate*, or microscopic state of the system, is uniquely described by 6N variables. In a 6N-dimensional coordinate system we can plot this microstate as a point. Such 6N-dimensional coordinate system is called *phase space*. We can also describe the system in terms of its number of molecules N, its energy E and its volume V. From the microstate we can easily calculate the macrostate, or macroscopic state of the system, in terms of number of particles N, volume V and energy E. If the system is isolated and in thermodynamic equilibrium, the macrostate will have constant values of N, V, and E while the system can change between different microstates with the same values for N, V and E. There is a large number of microstates that describe the same macrostate of the system. In the phase space, the microstates that are compatible with the macrostate NVE will define a (hyper)volume described by a density function $\mathcal{N}(\boldsymbol{q},\boldsymbol{v})$. The crucial postulate of statistical mechanics is that all these microstates are equally likely:

$$\mathcal{N}(\boldsymbol{q},\boldsymbol{v}) = \delta\big(H(\boldsymbol{q},\boldsymbol{v}) - E\big) \tag{1.16}$$

H is the Hamiltonian function, which is the total energy of the system. $\delta(x)$ is the Dirac's delta function, which is zero for every x except when x=0, with $\delta(0)=\infty$. The integral of Dirac's delta function equals the unity. This microstate density is called *microcanonical ensemble*.

The thermodynamic properties of the system can be obtained from the properties of the microstates. If Ω is the number of microstates compatible with one single macrostate, we have[80]:

$$S = k_B \cdot \ln \Omega \tag{1.17}$$

where k_B is the *Boltzmann's constant* ($1.3806503 \cdot 10^{-23}$ m^2 kg s^{-2} K^{-1}) and S the entropy of the system. Usually we not only wish to describe isolated systems, but systems in thermal equilibrium where N, V and the temperature T are constant. In that case, following a similar formulation we obtain a different microstate density called *canonical ensemble*. In absence of electromagnetic fields, the velocities of the particles can be integrated to obtain:

$$\mathcal{N}(\boldsymbol{q}) = \frac{\exp(-\beta E_i)}{\sum_j \exp(-\beta E_j)} = \frac{\exp(-\beta E_i)}{Q(N,V,T)}, \beta = \frac{1}{k_B \cdot T} \tag{1.18}$$

were $\mathcal{N}(\boldsymbol{q})$ is the probability that the system is in the microstate i with energy E_i. The numerator is called *Boltzmann factor* and the summation in the denominator is a normalization factor called the *partition function* of the system: Q(N,V,T). From the partition function we can obtain all the thermodynamic information on the system, as we can directly compute the Helmholtz free energy as a function of N, V and T[80]:

$$A(N,V,T) = -k_B T \ln Q(N,V,T) \tag{1.19}$$

However, Q(N,V,T) can only be calculated exactly for a limited number of systems such as the ideal gas. Similarly, we can calculate the microstate density in other ensembles. For example, in the *grand-canonical*, or μVT ensemble, where the volume, temperature and chemical potential μ are constant, the density of microstates is, in absence of electromagnetic fields:

$$\mathcal{N}(\boldsymbol{q}, N) = \frac{V^N}{\Lambda^{3N} N!} \frac{\exp(\beta \mu N_i - \beta E_i)}{\sum_j \exp(\beta \mu N_j - \beta E_j)} \tag{1.20}$$

where Λ is the thermal de Broglie wavelength:

$$\Lambda = \frac{h}{\sqrt{2\pi \cdot mkT}} \tag{1.21}$$

h is the Plank's constant ($6.626 \cdot 10^{-34}$ J s). From these probabilities we can obtain expressions for the thermodynamic potentials. To calculate a property of the system, it is necessary to average the value of that property over all the possible microstates. For example, if A is the property we would like to measure in a canonical ensemble and <A> its average value, we will need to calculate:

$$\langle A \rangle = \frac{\sum_i A \cdot \exp(-\beta E_i)}{\sum_i \exp(-\beta E_i)} \tag{1.22}$$

In the next section, we will show how to compute averages of this type. Finally, we can argue that in a real experiment we measure a property of the system by averaging over the time evolution of the system. The *ergodic hypothesis* states that this time averaging equals the previous ensemble averaging[80]:

$$\langle A \rangle = \lim_{t \to \infty} \frac{1}{t} \int A(\boldsymbol{q}, \boldsymbol{v}) \cdot dt \tag{1.23}$$

Time averages Eq. (1.23) corresponds to Molecular Dynamic methods (integration of Newton's equations of motion, section 1.3.3.c). Averages over microstates Eq. (1.22) can be computed efficiently using Monte Carlo methods (section 1.3.3.b).

1.3.3.b. Monte Carlo

The objective of the Monte Carlo method is calculating system properties from the approach reflected in Eq. (1.22). The main problem we face is that the number of microstates is usually too large to be computed (it would take beyond the lifetime of the universe using all computers in the world). In addition, for most systems only a small fraction of the microstates has a Boltzmann factor different from zero[47]. Calculating Eq. (1.22) by enumeration or random shooting will therefore lead to zero for both the numerator and the denominator.

Although we can not calculate the numerator and denominator of Eq. (1.22) directly, it is still possible to estimate <A> numerically. This can be done using *importance sampling*. Suppose that we are able to

generate configurations *i* with an a-priori probability that is proportional to the Boltzmann factor. In this case:

$$\langle A \rangle = \lim_{n \to \infty} \frac{1}{n} \sum_{i=1}^{n} A(\boldsymbol{q}(i), \boldsymbol{v}(i)) \tag{1.24}$$

The *Metropolis Monte Carlo method* [81] can be used to generate such a sequence of configurations. Consider a starting microstate of the system *o*. We generate a new configuration *n*, and determine the probability π of changing the configuration *o* by *n*. This probability can be expressed as the probability of selecting such new configuration (α) multiplied by the probability of accepting it (*acc*):

$$\pi(o \to n) = \alpha(o \to n) \cdot acc(o \to n) \tag{1.25}$$

Whatever the rule is to move from one state to the next, the underlying equilibrium distribution $\mathcal{N}$ should not be destroyed. This condition leads to:

$$\mathcal{N}(o) \sum_{n} \pi(o \to n) = \sum_{n} \mathcal{N}(n) \pi(n \to o) \tag{1.26}$$

where the summation is over all possible new states that are accessible from the state *o*. This is the so-called *balance equation*. It is convenient to impose strict *detail balance* by requiring that all terms in Eq. (1.26) are equal[46,47,82]. With this condition, Eq. (1.26) is clearly satisfied, and we have:

$$\mathcal{N}(o) \cdot \alpha(o \to n) \cdot acc(o \to n) = \mathcal{N}(n) \cdot \alpha(n \to o) \cdot acc(n \to o) \tag{1.27}$$

A symmetric a-priori probability of selecting trial moves ($\alpha(o \to n) = \alpha(n \to o)$) leads, in the canonical ensemble, to:

$$\frac{acc(o \to n)}{acc(n \to o)} = \exp(-\beta[U(n) - U(o)]) = \exp(-\beta \Delta U) \tag{1.28}$$

There are many options for selecting the acceptance probability $acc(o \to n)$ that obey Eq. (1.28). The choice by Metropolis is[81]:

$$acc(o \to n) = \min(1, \exp(-\beta \Delta U)) \tag{1.29}$$

in which min(a,b) = a if a<b and vice versa.

It is important to start a Monte Carlo simulation from a representative equilibrium configuration. However, a randomly selected or arbitrary configuration may be far away from typical configurations at equilibrium. Therefore, one should neglect the first part of the simulation and not consider these configurations for computing averages Eq. (1.24).

A typical Monte Carlo simulation consists of the following, randomly selected, trial moves[47]:

• **Translation**. In this MC move, the position of the center of mass of a randomly selected molecule i in the system is displaced by a random vector:

$$x_i(n) = x_i(o) + \Delta(Random - 0.5)$$
$$y_i(n) = y_i(o) + \Delta(Random - 0.5) \qquad (1.30)$$
$$z_i(n) = z_i(o) + \Delta(Random - 0.5)$$

where Δ is the maximum displacement and *Random* is a uniformly distributed random number between 0 and 1. The value of Δ has to be chosen to have a reasonable fraction of accepted moves. If Δ is very small, most displacements will be accepted, but this will lead to a very inefficient sampling of the phase space. If Δ is very large, most of the trial moves will be rejected. The optimum value of Δ depends on the characteristics of the interaction potential. It has been suggested that the optimal value of Δ for the type of potentials we use in this work is such that approximately 50% of the trial moves is accepted[47]. The acceptance probability of this trial move is given by Eq. (1.29).

• **Rotation**. For molecules consisting of more than one interaction center, the rotational degrees of freedom of the molecule can be sampled by a random rotation. Either the x, y or z axis of the coordinate system can be selected as a rotation axis. For example, for a rotation around the z axis we will have:

$$r' = \begin{pmatrix} \cos\Delta\theta & -\sin\Delta\theta & 0 \\ \sin\Delta\theta & \cos\Delta\theta & 0 \\ 0 & 0 & 1 \end{pmatrix} \cdot r \qquad (1.31)$$

where r is the vector that contains the coordinates of a molecule, r' the coordinates after the rotation, and $\Delta\theta$ the rotated angle in a counterclockwise direction.

The maximum rotation angle is chosen such that on average a 50% of rotations are accepted[47]. The acceptance probability of this trial move is given by Eq. (1.29).

• **Insertion and deletion of molecules using the CBCM algorithm**. In the grand-canonical ensemble, the number of guest molecules present in the system is not constant. This ensemble is useful when we want to calculate *adsorption isotherms* in a porous material. The adsorption isotherm gives the number of guest molecules adsorbed as a function of pressure (or chemical potential) at a given temperature.

Inserting or deleting a randomly selected guest molecule of the system can be achieved with a conventional MC scheme[83]. When the system is very dense or the molecules are large, the probability of a successful insertion of a new molecule at a random position will be very small, as the inserted molecule will often overlap with molecules already present in the system, leading to very large interaction energies. The insertion of chain molecules can be improved with the Configurational-bias Monte Carlo (CBMC) method[84-87]. We insert the pseudo atoms of the molecule one by one, and select the most favorable positions from several insertion trials at each step. This procedure is repeated until the entire chain is grown. The non-random insertion of a chain introduces a bias in the generated configuration. This bias can be removed in the acceptance rule. The steps for inserting a molecule in the system with CBMC are[47]:

1. Generate k insertion positions for the first atom (pseudo atom) of the molecule. Calculate the interaction energy of the atom with the rest of the system at those positions $U_1(l)$, and select one position with probability:

$$P^l = \frac{\exp\left[-\beta U_1(l)\right]}{w_1} \qquad (1.32)$$

where

$$w_1 = \sum_{j=1}^{k} \exp\left[-\beta U_1(j)\right] \qquad (1.33)$$

2. For the next atom *i* of the molecule, generate k trial positions $\mathbf{b_i} = (b^1, b^2, ...b^k)$. These trial positions are generated according to the probability distribution:

$$P(\mathbf{b}_i) \propto \exp\left[-\beta U^{bonded}(\mathbf{b}_i)\right] \tag{1.34}$$

The probability of generating the orientations $\mathbf{b_i}$ is proportional to the Boltzmann factor, only taking into account the bonded interactions. In this way, we assure that we generate appropriate molecular geometries.

3. Calculate the non-bonded interactions of the k trials positions with the atoms already grown of the molecule and the rest of the system. Of all k trial positions for atom *i* we select one with probability:

$$P(\mathbf{b}_i^l) = \frac{\exp\left[-\beta U^{non-bonded}(\mathbf{b}_i^l)\right]}{w_i} \tag{1.35}$$

$$w_i = \sum_{j=1}^{k} \exp\left[-\beta U^{non-bonded}(\mathbf{b}_i^j)\right] \tag{1.36}$$

4. Repeat step 2 and 3 until the whole molecule of length M is grown, and calculate the *Rosenbluth factor* of the new configuration:

$$W(n) = \frac{1}{k^M} \prod_{i=1}^{M} w_i \tag{1.37}$$

The new molecule inserted in the system is transferred from an ideal gas reservoir in equilibrium with our system. We also need to calculate the Rosenbluth factor of the molecule in the old configuration, in this case a molecule in the ideal gas reservoir:

1. For the first atom *i* in the molecule, generate a set of k-1 trial insertions for that atom. For the rest of the atoms of the molecule, generate k-1 trial orientations from the Boltzmann distribution of the bonded interactions Eq. (1.34). Another k'th insertion and trial orientations are added in such a way that they generate the old configuration of the chain.

2. Compute the factors w_i from Eq. (1.33) and Eq. (1.36) for the k configurations generated for each atom i

3. Calculate the Rosenbluth factor of the old conformation:

$$W(o) = \frac{1}{k^M} \prod_{i=1}^{M} w_i \qquad (1.38)$$

The Rosenbluth factor of the old configuration can be calculated in advance from an independent simulation[47,52]. In this case, we need to calculate the average Rosenbluth factor of an ideal chain, $<W_{IG}>$. For calculating $<W_{IG}>$ we can apply the former procedure to a large, empty system with only one molecule present.

The acceptance probability that removes the bias in the insertion of a molecule is[47]:

$$acc(o \rightarrow n) = \min\left(1, \frac{V \exp(\beta\mu)}{\Lambda^3 (N+1)} \frac{W(n)}{\langle W_{IG} \rangle}\right) \qquad (1.39)$$

In a grand-canonical ensemble we also have to consider the possibility of removing molecules from the system. To obey detailed balance (Eq. (1.27)), the same procedure has to be applied to derive the acceptance rule for removing a guest molecule. The difference is that the old configuration is now a randomly selected molecule of the system. The acceptance rule for removing a guest molecule from the system equals:

$$acc(o \rightarrow n) = \min\left(1, \frac{\Lambda^3 N \exp(-\beta\mu)}{V} \frac{W(o)}{\langle W_{IG} \rangle}\right) \qquad (1.40)$$

The chemical potential of the system can be obtained from the fugacity f using the relation[80]:

$$f = \exp(\beta\mu) \qquad (1.41)$$

The pressure of the molecules in the reservoir can be calculated from the fugacity using the equation of state of the system[88,89].

When the molecule that has to be inserted is branched, the beads at the same branching point have to be inserted at the same time. This kind of insertion may be inefficient. To improve the biased insertion of branched molecules, new methods have been developed[52,76,90].

One limitation of the CBMC method is that, in very dense systems, the equilibration of the middle atoms of the molecule is very slow. With CBMC it is possible to insert a molecule with either end restricted to be fixed at one position, as it happens with ring molecules. CBMC does not sample efficiently the central atom positions of molecules with fixed ends. *Concerted rotation*, *rebridging*, and *end-bridging* Monte Carlo schemes have been developed to solve these problems for dense polymers[91-93].

• **Regrow**. In general, molecular models contain non-rigid bonded interactions. We can account for the internal degrees of freedom of a molecule with a MC regrow move. There are different possibilities for regrowing a molecule:

　　　1. Full regrow. A randomly selected molecule is removed from the system and inserted back at a random position

　　　2. Partial regrow. Only one part of the molecule is regrown. The rest of the atoms of the molecule keep their position.

In this work we will only use the first type of regrow employing a CBMC scheme. This MC move is equivalent to a random translation of a molecule that also changes its internal configuration.

• **Identity change**. This MC move is used to improve the sampling of systems containing a mixture of different molecules. In this scheme, a molecule of the system is selected at random and deleted. At the same position of the center of mass of the deleted molecule, a new molecule with a randomly selected identity is inserted. Simulations using this type of MC moves allow the sampling of the phase space in the *semigrand-canonical* ensemble[47,94]. If we define the *fugacity fraction* as:

$$\xi_i = \frac{f_i}{\sum_{j=1}^{N} f_j} \tag{1.42}$$

the acceptance probability of this move is:

$$acc(o \rightarrow n) = \min\left(1, \frac{\xi_i^n}{\xi_i^0} \exp(-\beta \Delta U)\right) \qquad (1.43)$$

where f_i is the fugacity of component i and N the number of different molecule types in the system. The insertion/deletion of molecules can also be performed using a CBMC scheme, although the acceptance probability has to change accordingly.

Widom insertion. This technique can be used to calculate Henry coefficients and heats of adsorption of molecules in microporous materials. We describe it in this section because in this work it makes use of the CBMC method. At low pressures, the adsorption of molecules in a microporous material follows the Henry's law:

$$c = k_H P \qquad (1.44)$$

where P is the pressure of the system, k_H the Henry coefficient and c the concentration of adsorbed molecules. The units we will use in this work for k_H will be mol kg^{-1} Pa^{-1}. The Henry coefficient can be calculated from *Widom's test particle* method[95,96]:

$$k_H = \frac{\beta}{\rho} \cdot \frac{\langle W \rangle}{\langle W_{IG} \rangle} \qquad (1.45)$$

where ρ is the density of the host framework expressed in mol/cm^3 (therefore, β must be expressed in the units J^{-1}), $<W>$ is the average Rosenbluth factor of a single molecule in the host framework and $<W_{IG}>$ the average Rosenbluth factor of an isolated molecule (i.e., in ideal gas conditions). The Widom test particle method consists in inserting one molecule in the system, and calculating its energy and its Rosentluth factor before deleting it. The system is left unchanged with this procedure. The heat of adsorption (or minus the enthalpy of adsorption) can be computed from[97]:

$$q = -\Delta H = \frac{\partial \ln(p/p_0)}{\partial \beta} = k_B T + \langle U_g \rangle + \langle U_N \rangle_N - \frac{\langle (U_N + u^+) \cdot W \rangle_N}{\langle W \rangle_N} \qquad (1.46)$$

where p and p_0 are the pressure and an arbitrary reference pressure respectively, $\beta = 1/(k_B T)$, with k_B the Boltzmann constant and T the absolute temperature, $<U_g>$ the average energy of an isolated guest

molecule and $<U_N>_N$ the total energy of the host framework with N guest molecules present, averaged in an ensemble at constant V, T and N guest molecules. $<(U_N+u^+)\cdot W>_N$ is the energy of the system plus one extra molecule inserted using Widom's test particle method, multiplied by the Rosenbluth factor W of the test particle and averaged in the ensemble at constant V, T and N. It is often convenient to use only part of the non-bonded energy u* to select trial segments, avoiding expensive energy calculations. This procedure leads to a modified Rosenbluth weight $<W^*>_N$[98]:

$$\langle W \rangle_N = \left\langle W^* \exp(-\beta\delta) \right\rangle_N \tag{1.47}$$

If the chain has M atoms i, $j(i)$ is the selected trial direction for atom i, and u is the total energy of one bead, we can write:

$$\delta = \sum_{i=1}^{M} (u_{i,j(i)} - u^*_{i,j(i)}) \tag{1.48}$$

To compute k_H and ΔH we simply need two independent simulations: the first one of a system at temperature T, volume V and N guest molecules, and the second one of an isolated guest molecule at the same temperature.

1.3.3.c. Molecular Dynamics

In previous sections we noticed that the ergodic hypothesis in the microcanonical ensemble Eq. (1.23) can be used to calculate average properties of a system. Instead of sampling the phase space by generating microstates according to their probability in the ensemble, we can follow the time evolution of the system. In order to calculate the average properties of the system, we need to know how to compute properties from the positions, velocities or forces of the particles. For example, in classical systems the temperature can be calculated from the equipartition princicle[99]:

$$T = \sum_{i=1}^{N} \frac{m_i v_i^2}{k_B N_f} \tag{1.49}$$

where N_f is the number of degrees of freedom of the system (equal to 3N − 3 for three-dimensional systems with a fixed total momentum), and v_i and m_i are the velocity and mass of particle i. In the

microcanonical ensemble the quantities N, V the total energy E and the total linear momentum should be conserved. As it happens with a real experiment, the values of the properties of the system fluctuate around the average equilibrium value. These fluctuations are usually related to thermodynamic quantities. For example, in the canonical ensemble the fluctuations in the energy are related to the heat capacity of the system at constant volume C_v[80]:

$$\left\langle U^2 \right\rangle - \left\langle U \right\rangle^2 = k_B T^2 C_V \tag{1.50}$$

What we need to do for calculating the time evolution of the system is integrating the equations of motion. In our case we have a classical model, so Newton's equations of motion[100] will describe the dynamics of our system. There are different methods to integrate Newton's equations, but in this work we will use the *velocity Verlet algorithm*[47] derived from Taylor expansions of the positions at time t:

$$r(t + \Delta t) = r(t) + v(t)\Delta t + \frac{f(t)}{m}\Delta t^2 + O(\Delta t^4) \tag{1.51}$$

$$v(t + \Delta t) = v(t) + \frac{f(t + \Delta t) + f(t)}{2m}\Delta t + O(\Delta t^2) \tag{1.52}$$

$$\boldsymbol{f}(\boldsymbol{r}) = -\left(\frac{\partial U(\boldsymbol{r})}{\partial x}, \frac{\partial U(\boldsymbol{r})}{\partial y}, \frac{\partial U(\boldsymbol{r})}{\partial z} \right) \tag{1.53}$$

The advantages of this algorithm is that it is very simple to implement, the error in the calculation of the positions is of order four in Δt, and it is time reversible just as Newton's equations. A key property of time reversible algorithms is that they have negligible energy drift for long times, which is necessary to describe systems with constant energy. Higher order algorithms allow the use of larger time steps, but in general they have large long-time energy drift and demand more memory and calculation time[47]. Δt has to be as large as possible, with the condition that the energy drift is still acceptable. The largest acceptable time step is determined by the stiffest interaction potential in the system. This is often limited by the bonded potentials. When one type of interaction imposes a much smaller time step than the rest of interactions of the system, the multiple time step technique can be used[101]. With this method, the high frequency interactions are integrated using a small time step, and the low frequency are integrated using larger time steps. The advantage of this method is that it preserves the time reversibility, and the most expensive interactions are calculated only once every several time steps.

The velocity Verlet algorithm introduces an error in the calculation of the trajectory of order $(\Delta t)^4$. This means that, for long times, the trajectory of the particles of the system may be very different from the real trajectory. This is not a problem for the calculation of properties averages. Molecular Dynamics does not intend to calculate the trajectory of the particles as accurately as possible, but to compute representative trajectories. The trajectories generated by the Verlet algorithm provide microstates with the correct volume, number of particles and energy of the system, sampling the phase space efficiently[47].

When the molecules, or a portion of the molecules, are modeled as rigid, it is only necessary to update the center of mass of the molecules and their orientation. Translation of molecules is calculated by integrating the equations of motion for their center of mass. Rotation of molecules around their center of mass is taken into account considering the total torque exerted by the external forces on individual molecules. On the other hand, if the bonded interactions impose constrains the positions of every atom of a single molecule have to be integrated. The integration of the atomic positions of one molecule can lead to the rupture of the bonds between atoms. To avoid molecules breaking, the bonded forces are calculated after every integration step, and the atomic positions in every molecule are recomputed to satisfy the bond constraints. In this work, this flexible constrain imposition is performed iteratively using the RATTLE algorithm[102].

In the same way as in Monte Carlo simulations, when we start a simulation in MD from a general, arbitrary configuration we have to equilibrate the system. During this time the system relaxes and large interaction energies are removed. Ensemble averages are not computed during this period. It is also desirable that the position of the center of mass of a system with a flexible framework does not change along the simulation, as the framework can exchange linear momentum with the guest molecules. During the equilibration we will also remove the momentum of the center of mass shifting the velocities of the different molecules in the system. This is equivalent to consider that there are no external forces acting on the system.

Up to this moment we have described the method of Molecular Dynamics in the NVE, or microcanonical ensemble. In some occasions the system is naturally described in a different ensemble, such as the NVT or NPT ensemble. To simulate a system in the NVT ensemble using MD we need a method to control the temperature of the system. In this case the total energy is not conserved. With the *Nosé-Hoover chain* method[103-105] we can generate the correct ensemble distribution. It consists in introducing additional, artificial coordinates (and therefore, velocities) in an extended Lagrangian formulation of the system. The pseudo-Hamiltonian obtained from this Lagrangian is a constant that represents the conserved energy of

the extended system. The extended momenta of the pseudo-Hamiltonian represent the other conserved properties of the system. In a system of N particles, the conserved quantity equals:

$$H_{NHC} = \mathcal{H}(\boldsymbol{r}, \boldsymbol{p}) + \sum_{k=1}^{M} \frac{p_{\xi,\kappa}^2}{2Q_\kappa} + Lk_BT\xi_1 + \sum_{k=2}^{M} k_BT\xi_\kappa \qquad (1.54)$$

where $L=3N$ (considering a three-dimensional system), M is the chain length, $\mathcal{H}(\boldsymbol{r},\boldsymbol{p})$ the Hamiltonian of the original system, ξ_k the additional coordinates and p_ξ their generalized momentum. Q is an effective mass associated to the coordinate ξ:

$$Q = \frac{l+1}{\beta\tau} \qquad (1.55)$$

with l the number of translational degrees of freedom of the system and τ the time scale of the thermostat.

Diffusion. Diffusion is a time dependent process, constituted by the motion of molecules in space. According to *Fick's law*, the flux $\boldsymbol{j}$ of the diffusing molecules is proportional to the gradient of the concentration c[47]:

$$\boldsymbol{j} = -D\,\nabla c \qquad (1.56)$$

where D is called the *Fick's diffusion coefficient*. In the alternative *Onsager formulation*, the flux of diffusion molecules is related to the gradient of chemical potential by the *Onsager matrix*. This matrix can be directly calculated from MD calculations[106]. The Onsager formulation is equivalent to the *Maxwell-Stefan formulation*[106]. The Maxwell-Stefan formulation balances diffusive and drag forces. The Fick equation and the Maxwell-Stefan descriptions are related by the matrix of thermodynamic factors Γ. While the Maxwell-Stefan diffusivities do not strongly vary with concentration, the Γ matrix does. In the limit of low concentration, the Fick and the Maxwell-Stefan diffusion coefficients are identical to *self-diffusion* coefficients. The *Einstein equation*[47] relates the self-diffusion coefficient with the square of the distance over which the molecules have moved in a time interval t. This is also called the *mean square displacement*:

$$2dD = \lim_{t\to\infty} \frac{\partial\left\langle \Delta r(t)^2 \right\rangle}{\partial t} = \lim_{t\to\infty} \frac{\partial\left\langle \frac{1}{N}\sum_{i=1}^{N}\Delta r_i(t)^2 \right\rangle}{\partial t} \qquad (1.57)$$

where d is the dimensionality of the system and N the number of particles. From a computational point of view, it is much easier to calculate self-diffusion coefficients than Maxwell-Stefan diffusion coefficients.

1.3.4.d Ewald summation

In section 1.3.1 and 1.3.2 we introduced the models we use to describe the frameworks and the molecules in our system. These models consist of pseudo atoms that often carry a partial charge. In a periodic system with N particles, the electrostatic energy of the system will be, considering Eq. (1.6) and Eq. (1.7):

$$U^{Coulomb} = \frac{1}{2} \frac{1}{4\pi\varepsilon_0} \sum_{i=1}^{N} q_i \phi(r_i) \tag{1.58}$$

with

$$\phi(r_i) = \sum_{j=1, j\neq i}^{N} \frac{q_j}{r_{ij}} + \sum_{n>1} \sum_{j=1}^{N} \frac{q_j}{\left| r_{ij} + nL \right|} \tag{1.59}$$

Here the summation is performed for every particle and every periodic image n of the system. For simplicity, we considered the system to be cubic with length *L*. The calculation has to be performed for every periodic image, as the electrostatic interactions are long ranged. The problem of Eq. (1.59) is that it is *conditionally convergent*, i.e, its value depends on the order of summation[46]. When the charges in the system are shielded, as is the case of many models of liquid water, in first approximation we can truncate the interaction at a certain cutoff as we did with the dispersive potentials Eq. (1.5)[97]. When this is not the case, as for a system of polar molecules adsorbed in a framework, the error introduced using this truncation can be large[107]. The method of simple truncation is not generally accepted anymore, as it can introduce artifacts in the system[47,108-110].

The Ewald summation[111] is the generally accepted method to calculate the electrostatic interactions in periodic systems, although other methods have been suggested[97]. We will use Ewald summation in this work. This method is exact, and although it is computationally expensive, it is still efficient for systems containing of the order of 10^5 particles[47]. For larger systems, equivalent methods like Particle Mesh Ewald (PME) are more efficient[47]. Recently, the Wolf method was proposed as a pairwise alternative for the Ewald summation, but it was shown that this method does not work well for zeolites[97,112,113]. The technique used in the Ewald method consists in artificially screening the point charges, and correct for the artificial screening afterwards. In this way, the effective electrostatic potential is short ranged and a nearest-image convention can be used (see section 1.3)[47]. A schematic representation of this procedure is shown in Figure 1.10.
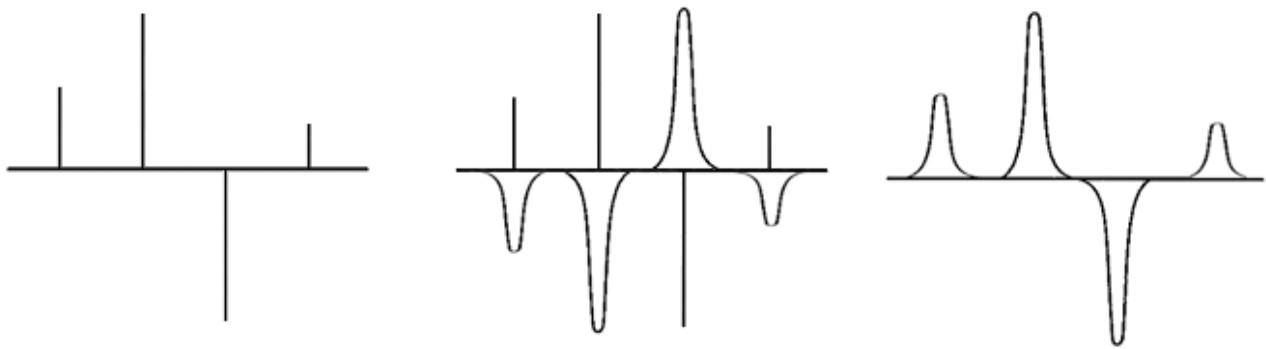
Figure 1.10. *Screening technique used in the Ewald summation. The original set of point charges is written as the sum of two contributions: (1) the set of point charges screened by Gaussian charge distributions (real part) and (2) Gaussian charge distributions that cancel the Gaussian charge distributions in (1) (Fourier part).*

The contribution of the set of screened charges to the energy is called 'real energy' and the correction for the artificial screening the 'Fourier energy'. The screening is realized with Gaussian charge density functions, which have a well known Fourier transform. In a three dimensional system, the Gaussian charge distributions equals:

$$\rho^{Gauss}(\boldsymbol{r}) = -q_i \left(\frac{\alpha}{\pi} \right)^{3/2} \exp(-\alpha \boldsymbol{r}^2) \qquad (1.60)$$

where $\sqrt{2/\alpha}$ is the width of the Gaussian. Fourier transform methods are widely used in periodic systems. The Fourier transform of a function $f(\mathbf{r})$ is:

$$f(\boldsymbol{r}) = \frac{1}{V} \sum_{l=-\infty}^{\infty} \tilde{f}(k) \exp(i\boldsymbol{k} \bullet \boldsymbol{r}) \qquad (1.61)$$

In this equation, $\boldsymbol{k} = (2\pi/L)\,\mathbf{l}$, being $\mathbf{l}$ the lattice vectors in Fourier space. Both the number of lattice vectors and the width of the Gaussian functions are selected according to the desired precision. The coefficients of the sum of Eq. (1.61) are:

$$\tilde{f}(k) = \int_V f(\boldsymbol{r}) \exp(-i\boldsymbol{k} \bullet \boldsymbol{r}) d\boldsymbol{r} \qquad (1.62)$$

Solving the Poisson's equation in the Fourier space, we compute the electrostatic energy in the Fourier space:

$$U^{Coulomb} = \frac{1}{2V\varepsilon_0} \sum_{k\neq 0} \frac{1}{k^2} |\rho(\mathbf{k})|^2 \exp\left(-\frac{k^2}{4\alpha}\right) - \frac{1}{4\pi\varepsilon_0} \sqrt{\frac{\alpha}{\pi}} \sum_{i=1}^{N} q_i^2 + \frac{1}{4\pi\varepsilon_0} \sum_{i<j}^{N} \frac{q_i q_j erfc(\sqrt{\alpha}\,r_{ij})}{r_{ij}} \quad (1.63)$$

The first summand correspond to the Fourier energy, and the third to the real energy, where:

$$\rho(\mathbf{k}) \equiv \sum_{i=1}^{N} q_i \exp(i\mathbf{k} \bullet \mathbf{r}_i) \qquad erfc(x) = 1 - \frac{2}{\sqrt{\pi}} \int_0^x \exp(-t^2)dt \quad (1.64)$$

The Fourier part includes the interaction energy of one particle with all its periodic images, also with itself. In agreement with Eq. (1.59), to remove the interaction energy of every particle with itself (although not with the rest of its periodic images) to the Fourier energy, we have to subtract the *self-interaction energy*. The self-interaction energy is the second summand of Eq. (1.63).

In the case of molecular systems, the interaction energy between different atoms of the same molecule is included in the real part of the summation. To remove the intra molecular energy for atoms separated less than three bond lengths (section 1.3.1.b), it is necessary to add one last term to Eq. (1.63), the *exclusion energy*:

$$U^{exclussion} = -\frac{1}{4\pi\varepsilon_0} \sum_{molecules} \sum_{\substack{i,j=1 \\ j-i>3}}^{M} \frac{q_i q_j erf(\boldsymbol{\alpha} \cdot r_{ij})}{r_{ij}} \quad (1.65)$$

$$erf(x) = \frac{2}{\sqrt{\pi}} \int_0^x \exp(-t^2)dt = 1 - erfc(x) \quad (1.66)$$

Although this expression for the energy is more complicated than Eq. (1.59), it converges quickly. The potential energy of an infinite periodic system of charges depends on the boundary conditions at infinity[114]. The reason is that the material surrounding the system generates a reaction field depending on the electric field of the system. To eliminate the terms that should be added to the energy from the reaction field, we can consider that the system is surrounded by a conductor material with infinite dielectric constant (*tin foil boundary conditions*).

1.3.4. Outline and scope of this thesis

In this work we will study the adsorption, diffusion, and separation of water and other molecules in two different types of crystalline porous materials, zeolites and Metal-Organic Frameworks (MOFs), using molecular simulation techniques. While zeolites are hydrophobic in their pure siliceous form, MOFs are generally hydrophilic. This difference is responsible for completely different adsorption behavior of water in these materials.

The key objective of this study is to obtain a molecular understanding of water adsorption in zeolites and metal-organic frameworks. Molecular simulations can be used for this purpose. There exists a complete parallelism between a real experiment and a molecular simulation experiment. In both cases, the aim is to measure some properties of the system of study. This information will be later analyzed for example, to characterize the system, calculate other properties of the system or compare the results with a theoretical model that allows making predictions for systems similar to the case study. This may ultimately lead to a fundamental understanding at the molecular scale.

There are clear advantages in using simulations instead of performing real experiments. One of the most important factors is the cost. In a simulation study, the only "material" needed is one or several computers, which can be used for different types of calculations. In a real experiment, a different piece of equipment is usually needed for measuring every individual property of the system, and some materials can be very expensive due to their low availability, difficult synthesis or need for high purity. In a simulation we also have a perfect control of all variables of the system. We can simulate at conditions that are not experimentally available or are difficult to achieve, such as systems at very high pressures or in the limit of zero concentration of guest molecules. Molecular simulations provide molecular detail on the processes involved in the experiment. This insight is difficult -if not impossible- to obtain in an experiment. Simulation also provides a perfect benchmark to test theories, as it is possible to study a theoretical system that is not available experimentally. For example, it is possible to modify different parameters of a given force field to test their influence on the properties of the system.

The main limitation of a molecular simulation experiment is that it depends on molecular models that are not always available and assumptions that simplify the description of the system. If no model is available for our study, we need to develop a new, appropriate one. Developing a new model is usually a very time consuming task. The time required for the simulation can also be quite time consuming. If the description of the system is more detailed, the simulation time generally increases. Fortunately, computers are becoming faster every day, and also the use of parallel computation may reduce the simulation time

considerably, allowing the use of more complex models that describe the system more realistically. The models used are not always suitable to study certain properties of the system, reducing the applicability of the simulation. The reason is that force fields do not always give a realistic description of the relevant characteristics of the system. Force field parameters are usually fitted to very specific data at certain conditions, failing to describe very specific situations. Finally, some models and calculation methods can not be used to reproduce a particular property of a given system because the calculation method introduces artifacts. For example, in systems with periodic boundaries one has to take great care when describing propagating waves. If special simulation methods are not used, one may artificially generate stationary waves with a wave length that is a multiple of the unit cell size.

We use a molecular simulation method where all the atoms of the system are modeled implicitly or explicitly. The interactions are classical, force field based. The description of the system is neither quantum mechanical nor relativistic. In the experimental situation, the velocity of the guest molecules is not large, and it has been shown that it is not necessary to introduce quantum effects for an accurate calculation of the specific properties that we compute here at the particular conditions of the study. We are not considering the possibility of chemical reactions, as they do not occur experimentally for the systems used in this study.

In chapter 2 we will study the adsorption of water in silicalite, a pure siliceous zeolite and therefore a hydrophobic material. We will explore different approaches to model the experimental adsorption data. We identify several problems of molecular simulations and force fields for this system, mainly the large sensitivity of the results with small changes in the force field parameters, and propose the use of a flexible framework to solve some of these problems. We apply the same simulation methods to other types of hydrophobic zeolites, finding similar problems in the description of water adsorption. In chapter 3 we will describe the separation of water/alcohol mixtures in another hydrophobic zeolite, pure siliceous DD3R, both using experimental data and molecular simulations. Despite the limitations of the force fields to describe the adsorption of water and alcohols in hydrophobic zeolites, we will use force fields available from the literature to give a qualitative description of this type of separation. Therefore, we will employ molecular simulations to calculate adsorption and diffusion of water, methanol and ethanol in DDR-type zeolite at different temperatures. We will use different models and approximations in order to compare experimental and simulation data. We will identify the reason for the high selectivity of water over alcohols, which originates from differences in the diffusivities of water and alcohols, and not from adsorption selectivity. In chapter 4, we will study Cu-BTC, a well known metal-organic framework (MOF) that is stable upon adsorption of water at standard conditions, and that has a hydrophilic character.

We will develop a new set of force field parameters able to reproduce the experimental adsorption isotherm of water in Cu-BTC, using a method that can be generalized to other types of MOFs. We will compare the adsorption of water with the adsorption of other type of molecules in Cu-BTC. In particular, we will focus our attention on the adsorption sites of molecules at low loading, their differential heats of adsorption, and their Henry coefficients, being the large dipole moment of water the reason for the large differences in adsorption behavior between water and other molecules in microporous materials.

In chapter 5, we will continue describing the adsorption of other molecules in the MOF Cu-BTC, concentrating our attention on the preferential adsorption siting of small quadrupolar and nonpolar molecules at low pressures. In this study we will combine again experimental measurements and Monte Carlo simulations. Adsorption isotherms, Henry coefficients, and heats of adsorption will be computed and compared with experimental data. To obtain adsorption data directly comparable with experimental measurements, it will be necessary to rescale the adsorption data obtained by molecular simulation using the nitrogen isotherm as a reference. Finally, we will relate the molecular siting of the different components in the structure with their relative quadrupole moment. The larger the quadrupole moment, the closer the molecules adsorb to the metal centers of Cu-BTC. Non polar molecules prefer to adsorb at the entropically favorable site, the side pockets of the structure.

In chapter 6 we will study the separation of gas mixtures, and gas storage capacity in MOFs, applied to natural gas. We will compare the performance of the MOFs Cu-BTC and IRMOF-1 for separation and storage. We will compute adsorption isotherms and locate the preferential adsorption siting for the main gasses contained in natural gas, both for the pure-component and for mixtures. Separation selectivities and storage capacity will be calculated from the adsorption data. While IRMOF-1 performs better for storage, Cu-BTC is better suited for molecular separation.

In chapter 7 we will study the separation performance of another MOF, MIL-47, for xylene isomers by Monte Carlo simulations. The experimental adsorption isotherms, heats of adsorption and Henry coefficients of xylene isomers at temperatures between 343 K and 423 K will be computed and compared with experimental data. The Ideal Adsorption Solution Theory (IAST) will be used to predict the adsorption of xylene mixtures from pure-component data. This method gives an excellent agreement with experimental data, and is a valuable tool for this system as the experimental diffusion of the xylene molecules in this structure is very slow. We will calculate the adsorption selectivities of the different xylene isomers from the computed adsorption data. The reason for the different adsorption preference of the xylene isomers is steric. Ortho-xylene packs efficiently in a nearly T-type arrangement. P-xylene aligns its CH_3 groups, minimizing the molecule-molecule interactions. M-xylene can not pack efficiently and for that reason is the less adsorbed isomer.

2

Adsorption of water in hydrophobic zeolites

We have performed a molecular simulation study on water adsorption in hydrophobic zeolites. The framework structures are truly periodic and therefore the Ewald summation is the natural choice for computing the Coulombic interactions. However, few water models have been parameterized using this method. The adsorption results are extremely sensitive to the water model used, the framework positions in the orthorhombic structure and the atomic charges of the zeolite framework. This chapter provides insight on the identification of the potential limitations of available force fields and models, and to the point charges used for the zeolite atoms, when they are applied to a highly hydrophobic system. We discuss feasible routes to conciliate simulation and experimental results.

2.1. Introduction

Zeolites have nowadays a great importance in industry, as they have wide applications in catalysis, molecular sieving and gas storage[115]. In addition, water is probably the most important molecule on earth, as it is present in most biological and geological processes. Currently, the main use of zeolites in the presence of water is the removal of a wide range of pollutants from water, for example industrial dyes, heavy metals, hydrocarbons and waste oils[116-121]. The zeolites selected for this use are usually cheap natural zeolites such as clinoptilolite or mordenite, although synthetic materials have also been used[122]. Interestingly, it has been suggested that water can be present in Mars rocks containing zeolites[123]. Although there are many studies on water in zeolites many of the phenomena related to the presence of water in these structures, such as adsorption or cation exchange, have not been well described nor yet fully understood. Experimental data obtained by different authors or using different techniques often lead to different results, as is the case with adsorption isotherms[124-128]. The most likely reason for this void is the exceptional nature of water. Water is a very simple molecule composed by only three atoms, and yet its behaviour is quite extraordinary and not completely understood. The behaviour of water is quite different from what is found for other materials[129], although deciding if these properties are anomalous depends on the materials used to compare[129,130].

Classical molecular simulations are normally used to calculate adsorption isotherms and diffusion in porous materials. In the search for speed and simplicity in these calculations, simple force fields are desirable. Hydrocarbons and common molecules such as nitrogen or carbon dioxide adsorbed in zeolites are examples of systems that can easily be studied with this kind of methods, obtaining adsorption data that match experiments[45,131-133]. Similar approaches have been used for water in zeolites, but with less success[134,135]. This is attributed to the need of long equilibration cycles, and to the fact that small changes in the potential parameters largely influence the computed values[8].

Many different water models have been proposed during the last decades in an effort to reproduce its most important properties. For example, a review by Guillot[59] gathers forty six different water models. None of these models is able to simultaneously reproduce all properties of water, such as the location of the density maximum and the critical point. Water models have become more and more complex with time in a search for correctly predicting the largest number of properties. Some models include multipoles[136] or polarization[137,138] with moderate success. It is worth mentioning non-atomistic models and models fitted after ab-initio simulations that lead to promising results, as they account for most of the abnormalities of water[62,139,140].

Most simulation studies of water in zeolites use simple models for water, mainly SPC and Tip4p. Furthermore, most of the studies concentrate on two types of zeolites, faujasite-type framework (FAU) and silicalite-type framework (MFI). Most simulation efforts have been focused on the study of the interaction of water with pure siliceous zeolites or alumina exchanged zeolites[8,134,135,141-148]. The first type of zeolites is known to be hydrophobic, while the second ones are hydrophilic.

Adsorption and diffusion of water in MFI and FAU type zeolites have been reported by a variety of authors using several models for water. The most popular model is Tip4p[66], has been used by Beauvais *et al.*[141] to described the location of the sodium cations in FAU in the presence of water, by Di Lella *et al.*[142] to calculate the adsorption isotherms and cation distribution in FAU and MFI, by Trzpit *et al.*[143] and by Yang *et al.*[149] to study water diffusion in MFI or by Cailliez *et al.*[145] to study the interaction of water with the possible defects of the zeolite MFI. Desbiens *et al.*[134,146] computed adsorption isotherms in MFI with different partial charges for the framework atoms not only using the Tip4p water model[66], but also with the Tip5p[60], MSPC/E[150] and the polarizable DEC[151] model. Ramachandran *et al.*[8] simulated adsorption of water in MFI with Tip4p[66] and SPC/E[64], in an attempt to model small defects in the framework with extra water molecules. The SPC[63] water model has been also widely used for adsorption of water in zeolites. Hence, Pellenq *et al.*[147] used this model in MFI, including polarization for all the atoms of the system, to study polarization effects, configuration energy and heats of adsorption. Puibasset *et al.*[135] used this simple model of water in conjunction with a more complex, polarizable potential for the water-zeolite interactions in MFI to study adsorption and formation of water clusters[63]. Other models for water such as Tips2[152] have also been used by Halasz *et al.*[148] to compute the adsorption isotherms of water in different faujasites, and similar studies with similar techniques and models have been performed in other types of zeolites, for example in zeolite A (LTA)[153], heulandite (HEU) and clinoptilolite (CLI)[154].

The overwhelming majority of water models use a direct pairwise Coulombic interaction truncated and shifted at 9 or 10 Angstrom. This may give reasonable results for pure water as a liquid due to a large effective charge screening but it prohibits transferability to multi-component or adsorptive systems where such a screening is absent. Moreover, zeolites are crystalline materials described by a periodic unit cell. For systems that are periodic, the long-range, electrostatic interactions can be computed exactly up to an arbitrary precision[47]. Recently, one has become more aware of the special nature of charge interactions in nanoporous materials. Straightforward truncated, pairwise Coulombic calculations including methods like the Wolf-method turn out to be non-transferable to zeolites because of the non-uniform local density (dense framework with open voids)[97]. The work described here provides a simulation study on water adsorption in MFI-type zeolite using classical force fields to identify the possible limitations of available

methods and force fields parameters when they are applied to this special and highly hydrophobic system. We also explore possible routes to conciliate simulation and experimental results.

2.2. Simulation details

Adsorption isotherms are calculated in the grand-canonical ensemble, in which the temperature T, the volume V, and the chemical potential μ are fixed[80]. The imposed chemical potential μ is related to the fugacity and can be computed from the equation of state for a given pressure. The gas phase in the reservoir was treated as an ideal gas, as the pressures considered were low. In the case of liquid water, the NIST database[155] is used to obtain the chemical potential. For water, this database covers a validity range for temperatures from the melting line (lowest temperature 251.2 K at 209.9 MPa) to 1273 K and pressures up to 1000 MPa. The equation of state for a particular molecular model could be computed instead, but this calculation is long and is subject to large error bars. Some studies have shown that the deviation between the calculated and the experimental chemical potential of water is negligible in a large range far from the critical conditions[134]. For high-density systems, such as liquid water, the probability of successfully inserting molecules in the system is very low. For that reason, the insertion/deletion of molecules in the system was performed using the Configurational-bias Monte Carlo technique[84] (40% of the MC moves) while other MC moves were attempted during the simulation: regrow (20%), rotation (20%) and translation (20%) of a randomly selected molecule. The maximum translational and rotational displacements were adjusted to achieve an acceptance probability of 50%. The pore volume in the frameworks was calculated using the Widom particle insertion method[156]. The Henry coefficients and heats of adsorption at zero coverage were computed using MC in the NVT ensemble. The Henry coefficient is related to the excess chemical potential, which is computed using Widom's test particle method[156].

For calculating the liquid density of water, Molecular Dynamic simulations in the NPT ensemble are performed[47]. In these simulations, a fixed number of guest molecules are placed in a cubic box with an initial length of 25Å, and then the box length is allowed to change. All the potentials were truncated to a different *cutoff* radius and shifted depending on the water model used. The box length was always at least twice the size of the *cutoff* radius. The time step used was 1 fs ($1 \cdot 10^{-15}$ seconds). The temperature and pressure of the system were controlled with Nosé-Hoover thermostat and manostat chains[157] of length three, respectively (time scale equal to 0.15 ps).

Monte Carlo simulations are performed in cycles, and in each cycle trial moves are chosen at random. The number of MC moves per cycle is equal to the number of guest molecules present in the system, with a

minimum of 20 moves per cycle. More details on the simulation technique can be found elsewhere[45,47,52,153,158]. In the case of calculations of water density or water adsorbed in zeolites, it has been repeatedly reported that the number of MC or MD steps necessary for equilibration of the system is unusually large[8]. This is most noticeable when simulating adsorption inside zeolites in the region that is between the inflexion point and the saturation zone, as in this region the shape of isotherm is very steep. Water molecules interact more strongly with themselves than with the zeolite, and form clusters that grow until they fall apart and the process begins again[159]. In this way, to obtain a proper statistic description of the system from the simulation, the number of cycles has to be large. For the critical zone of the isotherm, up to $5 \cdot 10^5$ initialization cycles are needed; for the other points of the isotherm $1 \cdot 10^5$ initialization cycles are used and $2 \cdot 10^5$ for production. For the NPT ensemble $5 \cdot 10^4$ integration steps are used for equilibration and at least $2 \cdot 10^5$ for production.

The Tip5pEw[74] model is suitable for studying adsorption of water in zeolites, because its properties have been refitted using Ewald sums and the adsorption isotherms can be computed efficiently. There are other models that also have been parameterized with Ewald sums, such as Tip4pEw[69], Tip3p-PME[160], SPC/FW[65], or SWM4-DP[161]. The last two are flexible water models and therefore their use would increase the simulation time. In any case, flexible water models could be interesting when studying mixtures of water with large molecules or interaction with ions, as it has been shown that flexibility and polarizability can be important in this case[59,161,162]. No hydrolysis is observed in the adsorption of water in zeolites due to the weak interaction of water with the zeolite[163,164], so this effect was not included in our simulations.

Hydrocarbons were modelled using a united atom model, in which CH_x groups are considered as single, chargeless interaction centres with their own effective potential[165]. The bond-stretching, bond-bending and torsion potentials of the alkane, as well as the alkane-alkane and alkane-zeolite potentials, were obtained from a recent parameterisation that accurately describes the adsorption isotherms of alkanes[166]. A rigid atomistic model of CO_2 is used[78] with a bond length of 1.16 Å. Each atom of CO_2 has a partial charge and the dispersive interactions between the molecules are described by a Lennard-Jones potential. The interaction with the zeolite is taken from García-Pérez *et al.*[132]. All Lennard-Jones parameters and atomic charges used in this work are listed in Table 2.1.

Atom(s)	ε/k_b [K]	σ [Å]	q [e]
Si[45]			2.05
O_{zeo}[167]	93.53	3.0	-1.025
O_{water}[74]	89.516	3.097	
H_{water}[74]			0.241
D_{water}[74]			-0.241
C_{CO2}[78]	28.129	2.76	0.6512
C_{CO2} - O_{zeo}[132]	50.2	2.7815	
O_{CO2}[78]	80.507	3.033	-0.3256
O_{CO2}- O_{zeo}[132]	84.93	2.9195	
CH_3[165]	108.0	3.76	
$CH_3 - O_{zeo}$[166]	93.0	3.48	
CH_2[165]	56.0	3.96	
$CH_2 - O_{zeo}$[166]	60.5	3.58	

Table 2.1. *Lennard-Jones parameters and initial partial charges used in this work. Lorentz-Berthelot mixing rules are used for the interaction between water and the zeolite. The Tip5pEw water model has two dummy atoms (D).*

2.3. Results and Discussion

Choosing Water Models. Different researchers have used a wide range of classical water models to describe the different properties of water in zeolites. The bond length and bond angle of these simple models were usually taken from the experimental gas phase values, while the non-bonded interactions were adjusted to reproduce the most important properties of water and particularly the water density at standard conditions. These models were fitted for different *cutoff* values for the Coulombic and Lennard-Jones interactions. We found large differences between simulations that use the Ewald summation and those that use a direct pairwise potential with spherical *cutoff* [107]. Some authors claim that particular models of water such as Tip4p/2005[168] or SPC/Fw[65] are better than others when they are compared at the same simulation conditions (cutoff radius, use of switching functions, method to evaluate the Coulombic energy). However, it has been shown that the particular simulation conditions are vital for the final result of a given simulation[107]. To calculate water properties using one particular water model, the specific simulation conditions used for the parameterization of that model should be used. If this is not the case, deviations from the expected behaviour can be observed, and therefore the former comparison does not make any sense. To illustrate this point, Figure 2.1 compares the water density obtained at 1 atm. in the temperature region that spans from -30ºC to 110ºC using a variety of models. The density was computed

using Molecular Dynamics simulations in the NPT ensemble with SPC[63], Tip4p[66], Tip5p[60], and Tip5pEw[74] models for water. Besides the experimental data, we plot water densities obtained with a) the parameters that were originally used to fit the particular water model, and b) the same parameters *but* using Ewald summations and a Lennard-Jones *cutoff* of 12 Å. Most of the models give a precise estimation of the density at 25ºC using the original parameters, as they were adjusted to reproduce this value. Among the models tested, only Tip5p and Tip5pEw reproduce the maximum of density around 4°C using the originally reported parameters. Note that the Tip5pEw is the only model that also matches the experimental density using conditions other than those considered in the original fitting. This can be easily explained since Tip5pEw model was originally fitted using Ewald summations and a variable Lennard-Jones *cutoff* equal to half the box length, which was always close to 12 Å. Furthermore, with Tip5pEw we obtain the best results for the density as a function of temperature. In addition, the Tip5pEw model reproduces perfectly other important properties of water like the liquid structure. The radial distribution function of this model compared with experimental x-ray data can be found in the Appendix (Figure A).
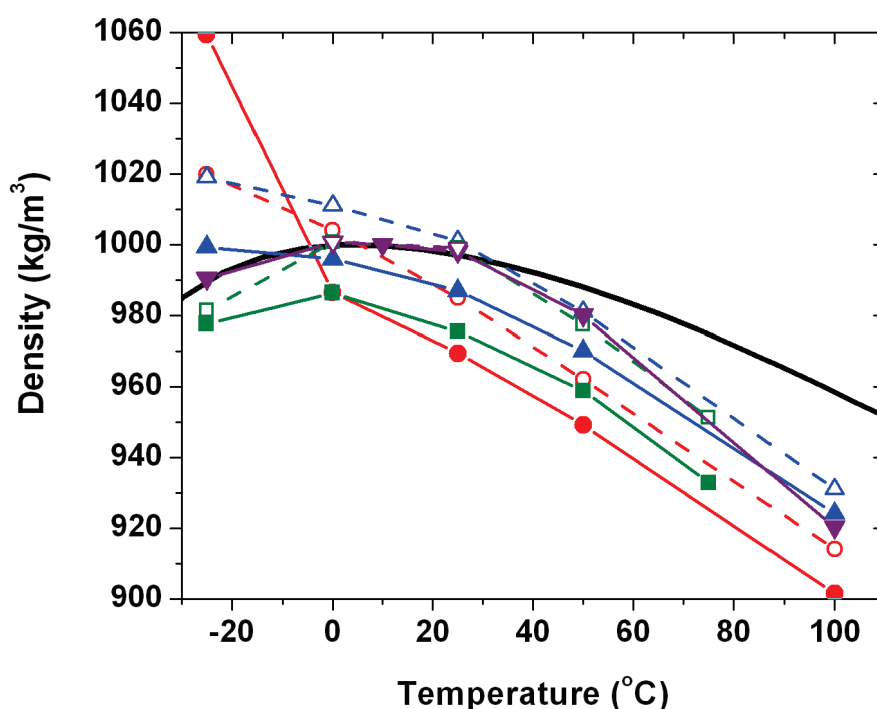
Figure 2.1. *Experimental[155] (black line) and calculated water density as a function of temperature at 1 atm. Simulations were performed using the SPC (circles), Tip4p (up triangles), Tip5p (squares) and Tip5pEw (down triangles) models for water. Simulation data with the original fitting parameters are represented with open symbols, and those using Ewald sums and a Lennard-Jones cutoff of 12 Å are represented with solid symbols. Lines are a guide to the eye.*

Although experimentally the bulk dipole moment of water is reduced upon adsorption in zeolites, the polarization induced by the zeolite in water is rather small, as well as the influence of the zeolite in the hydrogen bonds of water[169,170]. Quantum mechanical simulations have also found problems describing the polarization of water molecules in zeolites[147]. As polarity is more important than polarizability in the adsorption of molecules in these materials[171], in our study we select the non polarisable Tip5pEw[74] model for water. This corresponds to be a Tip5p model parameterized for Ewald sums. Similar models such as Tip4pEw[69], Tip3p-PME[160], SPC/FW[65] or SWM4-DP[161] are also possible candidates, though some of them are flexible or polarisable and they might give a better description of some particular properties of the system at a larger computational cost. The SPC, Tip4p and other similar models can also be used in the study of water adsorption in zeolites, but due to the importance of the long range interactions, their Ewald-fitted versions should be used instead.

Differences between the two characterizations of silicalite. There are two different characterizations of the orthorhombic structure of silicalite, one from Olson *et al.*[172] and another from van Koninsveld *et al.*[173]. Both structures are similar with slight differences in the atomic positions, as can be seen in Figure 2.2. Computing the pore volumes using the Widom insertion technique lead to 0.166 cm^3/g and 0.163 cm^3/g for the structures of Olson and van Koningsveld, respectively. The two structures differ mainly at the channel intersections. The maximum deviation between equivalent atoms is lower than 0.37 Å. These differences have been shown to be important when simulating tight-fitting molecules such as benzene and xylene, as they can lead to large changes in the computed properties attributed to the different electrostatic potential felt by the molecules at the intersections[174].

Water is a small molecule that does not interact strongly with silicalite, so the adsorption in the two structures of MFI is expected to be similar. Figure 2.3 compares experimental[146,175] and simulation data for water adsorption in both MFI structures at 300 K. For this particular study, we use the Tip4p model at the same simulation conditions than previous groups[134,142], assigning a partial charge of 1.4 e to the silicon atoms of the framework (and therefore a partial charge of -0.7 e to the oxygen atoms). Although the adsorption isotherms for both frameworks have a similar shape, for a fixed loading the pressure differs up to 60 MPa. This large difference between the isotherms calculated in the two different structures is completely unexpected if compared to the isotherms calculated for other molecules of similar size such as propane (Figure 2.4) and carbon dioxide (Figure 2.5). These molecules accurately reproduce the experimental data[132,176]. Differences between isotherms are minor for the non-polar propane and low for the quadrupolar carbon dioxide, suggesting that the discrepancies in the adsorption isotherms for water can be mainly attributed to the water dipole moment.
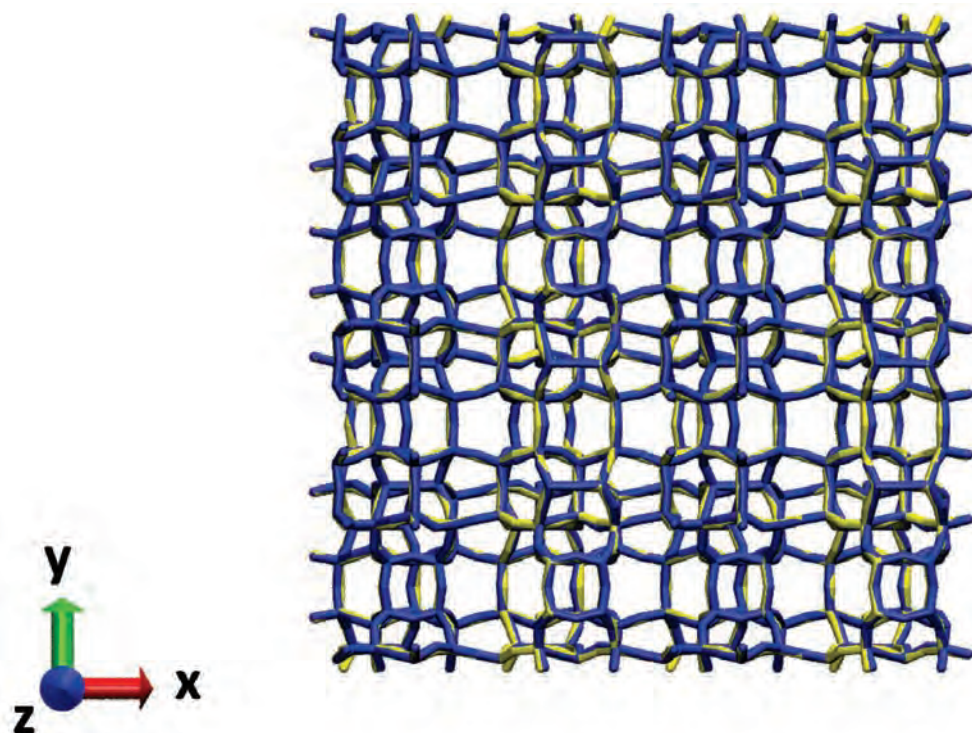
Figure 2.2. *Snapshot of the two orthorhombic characterizations of MFI, which shows little differences in atomic positions. Yellow, van Koningsveld characterizatio[173]; blue, Olson characterization[172]. Straight channels are orientated along the y direction, zig-zag channels are on the xz planes.*
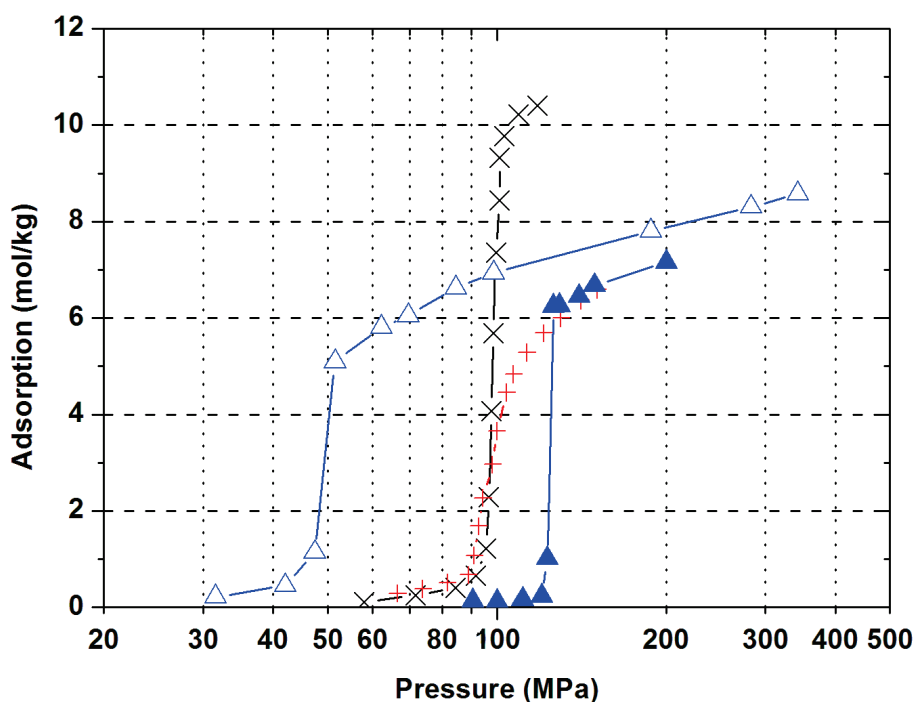

Figure 2.3. *Experimental[146,175] (X and +) and calculated adsorption isotherms of water in MFI structures at 300 K. Simulations were performed using the Tip4p water model for the Olson (open triangles) and the van Koningsveld (closed triangles) structure assigning a partial charge of 1.4 e to the Si atoms of the framework. The lines are a guide to the eye.*
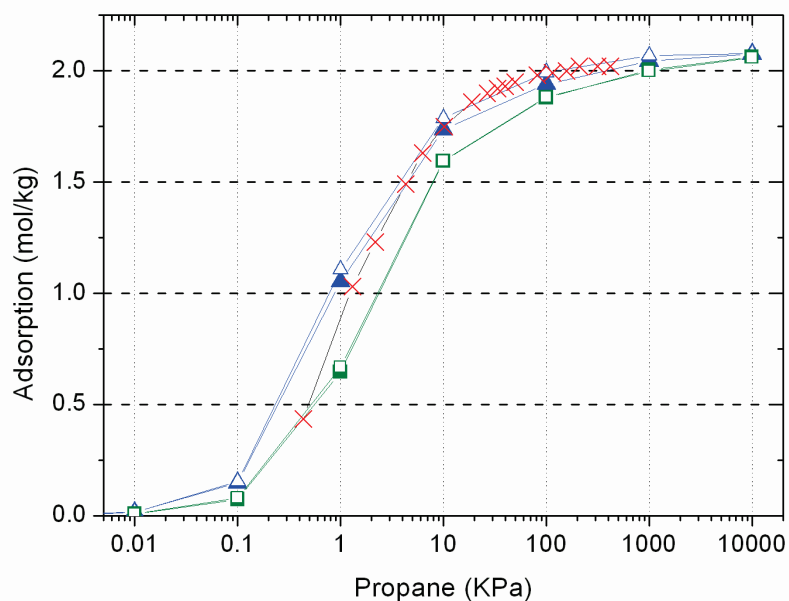
Figure 2.4 *Experimental[176] (X) at 303 K and calculated adsorption isotherms of propane in MFI at 298 K. Simulations were performed using the Olson (open symbols) and the van Koningsveld (closed symbols) structures, assigning a partial charge of 2.05 e to the Si atoms of the rigid (triangles) and flexible (squares) framework. The lines are a guide to the eye.*

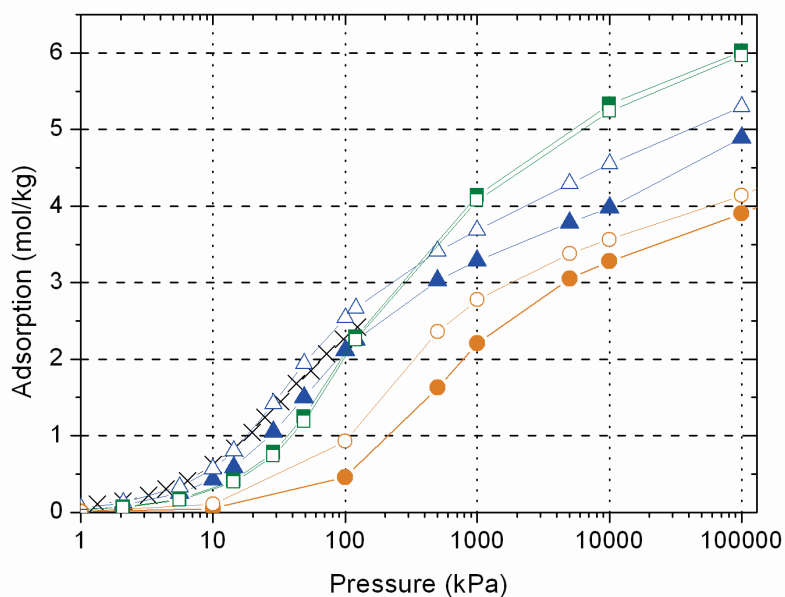**Figure 2.5.** *Experimental[132] (X) and calculated adsorption isotherms of carbon dioxide in MFI at 273 K. Simulations were performed for the Olson (open symbols) and the van Koningsveld (closed symbols) structures, assigning partial charges of 2.05e (triangles) and 0.5e (circles) to the Si atoms of the framework, and with a flexible framework and a partial charge of 2.05e (squares). The lines are a guide to the eye.*
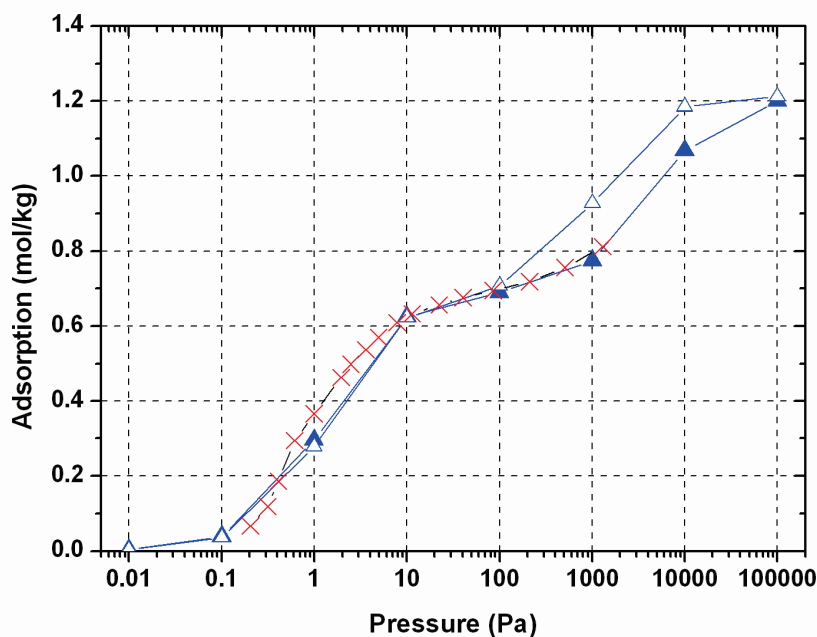
Figure 2.6. *Experimental[177] (X) and calculated adsorption isotherms of n-heptane in MFI at 347 K using the Olson (open triangles) and the van Koningsveld (closed triangles) structure. The lines are a guide to the eye.*

Larger, non-polar molecules such as n-heptane show similar adsorption for both structures at the lower and the higher pressure regions. However, at intermediate pressures the adsorption in the structure of Olson is notably higher than in the van Koningsveld structure. The calculated and experimental isotherms[177] are shown in Figure 2.6. The differences are most likely enhanced due to the commensurate "freezing" of n-heptane in the sinusoidal channels[178]. This affects the adsorption at the channel intersections, where the differences between the zeolite structures are the largest[178].

Similar studies have been performed for other water models. For example, calculated adsorption isotherms for the flexible models SPCFw[65] and F3C[67] in both structures are shown in Figure 2.7. These models showed reduced pressure differences for the condensation point in the two different characterizations of MFI, since condensation takes place at low pressures. Apart from this result, large deviations between the two isotherms are observed as for the other models. Furthermore, the isotherms deviate significantly from the experimental data. The adsorption isotherms obtained for the Tip5pEw model are shown in Figure 2.8. In this case, the differences are much larger than for the rest of the models tested. The reason is that, for Olson framework, the condensation takes place at low pressures due to a water phase transition. These results suggest that the differences originate from the particular behavior of water in this type of material and not from the details of the force field used. In particular, the large dipole moment of water must play an important role in the adsorption. The differences in adsorption in both characterizations also increase with the dipole or quadrupole moment of the molecule, from propane to

carbon dioxide and finally water, due to the large differences in the electrostatic energy at the channel intersections of MFI between both structures. In all cases, the adsorption capacity in the structure of Olson is larger than in the structure of van Koningsveld, since the first has a slightly larger pore volume.

To better understand the sensitivity of water to small changes in the zeolite structure, we have generated a series of new structures along a path that continuously transforms the van Koningsveld into the Olson structure. For every generated structure, we have computed the heats of adsorption of water, carbon dioxide, and propane as shown in Figure 2.9. In the case of propane and carbon dioxide, the heat of adsorption remains practically constant for every structure generated, indicating that the adsorption is barely influenced by small changes in the zeolite structure. This point supports our previous observation that the adsorption isotherms of these molecules in the Olson and van Koningsveld structures do not show large differences. For water, structures with less than 0.2 Å of difference from the van Koningsveld have a similar heat of adsorption. However, structures that differ more than this value from the van Koningsveld structure (and therefore closer to the Olson structure) have a significant lower heat of adsorption. Apparently the adsorption of water in the Olson structure is much more sensitive to changes in the atomic positions than the van Koningsveld structure. This could be an indication that the van Koningsveld structure gives a better description of the experimental adsorption isotherm of water in MFI.

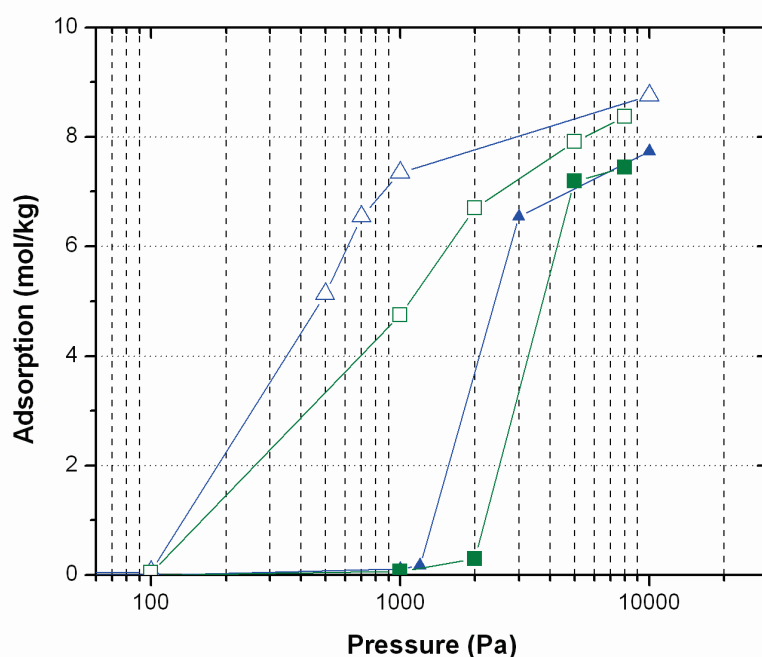**Figure 2.7.** *Calculated adsorption isotherms for water in MFI at 300 K using the SPCFw (triangles) and F3C (squares) models. Simulations were performed for the Olson (open symbols) and the van Koningsveld (closed symbols) structures, assigning a partial charge of 2.05 e to the Si atoms of the framework. The experimental isotherms lay at higher pressures and are not shown. The lines are a guide to the eye.*
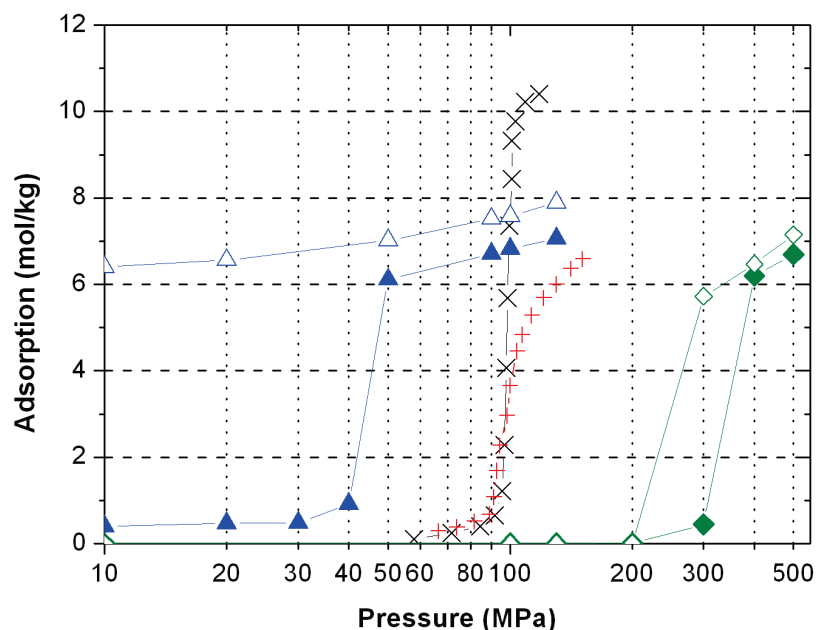
Figure 2.8. *Experimental[146,175] (+ and x) and calculated adsorption isotherms for water in MFI at 300 K using the Tip5pEw model. Simulations were performed using the Olson (open symbols) and the van Koningsveld (solid symbols) structure for the framework, assigning a partial charge of 2.05 e (triangles) and 0.5 e (diamonds) to the Si atoms of the framework. The lines are a guide to the eye.*

To illustrate the importance of the channel intersections of MFI in the adsorption of water, we have calculated the Henry coefficients and heats of adsorption at different locations of the zeolite: straight channels, zig-zag channels and intersections (Table 2.2). While in both types of channels the values are similar for both structures, in the intersections the differences are quite large. The heats of adsorption for the Olson structure are twice than those for the van Koningsveld structure, and the Henry coefficients are three orders of magnitude larger for the Olson structure. Furthermore, the Henry coefficients indicate that the preferential adsorption sites are the zig-zag channels for the van Koningsveld structure, and the intersections for the Olson structure. This explains the large differences in heat of adsorption found for the whole structure.
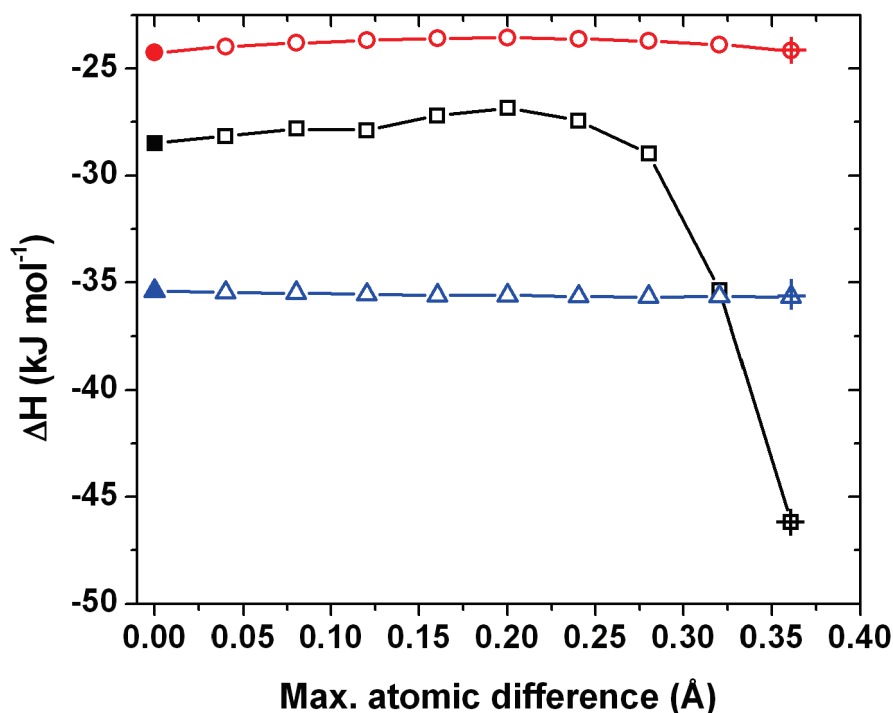
Figure 2.9. *Calculated heats of adsorption of water (squares), carbon dioxide (circles) and propane (triangles) in different test structures of MFI at 298 K, where the partial charge of the Si atoms of the framework is 2.05 e. The maximum difference between the atom positions of the van Koningsveld and the test structure is represented at the horizontal axis. The generated structures (open symbols) perform a continuous change from the van Koningsveld (closed symbols) to the Olson structure (crossed symbols).*

Location	K_H (mol kg^{-1} Pa^{-1})		ΔH (kJ mol^{-1})	
	van Koningsveld	Olson	van Koningsveld	Olson
straight channels	$6.2 \cdot 10^{-6}$ (6)	$1.7 \cdot 10^{-5}$ (1)	-24.7 (6)	-27.8 (2)
zig-zag channels	$1.7 \cdot 10^{-5}$ (3)	$1.7 \cdot 10^{-5}$ (1)	-30.3 (9)	-28.9 (2.3)
intersections	$7.9 \cdot 10^{-7}$ (5)	$6.0 \cdot 10^{-4}$ (1.4)	-17.2 (4)	-44.9 (2.1)
whole structure	$2.5 \cdot 10^{-5}$ (3)	$5.7 \cdot 10^{-4}$ (1.0)	-28.9 (1.0)	-44.6 (4.3)

Table 2.2. *Henry coefficients, and heats of adsorption of water in MFI, calculated in the Olson and van Koningsveld characterizations of MFI and at different locations in the structure: straight channels, zig-zag channels, and intersections. The value obtained for the whole structure is also included for comparison. The values in parenthesis indicate the error in the last digits.*

The sensitivity of water to the force field parameters can be attributed to the hydrophobic character of all-silica zeolites and not only to the MFI structure. We have performed a parallel study with all-silica DDR, MFI, and LTA zeolites. While MFI is a system of intersecting channels, DDR is formed only by longitudinal channels and LTA is a cage-like structure. For every atom of the structures, we defined a random direction of translation and a random displacement, keeping the size of the unit cell fixed. The maximum displacement was set to be shorter than the maximum difference between the two characterizations of MFI, and a continuous series of structures were generated in line with the previous study. The heats of adsorption of water in the resulting structures are shown in Figure 2.10. The general trend of the heat of adsorption with the increasing distortion is the same for all structures. It is important to note that the gradient of the curves for all the zeolites considered is similar, which could be indicative of a general behavior for all-silica zeolites. As in the former study, the structures closer to the initial one have a heat of adsorption very similar to the original value, although the displacement at which the drop in the heat of adsorption takes place is shorter. A comparison with the behavior of the hydrophilic Metal Organic Framework Cu-BTC (section 3) can be found in the Appendix (Figure B).
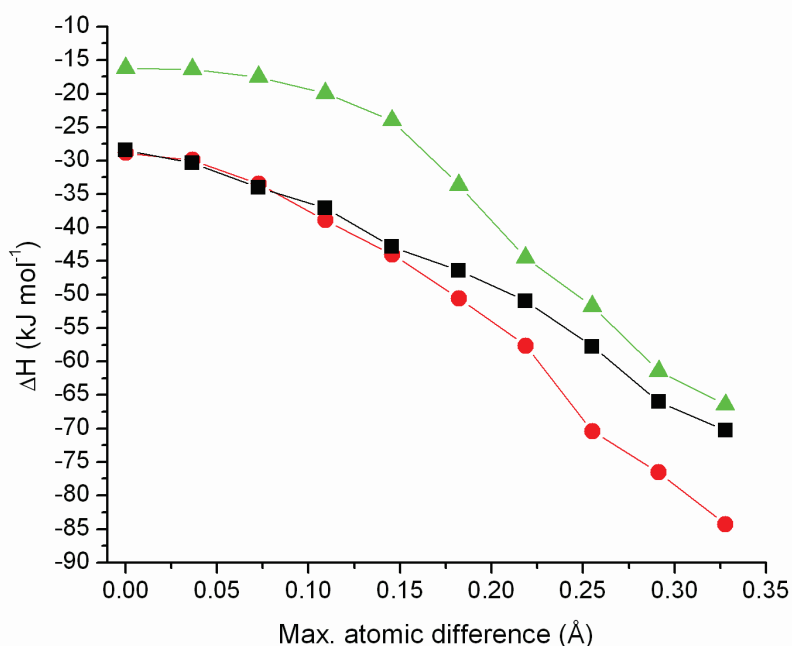
Figure 2.10. *Calculated heats of adsorption for water in test structures of pure siliceous MFI (squares), DDR (circles) and LTA (triangles) at 298 K, where the partial charge of the Si atoms of the framework is 2.05 e. The maximum difference between the atom positions of the original and the test structures is displayed at the horizontal axis. For each structure, the atoms are progressively displaced independently along a random direction until a random maximum displacement is reached. Random directions and random maximum displacements are generated for each atom.*

The influence of the electrostatic interactions in the adsorption of polar molecules was studied, progressively reducing the point charge of the Si atoms in the structure from 2.05 e to 0.5 e. To keep the electrostatic neutrality of the structure, the charge of the oxygen atoms were changed accordingly and made equal to half the charge of the silica atoms with opposite sign. In the case of non-polar molecules such as alkanes no effect is observed, as electrostatic interactions between the adsorbed molecules and the framework are not present in the force field. In Figure 2.5 it is shown that for carbon dioxide a small shift of the isotherm at high pressure is observed when decreasing the silicon charge. This shift can be explained by the lower interaction of the host molecules with the structure, although the differences on adsorption for the two characterizations remain similar. We found a complete different behavior for the Tip5pEw water model (Figure 2.8), where the decrease in the silicon charge induces a large shift of the complete isotherm to much higher pressures and reduces adsorption differences between the structures.

Choosing Atomic Charges for the Framework. The influence of charge and structure was studied for different water models. The Henry coefficients and heat of adsorption of the SPC, Tip3p, Tip4p, Tip5p, Tip5pEw and Tip6p models were calculated for the Olson and the van Koningsveld structures with a partial charge for the silica atoms of 2.05 e, 0.786 e, and 0.5 e. The obtained results are presented in Table 2.3 showing little differences between different models at the same simulation conditions. This is consistent with our previous assumption that the particular behavior of water in zeolites is due to its large dipole moment. The differences between the Olson and the van Koningsveld structures are remarkable when we use a larger charge for the silicon atoms: there is a difference of one order of magnitude in the Henry coefficient, and the heats of adsorption in the Olson structure are around 50% larger than those in van Koningsveld structure. When we decrease the charge of the silicon atoms, these differences also decrease, indicating again the importance of the electrostatic interactions for the special behavior of water.

The importance of the framework charges in the adsorption of water inspired us to try to fit the water-zeolite interaction parameters, as well as the point charges of the atoms of the framework, aiming to reproduce the experimental adsorption isotherms. However, we failed to find such a set of parameters since the shape of the experimental isotherm is very steep in the inflexion region, and therefore very sensitive to the parameters of the interaction potential.

A

q (e)	Structure	SPC[63]	Tip3p[66]	Tip4p[68]	Tip5p[60]	Tip5pEw[74]	Tip6p[179]
2.05	van K.	$2.4 \cdot 10^{-5}$ (3)	$2.1 \cdot 10^{-5}$ (3)	$2.0 \cdot 10^{-5}$ (3)	$2.0 \cdot 10^{-5}$ (2)	$2.5 \cdot 10^{-5}$ (3)	$2.2 \cdot 10^{-5}$ (2)
	Olson	$3.0 \cdot 10^{-4}$ (9)	$3.7 \cdot 10^{-4}$ (1)	$1.5 \cdot 10^{-4}$ (1.0)	$5.2 \cdot 10^{-4}$ (5.9)	$8.3 \cdot 10^{-4}$ (7.2)	$1.1 \cdot 10^{-4}$ (2)
0.786	van K.	$8.0 \cdot 10^{-7}$ (1)	$8.0 \cdot 10^{-7}$ (1)	$8.1 \cdot 10^{-7}$ (1)	$8.1 \cdot 10^{-7}$ (1)	$9.3 \cdot 10^{-7}$ (1)	$1.1 \cdot 10^{-6}$ (1)
	Olson	$1.0 \cdot 10^{-6}$ (1)	$1.0 \cdot 10^{-6}$ (1)	$9.9 \cdot 10^{-7}$ (1)	$1.0 \cdot 10^{-6}$ (1)	$1.2 \cdot 10^{-6}$ (1)	$1.3 \cdot 10^{-6}$ (1)
0.5	van K.	$5.8 \cdot 10^{-7}$ (1)	$5.8 \cdot 10^{-7}$ (1)	$6.0 \cdot 10^{-7}$ (1)	$6.0 \cdot 10^{-7}$ (1)	$6.9 \cdot 10^{-7}$ (1)	$8.4 \cdot 10^{-7}$ (1)
	Olson	$6.3 \cdot 10^{-7}$ (1)	$6.3 \cdot 10^{-7}$ (1)	$6.4 \cdot 10^{-7}$ (1)	$6.5 \cdot 10^{-7}$ (1)	$7.5 \cdot 10^{-7}$ (1)	$8.9 \cdot 10^{-7}$ (1)

B

q (e)	Structure	SPC[63]	Tip3p[66]	Tip4p[68]	Tip5p[60]	Tip5pEw[74]	Tip6p[179]
2.05	van K.	-28.5 (8)	-27.8 (8)	-27.4 (9)	-28.3 (9)	-28.9 (1.0)	-27.1 (8)
	Olson	-41.7 (2.1)	-42.0 (2.6)	-36.6 (5.0)	-44.9 (2.5)	-44.6 (4.3)	-35.0 (1.9)
0.786	van K.	-12.8 (1)	-12.8 (1)	-12.8 (1)	-12.8 (1)	-13.2 (1)	-13.6 (1)
	Olson	-13.7 (1)	-13.7 (1)	-13.6 (1)	-13.6 (1)	-14.1 (1)	-14.2 (1)
0.5	van K.	-11.2 (1)	-11.2 (1)	-11.3 (1)	-11.3 (1)	-11.6 (1)	-12.1 (1)
	Olson	-11.5 (1)	-11.6 (1)	-11.6 (1)	-11.5 (1)	-11.9 (1)	-12.3 (1)

Table 2.3. *Henry coefficients (A) in mol kg^{-1} Pa^{-1} and heats of adsorption (B) in kJ mol^{-1} of water in MFI, calculated with different water models, the two different, orthorhombic characterizations of MFI and different partial charges for the silica atoms of the structure (q). The values in parenthesis indicate the error in the last digits.*

Framework flexibility. The use of rigid frameworks has been proved to be accurate enough when studying adsorption of small molecules in zeolites[56], while in the case of large molecules framework flexibility can be crucial. It has been demonstrated that the adsorption isotherms of benzene and xylene for the rigid Olson and van Koningsveld structures are significantly different[174]. As water presents the same behaviour, it is worthwhile investigating the effect of framework flexibility on water adsorption. The isotherms for flexible Olson and van Koningsveld structures obtained for propane and carbon dioxide are shown in Figures 2.4 and 2.5. The introduction of framework flexibility decreases the differences in adsorption in the Olson and in the van Koningsveld structure for both molecules, without deviating to a large extent from the isotherm in the rigid structures.
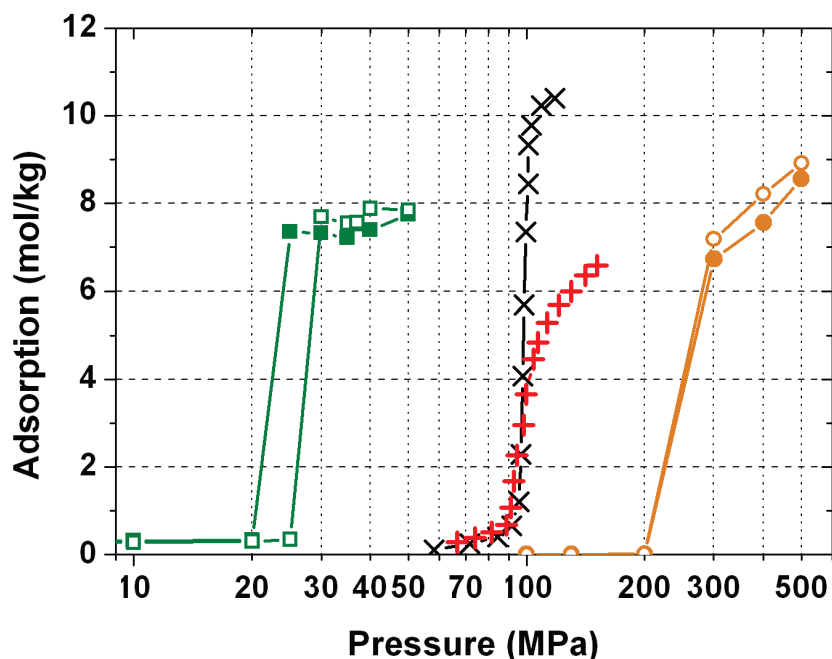
Figure 2.11. *Experimental[146,175] (+ and x) and calculated adsorption isotherms for water in MFI at 300 K using the Tip5pEw model. Simulations were performed using flexible framework models for both the Olson (open symbols) and the van Koningsveld (solid symbols) structures, assigning a partial charge of 2.05 e (squares) and 0.786 e (circles) to the Si atoms of the framework. The lines are a guide to the eye.*

In Figure 2.11 we represent the adsorption isotherm of Tip5pEw water in the two flexible structures of MFI, with different charges for the Si atoms of the zeolite: 2.05 e and 0.786 e. It is remarkable that the differences in the isotherms obtained for the two structures are much smaller than using rigid frameworks. In both cases, the resulting isotherms lay between the isotherms in the rigid structure at similar conditions. Including flexibility is comparable to having an average zeolite made up from the combination of the two rigid structures. We believe that including framework flexibility is the most convenient to remove some of the large sensitivity of the isotherm to small changes in the force field parameters.

2.4. Conclusions

The adsorption properties of water in zeolites are difficult to describe both experimentally and by molecular simulations. The experiments are complicated by the fact that water adsorbs at very low pressure at defects in the crystal. Therefore, the pressure where the sharp increase in adsorption occurs is very sensitive to defects, as well as to the structural crystallographic positions (in addition to pore blockage/collapse etc.). Concerning the corresponding molecular simulations, there are only a few water models that are suitably calibrated for studying water adsorption in zeolites. The Tip5pEw model is

calibrated using the Ewald summation and reproduces well the bulk properties of water. Therefore, it is a suitable candidate to describe water in a periodic environment, though there is still much uncertainty in the correct values of the partial charges, especially of the framework atoms. The dipole moment of water results in behavior that is completely different from other molecules with similar size but without dipole moment, so the partial charge of the zeolite atoms is a critical parameter that has to be chosen carefully. The adsorption of water is also very sensitive to small changes in the precise location of the zeolite atoms. We provided evidence that this sensitivity is directly related to the coupling of the dipole of the water molecules with the electric field induced by the zeolite. Therefore, one has to be cautious when computing the properties of water and highly polar molecules in hydrophobic structures.

3

Water-Alcohol separation in zeolites

This study comprises both experimental measurement as well as molecular modeling of the adsorption of water, methanol, and ethanol on the hydrophobic all-silica decadodecasil 3R (DD3R) zeolite. The simulation data are compared with permeation data of these components, measured using a DD3R membrane under pervaporation conditions. The pure-component isotherms are measured by vapor-phase adsorption and are calculated by grand canonical Monte Carlo (GCMC) simulations. The simulations are conducted using molecular models from the literature, without any adjustments. The simulation results are in fair agreement with the experimental adsorption data. Computed mixture adsorption isotherms show that the water loading is significantly increased as compared to pure-component adsorption. The shape of the computed water isotherm changes from type II to type I when alcohol is present. The loading of both methanol and ethanol at low fugacities is slightly enhanced by the presence of water. The self-diffusivites are calculated using MD simulations. The self-diffusivity of water in DD3R is substantially larger than the diffusivites of both alcohols but is decreased in the presence of methanol or ethanol. The ethanol diffusivity is too low to be determined by conventional MD simulations. The flux calculated from the MD and GCMC results over predicts the experimental values, but the predicted membrane selectivity corresponds well to the experimental data. The mechanism of separation in the dewatering of alcohols using a hydrophobic DD3R membrane is based on the high diffusivity of water as compared to that of the alcohols, where especially ethanol suffers from diffusion limitations.

3.1. Introduction

Small pore zeolites have gained increasing interest in the fields of membrane technology and sensor applications. All-silica deca-dodecasil 3R (DD3R) has been successfully applied for CO_2/CH_4 separation[180-182] and de-watering of alcohols and other organic solvents[183,184]. Also, hydroxy sodalite (SOD) membranes have been successfully synthesized and tested for absolute water separation[185,186]. Because of the pronounced size selectivity of these small pore zeolites, they are also well suited for sensor applications. Dehydration of alcohols is already performed on an industrial scale using LTA-type zeolite membranes[187,188]. To design and optimize these types of membrane separation processes, understanding and modeling the behavior of water and alcohols in zeolite membranes is of key importance.

The DD3R (DDR-type zeolite topology) consists of window-connected cages, which makes this material a member of the group of clathrasils[189]. The crystal structure is built by corner-sharing SiO_4 tetrahedra that are connected to pseudo-hexagonal layers of face-sharing pentagonal dodecahedra (5^{12} cages). These layers are stacked in an ABCABC sequence and are interconnected by additional SiO_4 tetrahedra that form six-membered rings between the layers. Thus, two new types of cage arise, a small decahedron, $4^35^66^1$ cage, and a large 19-hedron, $4^35^{12}6^18^3$ cage (Figure 3.1). By connecting the 19-hedra cavities through a single 8-ring with an aperture of 4.4 x 3.6 Å, a two-dimensional channel system is formed, which is accessible to small molecules after detemplation by thermal treatment at 773 K - 973 K or ozonication at 473 K[190]. The small decahedron and pentagonal cages are only accessible through four-ring and five-ring windows; therefore, they are inaccessible for adsorbed guest molecules. Three different materials with the DDR-type topology have been reported in the literature: all-silica deca-dodecasil 3R (DD3R)[189], sigma-1[191] and ZSM-58[192]. For the synthesis of DD3R and sigma-1, 1-adamantanamine (1-ADA) is used as structure directing agent (SDA), while methyltropinium iodide (MTI) is used as the SDA in the synthesis of ZSM-58. A DDR unit cell contains six 19-hedra cavities, each of which has a volume of approximately 0.35 nm[181,193].

NGK insulators (Japan) have developed a high-silica DD3R zeolite membrane (Si/Al ratio = 980) consisting of a 2 μm zeolite layer deposited on an asymmetric α-alumina support[194,195]. These membranes have been successfully tested in gas separation experiments, for example, CO_2/CH_4[180,181,196], and in dehydration of solvents and acids[183,184]. Adsorption of several gasses and vapors on DD3R powder has been measured. Zhu *et al.* reported adsorption of several saturated and unsaturated hydrocarbons on DD3R[193,197]. DD3R zeolite exhibits selective adsorption of 1,3-butadiene and *trans*-2-butene over 1-butene and *cis*-2-butene revealing the size and shape selectivity of the DD3R zeolite[193]. Den Exter *et al.* investigated the adsorption of water on DD3R[198] and showed that the zeolite adsorbs water only to a very

small extent, confirming its hydrophobic character. Nevertheless, the DD3R membranes have shown to remove water from alcohols at high selectivity under pervaporation conditions[183,184]. Pervaporation is a mode of operation in membrane separation processes (Figure 3.2), where a liquid mixture is fed to a membrane while a low pressure or gas purge is applied to the permeate side. One or more components from the feed mixture selectively permeate through the membrane and evaporate into the vapor phase (hence, the word "pervaporation"). In an earlier study[184], we reported pure-component permeation fluxes of water, methanol and ethanol as well as mixtures of these components at temperatures ranging from 344 K to 398 K. The mixture measurements were conducted at liquid molar feed fractions of water of x_w = 0.1 – 0.5, leading to water/ethanol separation factors of up to $\alpha_{w,e}$ = 1500 and $\alpha_{w,m}$ = 9 for water/methanol.

The behavior of water in hydrophobic zeolites is complex, and water adsorption and permeation through small-pore hydrophobic zeolite membranes, such as DDR, have not been extensively studied. Molecular simulations of the adsorption and diffusion of several compounds in the DDR-type structure are reported, but these involve mainly gaseous components, such as CH_4, CO_2 and N_2[199-201]. There is a large number of simulation studies on water in hydrophobic zeolites, although the system considered is nearly exclusively silicalite-1[202]. One of the few studies focused on water in a hydrophobic small-pore zeolite is reported by Coudert *et al.*, who studied the behavior of adsorbed water in all-silica LTA zeolite by means of the Carr-Parrinello molecular dynamics method (CPMD)[169]. However, so far, no studies are reported on molecular modeling of water and alcohols in hydrophobic DDR-type zeolites.
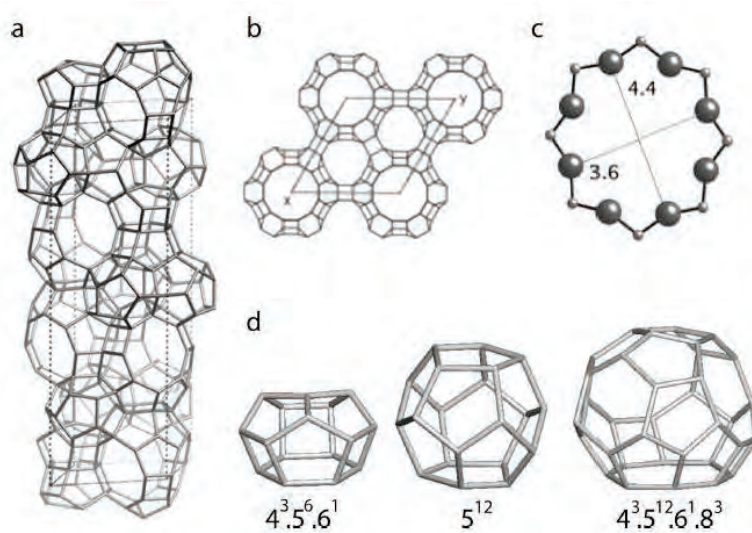

Figure 3.1. *The DDR-type topology unit cell (a) normal to and (b) down on the [001] plane; (c) the window opening, and (d) the decahedron, pentagonal, and 19-hedra cages that build up the structure* [9].

Demontis *et al.* demonstrated the complex temperature dependent behavior of water in silicalite-1 by molecular dynamics (MD) simulations including full flexibility of both the water molecules as well as the zeolite framework[203]. Desbiens *et al.* were able to reproduce experimental isotherms of water in silicalite-1 using simple models and (GCMC) simulations, applying the Tip4P and MSPC/E potentials for water and a rigid zeolite framework[146]. Similar interaction potentials have also been used to study adsorption of water and aromatic in the hydrophilic NaY zeolite[141]. Puibasset *et al.* used the PN-TrAZ water model in GCMC simulations of water in silicalite-1; however, the SPC model describing the confided water had to be adjusted to allow for a quantitative agreement with experimental data[135]. Fleys *et al.* used the Compass force field to reproduce water adsorption isotherms on silicalite-1 and de-aluminated zeolite Y[204,205]. The under prediction of the water loading at low pressures was attributed to crystalline defects, resulting in silanol groups within the zeolite framework. Trzpit *et al.* studied the effect of local defects on water adsorption in silicalite-1, enabling qualitative reproduction of the experimentally observed adsorption behavior[143].

The adsorption of methanol and ethanol in zeolites is less comprehensively studied by computational methods. Usually, the adsorption of these compounds is studied in the presence of water. The works of Vigner-Maeder *et al.*[206] and Pelmenschikov *et al.*[207] are two pioneering *ab-initio* studies of methanol adsorption in silicalite-1 where the adsorption energies, enthalpies of adsorption, influence of defects and potential maps are calculated. Hinderer *et al.* [208] proposed a Monte Carlo scheme together with a lattice representation of silicalite-1 to study the diffusion of methanol, including the possibility of chemical reactions in the system. Plant *et al.* studied water/methanol diffusion in a NaY zeolite, describing the temperature dependence, the hydrogen bonding and the interaction with the cations[209]. Gupta *et al.* studied water/ethanol adsorption in silicalite-1, indicating the preferential adsorption siting of different molecules[210]. Lu *et al.* simulated the adsorption and separation performance of water and methanol mixtures in MFI, MOR, CFI and DON zeolites[211].

Several studies compared the zeolite membrane performance with molecular simulations. Takaba *et al.* employed dual ensemble Monte Carlo (DEMC) simulations to obtain the adsorption and diffusivities of water, ethanol and binary mixtures in pervaporation across a silicalite-1 membrane[212]. Jia *et al.* studied pervaporation of different components and binary mixtures in silicalite-1, zeolite A, and chabazite membranes by MD simulations[213]. Furukawa *et al.* used non-equilibrium molecular dynamics (NEMD) simulations to study adsorption of ethanol/water mixtures in a hydrophilic NaA membrane, suggesting that the high selectivity for water is a cooperative effect of the adsorption selectivity and the high diffusivity of water within the zeolite[214]. Yang *et al.* studied methanol/water[149] and ethanol/water[215] permeation across silicalite-1 membranes by combining GCMC and MD simulations in the NVT-ensemble. They were able to qualitatively predict the separation factor and fluxes, while the discrepancies

between simulations and measurements were attributed to the existence of crystalline defects in the experimental systems. Modeling an idealized zeolite will always give a discrepancy with real systems, since zeolite crystals often consist of complex intergrown structures with internal grain boundaries and defects containing silanol groups and varying pore orientations[216].

This study is focused on measuring and simulating the adsorption and diffusion of water, methanol and ethanol on an all-silica DD3R zeolite to elucidate the mechanism of water transport and separation in DD3R zeolite membranes. To our knowledge, there is no force field that quantitavely describes the adsorption and diffusion of water and alcohols in DDR-type zeolites. The development of a force field that accurately describes the adsorption of water in hydrophobic zeolites is subject to severe difficulties, as adsorption is extremely sensitive to the force field parameters, the atomic positions of the framework atoms, and the partial charges of the framework atoms[217]. Therefore, the objective of the simulation work presented in this study is to provide a qualitative explanation of the phenomena found experimentally using force fields taken directly from the literature. The calculated mixture adsorption isotherms are supplemented with self-diffusivities obtained by MD simulations and used to predict the component fluxes and selectivities in alcohol dehydration under pervaporation conditions.
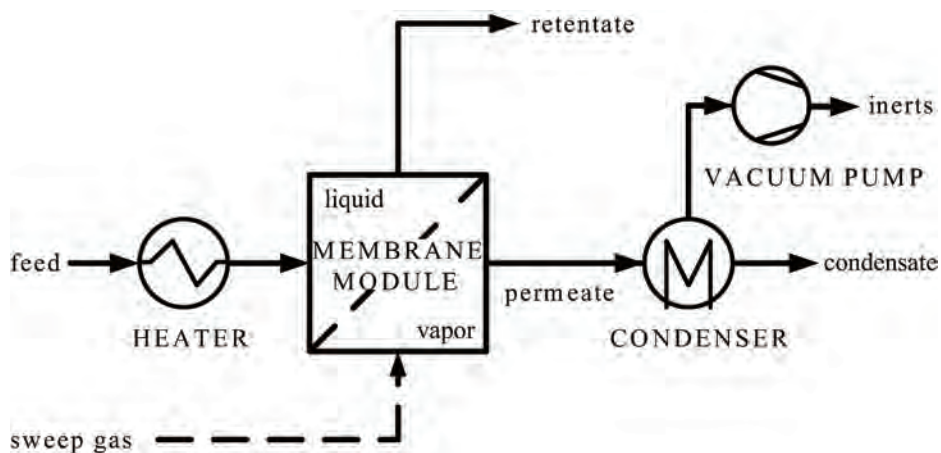

Figure 3.2. *Schematic representation of a pervaporation process.*

3.2. Experimental details

Synthesis

To perform adsorption experiments, DD3R were prepared by the method described by Gascon *et al.*[218]. All chemicals were purchased from Aldrich and used as received, without further preliminary purification. The synthesis mixture had the molar ratio of 1-ADA/SiO$_2$/ethylenediamine (EDA)/H$_2$O = 47:100:404:11240 and it was prepared as follows. 1.72 g of 1-ADA (97 wt%) was dissolved in 5.76 g EDA ($\geq$ 99 wt%) and placed in an ultrasonic bath for 1 h. Water (38 g) was then added rapidly. The mixture was placed in a shaking machine for 1 h. After heating to 368 K for 1 h while stirring, the mixture was cooled down in ice. Aerosil 200 (1.41 g) was then slowly added while the solution was stirred vigorously. The mixture was again heated to 368 K in an open vessel while stirring until the solution became clear (the solution changed from white to almost transparent). As-synthesised DD3R crystals (0.01 g) were added as seeds. The resulting solution is placed in a Teflon lined autoclave and heated under hydrothermal conditions (autogenous pressure) to 433 K for 2 days under rotation at 60 rpm. The synthesized samples were calcined at 873 K for 6 h using a heating and cooling rate of 60 K h^{-1}. The calcination was carried out in static air (Carbolite CSF1100).

The synthesized DD3R crystals were homogeneous diamond like crystals, as reported by den Exter *et al.*[198]. The size of the crystals was 2.7 μm, measured by laser diffraction, and the micropore volume of 0.13 cm^3 g^{-1} was determined by nitrogen adsorption at 77 K using the *t*-plot method[190].

Adsorption

The synthesized zeolite crystals are used for adsorption measurement of water, ethanol and methanol. The single-component vapor adsorption (Quantachrome Autosorb-6B) experiments were conducted to determine the adsorption isotherms at different temperatures. Prior to the vapor-phase adsorption measurements, the samples were dried in vacuum at 573 K in order to remove moisture and other volatile components (the weight of the sample after drying was used in the calculations). The adsorption and desorption isotherms were measured at 273 K, 303 K and 333 K, which is the maximum temperature for vapor adsorption in this setup.

Analysis of the permeation experiments

Pure-component, and mixture permeation of water, ethanol and methanol were previously reported[5]. These permeation measurements were conducted under pervaporation conditions, applying vacuum with a permeate pressure of p^{perm} = 1 kPa. In this study, we use the pure-component measurements as well as

measurements of the binary alcohol/water mixtures for comparison and validation of the calculated adsorption data and for calculation of diffusivity data.

The Maxwell-Stefan (M-S) equations are generally used to model mass transport in zeolites and zeolite membranes[219-221]. They have been successfully applied to several systems[222-224]. These equations balance the driving forces with the friction exerted on molecules and are consistent with the theory of irreversible thermodynamics[225,226]. In the case of transport through a porous membrane, the membrane can be viewed as a component, M. Using the membrane as frame of reference (choosing the membrane velocity, $v_M = 0$), the M-S equations for an n-component system can be written as[227]

$$-\rho_z \frac{\theta_i \nabla \mu_{i,T}}{RT} = \sum_{\substack{j=1 \\ j \neq i}}^{N} \frac{\left(q_j N_i - q_i N_j\right)}{q_i^{sat} q_j^{sat} Đ_{ij}} + \frac{N_i}{q_i^{sat} Đ_{iM}} \tag{3.1}$$

where $\nabla \mu_{i,T}$ denotes the chemical potential gradient at constant temperature as the driving force for mass transport, N_i denotes the mass flux of component i, $Đ_{iM}$ is the M-S diffusivity of component i in the microporous membrane, $Đ_{ij}$ is the M-S cross-diffusivity that accounts for the interaction between permeating components, and θ_i denotes the fractional loading, defined as the ratio of the loading q_i over the saturation loading q_i^{sat}

$$\theta = \frac{q_i}{q_i^{sat}} \tag{3.2}$$

In small pore zeolites, the interaction between species within the zeolite can be neglected (i.e., $Đ_{ij} = 0$)[228]. When only transport in the z direction is considered, Eq. (3.1) reduces to

$$-\frac{\theta_i}{RT} \frac{d\mu_{i,T}}{dz} = \frac{N_i}{\rho_z q_i^{sat} Đ_{iM}} \tag{3.3}$$

The chemical potential gradient can be converted to a gradient in loading using the thermodynamic correction factor, Γ_{ij}, which relates the fractional loading θ_i to the fugacity f_i[219]

$$\frac{\theta_i}{RT} \frac{d\mu_{i,T}}{dz} = \Gamma_{ij} \frac{d\theta_i}{dz} \tag{3.4}$$

where

$$\Gamma_{ij} = \frac{\theta_i}{f_i} \frac{\partial f_i}{\partial \theta_j} = \frac{q_j^{sat}}{q_i^{sat}} \frac{q_i}{f_i} \frac{\partial f_i}{\partial q_i} \qquad (3.5)$$

When the driving force is expressed as the gradient in loading, $(dq_i/dz) = q_i^{sat}(d\theta_i/dz)$, the flux can be expressed as[227]

$$N_i = -\rho_z \mathcal{D}_{iM} \left[\Gamma_{ii} \nabla q_i + \Gamma_{ij} \frac{q_i^{sat}}{q_j^{sat}} \nabla q_j \right] \qquad i \neq j \qquad (3.6)$$

where ρ_z denotes the density of the zeolite. We assume the membrane thickness to be sufficiently thin so that the differentials in loading can be replaced by differences over the membrane. By taking an average value of Γ_{ij} ($i, j = 1, 2, …, n$), Eq. (3.6) simplifies to

$$N_i = -\frac{\rho_z \mathcal{D}_{iM}}{\delta} \left[\langle \Gamma_{ii} \rangle \Delta q_i + \langle \Gamma_{ij} \rangle \frac{q_i^{sat}}{q_j^{sat}} \Delta q_j \right] \qquad i \neq j \qquad (3.7)$$

where δ denotes the membrane thickness and $\Delta q_i = q_i^{perm} - q_i^{feed}$. The value of Γ_{ij} is approximated by averaging the value obtained at the permeate and the feed side conditions

$$\langle \Gamma_{ij} \rangle = \frac{\Gamma_{ij}^{feed} + \Gamma_{ij}^{perm}}{2} \qquad i, j = 1, 2, …, n \qquad (3.8)$$

The temperature dependence of the self-diffusivity at constant loading is generally described by an Arrhenius type of equation, using an activation energy, E_A.

$$D_i^s = D_{i,0}^s \exp\left(-\frac{E_{A,i}}{RT}\right) \qquad (3.9)$$

In pervaporation processes, the liquid feed side fugacity, f_i^{feed}, can be calculated using[229]

$$f_i^{feed} = x_i^{feed} \gamma_i \, p_i^{sat} \phi_i^{sat} \exp\left[\frac{V_{m,i}^l \left(p - p_i^{sat}\right)}{RT}\right] \tag{3.10}$$

where x_i^{feed} is the liquid mole fraction and γ_i denotes the activity coefficient in the mixture, p is the system pressure, and $V_{m,i}^l$ is the partial molar volume of component i in the liquid feed. The Antoine equation is used to calculate the vapor pressure, p_i^{sat}, as a function of temperature[230]. The fugacity coefficient ϕ_i^{sat} and the Poynting factor (exponent term in Eq. (3.10)) can be assumed to be equal to unity at pervaporation conditions. In this study, the activity coefficients were calculated using the NRTL Gibbs excess energy model.

To calculate the adsorption from a given liquid feed, the fugacities were calculated, and these were used as input for the GCMC calculations. The composition can be expressed as the ratio of the component fugacity over the sum of the fugacities of all species in the mixture

$$Y_i = \frac{f_i}{\sum_{j=1}^{N} f_j} \tag{3.11}$$

As the permeate side is operated at low pressures, it is well approximated by the ideal gas limit

$$f_i^{perm} = p_i^{perm} = y_i^{perm} p^{perm} \tag{3.12}$$

and therefore, the fugacity ratio at the permeate side equals the vapor mole fraction, y_i^{perm}.

In experimental studies, the permeation is often described by the permeance, Π_i, defined as the ratio of the flux and the difference in fugacity over the membrane[231]. The temperature dependency of the permeance is the characterized by an apparent activation energy, E_{app}, which can be seen as the sum of the activation energy of diffusion and the enthalpy of adsorption[232].

3.3. Simulation details

Adsorption isotherms in confined systems are conveniently computed using GCMC simulations, in which the temperature, the volume and the chemical potential of the system are imposed. The imposed chemical potential is directly related to the fugacity, which is used as input for the simulations. At high density, the probability of successfully inserting a molecule in the system is very low. Therefore, the insertion and deletion of molecules in and from the system were performed using a configurational-bias Monte Carlo (CBMC) technique[47] in combination with other MC moves, namely, regrow, rotation, and translation. In the case of ethanol/water mixtures, identity change moves were also used to increase the performance of the simulation[47]. More details on this simulation technique can be found elsewhere[52,166]. The saturation loadings were calculated from a single adsorption simulation at a high fugacity. The enthalpies of adsorption were computed as the isosteric heats of adsorption at zero loading using MC simulations in the NVT ensemble[97].

There are several diffusion coefficients that can be used to describe the motion of molecules within a zeolite. Generally, the Fick, or transport diffusivity, D_i^T, is the most intuitive definition of a diffusion coefficient, relating a molar flux to a gradient in concentration[233]. The actual thermodynamic driving force for transport is, however, the gradient in chemical potential[234]. Using the framework of irreversible thermodynamics, the collective, corrected, or Maxwell-Stefan (M-S) diffusivity, D_i, can be defined, relating the thermodynamic driving force to a molar flux[232]. The self diffusivity, D_i^s, describes the motion of individual particles and can be related to the mean square displacement of the individual molecules during equilibrium MD simulations by the Einstein equation[235] (Eq. 1.57). The M-S and the transport diffusivity can be obtained from NEMD but also from equilibrium MD simulations by considering the collective motion of molecules[221,235].

In this study, water is modeled using the Tip5pEw potential[74]. The alcohols are described with the TraPPE force field[236], which was also applied by Jakobtorweihen *et al.* for modeling the adsorption of ethene, propene and *trans*-2-butene in DD3R[201]. No hydrolysis is expected during the adsorption of these molecules in zeolites under the conditions applied[163,209]. Intramolecular potentials are included to describe the flexibility of alcohols, while the water molecules are kept rigid. The bond lengths are fixed for all molecules. Bond bending potentials are considered for methanol and ethanol, and a torsion potential is used for ethanol[236].

Self diffusivities were calculated from the mean square displacement (MSD) of the molecules by the Einstein equation[225] and using transition-state theory (TST)[237-239]. The MSD was obtained by means of Molecular Dynamic (MD) simulations in the canonical ensemble[47]. The equations of movement were

integrated using the Verlet algorithm with a time-step of 0.5 fs. The temperature in the system was controlled with a Nosé-Hoover chain thermostat (chain length of 3). In order to compute the diffusivity of water and methanol, we have performed MD simulations of at least 10 ns. The square root of the mean square displacement was at least 60 Å, and we verified that this is sufficiently large to correctly compute the diffusivity. The transport diffusivities were calculated using the Onsager formulation, relating the diffusivity to the collective displacement of all molecules in the simulation box[235]. Due to the slow diffusion of the relatively large ethanol molecule within the DDR-type structure, it was not possible to obtain their diffusivity from conventional MD simulations. Therefore, the TST method[47] was used to obtain a more accurate value of the ethanol diffusivity.

The values of Γ_{ij} can be directly obtained from the GCMC results. In this study, we used a method inspired by the approach of Chen *et at.*[240] to calculate Γ_{ij}.

The crystallographic positions of the zeolite atoms were obtained from XRD characterization data of the structure[241]. The simulations were performed using 1 x 2 x 1 unit cells with periodic boundary conditions, so that the size of the simulation box was more than twice the Lennard-Jones cutoff radius, being the cutoff radius 12 Å. To reduce the calculation time, the simulations were performed considering a rigid framework[56]. Since the $4^3 5^6 6^1$ and the 5^{12} cages of the DDR-type structure only contain five membered ring windows, they are inaccessible for adsorbed species. To ensure that no molecules were adsorbed in these cages during the simulations, they were blocked using the same blocking positions as in ref. [201].

The models of Beerdsen *et al.*[242,243] and Calero *et al.*[45,244] were used to assign partial charges to the zeolite atoms. The coulombic interactions were calculated using Ewald summations with a relative precision of 10^{-6} [46]. The non-coulombic interactions between non-bonded atoms or atom groups were modeled using 12-6 Lennard-Jones potentials, truncated and shifted at the cutoff of 12 Å.

The van der Waals interactions between the adsorbates and the framework are dominated by the dispersive forces between the atom groups of the sorbed molecules and the oxygen atoms of the zeolite[53,54]. For this reason, they were modeled through an effective potential that only takes the oxygen atoms of the zeolite structure into account. One set of potential parameters that has been used in previous studies on water adsorption in zeolites was implemented[167], together with Lorentz-Berthelot mixing rules in order to account for the rest of the interactions. All parameters for non-bonded interactions used in this work are listed in Table 3.1.

atom	$\varepsilon/k_B/K$	$\sigma/\text{Å}$	q/e	ref.
Si (zeolite)			2.05	45
O (zeolite)	93.53	3.0	-1.025	167
O (water)	89.516	3.097		74
H (water)			0.241	74
M (water)			-0.241	74
CH$_3$ (methanol)	98.0	3.75	0.265	236
CH$_3$ (ethanol)	98.0	3.75		236
CH$_2$ (alcohol)	46.0	3.95	0.265	236
O (alcohol)	93.0	3.02	-0.7	236
H (alcohol)			0.435	236

Table 3.1. *Force field parameters used in the simulations. The water model has two off-center charges that are labeled M in the table. The name "alcohol" refers to both methanol and ethanol molecules.*

3.4. Results

Single component adsorption

The experimental adsorption and desorption isotherms and calculated adsorption isotherms for water, methanol and ethanol are shown in Figures 3.3, 3.4, and 3.5 respectively. No significant hysteresis effects were observed in the desorption measurements.

Adsorption data for water was previously published by den Exter *et al.*[198]. Our measurements at T = 333 K and T = 323 K correspond well with previous data, whereas at 303 K we find a somewhat lower adsorption loading. The form of the water adsorption isotherms (type II) is consistent with simple BET models valid for free surfaces of fine capillaries with no constraint imposed on the adsorption from the opposite wall. However, it is expected to resemble type IV adsorption when reaching saturation[245]. The calculated water loading, however, under predicts the experimental values (Figure 3.3). The calculated water isotherms resemble type III adsorption behavior at low fugacities, which is typical for water adsorption on hydrophobic surfaces[144].

The alcohol isotherms show a type I adsorption behavior, which is consistent with Langmuir adsorption (Figures 3.4 and 3.5). The fitted Langmuir parameters are given in Table 3.2. The calculated methanol and ethanol isotherms show a similar shape and order of magnitude as the experimental data. However, at low methanol fugacities, the calculated values are larger than the measured data, suggesting that the force field parameters are not well optimized for these types of systems.
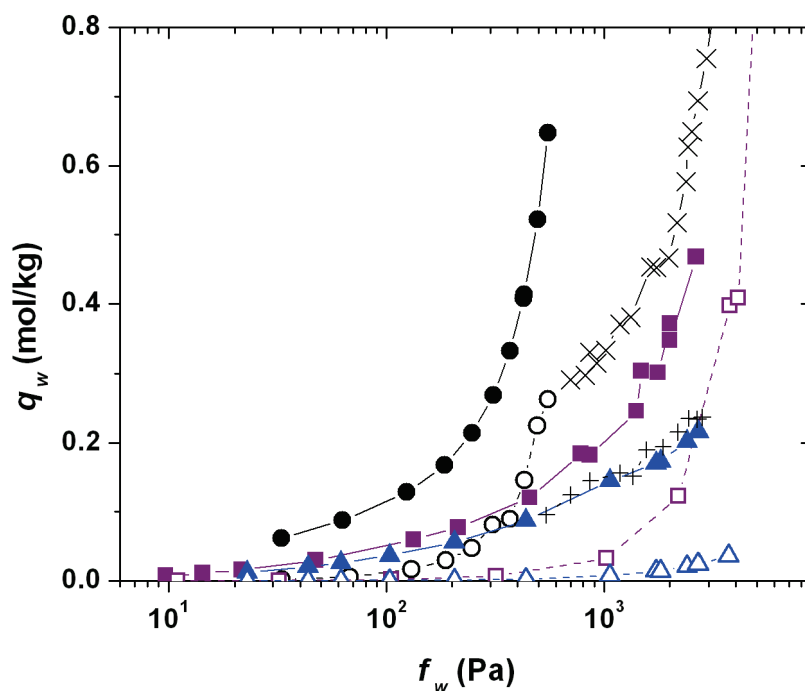
Figure 3.3. *Water adsorption isotherms at 273 K (circles), 303 K (squares), and 333 K (triangles) obtained in this study. Closed symbols, experimental data; open symbols, simulation data. X, +, experimental data at 303 K and 333 K respectively [198]. The solid and dashed lines are a guide to the eye for the experimental and calculated isotherms, respectively.*

The saturation loading is estimated by calculating the loading at a fugacity of 1 GPa and 303 K. This yields a saturation loading of 10.4, 4.2, and 2.6 mol kg^{-1} for water, methanol and ethanol, respectively (Figure 3.6). This corresponds to 12, 5 and 3 molecules per 19-hedra cage, respectively. The calculated water adsorption isotherm at 303 K resembles type V behavior. It should be noted that the water loading still showed a slight increase when increasing the fugacity from 100 MPa to 1 GPa, but the increase was within the accuracy of the simulations.

Mixture adsorption

Mixture adsorption isotherms have been computed at 303 K and 360 K at a constant ratio of the water fugacity, f_w, divided by the sum of the water and the alcohol fugacity, f_a, of y_w = 0.1, 0.2 and 0.5. At low fugacities, this equals the vapor mole fraction, y_w. Figures 3.7 and 3.8 show the mixture adsorption isotherms, together with the single component isotherms, at 303 K for methanol/water and ethanol/water mixtures, respectively. The loading of each component is given as a function of the total fugacity. The isotherms show that, at low fugacities, the water loading increases with the water fugacity ratio, while the alcohol loading shows only a slight decrease and the shape of the alcohol isotherm remains the same as for the single-component adsorption. The water adsorption is enhanced by the presence of alcohol. While

the methanol adsorption is practically insensitive to the presence of water, the adsorption of ethanol is largely enhanced by the presence of water, although it does not depend on the water concentration. The shape of the water isotherm changes from type V to type I, resembling the shape of the alcohol isotherms. Although the ideal adsorption solution theory (IAST) has shown to be able to describe the adsorption behavior of water and methanol on activated carbon[246], we checked that in this system the IAST fails to predict the mixture adsorption. The comparison between the IAST and the simulation data can be found in the Appendix (Figure C).

Figure 3.9 shows the binary adsorption isotherms as a function of the sum of the water and alcohol fugacities up to 180 kPa at 360 K and a constant water fugacity ratio of 0.2, which corresponds to a feed mole fraction of $x_w = 0.5$ and 0.2 for methanol/water and ethanol/water mixtures at 360 K, respectively. These conditions correspond to the feed conditions of the conducted pervaporation experiments, which are indicated by the dashed lines. The loading of each component at the feed side under the pervaporation conditions can be directly read from the vertical axis. The calculated water loading remains lower than the alcohol loading within the range of calculated total fugacities. The ethanol loading at the experimental feed condition is lower than that of the methanol, while the water loading is equal in both systems.
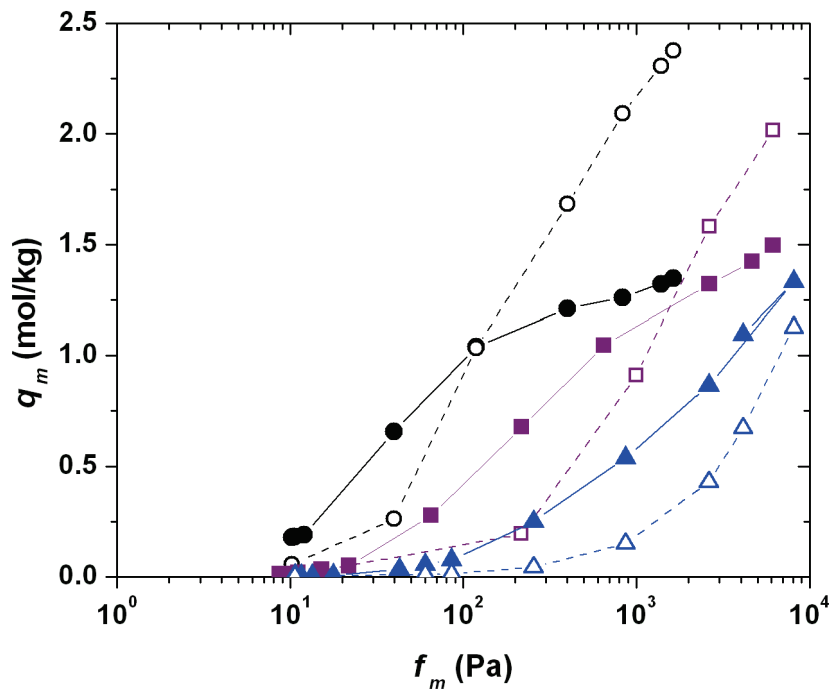

Figure 3.4. *Methanol adsorption isotherms at 273 K (circles), 303 K (squares), and 333 K (triangles) obtained in this study. Closed symbols, experimental data; open symbols, simulation data. The solid and dashed lines are a guide to the eye for the experimental and calculated isotherms, respectively.*

Figures 3.10 a and b show snapshots of methanol/water and ethanol/water mixtures, respectively. The figures show a larger loading of alcohols compared to water. The water molecules show a preferential adsorption in the vicinity of the alcohol groups of the adsorbed ethanol and methanol molecules, with which hydrogen bonds are formed.

Diffusivities and permeation

To elucidate the separation mechanism of the selective water transport through the hydrophobic DD3R membrane, simulation data is combined with data from permeation measurements conducted under pervaporation conditions. To assess the diffusivity of the components, the feed conditions of the pervaporation experiment of pure-component and mixture permeation are taken as input to calculate the loading at the feed side. The self-diffusivities and transport diffusivities, calculated by MD simulations and the thermodynamic correction factor, are computed. In the calculations, a zeolite density of $\rho_z = 1700$ kg m^{-3} was used, which follows from the unit cell dimensions[9], and a membrane thickness of 2 μm was assumed.
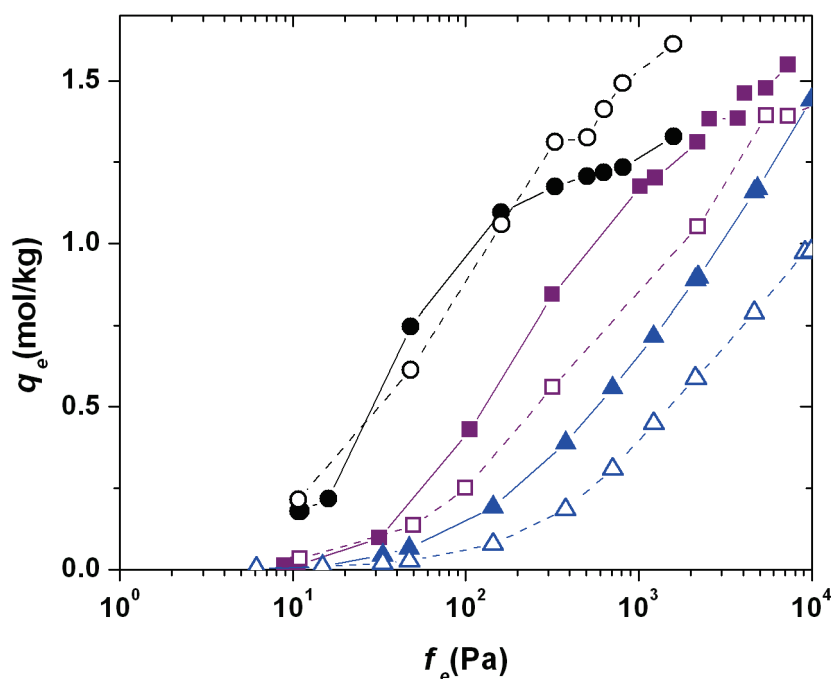

Figure 3.5. *Ethanol adsorption isotherms at 273 K (circles), 303 K (squares), and 333 K (triangles) obtained in this study. Closed symbols, experimental data; open symbols, simulation data. The solid and dashed lines are a guide to the eye for the experimental and calculated isotherms, respectively.*

T/K	methanol		Ethanol	
	q_i^{sat}/mol kg^{-1}	K_i/10^{-3} Pa s^{-1}	q_i^{sat}/mol kg^{-1}	K_i/10^{-3} Pa s^{-1}
273	1.39 ± 0.03	18.18 ± 1.77	1.38 ± 0.03	16.81 ± 1.82
303	1.53 ± 0.03	3.30 ± 0.29	1.51 ± 0.02	3.52 ± 0.29
333	1.60 ± 0.06	0.53 ± 0.05	1.55 ± 0.05	0.70 ± 0.07

Table 3.2. *Fitted Langmuir parameters [$q_i = q_i^{sat} (K_i f_i / (1 + K_i f_i))$] from the measured isotherms of methanol and ethanol on DD3R at 273 K, 303 K and 333 K.*

At the conditions of the pure-component permeation experiments, the calculations predicts a water loading at the feed side of the membrane which is a factor 2 to 3 lower than for the alcohols (Table 3.3). To assess the temperature dependence of the diffusivity, the self-diffusivities of water and methanol at constant loading were computed. The loading was kept constant at the value corresponding to the equilibrium loading at 360 K. The values are listed as a function of the temperature in Table 3.4 and plotted in Figure 3.11. The calculated feed side loading and the self-diffusivities for the methanol/water and ethanol/water mixtures are listed in Tables 3.5 and 3.6, respectively. The measured permeate side water mole fraction, y_w^{perm}, and the feed composition, x_w^{feed}, are also given, which give a measure for the selectivity. Although the presence of alcohol enhances water adsorption, at the feed conditions of the mixture permeation experiments, the simulation data suggest that the molar water loading is still only half of the alcohol loading. For water, the M-S diffusivity has been calculated and is on the same order of magnitude as the self-diffusivity. For the alcohols, the M-S diffusivity could not be obtained due to the range of values which can be calculated using MD simulations. The ethanol molecules did not escape from the 19-hedra cage within the duration of the simulation (>20 ns). Therefore, we have estimated this diffusivity at 360 K in pure siliceous DDR using TST and the method described in ref. [239]. We obtained a free-energy barrier of 16.6 k$_B$T, corresponding to a diffusivity of $3 \cdot 10^{-14}$ m^2 s^{-1}. As TST provides an upper limit for the diffusivity[47,247], the actual diffusivity of ethanol is even lower. This clearly shows that the diffusivity of ethanol is much lower than the diffusivity of methanol and water. In the remainder of this study, we will consider a diffusivity of $3 \cdot 10^{-14}$ m^2 s^{-1} for ethanol. The ethanol diffusivity is similar to the diffusivity of ethylene in high-silica DDR[248]. In the remainder of this study, only the self-diffusivities are reported, which are assumed to be similar to the M-S diffusivities. As a first model approximation, the self-diffusivities are only calculated for the feed side conditions of the pervaporation experiments, and are assumed to be constant.

For mixture permeation at 360 K, the self-diffusivities are given as a function of the feed side composition, x_w (Figure 3.12). The calculated diffusivities of water are larger than those for the alcohols and increase with temperature and concentration. The increase with temperature and concentration also holds for ethanol, while the calculated methanol diffusivity is practically constant.

For the mixture permeation at $x_w = 0.2$ and 360 K, the values of $\langle\Gamma_{ij}\rangle$ were determined and combined with the loading to predict the flux through the membrane using Eq. 3.7. The value of the ethanol diffusivity in the mixture is estimated at 10^{-14} m^2 s^{-1}. From the permeate composition, the water separation factors are predicted at 8.7 and 2029 for methanol/water and ethanol/water, respectively, which corresponds well to the experimentally determined values (6.8 and 1025).

The activation energies of the single-component transport diffusivities are calculated from the data in Table 3.4 using Eq. 3.9 and are listed in Table 3.8. The same table also shows the apparent activation energy calculated from the permeance, as was reported earlier[184], and the average enthalpies of adsorption calculated as the isosteric heats of adsorption at zero loading from 348 K to 373 K. The enthalpy of adsorption increases with temperature, but the values from 348 K to 373 K only differ by less than 6%.
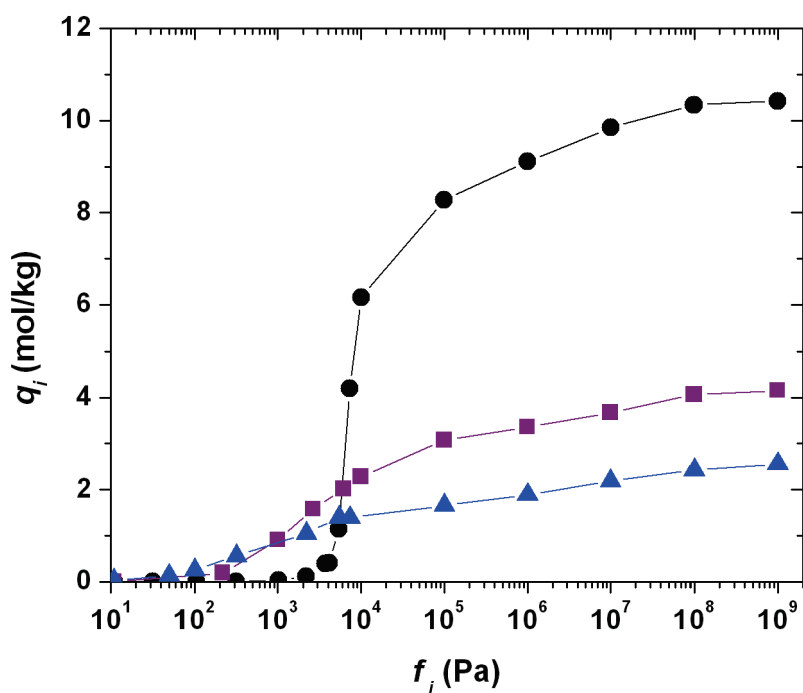

Figure 3.6. *Water (circles), methanol (squares), and ethanol (triangles) adsorption isotherms obtained by simulation up to 1 GPa at 303 K.*

Figure 3.7. *Experimental (exp) pure-component and calculated (sim) methanol/water adsorption isotherms at 303 K for water fugacity ratios of y_w = 0, 0.1, 0.2, 0.5 and 1. The loading of (a) water and (b) methanol is shown as a function of the component fugacity. The solid lines indicate the experimental pure-component isotherms.*
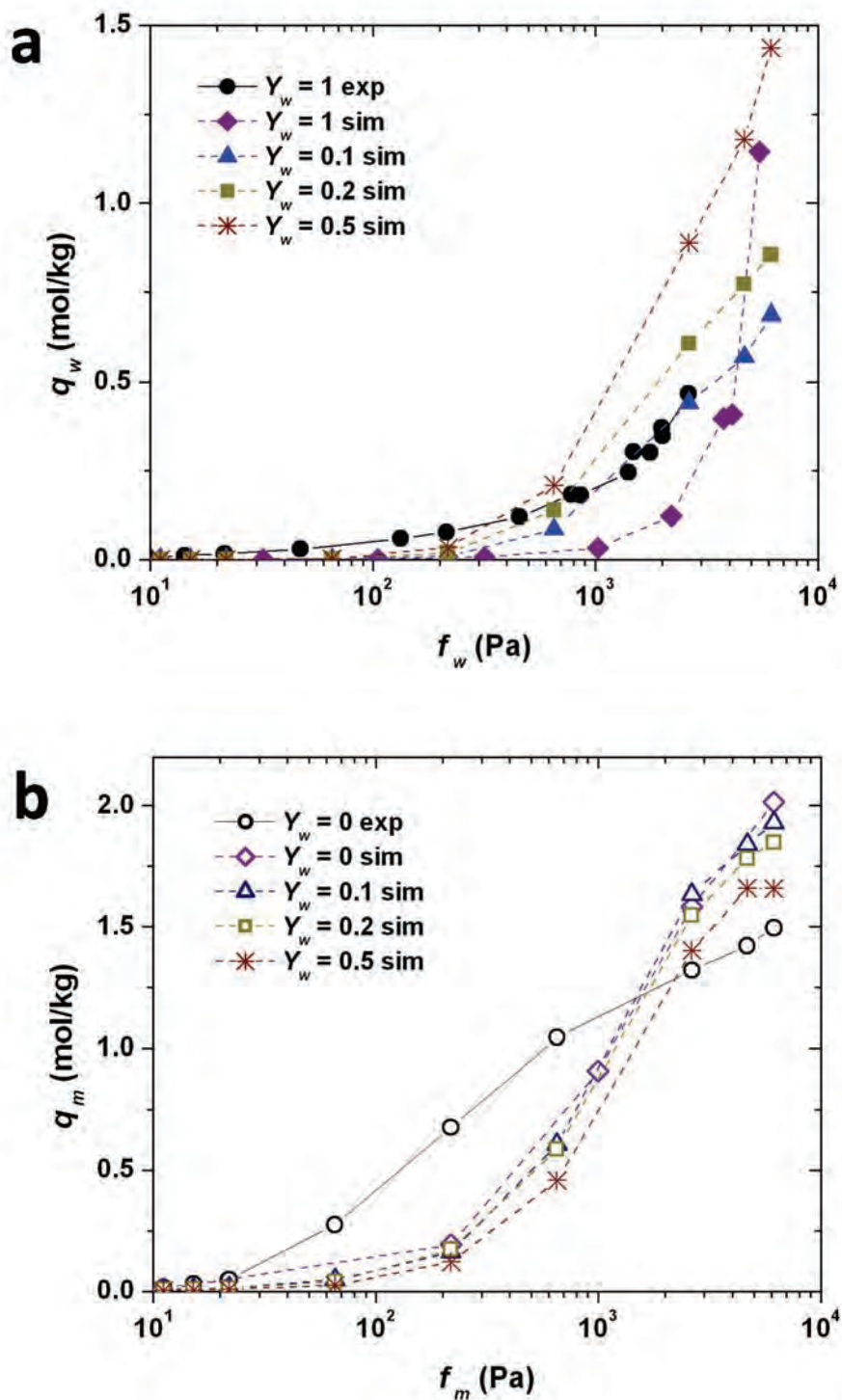
Figure 3.8. *Experimental (exp) pure-component and calculated (sim) ethanol/water adsorption isotherms at 303 K for water fugacity ratios of y_w = 0, 0.1, 0.2, 0.5 and 1. The loading of (a) water and (b) ethanol is shown as a function of the component fugacity. The solid lines indicate the experimental pure-component isotherms.*
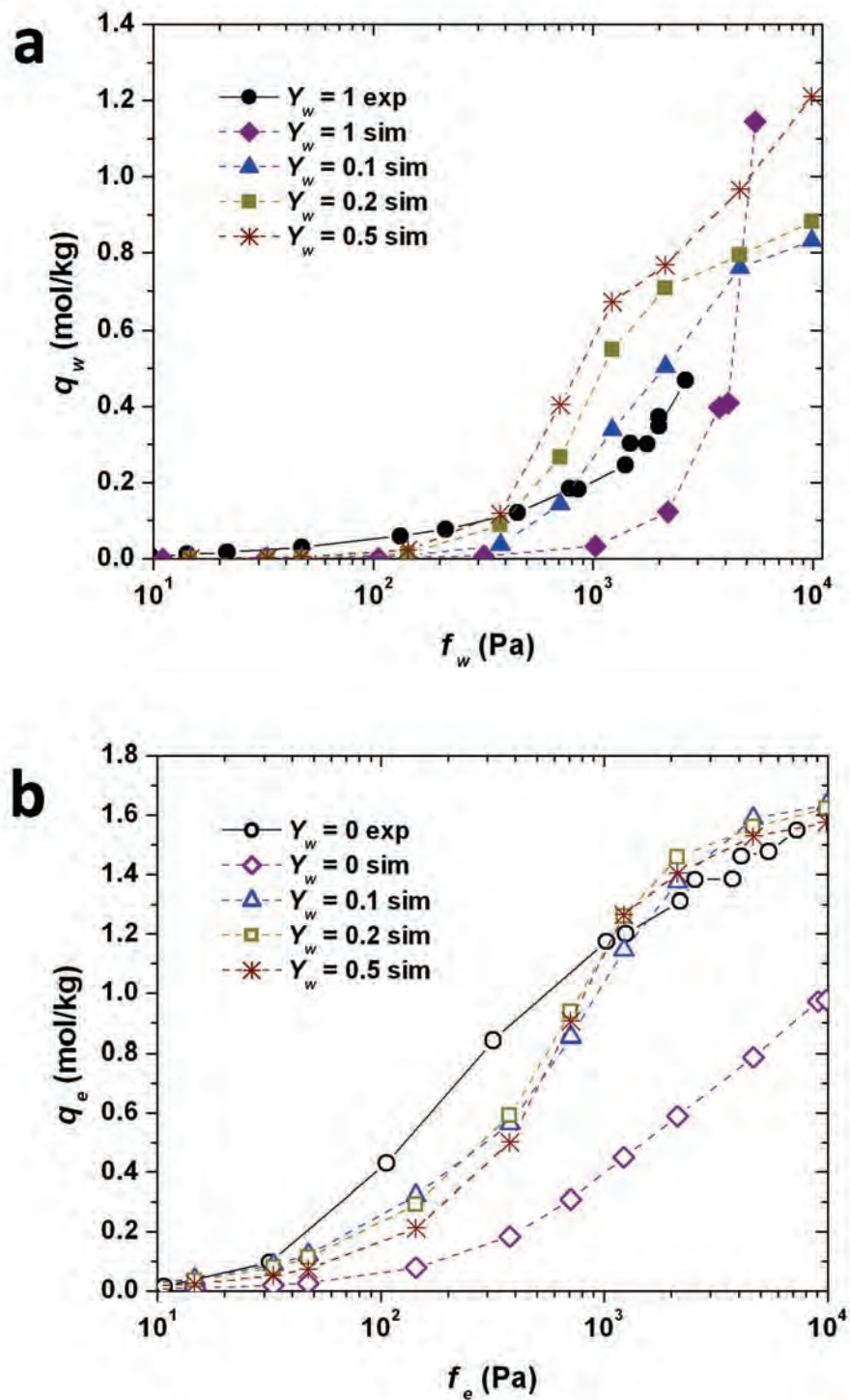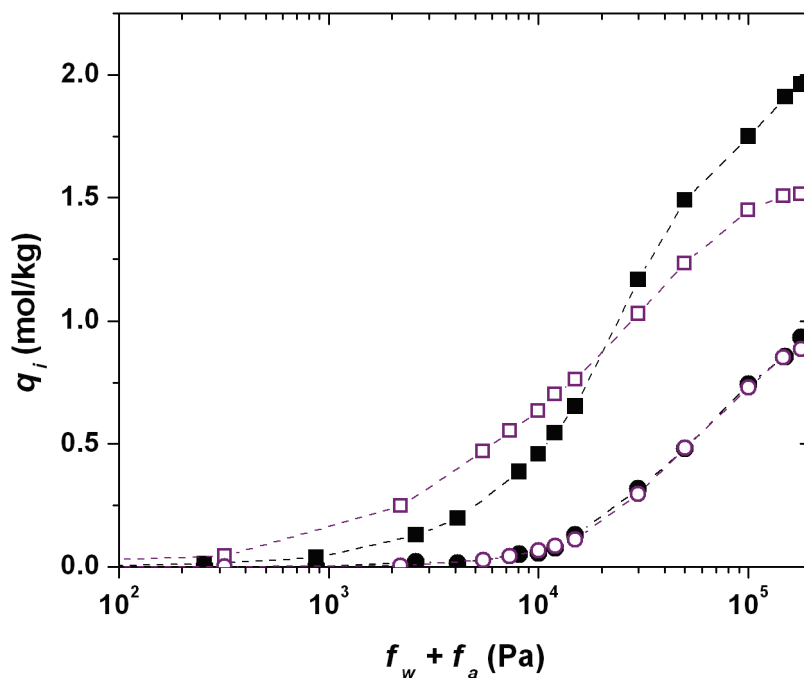
Figure 3.9. *Simulated mixture adsorption isotherm of water (closed circles) and methanol (closed squares) in methanol/water mixtures and water (open circles) and ethanol (open squares) in ethanol/water mixtures at 360 K and a water feed fugacity ratio of $y_w = 0.2$ as a function of the total fugacity.*

3.5. Discussion

The measured water adsorption isotherms are in fair agreement with the data reported by den Exter *et at.*[198].The calculated loading under predicts the actual loading at low fugacities. The measured adsorption resembles type II/IV behavior, while the calculated isotherm corresponds to type III/V (Figures 3.3 and 3.6). This can be partially attributed to the presence of crystalline defects in the zeolite sample, such as silanol groups, which have a strong effect on the water adsorption, specially at the low end of the loadings (and fugacities)[143]. This is also the region where deviations of the simulations are more apparent. Furthermore, a deviation from the experimental values is expected since the molecular models and force field parameters were taken directly from the literature, without further adjustment. Optimizing these force field parameters was beyond the scope of this work.

Both the calculated and the measured alcohol isotherms resemble type I adsorption. The experimentally determined alcohol loading is fairly well described by a single-site Langmuir adsorption isotherm (Figures 3.4 and 3.5). The Langmuir adsorption parameters of methanol and ethanol are very similar

(Table 3.2). However, the decrease in saturation loading with temperature shows that this value does not resemble complete saturation.

The water adsorption is enhanced by the presence of alcohol and vice versa. This adsorption behavior is comparable to the one observed for methanol/water coadsorption on activated carbon[246-249]. The increased adsorption in the mixture as compared to single-component adsorption is significantly more pronounced for water than for alcohols. Such an increase in water loading was also observed by Jia *et al.*, who conducted molecular simulations for ethanol/water in silicalite-1[213]. However, in the study on silicalite-1 it was observed that the ethanol loading decreased, while in this study the alcohol loading at constant total fugacity increased, although was independent of the water content. This effect can be attributed to water adsorption in the vicinity of the polar OH groups of the adsorbed alcohols (Figure 3.10). The shape of the water isotherm changes in the presence of alcohol from a type III/V to a type I, similar to the alcohol adsorption (Figures 3.7a and 3.8a). Because of this complex behavior, the estimation of mixture adsorption from pure-component data is not trivial. The mixture adsorption calculated from pure-component data using IAST did not give a good description of the mixture adsorption (Appendix, Fig. C).
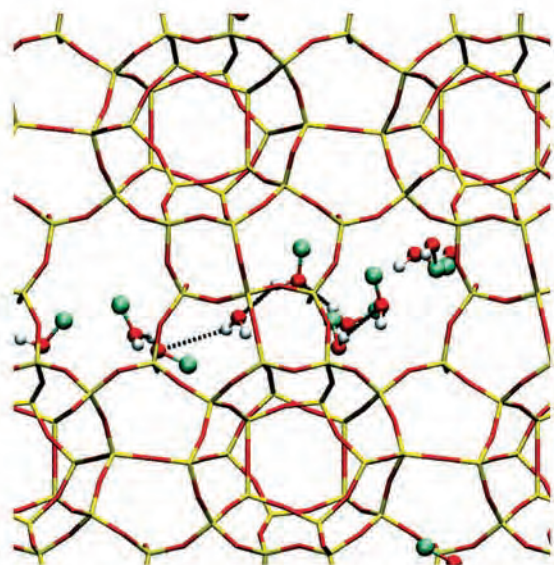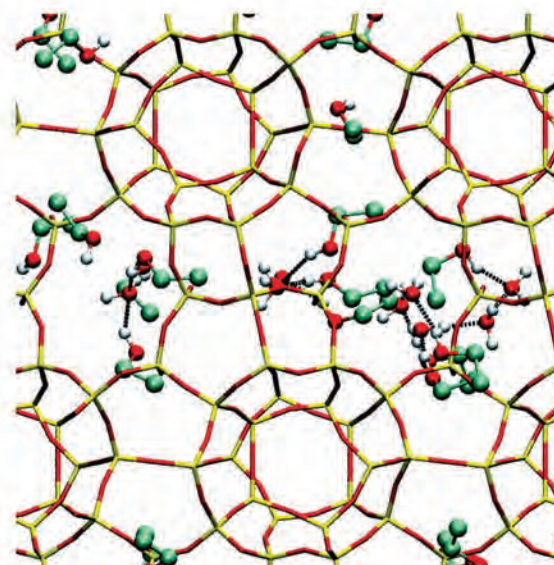
(a) Methanol/water   (b) Ethanol/water

Figure 3.10. *Snapshots of (a) methanol/water and (b) ethanol/water mixture adsorption on DD3R at 360 K and 15kPa. The hydrogen bonds are marked with dotted lines.*

The calculated pure-component molar loadings at the feed side of the pervaporation conditions (Table 3.3) reveal the water adsorption increases with temperature, whereas the alcohol adsorption decreases. This shows that the increase in vapor pressure for water, and therefore the driving force for adsorption, over compensates the decrease in the host-guest interaction. This is in agreement with the lower enthalpy of adsorption for water as compared to alcohols (Table 3.8). At high fugacities (~100 kPa), the calculated pure component water adsorption surpasses the alcohol adsorption (Figure 3.6).

The calculated saturation loadings are comparable to values reported for LTA-type zeolites, which are 15, 6 and 4 mol kg^{-1} (204, 82, and 55 molecules per unit cell) for water, methanol, and ethanol, respectively[250,251]. Adsorption of 1 mol kg^{-1} in DD3R corresponds to 14.4 adsorbed molecules per unit cell and 1.2 molecules per 19-hedra cage (12 cages per unit cell). In the LTA zeolite structure, which contains only one α-cage and one β-cage per unit cell, 1 mol kg^{-1} equals 13.6 molecules per unit cell. Since in DDR-type zeolite only the 19-hedra cages are accessible and in LTA the complete internal void volume is accessible for water, the saturation loading on DD3R is expected to be lower. Corma *et at.* reported a water loading of 0.6 mol kg^{-1} at 298 K and 2 kPa on all-silica LTA[252], which is larger than the measured 0.35 mol kg^{-1} on DD3R at 303 K and similar pressure. Coudert *et al.* reported a water saturation loading in the all-silica LTA calculated by GCMC simulations of 1.5 mol kg^{-1} [169], suggesting that the pressure at which this loading was calculated was not sufficient to obtain full saturation.

T/K	q_i^{feed}/mol kg-^{1}	q_i^{perm}/mol kg-^{1}	D_i^s/m^2 s^{-1}
		Water	
348	0.87	0.004	$3.61 \pm 0.01 \cdot 10^{-10}$
360	0.97	0.003	$6.10 \pm 0.04 \cdot 10^{-10}$
373	1.11	0.002	$5.89 \pm 0.04 \cdot 10^{-10}$
		Methanol	
348	2.46	0.09	$3.36 \pm 0.01 \cdot 10^{-11}$
360	2.39	0.05	$3.55 \pm 0.01 \cdot 10^{-11}$
373	2.36	0.03	$4.80 \pm 0.02 \cdot 10^{-11}$
		Ethanol	
348	1.49	0.23	$<3 \cdot 10^{-14}$
360	1.42	0.15	$<3 \cdot 10^{-14}$
373	1.39	0.10	$<3 \cdot 10^{-14}$

Table 3.3. *Self-diffusivities calculated from MD simulations and TST (ethanol), and pure-component loadings calculated from GCMC simulations at the feed and permeate sides for pure-component permeation of water, methanol and ethanol. The permeate side pressure was maintained at 1 kPa.*

T/K	$D_w^s/m^2\,s^{-1}$	$D_m^s/m^2\,s^{-1}$
303	$1.43 \pm 0.01 \cdot 10^{-10}$	$1.91 \pm 0.03 \cdot 10^{-11}$
348	$3.58 \pm 0.01 \cdot 10^{-10}$	$3.00 \pm 0.03 \cdot 10^{-11}$
360	$6.10 \pm 0.04 \cdot 10^{-10}$	$3.55 \pm 0.01 \cdot 10^{-11}$
373	$6.76 \pm 0.05 \cdot 10^{-10}$	$4.80 \pm 0.02 \cdot 10^{-11}$

Table 3.4. *Single-component self-diffusivities for water and methanol, calculated from MD simulations at a constant loading of 0.97 and 2.39 mol kg^{-1} (14 and 35 molecules per unit cell).*
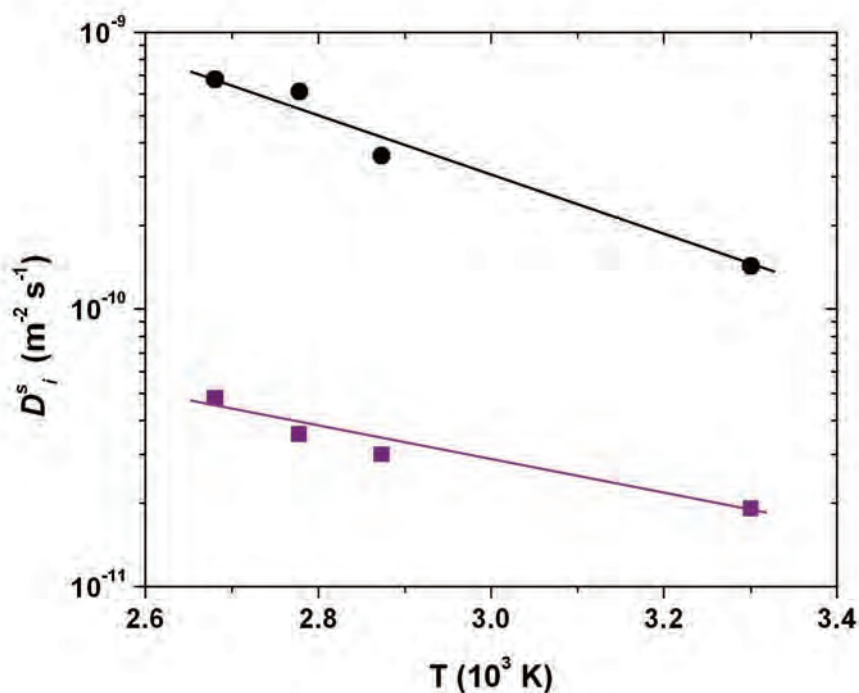

Figure 3.11. *The logarithm of the self-diffusivity, D_i^s, versus the reciprocal temperature for pure-component permeation of water (circles) and methanol (squares). The data are also listed in table 3.4. The lines indicate the linear trend expected from Eq. (3.9).*

The calculated alcohol saturation loadings using GCMC simulations are larger than the values found by fitting the Langmuir isotherms. This deviation and the increase of the fitted saturation loading with temperature could indicate that the Langmuir adsorption isotherm fitted at low pressures does not describe the full adsorption behavior. The fitted saturation loadings (Table 3.2) are similar to reported values obtained by fitting Langmuir isotherms for methane (1.7 mol kg^{-1}) and ethane (0.8 mol kg^{-1}) in DD3R[197,253]. Both the calculated and experimental values of the ethanol loading are approximately three times larger than reported loadings for ethane[197]. The loadings of methanol and ethanol are also larger than reported loadings for methane, ethane, and ethene on ZSM-58[248]. The calculated water saturation

loading on DD3R is substantially higher than the 6.9 mol kg^{-1} (41 molecules per unit cell) reported for water in silicalite-1, which corresponds to a density inside the zeolite of 85% of the bulk liquid value[135,146]. To obtain the actual saturation loading of water on DD3R, adsorption measurements over a wide pressure range need to be conducted, as was already reported for water in silicalite-1[143].

The enthalpies of adsorption show a small increase with temperature, but since the values in the temperature range concerned differ by less than 6%, an average value is used (Table 3.8). The calculated values for alcohols (-40 and -47 kJ mol^{-1} for methanol and ethanol, respectively) are comparable to values reported for adsorption on silicalite-1[254]. For water, the computed value of -26 kJ mol^{-1} was comparable to the -20 kJ mol^{-1} reported by Fleys *et al.* for silicalite-1[204]. Den Exter obtained an enthalpy of adsorption of -50 kJ mol^{-1} at zero loading by fitting the experimentally measured water isotherms on DDR-type zeolite (which is in agreement with the data obtained in this study) to a BET isotherm[245].

The water and methanol self-diffusivities at constant loading increase with temperature. The sum of the activation energy and the enthalpies of adsorption, obtained by the GCMC simulations, correspond well with the apparent activation energy E_{app} calculated from the pure-component permeances[232] (Table 3.8). This indicates that the temperature dependency of neither the adsorption nor the diffusion is dominating.

At equal component fugacities, the water loading (computed using the Tip5pEw force field) is similar to the loading of alcohols. However, despite the improved water adsorption in the presence of the alcohols, the calculations indicate that the water loading at the feed side during pervaporation experiments is at most 50% of the alcohol loading (Tables 3.5 and 3.6). This shows that preferential adsorption is not the cause of the observed separation selectivities of the membrane. The high water selectivities obtained in the pervaporation experiments should be attributed to the difference in diffusivity.

For methanol and ethanol, the adsorption behavior is consistent with Langmuir adsorption. Moreover, the size of the DD3R cage window is similar to the molecular diameters of the alcohols[184]. The calculated pure-component transport diffusivity of water is 1 order of magnitude larger than the methanol diffusivity and even 3 orders of magnitude larger than the ethanol diffusivity. This identifies the difference in diffusivity as the major separating mechanism for the dewatering of alcohols using DD3R membranes. The calculated diffusivity of water is lower than the reported values for water in silicalite-1[203]. The diffusivity found for methanol is about 1 order of magnitude larger than the reported value for methane[248]. For ethanol, TST was used to obtain a more accurate value of the ethanol diffusivity, as the MD approach is inadequate due to the long required simulation time.

T/K	x_w^{feed} [184]	q_w^{feed}/mol kg^{-1}	q_m^{feed}/mol kg^{-1}	y_w^{perm} [184]	q_w^{perm}/mol kg^{-1}	q_m^{perm}/mol kg^{-1}	D_w^s/m^2 s^{-1}	D_m^s/m^2 s^{-1}
348	0.20	0.69	2.15	0.59	0.011	0.067	$1.49 \pm 0.02 \cdot 10^{-10}$	$1.48 \pm 0.01 \cdot 10^{-11}$
360	0.10	0.42	2.18	0.45	0.062	0.006	$1.43 \pm 0.01 \cdot 10^{-10}$	$2.02 \pm 0.01 \cdot 10^{-11}$
360	0.20	0.59	2.12	0.63	0.031	0.004	$2.04 \pm 0.01 \cdot 10^{-10}$	$1.91 \pm 0.01 \cdot 10^{-11}$
360	0.50	1.00	1.94	0.84	0.015	0.005	$2.55 \pm 0.02 \cdot 10^{-10}$	$1.48 \pm 0.01 \cdot 10^{-11}$
373	0.20	0.59	2.08	0.64	0.002	0.018	$1.05 \pm 0.03 \cdot 10^{-10}$	$3.14 \pm 0.03 \cdot 10^{-11}$

Table 3.5. *Methanol/water feed and permeate side composition and loading, and feed side self-diffusivities. The permeate side pressure in the pervaporation experiments is 1.5 kPa.*

T/K	x_w^{feed} [184]	q_w^{feed}/mol kg^{-1}	q_m^{feed}/mol kg^{-1}	y_w^{perm} [184]	q_w^{perm}/mol kg^{-1}	q_m^{perm}/mol kg^{-1}	D_w^s/m^2 s^{-1}	D_m^s/m^2 s^{-1}
348	0.10	0.80	1.63	0.993	0.0056	0.013	$4.45 \pm 0.06 \cdot 10^{-11}$	$<3 \cdot 10^{-14}$
360	0.20	0.83	1.59	0.996	0.0017	0.007	$5.75 \pm 0.04 \cdot 10^{-11}$	$<3 \cdot 10^{-14}$
360	0.30	0.94	1.56	0.998	0.0004	0.004	$7.79 \pm 0.20 \cdot 10^{-11}$	$<3 \cdot 10^{-14}$
373	0.20	0.83	1.53	0.997	0.0043	0.001	$1.44 \pm 0.20 \cdot 10^{-11}$	$<3 \cdot 10^{-14}$

Table 3.6. *Ethanol/water feed and permeate side composition and loading, and feed side self-diffusivities. The permeate side pressure in the pervaporation experiments is 1.5 kPa.*

component	Γ_{ii}^{feed}	Γ_{ij}^{feed}	Γ_{ii}^{perm}	Γ_{ij}^{perm}	N_i^{exp}/mol m^{-2} s^{-1}	N_i^{pred}/mol m^{-2} s^{-1}	$y_i^{perm,exp}$	$y_i^{perm,pred}$
				Methanol/Water				
water	2.31	0.42	0.91	-0.01	0.023	0.40	0.63	0.69
methanol	9.20	0.99	0.23	-0.05	0.013	0.19	0.37	0.31
				Ethanol/Water				
water	1.74	1.65	1.00	-0.30	0.015	0.25	0.996	0.998
ethanol	6.15	0.48	1.00	-0.04	$0.59 \cdot 10^{-4}$	$4.9 \cdot 10^{-4}$	0.004	0.002

Table 3.7. *Measured (N_i^{exp}) and predicted (N_i^{pred}) component fluxes using Eq. (3.7) and Eq. (3.8), and the thermodynamic correction factors at the feed and permeate side conditions in methanol/water and ethanol/water pervaporation at $x_w = 0.2$ and $T = 360$ K. The permeate side pressure in the experiments was maintained at 1.5 kPa.*
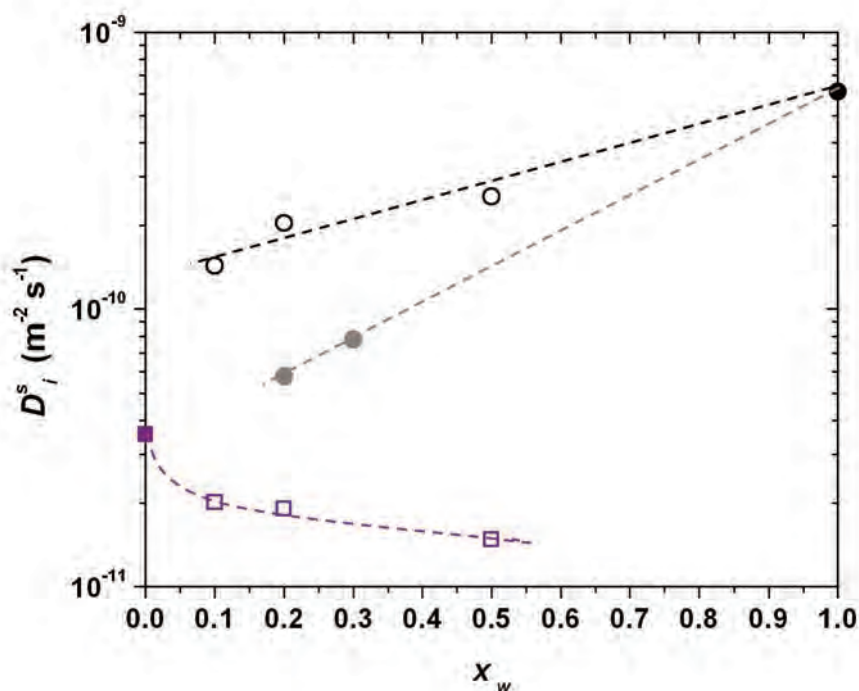
Figure 3.12. *The logarithm of the self-diffusivity, D_i^s, versus the water feed mole fraction, x_w, for pure-component permeation of water (closed black circles) and methanol (squares), water (open circles) and methanol (open squares) in methanol/water mixtures, and water (closed gray circles) in ethanol/water mixtures at 360 K. The data are also listed in tables 3.3, 3.5 and 3.6. The dashed lines indicate a guide to the eye.*

To investigate the influence of the thermostat in the simulations, we computed the diffusivity of water and methanol at 360 K using MD, both in the NVT ensemble (using the Nosé-Hoover thermostat) and in the NVE ensemble. We found that the diffusivity computed in the NVE ensemble was 25% larger than in the NVT ensemble. This clearly shows that in our case, the thermostat only plays a minor role in the dynamics.

To investigate the possible effect of framework flexibility, we have performed additional MD simulations using the flexible zeolite model of Demontis and Suffritti[255]. In this model, interactions between framework zeolite atoms are described by harmonic springs, using equilibrium bond lengths taken from the crystal structure of DDR-type zeolite. Electrostatic interactions between framework atoms are not taken into account. Electrostatic interactions between guest molecules, and between guest molecules and the framework, are handled using the Wolf method[112]. At 373 K, we found that the diffusivity of water and methanol in a flexible framework is ~50% lower than for a rigid zeolite. We also verified that the use of the Wolf method instead of the Ewald summation does not change the diffusivity. These preliminary simulations clearly show that framework flexibility indeed influences the diffusion of water in DDR-type

zeolite, but that the main conclusion of our work (water is diffusing much faster than methanol, and methanol is diffusing much faster than ethanol) is unaffected.

In methanol/water mixture permeation, the methanol diffusivities are very similar to the values found for pure-component transport, while for water the diffusivities are a factor of 2 to 3 lower than for pure-component diffusion (Tables 3.3, 3.5 and 3.6). In the ethanol/water system, the diffusivity of water is reduced by 1 order of magnitude as compared to pure-component permeation. This trend agrees with the measured component fluxes under pervaporation conditions[184]. As the adsorption of the components is increased in the mixture, competitive adsorption does not explain this reduced mixture permeance. The stronger interactions, leading to higher adsorption in the mixtures, combined with steric hindrance of the adsorbed molecules blocking the cage windows are likely to reduce the diffusivity, leading to a lower permeance in mixtures. The seemingly unaffected permeance of methanol may be explained by a positive effect of the increased adsorption, balanced by a negative effect of a reduced diffusivity.

The calculated thermodynamic correction factors show that the presence of alcohol at permeate side conditions has a negative impact on the water flux and vice versa. This shows the same trend as the calculated self-diffusivities (Figure 3.12) and agrees with the experimental observation of a decrease in flux of both alcohol and water in mixture as compared to pure-component permeation[184].

The predicted values for the flux (Table 3.7) are one order of magnitude larger than the experimentally measured values. However, the calculated permeate composition deviates less than 10% from the experimental value. This discrepancy in the fluxes can be partly attributed to the assumption of a constant value for Γ_{ij}. Since the diffusivity of the alcohols is much lower than the diffusivity of water, it is expected that the average value of Γ_{ij} will be closer to the permeate side conditions.

component	$\Delta_{ads}H$/kJ mol^{-1}	E_A/kJ mol^{-1}	$E_{app}{}^5$/kJ mol^{-1}
water	-26.3	21.3	-9.1
methanol	-39.6	11.9	-32.4
ethanol	-46.6	-	-23.6

Table 3.8. *Average enthalpies of adsorption at zero loading computed by GCMC from 348 K to 373 K, the activation energy for the transport diffusivity, and the apparent activation energies of pervaporation as reported in reference 5 for water, methanol and ethanol on DD3R.*

It should be noted that the diffusivities obtained in the MD simulations assume a perfect crystalline membrane without micro- and macroscopic defects. This will not resemble the actual membrane, which consists of complex intergrown crystals with internal and external grain boundaries. Moreover, the DD3R membrane synthesized by NGK insulators consisted of a thin zeolite layer deposited on an α-alumina support. During the membrane synthesis, aluminum can be leached out of the support material and be incorporated into the zeolite structure, making the membrane material less hydrophobic than the separately synthesized crystals and the simulated zeolite framework. Furthermore, despite the high calcination temperature of the DD3R zeolite[190], silanol groups can still be present in the zeolite as crystalline defects. In silicalite-1, it has been observed that up to 8% of the Si is present as Si-OH[256]. These groups linearly increase the framework polarity and therewith the hydrophilicity[256,257].

Considering that no force field parameters were fitted, the calculated adsorption isotherms show a reasonable fit with the experimental adsorption data. To obtain a quantitative result that better matches the experimental isotherms, a refinement of the force field would be required, while taking proper account of the material imperfections such as silanol groups. The simulation results could also be improved by accounting for framework flexibility. Including framework flexibility has shown to increase the ethanol/water loading in silicalite-1 without affecting the sorption selectivity[213].

3.6. Conclusions

Adsorption isotherms for water, methanol, and ethanol on all-silica DD3R have been measured by single-component vapor-phase adsorption and calculated by GCMC simulations. The measured alcohol adsorption can be described by a single-site Langmuir adsorption isotherm. The MC simulations were able to qualitatively reproduce the adsorption behavior of the experimental isotherms. For water, the adsorption resembles type II adsorption. The water loading is under predicted by the calculations at pressures up to 2.5 kPa. The calculated loadings at high pressures of all of the components are higher than reported values for gases in DDR-type zeolites and are comparable to loadings on LTA-type zeolites. The molecular models and force field parameters were taken directly from literature without further adjustment. Nevertheless, the order of magnitude and the shape of the pure-component isotherms give a good resemblance of the experimental data.

Mixture adsorption isotherms and diffusivities have been calculated and compared with permeation data measured under pervaporation conditions. The calculated mixture isotherms show that the loading of both alcohols and water at constant component fugacity increases as compared to pure-component adsorption. Moreover, the shape of the water isotherm changes from type IV to type I. The decrease in water and

ethanol permeance in the mixture as compared to pure-component permeation is not caused by competitive adsorption. The increase in loading in mixture adsorption is significantly more profound for water than for alcohols, but this does not lead to adsorption selectivity for water at the feed conditions of the pervaporation experiments.

The self-diffusivities calculated by MD simulations and the calculated mixture isotherms show that the water permeation is at least 1-3 orders of magnitude larger than those of the alcohols. Although component fluxes predicted from the simulation data over predict the experimentally observed values by 1 order of magnitude, the permeate composition corresponds well with experimental data. The selective water transport through DD3R zeolite membranes can, therefore, be explained by the higher diffusivity of water in the hydrophobic DD3R.

4

Adsorption of water in Cu-BTC

Molecular simulations were performed to study the adsorption behavior of water in the metal-organic framework Cu-BTC. This is one of the better-known materials of this type that is stable upon water adsorption/desorption. The charge of the framework atoms was fitted to reproduce the available experimental adsorption isotherm. This new set of interaction parameters was used to calculate Henry coefficients as well as the energies, entropies, and enthalpies for the different adsorption sites. Our simulations show that water has a surprisingly large affinity for the metal center in Cu-BTC compared to other molecules such as carbon dioxide, nitrogen, oxygen, or hydrocarbons. This particular behavior could be further exploited for the separation of water from other compounds.

4.1. Introduction

Metal Organic Frameworks (MOFs) are a new type of materials that are attracting a great deal of attention as potential catalysts or materials for gas storage or separation[258-265]. They exhibit a periodic structure with pores, channels, large void spaces and a large surface area. Due to the wide range of potential linker molecules, the geometry of the framework can in principle be specifically designed for a particular application[266-269]. However, practical problems may arise after synthesizing a new MOF. For example, the framework may be unstable upon solvent removal after synthesis, reducing the applicability as adsorbent, or it may change its structure by widening or narrowing the pores significantly[270,271]. The solvent molecules used in the synthesis have a crucial effect on the formation of the final structure[272]. Water is easily encapsulated in some MOFs through coordination bonds or hydrogen bonds[273,274]. In all these processes, the water-MOF interaction is a key property. Understanding the interactions between water and different MOFs will be a major step forward in the design of new tailor-made materials for specific applications.
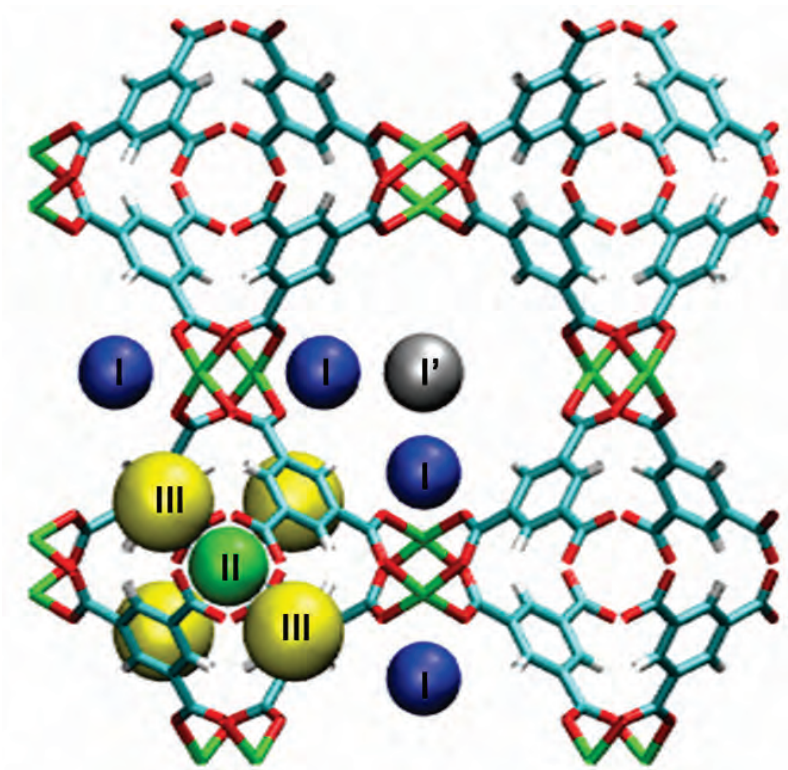

Figure 4.1. *Structure of Cu-BTC, showing the BTC molecules forming octahedra at the vertices linked by $Cu_2(COO)_4$ units: blue, carbon; white, hydrogen; green, copper; red, oxygen. The adsorption sites are also shown: site I, region close to the Cu atoms of the framework (blue spheres); site II, centre of the octahedral side pockets (green sphere); site III, windows of the octahedral side pockets (yellow spheres); site I', centre of the large Cu-BTC cages (gray sphere). The size and shape of the sites does not correspond to the size and shape of the spheres.*

Figure 4.2. *The crystallographically different atoms in Cu-BTC as defined in this work. We consider the following types of carbon atoms: Ca, linked to two oxygen atoms; Cb, linked to other three carbon atoms; Cc, linked to one hydrogen atom.*

MOFs with the same type of central metal atom may have similar properties. For example, Zn containing structures are in general very sensitive to water. Although a few of them are stable[275], most of them decompose after the adsorption of water or even in the presence of moist air[30,32,276]. This instability is a serious limitation to the potential industrial application of Zn containing MOFs, for example for hydrogen storage[276,277]. In contrast, Cu containing MOFs are often water stable[36,278-280] and therefore more interesting from an industrial point of view.

We use molecular simulations to explain the water adsorption behaviour in Cu-BTC (BTC: benzene-1,3,5-tricarboxylate). This MOF has garnered a great deal of attention since it was first reported by Chui *et al.*[36] in 1999. The framework consists of a metal coordination polymer based on Cu as the centre and BTC as the linker molecule, resulting in eight octahedral side pockets per unit cell at the vertices, built from the BTC molecules linked by dimeric cupric tetracarboxylate units, see Figure 4.1. To date studies of the interactions of water with MOFs are extremely scarce and only a few studies related to water in Cu-BTC have been published, most of them being experimental works. These studies deal with water adsorption[36,276,277,280,281], water saturation[282] and with the structural changes provoked by the adsorption and distribution of water in the structure[283]. Cu-BTC is also of potential interest for separating polar from non-polar components[265]. Simulations studies on Cu-BTC are scarce too, and most of them are focused on adsorption and separation of hydrocarbons and some small molecules such as Ar, N_2, O_2 and CO_2[265,284-287]. There is a single simulation study of water in MOFs that deals with the interactions of SPC water with

MOF-5[30]. The work described in this chapter is, to the best of our knowledge, the first simulation study of water reproducing experimental adsorption isotherms in MOFs.

4.2. Simulation details

The adsorption isotherms of water in Cu-BTC were computed using grand-canonical Monte Carlo (GCMC) simulations. The gas phase is considered as an ideal gas as we only considered pressures of at most 275 Pa. The insertion and deletion of water molecules in the system were performed using the Configurational-bias Monte Carlo technique[47]. The Henry coefficients, energies, enthalpies, and entropies of adsorption were computed from MC simulations in the NVT ensemble. During these simulations, the test particle method is used to collect information on the Rosenbluth weight. Detailed information about this method can be found elsewhere[52,97,166]. The MC simulations were performed in cycles, and in each cycle one of the following trial moves was selected at random for each water molecule: translation, rotation, regrow at a random position, or insertion or deletion of a water molecule (only for simulations in the grand-canonical ensemble). We used at least 10^9 Monte Carlo moves. Coulombic interactions were computed using the Ewald summation with a relative precision of 10^{-6}.

The water model used in this study is the Tip5pEw, which was parameterized for use with the Ewald summation[46,47]. The experimental liquid density of water at 298K (997.0 kg/m^3)[288] is well reproduced by this interaction potential (998.0 kg/m^3) from MD in the NPT ensemble, as well as the maximum of density around 4°C (Figure 2.1). The heat of vaporization of this model equals 43.4 kJ/mol, while the experimental value is 43.9 kJ/mol[74].

To construct the crystallographic atomic positions of the framework we used the crystal structure of Chui *et al.*[36]. This structure includes axial oxygen atoms weakly bonded to the Cu atoms, corresponding to water ligands. This adsorption study is performed on a dehydrated Cu-BTC; therefore, it was adopted with these oxygen atoms removed from the crystal structure. Cu-BTC is modelled as a rigid structure with Lennard-Jones parameters taken from the DREIDING force field[289], except those for Cu that were taken from the UFF force field[290]. The framework was kept rigid during the calculations, as it has been shown that at the simulation conditions this structure is quite rigid and that water adsorption is reversible[291]. Note that the development of flexible models for MOFs is still extremely complex, as shown by Dubbeldam *et al.* for the IRMOF family[57]. A single unit cell of dimensions $a = b = c = 26.343$ Å was used in the simulations. The unit cell contains 624 atoms of which 48 are copper, 192 oxygen, 96 hydrogen and 288 carbon (the latter classified in three groups depending on the neighbouring atoms, Ca: next to two oxygen

atoms, Cb: between three carbons, and Cc: linked to one hydrogen). The crystallographically different atoms are depicted in Figure 4.2. The Lennard-Jones interactions between the different atoms of the system where calculated using the Lorentz-Berthelot mixing rules[46]. Lennard-Jones interactions are truncated and shifted at 12 Å. This work highlights the importance of the Coulombic interactions for the determination of adsorption properties of water in MOFs. We demonstrate that experimental isotherms in this MOF can be reproduced exactly with molecular simulations using available force fields as a starting point. The partial charges of the framework atoms are slightly altered to fit the experimental data.

4.3. Results and discussion

We have considered several sets of partial charges for the atoms of Cu-BTC listed in Table 4.1. The initial atomic charges, labeled as set I, were taken from Frost and Snurr[292]. Set II was taken from the available charges for IRMOF-1[57], where the charge of copper was adjusted to make the structure charge neutral. The other sets used in this work were obtained by increasing all the charges of set II by 2, 4 and 6% respectively.

Our first finding was that the computed water adsorption using set I was 600 times lower than the experimental values[281]. Our simulations show that: first, it is not possible to reproduce the experimental adsorption isotherm by increasing or decreasing the partial charges of only a few atom types (always keeping the total structure charge neutral); second, variations on the framework charges lead to a drastic change of the adsorption; third, fixing the charge of Cu and changing the rest of the charges by a small amount did not influence the adsorption into a large extent. Therefore, to correctly reproduce the experimental adsorption of water in Cu-BTC the charge of all atoms was changed simultaneously. As a starting point, we took the set of charges inherited from IRMOF-1 (set II) and generated new sets of charges increasing all the charges simultaneously in steps of 1% until the experimental isotherm was reproduced.

	Cu	O	Ca	Cb	Cc	H
Set I	1.0	-0.6	0.7	0.0	-0.15	0.15
Set II	1.2	-0.6	0.475	0.125	-0.15	0.15
Set III	1.224	-0.612	0.4845	0.1275	-0.153	0.153
Set IV	1.248	-0.624	0.494	0.13	-0.156	0.156
Set V	1.272	-0.636	0.5035	0.1325	-0.159	0.159

Table 4.1. *Sets of point charges of Cu-BTC used in this work (in units of e). Set I, partial charges obtained by optimization of the electronic structure using GAUSSIAN[292]; set II, values for IRMOF-1 adapted to Cu-BTC[57]; sets III, IV and V are set II increased by 2%, 4% and 6% respectively. The labelling of the atoms is shown in Figure 4.2.*
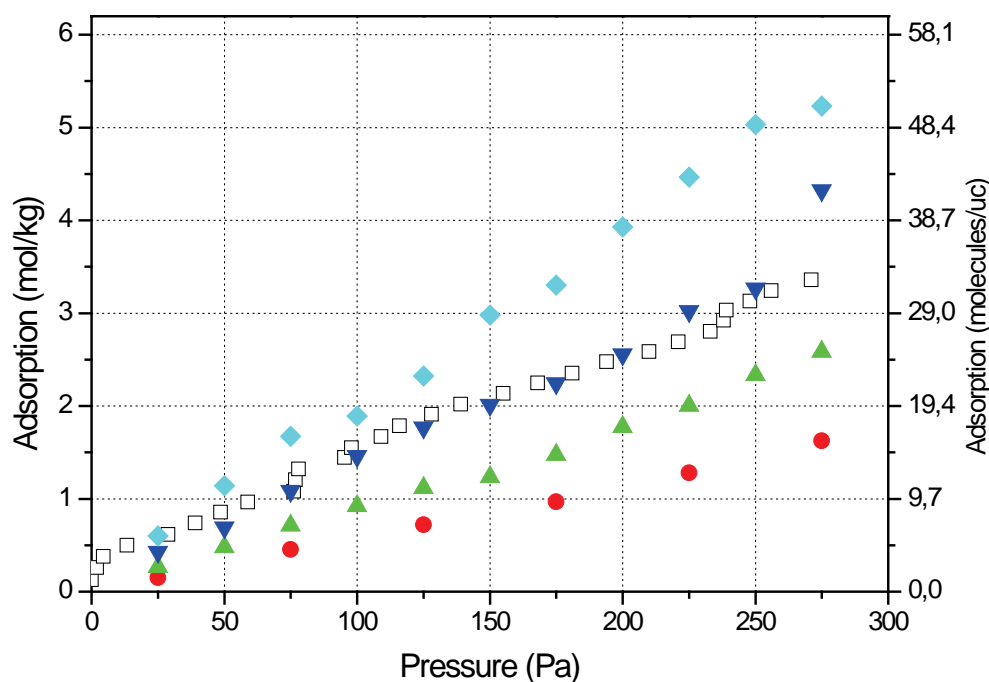

Figure 4.3. *Adsorption isotherms of water in Cu-BTC at 295K computed using the sets of partial charges of Table 4.1. Open squares, experimental data; circles, charge set II; triangles up, charge set III; triangles down, charge set IV; diamonds, charge set V. The isotherm for charge set I was not plotted because the adsorption was 600 times lower than the experimental values.*

The isotherms obtained with different sets of atomic charges are compared with the experimental data at 295K; see Figure 4.3. Set II qualitatively reproduces the linear trend of the experimental isotherm, but the adsorption is too low compared to experiments[281]. The set labelled as IV exactly reproduces the experimental data. Compared to set II, the partial charge of the atoms of Cu-BTC is increased, making the interaction between the metal sites and water stronger and preserving the linear shape of the isotherm. Higher pressures were not included in Figure 4.3 due to the lack of accurate experimental data in that region. The saturation loading computed in our simulations equals 34 mol/kg. This result is quite large compared with available experimental data, 15[293], 16[36] and 22 mol/kg[281]. This difference can be explained by the fact that, in the simulations, the crystal structure is perfect while in the experiment it contains defects or trapped molecules that were not removed after the synthesis, and different methods and adsorption equipment is used[38]. In other simulation studies of MOFs, a scaling factor for the adsorption has been used to account for the pore volume really accessible to the experimental material[294,295]. This is supported by the fact that in our simulation we measured a pore volume of 0.85 cm^3/gr using the Widom particle insertion method[47]. Various experimental studies reported pore volumes of 0.69, 0.33 and 0.66 cm^3/gr respectively[36,281,293].

P (Pa)	A	B	C	D
25	0.01	0.99	0.81	0.81
50	0.02	0.98	0.85	0.85
75	0.02	0.98	0.84	0.84
100	0.03	0.97	0.88	0.83
125	0.05	0.95	0.84	0.84
150	0.05	0.95	0.87	0.87
175	0.06	0.94	0.84	0.84
200	0.08	0.92	0.86	0.85
225	0.11	0.89	0.87	0.86
250	0.13	0.87	0.88	0.87
275	0.19	0.81	0.89	0.87

Table 4.2. *The various contributions to the interaction energy of water adsorbed in Cu-BTC at different pressures and a temperature of 295 K, expressed in parts per unit. A, fraction of energy that correspond to water-water interactions; B, fraction of energy that corresponds to water-Cu-BTC interactions; C, fraction of energy that is of electrostatic origin; D, fraction of electrostatic energy that corresponds to water-Cu-BTC interactions.*

In Table 4.2 we present the fraction of the total energy that corresponds to the water-water and to the water-MOF interactions for different pressures, as well as the fraction of the total and the water-MOF interaction that is of electrostatic origin. For all of the pressures considered, the total electrostatic energy is always larger than 80% of the total energy, and more than 80% of this is due to the water-MOF interactions. Furthermore, the total water-water interaction energy is always less than 20% of the total energy. This indicates that the adsorption is dominated by the electrostatic interaction between water and the framework atoms. This result may be surprising because water molecules interact via strong hydrogen bonds. The observation that the interactions between water molecules are weaker than those with the framework is corroborated with the computed enthalpies as a function of the loading. As shown in Figure 4.4, the heat of adsorption increases from 49 kJ/mol at zero coverage to 51 kJ/mol at around 4 molecules of water per unit cell, remaining almost constant from here to the loading of 42 molecules per unit cell. Note that this is significantly larger that the heat of vaporization of water (43.9 kJ/mol[74]).
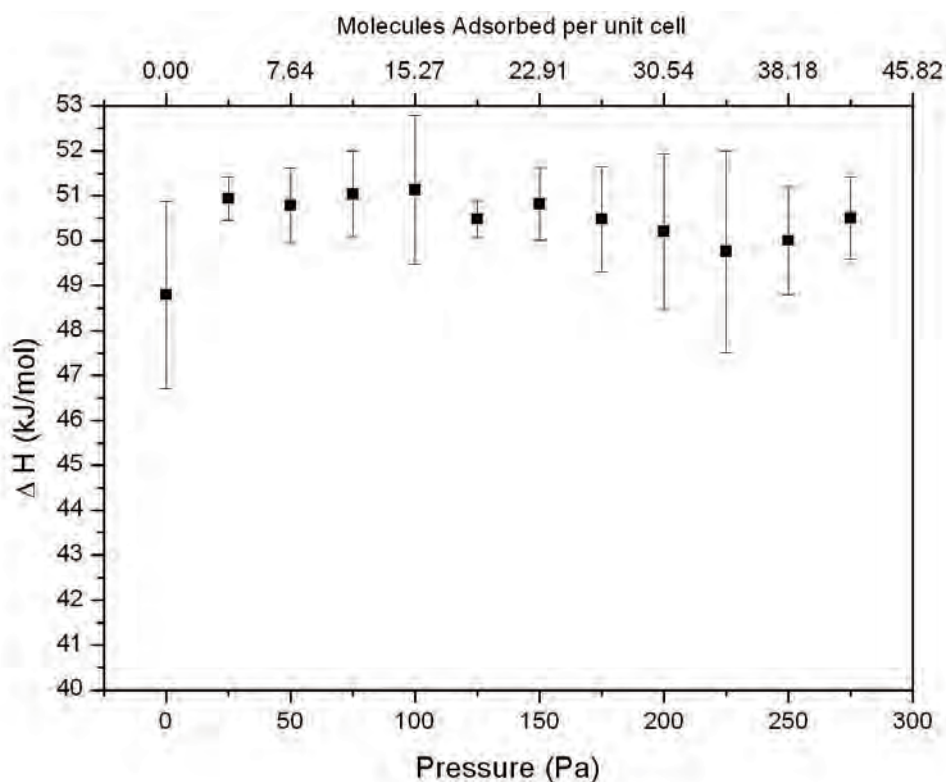

Figure 4.4. *Absolute value of the heats of adsorption of water in Cu-BTC at 295K as a function of loading. The simulation procedure for calculating the heat of adsorption is less precise when the electrostatic interactions are large. This is the case of the heat of adsorption of water at very low loading.*

Site	K_H (mol kg^{-1} Pa^{-1})	ΔU (kJ mol^{-1})	ΔH (kJ mol^{-1})	ΔA (kJ mol^{-1})	ΔG (kJ mol^{-1})	ΔS (kJ K^{-1} mol^{-1})
I	$2.0 \cdot 10^{-2}$ (5.3)	-45.6 (6.6)	-48.0 (6.6)	26.2 (6.4)	23.8 (6.4)	-243.4 (44.1)
I'	$4.6 \cdot 10^{-6}$ (0.2)	-14.0 (0.3)	-16.5 (0.3)	5.6 (0.1)	3.2 (0.1)	-66.7 (1.4)
III	$5.7 \cdot 10^{-6}$ (0.4)	-14.4 (0.4)	-16.8 (0.4)	6.2 (0.2)	3.7 (0.2)	-69.7 (1.9)
II + III	$6.2 \cdot 10^{-6}$ (0.2)	-14.2 (0.1)	-16.6 (0.1)	6.4 (0.1)	3.9 (0.1)	69.7 (0.6)
Total	$1.3 \cdot 10^{-2}$ (3.4)	-43.6 (3.9)	-46.1 (3.9)	25.1 (6.4)	22.7 (6.4)	-233.0 (34.8)

Table 4.3. *Calculated Henry coefficients, adsorption energies, entropies and enthalpies of adsorption of water in Cu-BTC at 295 for different adsorption sites using the charge set IV (see Table 4.1). The value in parenthesis indicates the error in the last digits. For example, -45.6 (6.6) means -45.6±6.6*

Set IV has been additionally used to identify the preferential location of water in the structure. The main adsorption sites on this metal organic framework were selected as explained by Liu *et al.*[296] for H_2 adsorption. Type I sites are located near the copper atoms of the structure, type II sites were assigned to the centre of the octahedral cages, and type III sites were located at the windows of the four open faces of the octahedral cage. In addition to these sites defined by Liu *et al.*[296], we also considered the type I′ adsorption site located at the large, central cavities. To assign each adsorbed water molecule to an adsorption site, we have used a distance criterion with a cutoff radius of 0.2 nm for site II; an spherical annulus of radius 0.2 nm and 0.55 nm for site III (site II being at its centre); the one of site I as 0.3 nm removing the intersection with site III, and finally we defined site I' as the rest of the volume not contained in the previous sites. In this way, every coordinate within the unit cell was assigned to one single site. The Cu-BTC structure with the defined adsorption sites is shown in Figure 4.1.

According to our simulations, water adsorbs preferentially close to the Cu atoms at an average distance of 2.35 Å, close to the experimental value of 2.19 Å obtained by Extended X-ray Absorption Fine Structure[291]. This is consistent with the fact that, after synthesis, Cu atoms are coordinated with water molecules[291] and that the metal sites of the MOF are activated when water is removed, allowing the adsorption of other molecules at those sites[283]. As we increase the pressure, the fraction of molecules close to the Cu atoms changes from 99% at 25Pa to 82% at 275 Pa. The rest of the molecules increasingly adsorb by layers in the large cages of Cu-BTC on the preadsorbed water as the pressure rises, and a small amount of them start filling the channels of the octahedral cages. As every water molecule adsorbs close to one of the Cu atoms, it is expected that the heat of adsorption does not strongly depend on the loading. This is what we found for loadings up to 42 water molecules per unit cell. No molecules were observed in the neighbourhood of the benzene groups or inside the octahedral pockets. We obtain the same behaviour

using the charge set II. These results provide evidence that the metallic atoms of the Cu-BTC structure are a crucial factor for understanding the water adsorption.

The calculated the Henry coefficients and the adsorption energies, entropies and enthalpies are shown in Table 4.3 for the different adsorption sites of Cu-BTC. The Henry coefficient obtained for site I is four orders of magnitude larger than for the other sites, while the energies, entropies and enthalpies are three times larger in absolute value than in the rest of the sites. These large differences between different sites are responsible for the large error bars obtained, especially for the values at zero loading. These values corroborate the strong preference of water for site I. It is interesting to note that the preferential adsorption site for water on Cu-BTC is completely different from those obtained for non-polar and quadrupolar molecules. Water preferentially adsorbs on site I whereas this site remains empty for hydrocarbons[286,287], argon[285], hydrogen[287], nitrogen[265], oxygen[265], and carbon dioxide[287]. The preferential adsorption site for these molecules is at the interior of the octahedral cages (site II), while very few molecules adsorb in the neighborhood of the Cu atoms of the framework. Only hydrogen at low temperatures has shown a tendency to adsorb by the Cu atoms of the framework[296], with a distance of 2.39 Å to the Cu atoms at its preferential adsorption site[297]. To illustrate this point, Figure 4.5 shows the probability distribution of water, methane and carbon dioxide adsorbed in Cu-BTC at low loading and 295 K. While water adsorbs mainly near the Cu atoms of the framework, methane and carbon dioxide adsorbs preferentially at the interior of the octahedral cages, the large channels of Cu-BTC, and the windows of the side pockets in that order.

Krungleviciute et al.[298] suggested that the preference of the molecules for adsorbing at the interior of the octahedral pockets is limited by the Lennard-Jones size parameter –sigma- for interactions between the molecule and the carbon atoms of the MOF, so that Ar ($\sigma=3.40$Å) can adsorb at the interior of the octahedra while CF_4 ($\sigma =3.99$Å) can not because of its large sigma value. This explanation is not valid for the water model we are using because, in our case, the maximum value of sigma for all the Lennard-Jones interactions in the system equals 3.28Å, which is lower than the value for Ar, and therefore, it should be adsorbed at the interior of the octahedral cages. Our simulations show that the dipole moment of the molecule may be the key to understand why the adsorption behaviour of water in Cu-BTC is different to other molecules. It has been previously suggested that Cu-BTC could be useful for separating molecules with different quadrupole moment[284]. Molecular simulations have shown that in a carbon dioxide/nitrogen mixture, carbon dioxide tends to be closer to the Cu atoms of Cu-BTC due to its larger quadrupole moment[265]. As water is one of the molecules in nature with the largest dipole moment, the affinity for the Cu atoms of the framework is expected to be larger, in agreement with our results. Furthermore, the

extremely high sensitivity of the partial charge of Cu for water adsorption indicates that the metal sites of the MOFs are the essential element for understanding the adsorption of water in MOFs.

4.4. Conclusions

We have studied the adsorption of water in the hydrophilic MOF Cu-BTC using molecular simulations. The adsorption of water in this structure is largely influenced by the partial charge placed on the metal atoms of the host framework, which are easily accessible to adsorbed molecules. To reproduce the experimental adsorption isotherm, the atomic partial charges of the structure had to be increased with respect to the charges calculated by quantum chemistry methods.

The adsorption of water in Cu-BTC is completely different to the adsorption of other molecules of similar size, such as methane, and CO_2. The water molecules adsorb preferently next to the open metal centers of the structure at low loadings. Other molecules prefer to adsorb at the entropically most favorable site, namely the side pockets of the structure. This strong preference of water for the metal centers becomes evident after the comparison of the Henry coefficients and heats of adsorption of the test molecules at the different adsorption sites of the structure. The reason for such a large adsorption behavior between water and other molecules is due to the large dipole moment of water. The most important contribution to the energy of adsorbed water molecules in Cu-BTC is due to the electrostatic interaction between the water dipole moment and metal centers of the structure.
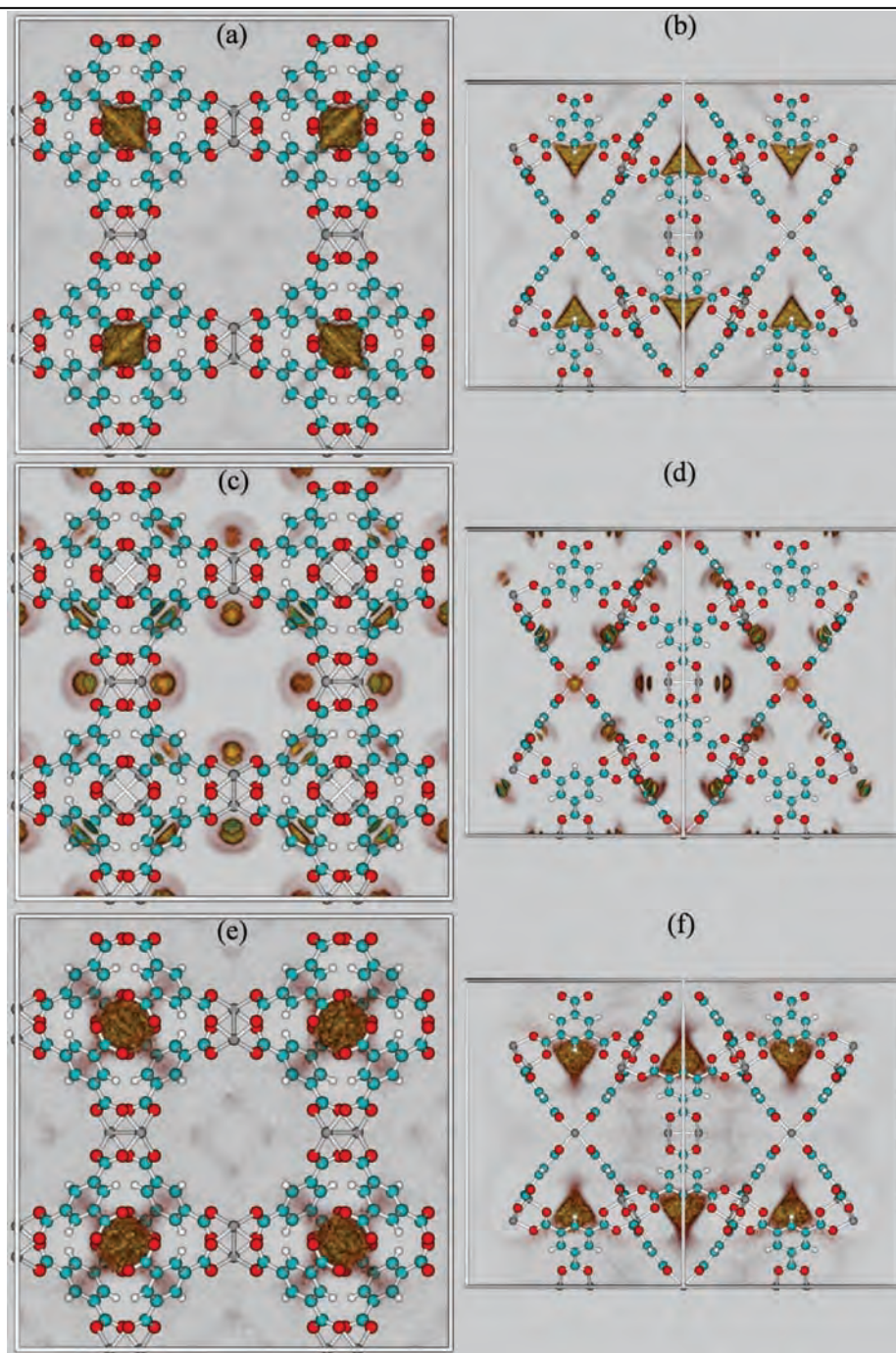
Figure 4.5. *Snapshots showing the different adsorption preference methane, water and carbon dioxide in Cu-BTC at low loading. The data are taken from the pure component simulations of water at 25 Pa, methane and carbon dioxide at 2 kPa at 295K. a) methane (front view); b) methane (side view); c) water (front view); d) water (side view); e) carbon dioxide (front view); f) carbon dioxide (side view). While water adsorbs very close to the Cu atoms of Cu-BTC (in gray colour), the other two molecules adsorb at the centre of the octahedral pockets and the site close to the Cu atoms is completely empty, although some traces can be found at other locations. At these low loadings we can find a weak coordination layer on the water molecules adsorbed on the Cu atoms and a complete absence of water at other adsorption sites. Additionally, water is much more concentrated at its main adsorption site than methane and carbon dioxide.*

Identification of adsorption sites in Cu-BTC

The adsorption of several quadrupolar and nonpolar gases on the Metal Organic Framework Cu-BTC has been studied by combining experimental measurements and Monte Carlo simulations. Four main adsorption sites for this structure have been identified: site I close to the copper atoms, site I′ in the bigger cavities, site II located in the small octahedral cages, and site III at the windows of the four open faces of the octahedral cage. Our simulations identify the octahedral cages (sites II and III) and the big cages (site I′) as the preferred positions for adsorption, while site I, near the copper atoms, remains empty over the entire range of pressures analyzed due to its reduced accessibility. The occupation of the different sites for ethane and propane in Cu-BTC proceeds similarly as for methane, and shows small differences for O_2 and N_2 that can be attributed to the quadrupole moment of these molecules. Site II is filled predominantly for methane (the nonpolar molecule), whereas for N_2, the occupation of II and I′ can be considered almost equivalent. The molecular sitting for O_2 shows an intermediate behavior between those observed for methane and for N_2. The differences between simulated and experimental data at elevated temperatures for propane are tentatively attributed to a reversible change in the lattice parameters of Cu-BTC by dehydration and by temperature, blocking the accessibility to site III and reducing that to site I′. Adsorption parameters of the investigated molecules have been determined from the simulations.

5.1. Introduction

Metal Organic Frameworks (MOFs) have become a novel field of research resulting in numerous publications during the recent years[299]. MOFs are crystalline nanoporous materials that consist of small metal-containing clusters connected three dimensionally by organic ligands. The ligands act as spacers, creating an open porous structure with very high pore volume and surface area. Due to their unusual variety in terms of chemical composition, accessibility and pore dimensions, MOFs are considered as promising candidates to address the current hurdles in gas storage, adsorption separations, and catalysis[300].

Among the many known MOFs, Copper Benzene Tricarboxylate ($Cu_3(BTC)_2$ or Cu-BTC) is one of the best characterized structures[291] together with the IRMOF series[268,301,302]. It was firstly reported in 1999 and named HKUST-1[36]. This electrically neutral framework is composed of dimeric cupric tricarboxylate units with a short Cu-Cu internuclear separation. Each metal completes its pseudo-octahedral coordination sphere with an axial water ligand opposite to the Cu-Cu vector[291]. After removing water from the framework, it becomes an open three dimensional porous structure with main channels of a square cross-section of about 9 Å diameter and tetrahedral side pockets of about 5 Å which are connected to the main channels by triangular windows of about 3.5 Å in diameter. It is commonly synthesized under mild hydrothermal conditions (383 K – 393 K), although it has also been synthesized electrochemically[300]. $Cu_3(BTC)_2$ shows a great potential for gas purification, separation[303], storage[304], and it could be also suitable for catalytic purposes due to its high Lewis acidity[305,306].

Despite the increasing amount of publications dealing with the synthesis of new MOFs, much less effort has been devoted to a better understanding of the interactions between the MOF and guest molecules[265,307-310]. Regarding Cu-BTC, Krungleviciute *et al.* analyzed the adsorption and kinetics of argon and carbon tetrafluoride providing experimental evidence that the former enter the octhahedral cages of Cu-BTC but not the latter[298,311]. Vishnyakov *et al.*[285] constructed the first molecular structural model and made a first description of the preferential adsorption sites for the adsorption of Ar at low temperatures, defining the sequence of adsorption as a gradual filling of the side pockets to a stepwise adsorption and condensation in the main channels. Further molecular modeling using grand-canonical Monte Carlo (GCMC) simulations and different force fields has been reported focusing mainly on small gas molecules (Ar, H_2, CH_4, and CO_2)[284,286,287,312-314]. However, a good agreement between experimental and simulated isotherms has not been obtained so far. This is likely due to experimental and simulation problems. As reviewed very recently[284], adsorption results from different experimental groups vary significantly due to crystal defects, the presence of guest molecules or just because of differences in the methods and adsorption equipment used [36,284,300,315].
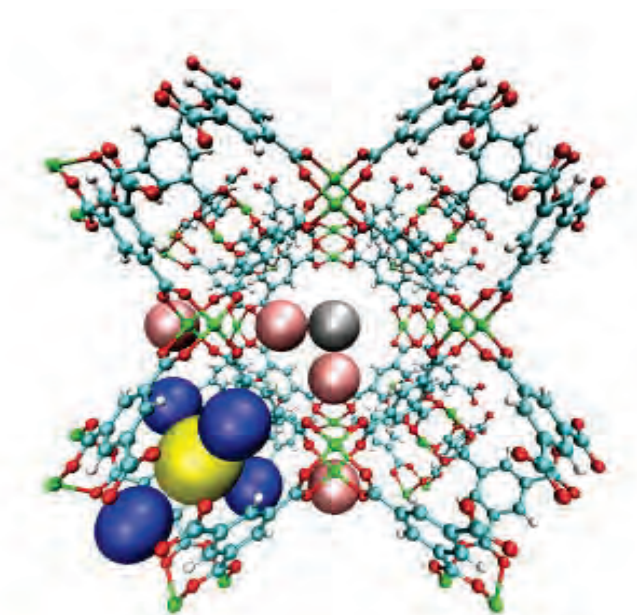
Figure 5.1. *Preferential adsorption sites in Cu-BTC labeled I, I', II, and III. Color spheres illustrate the positions of the different sites. Site I, region close to the Cu atoms of the framework (pink spheres); site II, centre of the octahedral side pockets (yellow sphere); site III, windows of the octahedral side pockets (blue spheres); and site I', centre of the large Cu-BTC cages (gray sphere).*
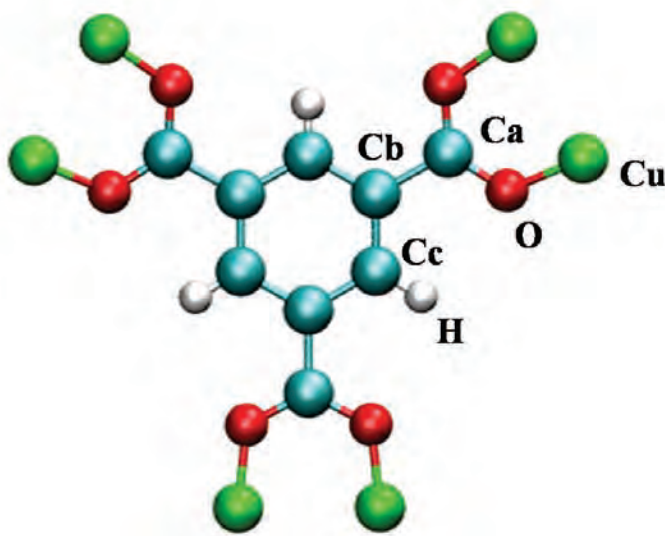

Figure 5.2. *The crystallographically different atoms used to define the Cu-BTC structure are labeled; the other labels follow by symmetry.*

The two main types of cavities in Cu-BTC make of this structure a potential good material not only for molecular adsorption but also for separations of gas mixtures. Therefore it is vital to properly understand the underlying mechanisms of adsorption in this material. We analyze here the adsorption of several molecules on Cu-BTC, determining the preferential adsorption sites in all cases. The interactions between the metal organic framework and quadrupolar and non polar gases have been studied by combining

experimental results and grand-canonical Monte Carlo simulations. High quality samples were synthesized and adsorption isotherms for methane, ethane, propane, nitrogen, and oxygen were determined. They were reconciled with isotherms calculated using simulation techniques previously used by the group of Prof. F. Kapteijn[132,158,199]. The comparison is used to analyze preferential adsorption sites for the different adsorbates as a function of pressure and coverage. To identify the main adsorption sites for this structure a similar procedure as the one reported by Liu *et al.*[296] is followed.

5.2. Experimental details

Copper (II) nitrate hydrate ($Cu(NO_3)_2 \cdot 3H_2O$) and 1,3,5-benzenetricarboxylic acid (trimesic acid) purchased from Aldrich, were used as received, without further purification. $Cu_3(BTC)_2$ crystals were prepared by the method described elsewhere[305], 0.875 g (3.6 mmol) $Cu(NO_3)_2 \cdot 3H_2O$ are dissolved in 12 ml de-ionized water (solution *A*) and mixed with 0.42 g (2.0 mmol) of trimesic acid dissolved in 12 ml ethanol (solution *B*). The resulting solution (*A+B*) is stirred for 30 minutes, placed in an autoclave and heated under hydrothermal conditions (autogenous pressure) to 383 for 18 hours. For entropic reasons, synthesis at a higher temperature can promote the loss of terminal ancillary ligands, while synthesis at lower temperatures would need much longer synthesis times to yield crystalline products[36].

A Micrometrics ASAP 2010 gas adsorption analyser (stainless steel version) was used to measure the adsorption isotherms. Prior to the gas-adsorption measurements, the samples were treated under vacuum at 423 K overnight in order to remove present solvents, moisture and other volatile components.

The crystalline materials were analyzed by X-ray diffraction (XRD) using a Bruker-AXS D5005 with CuKα radiation using internal (LaB6) standard. After correcting for sample displacement by using the calibrated positions of the LaB6, peak positions are accurately known within 0.01 degrees 2θ. Temperature Programmed XRD (TP-XRD) was performed under dry N_2 atmosphere using temperature ramps of 1 K/min. The experimental procedure was as follows: one hydrated sample (as synthesized) was introduced in the sample cell and XRD was measured at room temperature. The sample was dehydrated by increasing the temperature under N_2 flow (100 ml/min) up to 473 K overnight. Afterwards the temperature was reduced using the same ramp and XRD analyses of the dehydrated sample were collected at 473, 373 K and room temperature.

5.3. Simulation details

The computed adsorption isotherms were obtained from Grand-canonical Monte Carlo (GCMC) simulations, where the chemical potential, the temperature, and the volume are fixed. Pressure is transformed into fugacity using the Peng-Robinson equation of state, and fugacity can be directly related to the imposed chemical potential[243]. The Henry coefficients, energies, enthalpies, and entropies of adsorption were computed using MC in the NVT ensemble at 295 K. Detailed information about this method can be found elsewhere[97]. The MC moves were performed in cycles and in each cycle one move was chosen at random with a fixed probability of translation, rotation, and regrowth in a random position. We used at least 10^7 cycles and charge interactions were computed using Ewald sums with a relative precision of 10^{-6}. The Lennard-Jones potential is truncated and shifted with the cutoff distance set to 12 Å.

Cu-BTC is composed of benzene-1,3,5-tricarboxylate (BTC) ligands coordinating copper ions, forming large cavities and small octahedral cages. Adsorption sites on this metal organic framework were selected as explained by Liu *et al.*[296] for H_2 adsorption. We started this research considering those sites that can be briefly explained as follows: type I sites – 48 per unit cell– were considered at the copper atoms of the structure, type II sites – 8 per unit cell–were assigned to the centre of the octahedral cages, and type III sites – 8 per unit cell– were located at the windows of the four open faces of the octahedral cage. In addition to these sites defined by Liu *et al.*[296], we also considered the type I′ – 4 per unit cell – adsorption site located in the large central cavities. The cutoff radius of site II is chosen as 0.2 nm and site III as the spherical annulus between radius 0.2 and 0.55 nm. The cutoff radius of site I is chosen as 0.3 nm removing the intersection with site III, and finally we defined site I' as the rest of the volume not contained in the previous sites. In this way, every coordinate within the unit cell was assigned to one single site. The Cu-BTC structure with the defined adsorption sites is shown in Figure 5.1.

Cu-BTC is modeled as a rigid structure with Lennard-Jones parameters taken from DREIDING force field[289], except those for Cu that were taken from the UFF[290] force field. Atomic charges were taken from Frost and Snurr[292] and Lorentz-Berthelot mixing rules were used to calculate mixed Lennard-Jones parameters. One unit cell of Cu-BTC ($a = b = c = 26.343$ Å) was used in our simulations. The unit cell contains 624 atoms of which 48 are copper, 192 oxygen, 96 hydrogen, and 288 carbon (these latter classified in three groups depending on the atoms next to them, C*a*: next to two oxygen atoms, C*b*: between three carbons, and C*c*: linked to one hydrogen). We obtained a helium void fraction of 0.76. The crystal structure of Chui *et al.*[36] includes axial oxygen atoms weakly bonded to the Cu atoms, which correspond to water ligands. This adsorption study is performed on a dehydrated Cu-BTC; therefore it

was adopted by removing the latter oxygen atoms from the crystal structure. The crystallographically different atoms used in this work are depicted in Figure 5.2.

The interactions between guest molecules (alkanes, N_2, and O_2) with the Cu-BTC host framework are modeled by Lennard-Jones and Coulombic potentials. The Coulomb interactions in the system are calculated with Ewald summations. The alkanes (methane, ethane, and propane) are described with a united atom model[75], in which CH_x groups are considered as a single, chargeless interaction centers with their own effective potentials. The beads in the chain are connected by harmonic bonding potentials $U = 0.5\, k\, (r - r_0)^2$ with $k/k_B = 96500$ K and $r_0 = 1.54$ Å. The bond bending between three neighboring beads is modeled by a harmonic cosine bending potential $U = 0.5\, k\, (\theta - \theta_0)^2$ with $k/k_B = 62500$ K and $\theta_0 = 114°$. N_2 and O_2 were considered as small rigid molecules, using the model proposed by Murthy *et al.*[316] for N_2 and the model proposed by Mellot and Lignieres[317] for O_2. The partial charges of N_2 and O_2 were distributed over each molecule to reproduce experimental quadrupole moment. These models and potentials have been successfully employed to describe the adsorption in zeolites[132,133,158,318]. Table 5.1 summarizes the partial charges and intermolecular parameters used in this work.

Absolute adsorption was converted to excess adsorption for comparison with the experimental data[319,320]. The method used for the analysis of the preferential adsorption sites in Cu-BTC is similar to that used in our previous work on the locations and occupancies of ions in zeolites[45,244].

Cu-BTC				Adsorbed molecules			
Atom type	ε/k_B [K]	σ [Å]	Charge [e⁻][292]	Atom type	ε/k_B [K]	σ [Å]	Charge [e⁻]
Cu[290]	2.518	3.114	1.0	CH_4[75]	158.5	3.72	-
O[289]	48.19	3.03	-0.6	CH_3[75]	108.0	3.76	-
Ca[289]	47.86	3.47	0.7	CH_2[75]	56.0	3.96	-
Cb[289]	47.86	3.47	0.0	N (N_2)[316]	36.4	3.32	-0.40484
Cc[289]	47.86	3.47	-0.15	dummy (N_2)[316]	-	-	0.80968
H[289]	7.65	2.85	0.15	O (O_2)[317]	44.5	3.09	-0.112
				dummy (O_2)[317]	-	-	0.224

Table 5.1. *Partial charges and Lennard-Jones parameters for the structure and the adsorbed molecules used in this work. The N_2 and O_2 models have an extra off-center charge named 'dummy' in the table.*

5.4. Results and Discussion

Adsorption of N_2 at 77 K was obtained experimentally and by molecular simulations. Experimental results reveal a type I isotherm with no hysteresis loop. A surface area of 1366 m^2/g, a micropore volume of 0.55 cm^3/g and an external area of 30 m^2/g were calculated from the N_2 adsorption isotherm at 77 K. As reviewed very recently, these values are similar to the best reported specific surface areas reported for this material[284]. Our molecular simulations overestimate the maximum amount of nitrogen adsorbed since they were performed in a perfect crystal, without defects and where all pores are fully accessible. Therefore, differences between the experimental and simulated values can be attributed to small defects and residual solvent, guest molecules or nitrates after synthesis. Figure 5.3 compares the obtained adsorption isotherms at 77 K and shows that the ratio of the measured and simulated saturation loadings is 0.8 over the whole pressure range. Previous experimental data in this range of pressures were included for comparison[297]. The scaling factor provides a good measure of how much of the theoretical pore volume is accessible in the material used in the experiments[294,295]. Though it is possible to establish direct comparison between the experimental and the scaled simulation data, the exact position of the defects and remaining molecules after synthesis cannot be identified.

Molecular simulations also reproduce the experimental data for N_2 at higher temperatures. The agreement between the experimental and scaled isotherms obtained from simulations at 295 K is shown in Figure 5.4, providing detailed information about the molecular sitting. The occupation of the preferential adsorption sites as a function of pressure is included in Figure 5.4 before applying the scaling factor. Note that at high temperatures and at the experimental pressures considered in this work, saturation is far from reached and therefore scaling is not as relevant as it was at 77 K. Analysis of the occupancies of the individual adsorption sites from the non-scaled simulation data indicates that N_2 adsorbs preferentially in the octahedral cages (site II) and in the large cages (site I'). The windows of the octahedral cages are also occupied (site III) but to a lower extent. Site I, near the copper atoms, remains empty over the entire range of pressures analyzed in this work. This is consistent with the literature, since although the Cu(II) cations in principle should become available after dehydration, they show a rather low coordinative unsaturation[291] due to a change in position in the structure. The unit cell size also reduces[291].
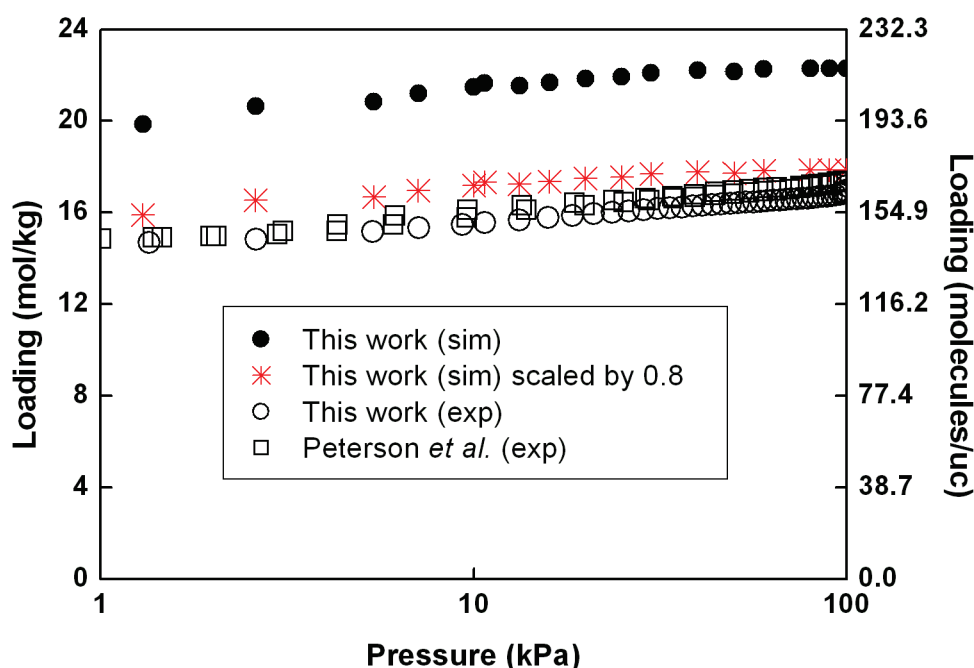
Figure 5.3. *Comparison of simulated and experimental N$_2$ adsorption isotherms in Cu-BTC at 77 K. Our experimental and simulation results are represented by open and filled circles, respectively. Scaled simulation data are represented by stars and previous experimental data[297] (squares) are included for comparison.*

The adsorption of O$_2$ and methane in Cu-BTC follows a similar behavior as N$_2$ as shown in Figures 5.5 (O$_2$) and 6 (methane) for our experimental and computed adsorption isotherms at 295 K. Available experimental[281] and simulation data[313,321] are included for comparison. The difference in the uptake measured in this work and that measured by Wang *et al.*[281] can be related to the different techniques and procedures used to obtain the isotherms; different synthesis procedures were employed, the MOFs were pelletized under pressure and crushed and sieved to particles of 1.4 mm[281]. In this case adsorption in the macropores can play a role at high pressures. The experimental isotherms reported in this paper were determined for the pure crystalline material, without further post-processing.

The contributions of the individual adsorption sites for O$_2$ and methane at 295 K are included in Figures 5.5 and 5.6, respectively. As observed before for N$_2$ the positions close to the copper are not filled and the octahedral cages (center and windows) as well as site I' are again the preferred locations for adsorption. The molecular sitting observed for O$_2$, N$_2$, and methane shows small differences that could be attributed to the quadrupole moment of the molecules. Hence, site II is filled predominantly for methane (the non-

polar molecule) whereas for N_2 the occupation of II and I' is almost equivalent. The quadrupole moment of an O_2 molecule is approximately four times smaller than that of a N_2 molecule, and consequently the molecular sitting shows a behavior intermediate between that observed for methane and for N_2.

The obtained adsorption isotherms for ethane at 295 K are shown in Figure 5.7. The adsorption mechanism for ethane in Cu-BTC is similar as for methane. It initiates at site II and at a loading of 0.8 mol kg^{-1} (corresponding to 8 molecules per unit cell) this site becomes saturated. The adsorption continues with occupation of sites I' and III, and as before site I remains empty. The computed Henry coefficients, energies, enthalpies, and entropies of adsorption at zero coverage and 295 K corroborate that II is the preferential adsorption site at low loading for all the molecules considered in this study. The obtained values are listed in Table 5.2.
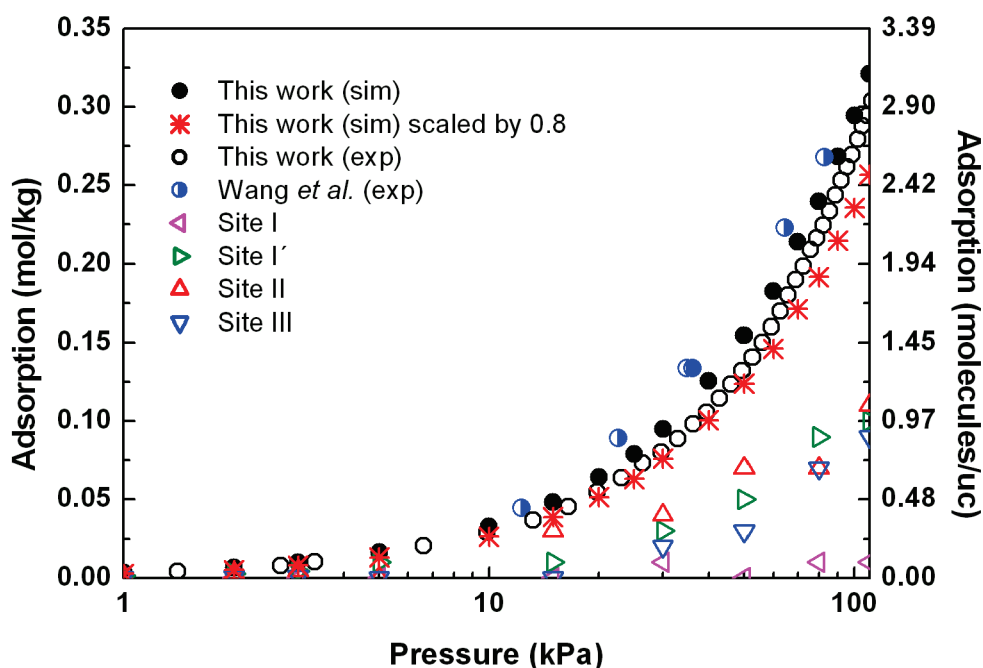

Figure 5.4. *Comparison of simulated and experimental N_2 adsorption isotherms in Cu-BTC at 295 K. Our experimental and simulation results are represented by open and filled circles, respectively. Computed adsorption for the different sites is represented by left triangles (Site I), right triangles (Site I'), up triangles (Site II) and down triangles (Site III). Scaled simulation data are represented by stars and previous experimental data[281] (half filled circles) are included for comparison.*
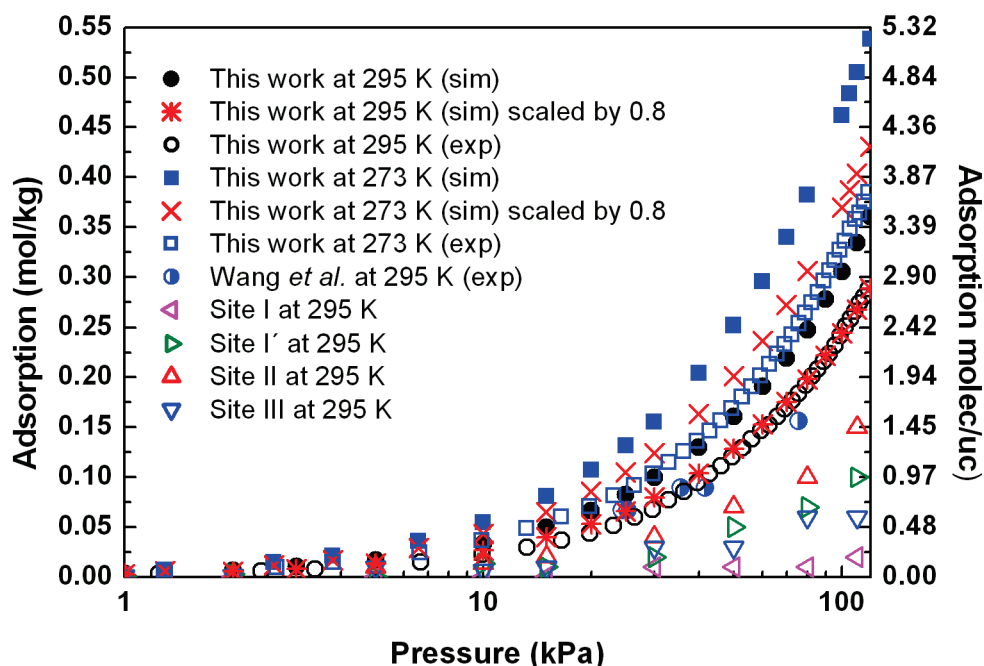
Figure 5.5. *Comparison of simulated and experimental O_2 adsorption isotherms in Cu-BTC at 295 K (circles) and 273 K (squares). Our experimental and simulation results are represented by open and filled symbols, respectively. Computed adsorption for the different sites at 295 K is represented by left triangles (Site I), right triangles (Site I'), up triangles (Site II) and down triangles (Site III). Scaled simulation data are represented by stars and crosses and previous experimental data [281] at 295 K (half filled circles) are included for comparison.*

The adsorption isotherms for propane were computed and measured experimentally at 283 K, 318 K, 353 K, and 383 K. The agreement between our measured and calculated isotherms is good at the lower temperature (Figure 5.8) but surprisingly poor at the higher temperatures (Figure 5.9), where simulations provide much higher loadings than those obtained experimentally, not only by our group but also by other authors[322]. Structural changes like reported for other metal organic frameworks[323] could account for this phenomenon. Indeed, a reduction of the cell volume, caused by the shrinking of the $[Cu_2C_4O_8]$ cage, is observed after dehydration[291]. If the MOF structure contracts with temperature, then the available space in site I' may be smaller or site III may even become inaccessible. Both phenomena yield lower loadings. To check if changes in the MOF structure happen due to temperature effects, temperature programmed XRD (XRTP) under N_2 atmosphere was performed. Figure 5.10 shows the XRD pattern of a hydrated sample (as synthesized) compared with the pattern for this material reported in the literature together with the comparison between hydrated and dehydrated samples measured at different temperatures. When two patterns are subtracted and only positive or negative peaks are observed this is due to a change in reflection intensity. If peak shifts occur, then pattern subtraction yields pairs of positive and negative peaks. As reported in literature, comparison between XRD at Room Temperature before and after

dehydration reveals changes in the relative intensity of several reflections[291] and the disappearance of the peak at $2\theta = 5.9$[305], related with a shrinking of the $[Cu_2C_4O_8]$ cage[291].

Even more interesting is the comparison between the XRD patterns of the dehydrated sample at different temperatures, the main reflections shift to larger 2θ values. By applying Bragg's law to the main reflections (plans 110, 220, 222, 400, 311, 330, and 440) a decrease of circa. 0.5 % in the lattice spacing could be calculated between the dehydrated sample at room temperature and the same sample at 373 K. A further decrease by 0.4 % occurred when increasing the temperature further to 473 K. Clearly, a reversible change occurs in the crystalline lattice of Cu-BTC when changing the temperature, which may affect the adsorptive properties of the material in terms of packing density or accessibility. Our data show two effects separately: The structure shrinks a) when water is removed and b) with increasing temperature (negative thermal expansion, NTE). We would like to highlight that for the first time a NTE for Cu-BTC is reported. The NTE was previously observed only for isoreticular metal-organic frameworks by Dubbeldam *et al.* [57].
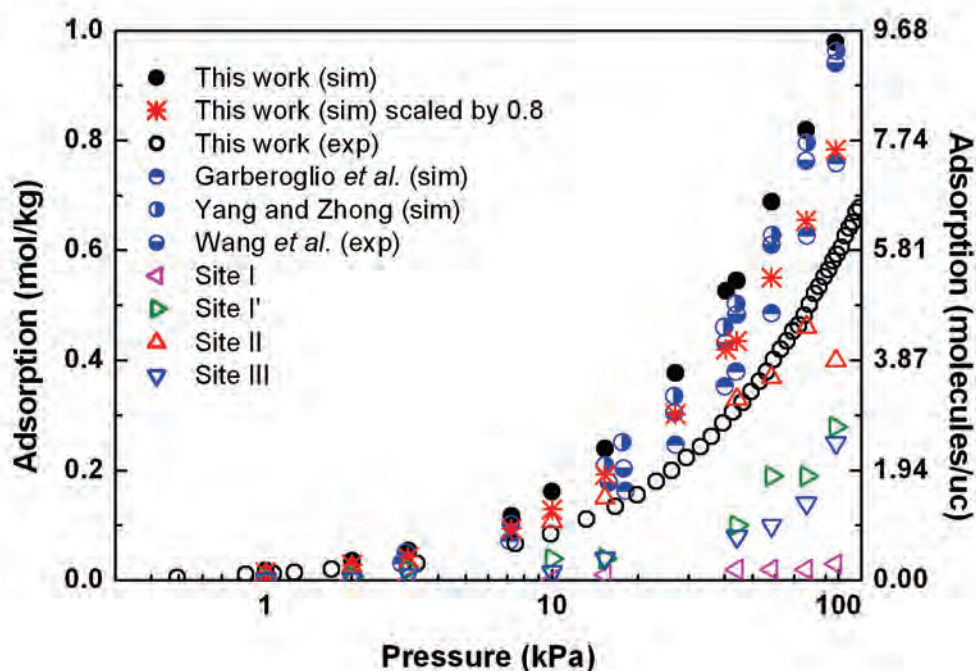

Figure 5.6. *Comparison of simulated and experimental methane adsorption isotherms in Cu-BTC at 295 K. Our experimental and simulation results are represented by open and filled circles, respectively. Computed adsorption for the different sites is represented by left triangles (Site I), right triangles (Site I'), up triangles (Site II) and down triangles (Site III). Scaled simulation data are represented by stars and previous experimental (◓) [281] and simulation data [313,321] (half filled circles ◑◐) are included for comparison.*
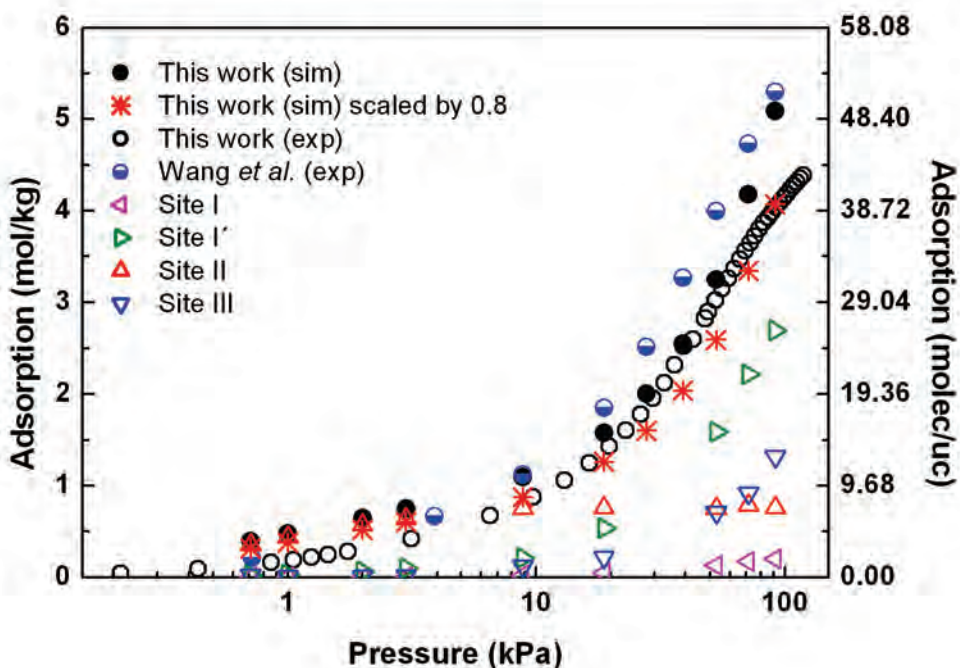
Figure 5.7. *Comparison of simulated and experimental ethane adsorption isotherms in Cu-BTC at 295 K. Our experimental and simulation results are represented by open and filled circles, respectively. Computed adsorption for the different sites is represented by left triangles (Site I), right triangles (Site I'), up triangles (Site II), and down triangles (Site III). Scaled simulation data are represented by stars and previous experimental data [281] (half filled circles) are included for comparison.*
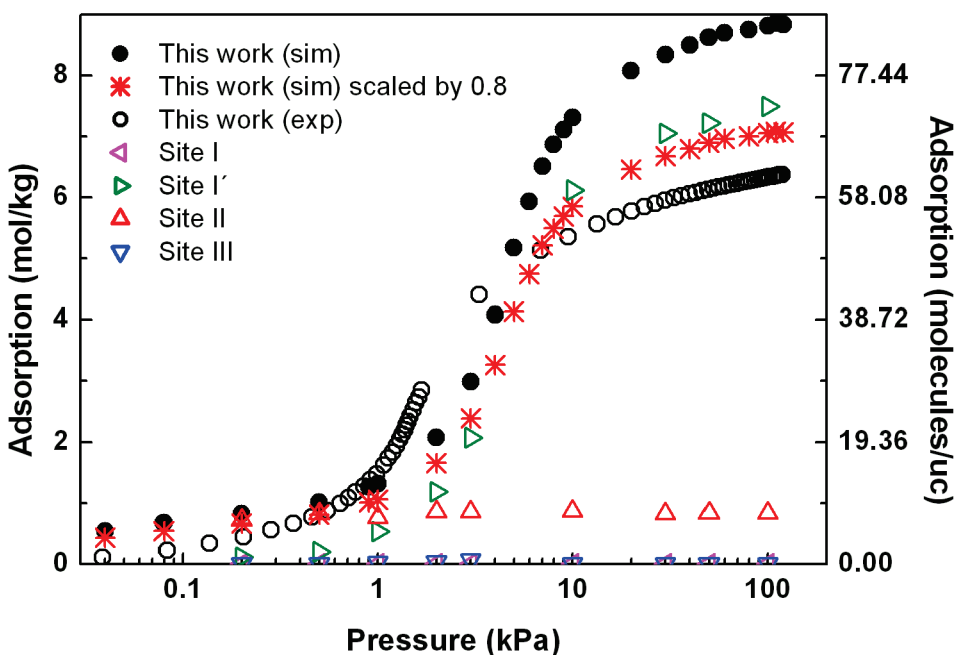

Figure 5.8. *Comparison of simulated and experimental propane adsorption isotherms in Cu-BTC at 283 K. Our experimental and simulation results are represented by open and filled circles, respectively. Computed adsorption for the different sites is represented by left triangles (Site I), right triangles (Site I'), up triangles (Site II), and down triangles (Site III). Scaled simulation data are represented by stars.*
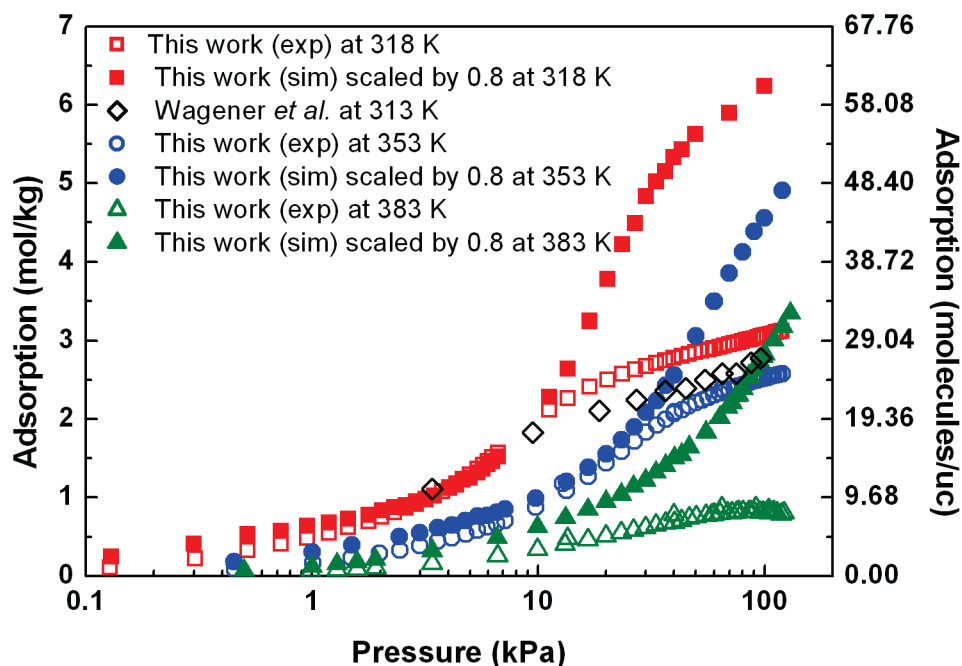
Figure 5.9. *Comparison of rescaled simulation results and experimental propane adsorption isotherms in Cu-BTC at 318 K, 353 K, and 383 K. Our experimental and rescaled simulation results are represented by open and filled symbols, respectively. Previous experimental data [322] (at 313 K) (diamonds) are included for comparison.*

The adsorption mechanism for propane is similar for the four temperatures studied in this work and only that at 283 K is plotted in Figure 5.8 for the sake of clarity. The occupation of the individual adsorption sites for propane at 283 K are also plotted in this figure. Again site II is filled up before the other sites. The site becomes saturated with 8 molecules per unit cell and after that loading propane starts to fill site I', leaving both site I and III almost empty. The same pore filling behaviour was found for higher temperatures (318 K, 353 K, and 383 K). Site I, related to the copper cations is inaccessible, due to the dehydration of the sample and the changed position of the copper. The molecular modelling has been performed with the structural parameters of the hydrated sample, the only information currently available, which does not account for these changed structural parameters. The low accessibility of site III is tentatively also attributed to these changed lattice parameters due to dehydration. The accessibility of this window site in case of the larger propane molecule in this study may be very sensitive to small changes, also explaining the increased divergence between the modelling and experimental results with increasing temperature. A fine-tuning of the structural parameters for the dehydrated sample and its temperature dependency is required to establish a full match.

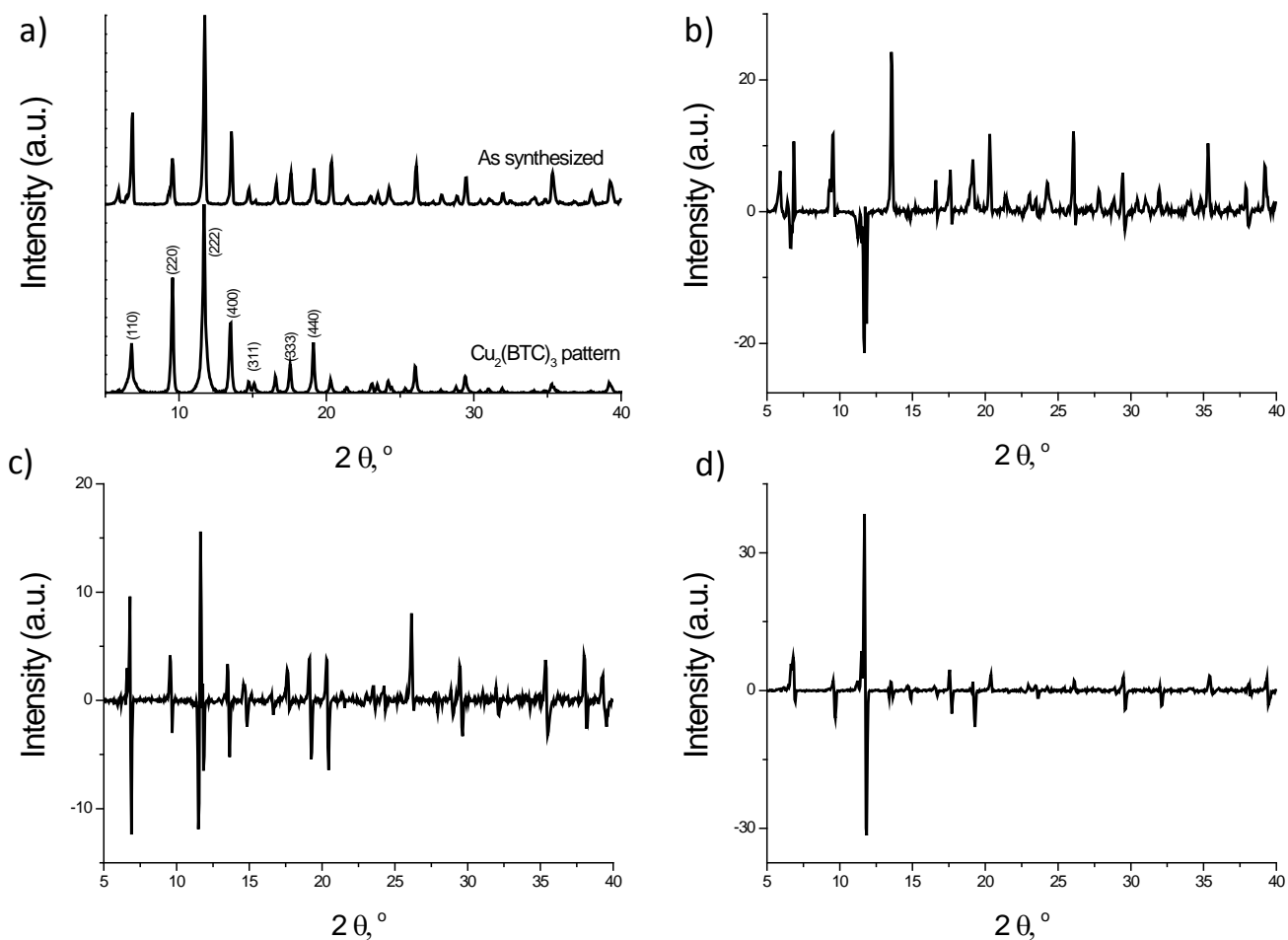**Figure 5.10.** *Temperature Programmed XRD results: a) comparison between the as-synthesized material and the Cu-BTC pattern. b) Difference of XRD patterns of the as synthesized sample (hydrated) and dehydrated sample at room temperature. c) Difference pattern of dehydrated sample at room temperature and dehydrated sample at 373 K. d) Difference pattern of dehydrated sample at 373 K and dehydrated sample at 473 K.*

Site	K_H/mol kg^{-1} Pa^{-1}	$-\Delta U$/kJ mol^{-1}	$-\Delta H$/kJ mol^{-1}	$-\Delta A$/kJ mol^{-1}	$-\Delta G$/kJ mol^{-1}	$-\Delta S$/J K^{-1}mol^{-1}
Methane						
I	$3.31 \cdot 10^{-6}$ (3)	9.07 (3)	11.52 (3)	4.82 (3)	7.27 (3)	14.4 (2)
I'	$3.88 \cdot 10^{-6}$ (4)	9.25 (2)	11.71 (2)	5.21 (2)	7.66 (2)	13.7 (1)
III	$5.08 \cdot 10^{-6}$ (3)	11.65 (5)	14.11 (5)	5.87 (1)	8.32 (1)	19.6 (2)
II + III	$1.78 \cdot 10^{-5}$ (1)	18.55 (3)	21.00 (3)	8.95 (2)	11.40 (2)	32.5 (1)
Cu-BTC	$1.83 \cdot 10^{-5}$ (2)	18.23 (4)	20.69 (4)	9.01 (3)	11.46 (3)	31.3 (2)
Ethane						
I	$2.44 \cdot 10^{-5}$ (2)	15.62 (3)	18.08 (3)	9.72 (2)	12.18 (2)	20.0 (2)
I'	$2.94 \cdot 10^{-5}$ (3)	15.78 (4)	18.24 (4)	10.18 (2)	12.63 (2)	19.0 (2)
III	$5.1 \cdot 10^{-5}$ (2)	23.5 (4)	26.0 (4)	11.54 (8)	14.00 (8)	41 (1)
II + III	$9.7 \cdot 10^{-4}$ (2)	34.77 (7)	37.22 (8)	18.76 (6)	21.22 (6)	54.3 (5)
Cu-BTC	$9.9 \cdot 10^{-4}$ (3)	34.7 (1)	37.1 (1)	18.80 (7)	21.25 (7)	53.9 (6)
Propane						
I	$3.3 \cdot 10^{-3}$ (9)	12.75 (2)	15.2 (2)	4.8 (6)	7.27 (6)	27 (2)
I'	$4 \cdot 10^{-3}$ (1)	12.94 (2)	15.39 (2)	5.2 (7)	7.66 (7)	26 (2)
III	$1.82 \cdot 10^{-3}$ (4)	44.0 (4)	46.5 (4)	20.30 (6)	22.75 (6)	80 (2)
II + III	$1.6 \cdot 10^{-2}$ (6)	46.9 (1)	49.4 (1)	25.5 (1)	28.0 (1)	72.2 (5)
Cu-BTC	$1.56 \cdot 10^{-2}$ (4)	46.86 (7)	49.31 (7)	25.56 (6)	28.01 (6)	49.67 (4)
Nitrogen						
I	$1.36 \cdot 10^{-6}$ (5)	6.60 (1)	9.06 (1)	2.65 (1)	5.10 (1)	13.39 (7)
I'	$1.54 \cdot 10^{-6}$ (6)	6.72(1)	9.17 (1)	2.956 (9)	5.409 (9)	12.77 (8)
III	$1.83 \cdot 10^{-6}$ (1)	8.29 (2)	10.74 (3)	3.37 (1)	5.82 (1)	16.7 (1)
II + III	$3.37 \cdot 10^{-6}$ (3)	11.76 (2)	14.21 (2)	4.87 (2)	7.32 (2)	23.4 (1)
Cu-BTC	$3.65 \cdot 10^{-6}$ (3)	11.49 (4)	13.94 (4)	5.06 (2)	7.51 (2)	21.8 (2)
Oxygen						
I	$1.3 \cdot 10^{-6}$ (8)	6.39 (1)	8.84 (1)	2.53 (1)	4.98 (1)	13.1 (1)
I'	$1.47 \cdot 10^{-6}$ (5)	6.551 (5)	9.003 (5)	2.841 (9)	5.294 (9)	12.57 (5)
III	$1.98 \cdot 10^{-6}$ (1)	8.85 (2)	11.30 (2)	3.56 (1)	6.01 (1)	17.9 (1)
II + III	$3.50 \cdot 10^{-6}$ (5)	11.72 (4)	14.18 (4)	4.96 (4)	7.41 (4)	22.9 (3)
Cu-BTC	$3.76 \cdot 10^{-6}$ (3)	11.42 (4)	13.88 (4)	5.13 (2)	7.60 (2)	21.3 (2)

Table 5.2. *Henry coefficients, energies, enthalpies, and entropies of adsorption computed at zero coverage for the different sites at 295 K. The values for site II+III were computed for the sphere with radius 0.55 nm centered at the middle of the octahedral cage. Site III is defined as the spherical annulus between radius 0.2 nm (site II) and 0.55 nm. The obtained error bars are shown in brackets.*

5.5. Conclusions

Cu-BTC consists of two types of cages, one of them is commensurate with small molecules and the other one is capable of adsorbing larger molecules. This characteristic could induce strong adsorption selectivity for mixtures. Optimization of separation selectivity requires proper understanding of the adsorption behavior of Cu-BTC. With this work we contributed to a better understanding of the interactions governing the Cu-BTC substrate, as well as the properties of the structure when water is removed. The observed negative thermal expansion for Cu-BTC has important implications for adsorption, because of the close match between small molecules and the small pockets. Future simulations should take this structural change into account to obtain a better match with experiments at higher temperatures.

Separation of natural gas in MOFs

We use Monte Carlo simulations to study the adsorption and separation of the natural gas components in IRMOF-1 and Cu-BTC metal–organic frameworks. We computed the adsorption isotherms of pure components, binary, and five-component mixtures analyzing the siting of the molecules in the structure for the different loadings. The bulk compositions studied for the mixtures were 50 : 50 and 90 : 10 for CH_4–CO_2, 90 : 10 for N_2–CO_2, and 95 : 2.0 : 1.5 : 1.0 : 0.5 for the CH_4–C_2H_6–N_2–CO_2–C_3H_8 mixture. We choose this composition because it is similar to an average sample of natural gas. Our simulations show that CO_2 is preferentially adsorbed over propane, ethane, methane and N_2 in the complete pressure range under study. Longer alkanes are favored over shorter alkanes and the lowest adsorption corresponds to N_2. Though IRMOF-1 has a significantly higher adsorption capacity than Cu-BTC, the adsorption selectivity of CO_2 over CH_4 and N_2 is found to be higher in the latter, proving that the separation efficiency is largely affected by the shape, the atomic composition and the type of linkers of the structure.

6.1. Introduction

Methane (CH_4) is one of the cleanest carbon fuels due to its low carbonaceous and particle emissions after combustion. It is also attractive for its low emissions of greenhouse gases per kW generated in industrial and energy production applications. Natural gas is composed of around 95% methane, traces of heavier gaseous hydrocarbons such as ethane (C_2H_6) and propane (C_3H_8), and other light gasses such as CO_2 and N_2. To obtain a cheap and clean fuel from natural gas it is important to purify it since the presence of CO_2 reduces the combustion power efficiency and contributes to greenhouse gas emissions[324,325].

Metal-organic frameworks (MOFs) are turning into promising materials for storage, separation, and purification of natural gas mixtures by adsorption. They are a new class of porous materials consisting of metal-oxide clusters and organic linkers[302,326-331] that can form pores and cavities of a desired shape and size by selecting linkers of specific length and metals of suitable coordination[35,264,268,302,320,330,332-338]. Experimental and simulation studies based on the adsorption and separation of natural gas and its components in MOFs are still scarce, and most of them are focused on the adsorption isotherms of CO_2, methane, N_2, and on CO_2/CH_4 binary mixtures[258,265,281,284,286,287,314,339-341].

The adsorption and separation processes of CO_2, methane, and ethane were analyzed using molecular simulations by Wang et al.[286] in Cu-BTC, by Babarao et al.[258], Keskin and Sholl[340], and Walton et al.[339] in IRMOF-1 and by Yang and Zhong[265,287] in both Cu-BTC and IRMOF-1 structures. Liu et al.[284] used experimental and theoretical methods to study the adsorption behavior of N_2 in Cu-BTC and Wang et al.[281] investigated the sorption properties of Cu-BTC for N_2, CO_2, methane, ethane and CO_2/CH_4 mixtures by a series of experimental methods. Zhou et al.[341] measured adsorption isotherms for CH_4 in IRMOF-1 over a large temperature and pressure range, and Millward and Yaghi[315] compared the volumetric CO_2 capacity for a variety of MOFs. In this work we go one step forward by analyzing the molecular sitting during the adsorption of the main components of natural gas and their mixtures. We use molecular simulations to obtain information about the performance of two highly porous MOFs, Cu-BTC and IRMOF-1, in the natural gas separation process. Cu-BTC (BTC: benzene-1,3,5-tricarboxylate) has garnered a great deal of attention since it was first reported by Chui et al.[36] in 1999. Its framework is a metal coordination polymer based on copper as the metal centre and benzene-1,3,5-tricarboxylates as the linker molecule. It is formed by primary building blocks connected to form a face-centered cubic crystal framework, and secondary building blocks forming octahedron-shaped pockets accessible for small molecules through small windows. IRMOF-1 belongs to the family of IsoReticular Metal-Organic Frameworks (IRMOFs) and was first synthesized by Yaghi and co-workers[35,268]. IRMOF-1 structure consists of a cubic array of $Zn_4O(CO_2)_6$ units connected by phenylene links. The linkage of the Zn_4O

complexes is forced to alternate between linkers pointing outwards and inwards, resulting in a structure with two alternating type of cavities: small cavities of about 10.9 Å, and larger cavities of about 14.4 Å diameter[35].

This work analyzes the storage capacity and adsorption behavior of CH_4, C_2H_6, N_2, CO_2, C_3H_8, and the separation of their mixtures in Cu-BTC and IRMOF-1. We focus not only on the adsorption capacities and selectivities but also on the preferential adsorption sites of the components as a function of pressure. In section 6.2 we describe the simulation methods and the models used for the MOFs and the adsorbates. The obtained adsorption isotherms, molecular sitting, and occupancies for pure components and mixtures are presented in section 6.3, followed by our concluding remarks in section 6.4.

6.2. Simulation details

Adsorption isotherms were calculated using grand-canonical Monte Carlo (GCMC) simulations, where the chemical potential, the temperature, and the volume are fixed. The fugacity, related directly to the imposed chemical potential[243], is obtained from the pressure using the Peng-Robinson equation of state. We used at least 10^7 MC cycles that consist of translation, rotation, regrow in random positions and change of identity for mixtures[342]. For comparison with experimental isotherms, absolute adsorption was converted to excess adsorption[319,320].

Atomic interactions were described by Lennard-Jones, while Coulomb potentials were computed with the Ewald summation technique, using a relative precision of 10^{-6}. The Lennard-Jones potential is truncated and shifted at a cutoff distance of 12 Å. The parameters for methane, ethane, and propane were taken from the united atom TraPPE model[75] in which the CH_x beads are considered as single, chargeless interaction centers. The beads are connected using a harmonic bond-potential $U = 0.5 \, k \, (r - r_0)^2$ with k/k_B = 96500 K and r_0 = 1.54 Å, and a harmonic bend potential $U = 0.5 \, k \, (\theta - \theta_0)^2$ with k/k_B = 62500 K and θ_0 = 114°. CO_2 and N_2 were considered as small rigid molecules, using the model proposed by Harris et $al.$[78] for CO_2 and the model proposed by Murthy et $al.$[316] for N_2. The partial charges of N_2 and CO_2 are chosen such that the experimental quadrupole moment is reproduced. These models and potentials have been successfully employed to describe the adsorption in zeolites[45,132,133,166].

Cu-BTC and IRMOF-1 frameworks are considered rigid with Lennard-Jones parameters taken from the DREIDING[289] force field except those for Cu, which were taken from the UFF[290] force field. The

Lorentz-Berthelot mixing rules were used to calculate Lennard-Jones parameters between unlike atoms, and the atomic charges for the MOFs were taken from Frost *et al.* and Dubbeldam *et al.*[57]. A single unit cell of IRMOF-1 (a = b = c = 25.832 Å) and a single unit cell of Cu-BTC (a = b = c = 26.343 Å) were used during the simulations. We obtained a helium void fraction of 0.82 for IRMOF-1 and 0.76 for Cu-BTC. The crystal structure of Chui *et al.* includes axial oxygen atoms weakly bonded to the Cu atoms, which correspond to water ligands. Our simulations have been performed on Cu-BTC with these oxygen atoms removed.

The method used for the analysis of preferential adsorption sites in MOFs is similar to that used on the locations and occupancies of ions in zeolites[45,244]. We have defined eight individual adsorption sites for IRMOF-1 and four for Cu-BTC, based on previous works that studied the adsorption sites of argon and nitrogen in IRMOF-1[294,343] and hydrogen in Cu-BTC[284]. The IRMOF-1 unit cell contains 8 Zn_4O tetrahedral clusters and 24 linker molecules, defining 4 small cavities and 4 large cavities. Five of the sites defined for IRMOF-1 are close to the Zn_4O cluster and the linker molecules (Sites I to V) and the other three form a second layer in the pores (Sites VI to VIII). Sites I and II are located in the large and small cages, respectively. Site III is located in the region that separates both types of cages. Sites IV and V are close to the linker molecules, above and beneath the center of the phenyl ring (site IV) and on the edges of it (site V). Sites VI and VII forming a layer above site IV, and site VIII located at the center of the small cage, above site II and surrounded by site V.

Cu-BTC is composed by benzene-1,3,5-tricarboxylate (BTC) ligands coordinating copper ions, forming large cavities and small octahedral cages. We have defined four adsorption sites on this structure; the sites labeled I, II, and III described by Liu *et al.*[296] as preferential adsorption sites for H_2 and one additional site that we labeled I'. Sites I and I' are located at the central cavities, in the center (site I') or close to the Cu^{2+} atoms (site I), and Sites II and III are located at the center and at the windows of the small octahedral cages, respectively.

6.3. Results and discussion

The adsorption isotherms and preferential adsorption sites in Cu-BTC and IRMOF-1 were obtained at 298 K for 1) pure component methane, ethane, propane, nitrogen, and carbon dioxide, 2) 50:50 and 90:10 CH_4/CO_2 binary mixtures, 3) 90:10 N_2/CO_2 binary mixtures and 4) 95:2:1.5:1:0.5 five component mixtures of methane, ethane, nitrogen, carbon dioxide and propane.

Adsorption of pure components. Simulated and available experimentally measured adsorption isotherms of pure methane, ethane, and propane in Cu-BTC and IRMOF-1 as a function of pressure are shown in Figure 6.1. The simulated isotherms are in good agreement with previous simulation results and experimental data[57,258,281,287,312,313,319,321,341,344]. The adsorption of the hydrocarbons increases with the number of carbon atoms in both structures for the complete pressure range under study. This is due to a combination of energetic effects and entropic effects[345]. At much higher pressures near saturation (not shown here) methane would absorb more as a consequence of a shape entropic effect[345] (methane fits better than ethane and propane into the partially occupied cavities). Adsorption isotherms of CO_2 and N_2 are shown in Figure 6.2 for Cu-BTC and IRMOF-1. The simulation results obtained for IRMOF-1 are in very good agreement with previous experimental values[281,315]. The agreement is also good for Cu-BTC at low pressures[57,258,286,287,312,315] though deviations are observed at higher pressures, where simulation data overestimates measured values for CO_2. Those deviations can be attributed to the force field accuracy and also to the fact that our framework is a rigid and perfect material, whereas experimental samples are flexible and they generally contain water and organic residues after synthesis leading to a decrease in the storage capacity. The partially charged CO_2 has stronger interaction with the framework than N_2 and therefore higher adsorption. For the same reason, the extent of CO_2 adsorption is larger than the one of methane in both MOFs over the entire pressure range under study, in which saturation is not reached. Direct comparison of the obtained adsorption isotherms for hydrocarbons and for N_2 and CO_2 for both structures proves that Cu-BTC is the best adsorbent at the lower pressures, and IRMOF-1 – with a larger pore volume and therefore more storage capacity- is the best adsorbent at the higher pressures. This can be attributed to entropic effects since the molecular packing is more efficient in the small octahedral cages of Cu-BTC –preferential adsorption sites at low pressures– than in the large cavities of IRMOF-1.
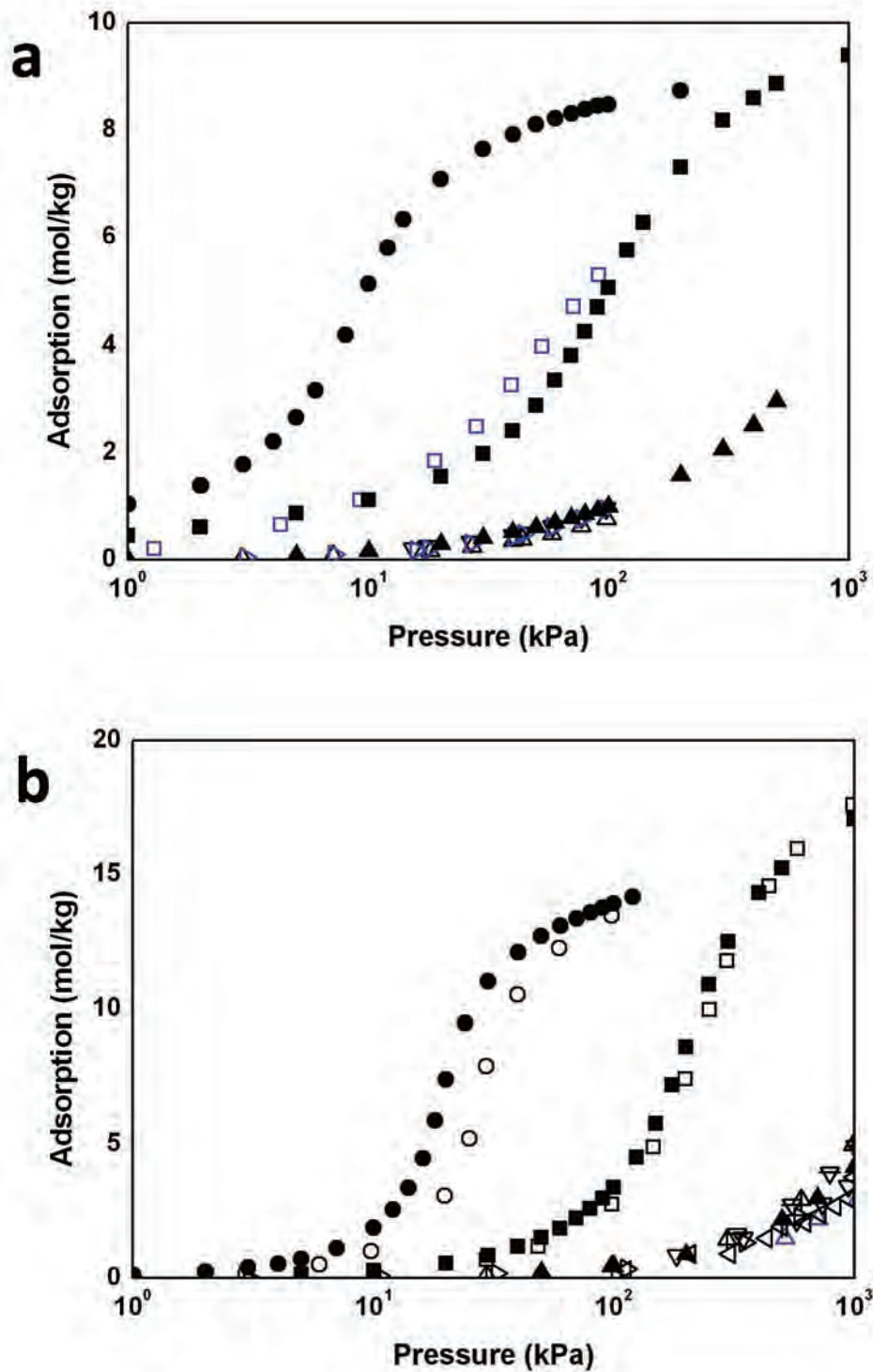
Figure 6.1. *Adsorption isotherms of pure methane (triangles), ethane (squares), and propane (circles) in Cu-BTC (a) and IRMOF-1 (b) at 298 K. Our simulated isotherms (closed symbols) are compared with previous experimental data* [281,341] *(open left triangles and squares in a and open triangles in b) and simulation data* [57,258,312,319,321,344] *(rest of the open symbols).*
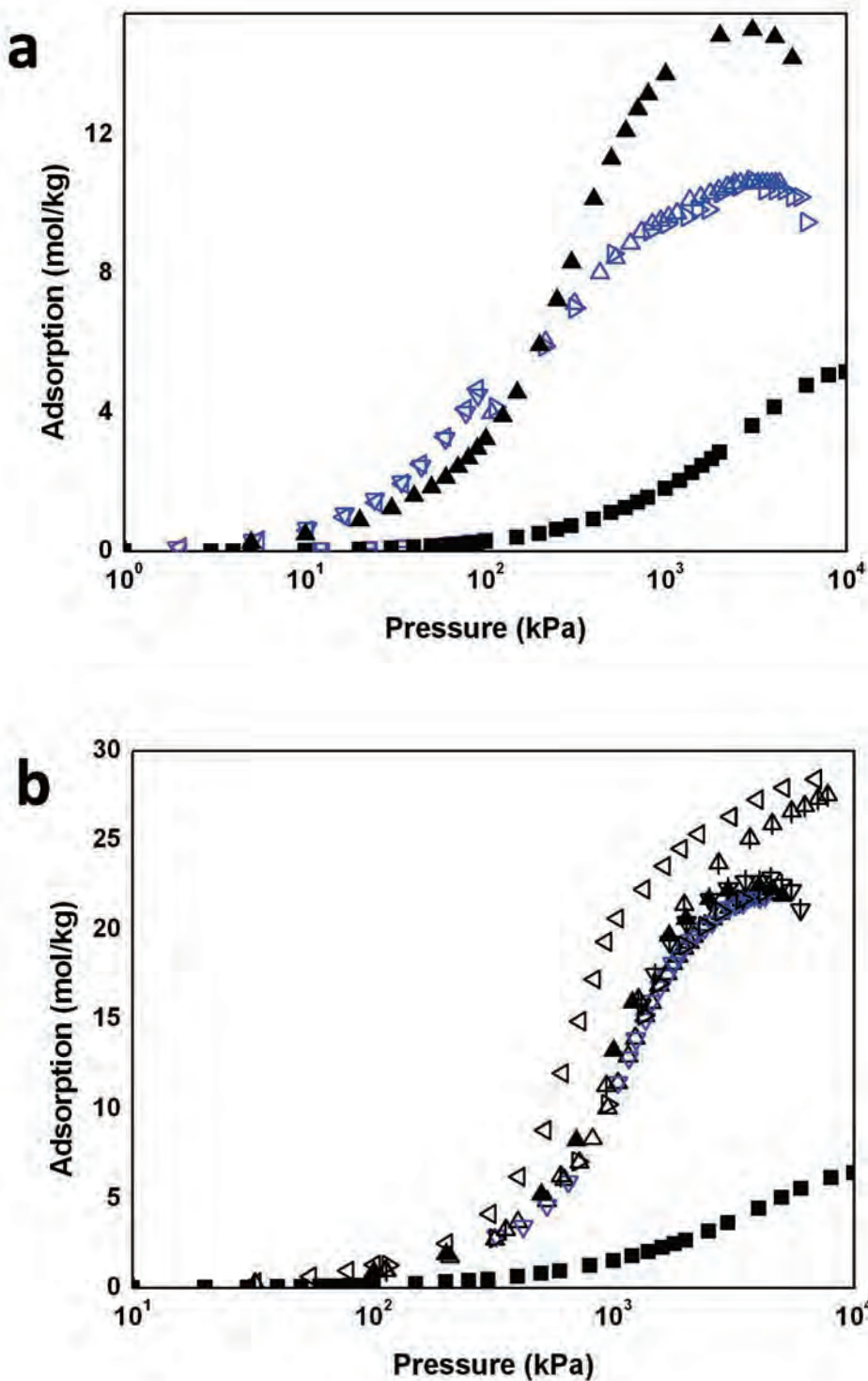
Figure 6.2. *Adsorption isotherms of pure CO_2 (triangles) and N_2 (squares) in Cu-BTC (a) and IRMOF-1 (b) at 298 K. Our simulated isotherms (closed symbols) are compared with previous experimental data [281,315] (open symbols in a and triangles down in b) and simulation data (rest of the open symbols).*

The adsorption behavior of carbon dioxide and methane as a function of pressure in Cu-BTC is depicted in Figure 6.3. At low pressures methane preferentially adsorb in the small octahedral cages of Cu-BTC (site II), while CO_2 not only adsorbs in the cages but also in the windows (site III). The adsorption of N_2 in the large cages (site I') is as important as in the octahedral cages, and the windows are also occupied (site III) but in a lower extent. Site II is also preferential adsorption site for longer alkanes at low pressures and the increase on the number of carbon atoms in the chain progressively reduces the adsorption on site III, being almost zero for propane. At higher pressures and once the octahedral cages are partially filled, the molecules adsorb more in the large cage (site I') and in the windows (site III). Site I, defined by Liu et al.[296] as a preferential adsorption position for hydrogen[296] remains empty for all adsorbates over the entire range of pressures.

A similar study was done for IRMOF-1, identifying the large cages (site I) and the region that separates large and small cages (site III) as preferential adsorption sites for pure component adsorption. Site III shows the highest occupation, followed by site I. Site II (small cages) was found almost empty. Most of the adsorbed molecules close to the linkers are found above and beneath the center of the phenyl ring (site IV) and only a few molecules are on the edges of the linkers (site V). Two out of the three additional sites described by Rowsel et al. for argon molecules[343] show very little adsorption in all cases. Those are the sites labeled as VI and VII that form a layer above the phenyl ring. The third additional site (site VIII) is almost empty at low pressures but a significant increase of adsorption is observed at higher pressures.

Adsorption of CH_4 and CO_2 binary mixtures. Figure 6.4 shows the computed adsorption selectivity for CO_2 relative to CH_4 defined as $(x_{CO2}/y_{CO2})/(x_{CH4}/y_{CH4})$, where x_{CO2} and x_{CH4} are the mole fractions in the adsorbed phase and y_{CO2} and y_{CH4} are the mole fractions in the bulk phase. Selectivities were computed for the 50:50 and for the 10:90 CO_2/CH_4 mixtures. The selectivity in Cu-BTC is the highest among the two adsorbents. CO_2 preferentially adsorbs in both MOFs due to the stronger interactions between the CO_2 molecules and the surfaces. Previous simulation data[258,287,340] –only available for the 50:50 equimolar mixture– was added for comparison, showing very good agreement for IRMOF-1. The selectivity for Cu-BTC obtained by simulations show similar trends than the experimental one, but the deviation is larger than for IRMOF-1. The force field used in this work is less accurate for Cu-BTC than for IRMOF-1 and a very small deviation in the number of adsorbed molecules may result in a larger deviation in selectivity. The selectivity in Cu-BTC is the highest among the two adsorbents despite the deviations, suggesting that this structure is a potentially good candidate to separate CO_2 and CH_4.
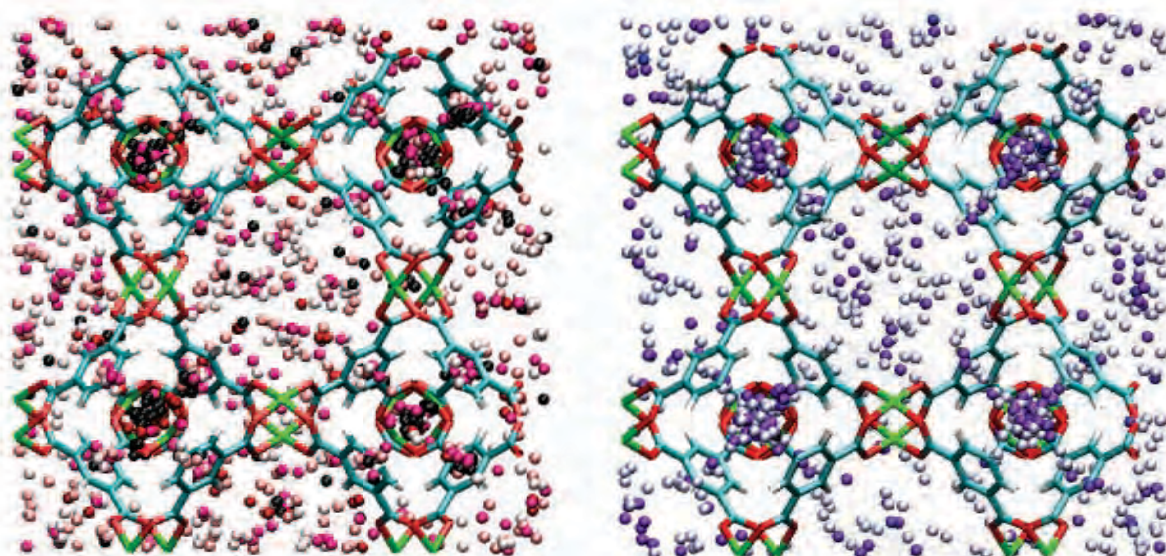
Figure 6.3. *Center-of-mass distributions of carbon dioxide (left) and methane (right) molecules adsorbed in Cu-BTC at 298 K for 2 kPa, 20 kPa, 200 kPa, 1000 kPa and 5000 kPa. The center of mass changes from darker to lighter color with increasing pressure. Simulations were performed using one (2 kPa), two (20 kPa), and four million (200 to 5000 kPa) MC steps. The snapshots are taken every 5000 steps for 2 kPa, 10000 steps for 20 kPa, and 20000 steps for the three higher pressures.*
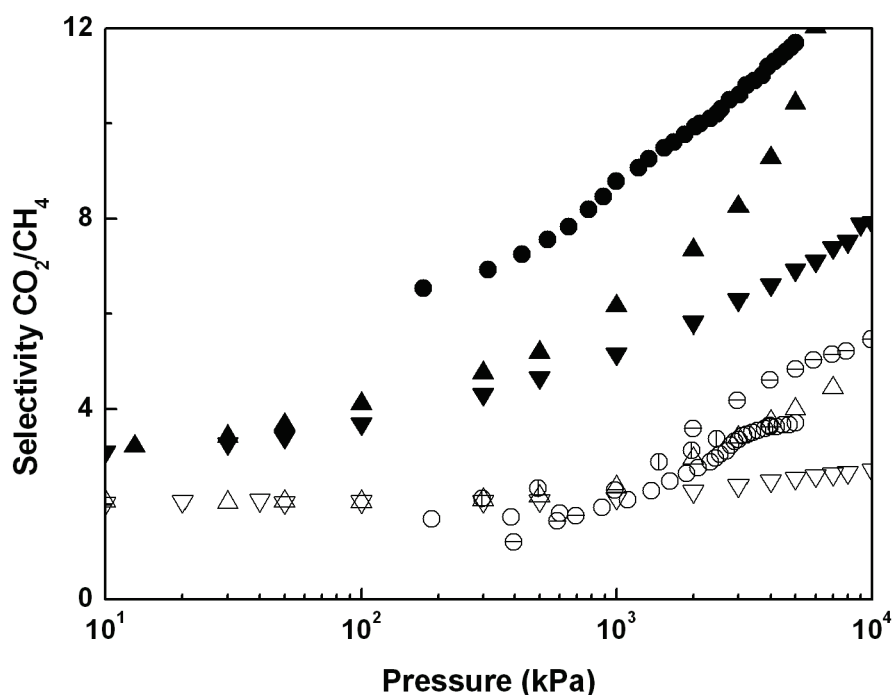

Figure 6.4. *Selectivity for CO_2 from the equimolar and the 10:90 mixtures of CO_2 and methane in Cu-BTC (closed symbols) and IRMOF-1 (open symbols) at 298 K. Our simulation results (up triangles for the equimolar and down triangles for the 10:90 mixture) are compared with previous simulation data [258,286,340] (different style of circles) available only for the equimolar mixtures.*
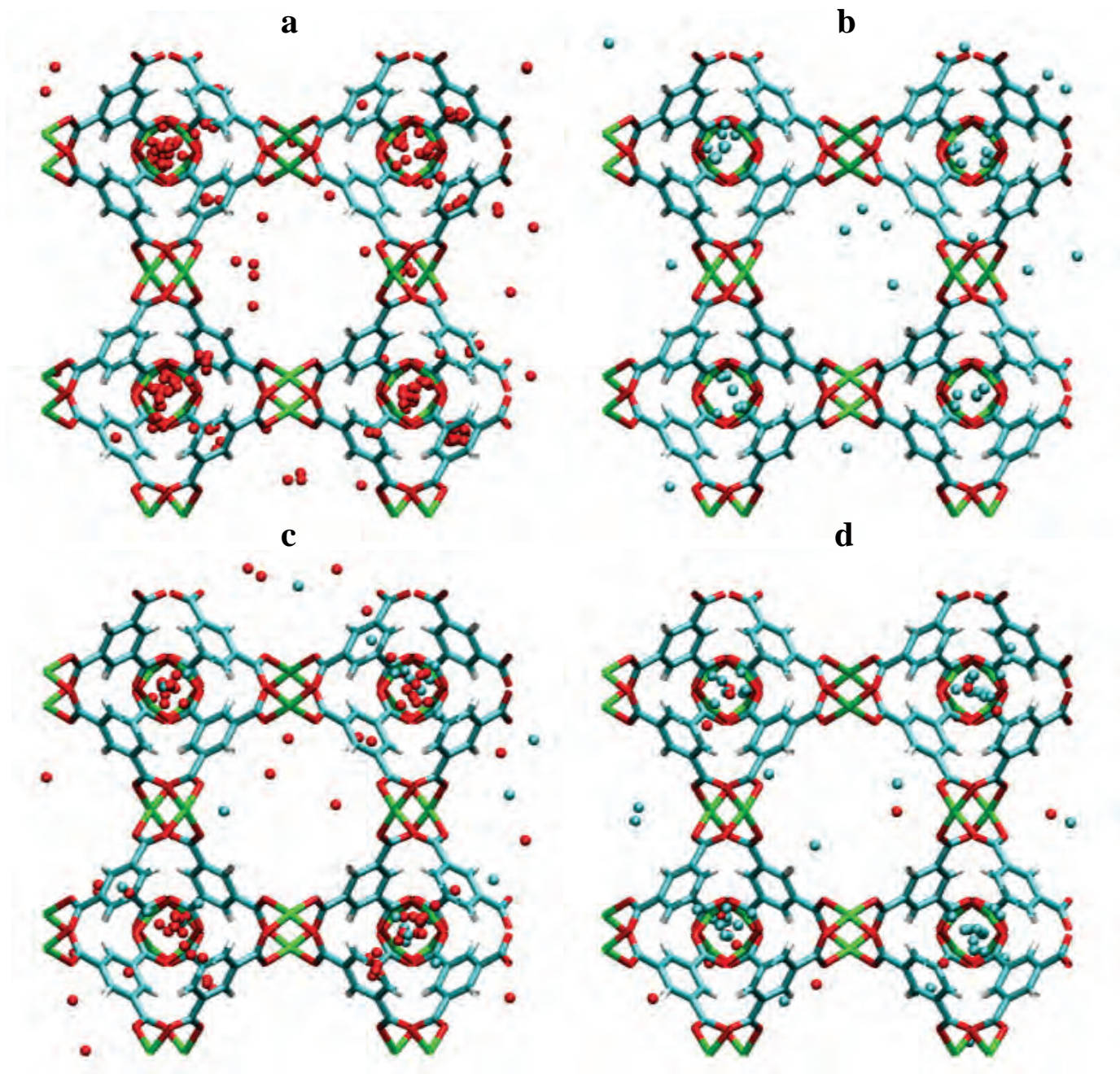
a

b

c

d

Figure 6.5. *Adsorption of molecules in Cu-BTC at 2 kPa and 298 K. Snapshots were taken every 5000 steps in a simulation of one million MC steps, and all the molecules in them were plotted. Only the center of mass of the molecules are drawn, CO_2 in red and methane in blue. (a) Pure CO_2, (b) pure methane, (c) 50:50 mixture CO_2/methane, and (d) 10:90 mixture CO_2/methane.*
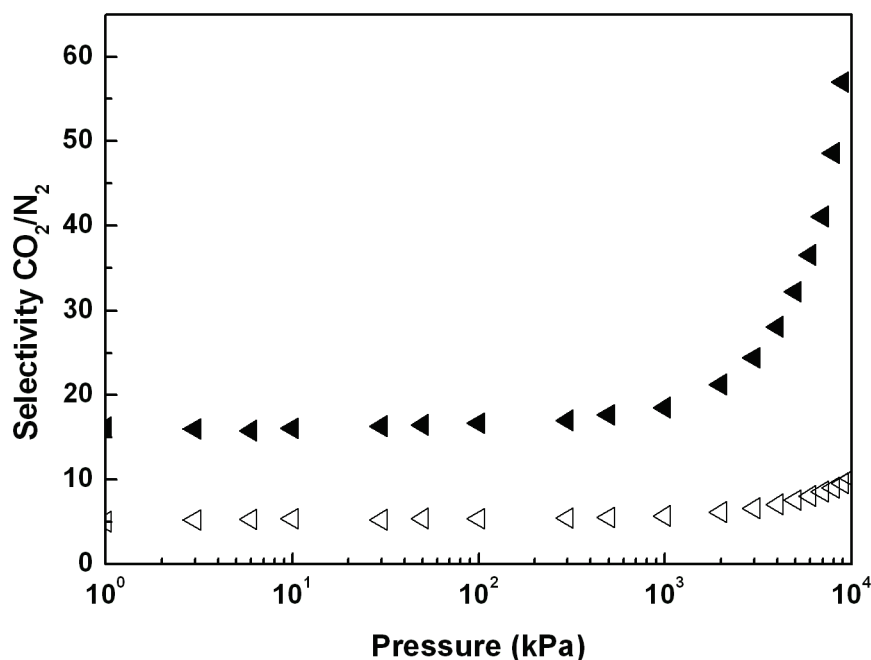
Figure 6.6. *Selectivity for CO_2 from the 10:90 binary mixture of CO_2 and N_2 in Cu-BTC (closed symbols) and IRMOF-1 (open symbols) at 298 K.*

The analysis of adsorption sites for the previous mixtures in Cu-BTC shows that at low pressures methane preferentially adsorbs in the octahedral cages displacing an important fraction of CO_2 molecules to the windows. At higher pressures and once the octahedral cages are full, site I' becomes the preferential adsorption site. The equilibrium snapshots are depicted in Figure 6.5. The sitting of methane and CO_2 molecules during adsorption of the binary mixture in IRMOF-1 shows the same trend as the pure components, being the large cages and the region that separates the large and the small cages the preferential adsorption sites.

Adsorption of CO_2 and N_2 binary mixtures. Figure 6.6 shows simulated adsorption selectivities for CO_2 relative to N_2 for the 10:90 CO_2/N_2 binary mixtures in both structures. Our results confirm a very strong preferential adsorption of CO_2 over N_2. This selectivity is much higher in Cu-BTC than in IRMOF-1 but the general trend is similar in the two materials and remains constant with pressure for the range that spans from 1 to 10^2 kPa. The selectivity for carbon dioxide from the binary mixture increases at higher pressures, and this increase is sharper in Cu-BTC than in IRMOF-1. This can be attributed to the differences in structure. The pores of Cu-BTC are smaller than those of IRMOF-1, leading to stronger confinement effects for CO_2 and favoring its packing.
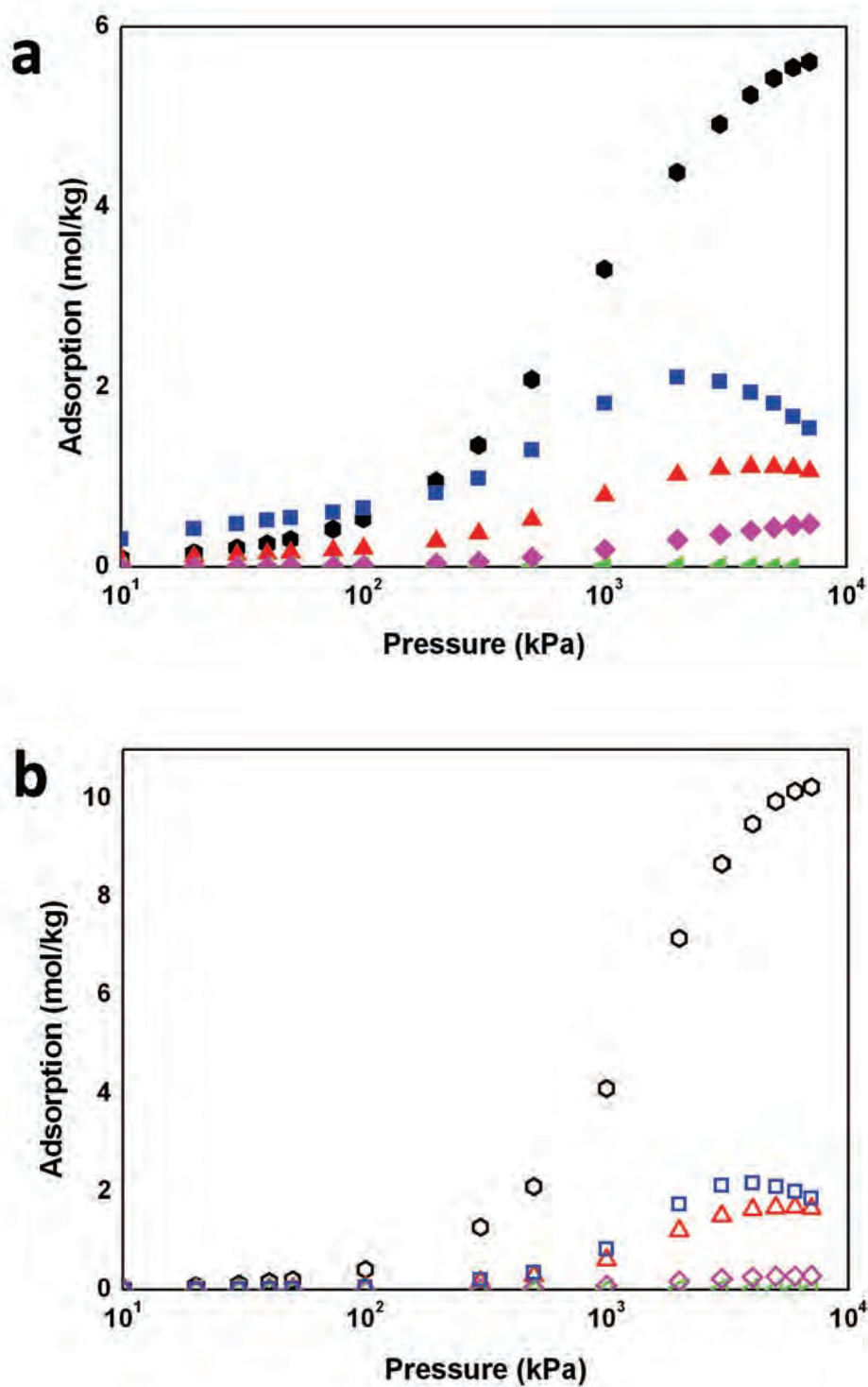
Figure 6.7. *Excess adsorption for the 95:2.0:1.0:0.5:1.5 mixture of methane (circles), ethane (triangles), N_2 (left triangles), CO_2 (rhombus) and propane (squares) in (a) Cu-BTC and (b) IRMOF-1 at 298 K.*
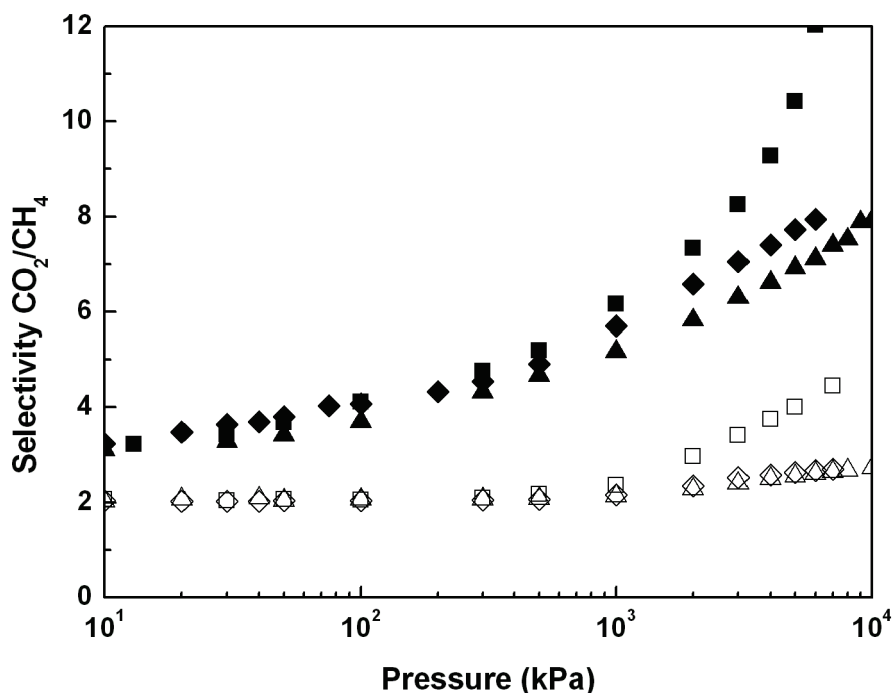
Figure 6.8. *Selectivity CO $_2$/CH $_4$ from the equimolar binary mixture (up triangles) and the 10:90 binary mixture (diamonds) compared with the selectivity CO $_2$/ CH $_4$ from the five components mixture (squares) in Cu-BTC (closed symbols) and IRMOF-1 (open symbols) at 298 K. The CO $_2$/ CH $_4$ composition ratio in the bulk for the five components mixture is 1:95.*

The analysis of the adsorption sites in Cu-BTC for this mixture shows competition for the octahedral cages. At low pressures, the order of preferential adsorption for carbon dioxide is site II > site III> site I', whereas for nitrogen is site I' > site II > site III. At the highest pressures the octahedral cages and the windows are already full increasing then the adsorption in the large cages (site I'). The sitting of CO_2 and N_2 in IRMOF-1 is similar to that for the pure components. The molecules preferentially adsorb in the large accessible cages and in the region that separates both types of cages, and most of the molecules adsorbed close to the linkers are located above and beneath the center of the phenyl ring

Adsorption of the five-component mixture.   Figure 6.7 shows the adsorption of a five-component mixture of methane, ethane, nitrogen, carbon dioxide, and propane in Cu-BTC and IRMOF-1 at the bulk partial fugacity ratio of 95:2.0:1.5:1.0:0.5. The isotherms show similar adsorption for all components but methane in both MOFs. At high pressures the amount of methane adsorbed in IRMOF-1 is larger than in Cu-BTC since the cavities of the former are larger than those of the latter. The selectivity between carbon dioxide and methane is similar to that of the corresponding binary systems as shown in Figure 6.8. Again

the carbon dioxide adsorption selectivity in Cu-BTC is much larger than in IRMOF-1, with a clearer increase with increasing pressure. This can be attributed to the combination of two effects; first, the electrostatic interactions between the carbon dioxide and the framework - that enhances CO_2 adsorption in both structures - and second, the strong confinement effects in the octahedral cages of Cu-BTC - that enhances the selectivity of carbon dioxide in this structure.

The analysis of the adsorption sites in Cu-BTC and IRMOF-1 for this mixture was further performed and shows that the molecular sitting for the mixture is similar to that observed for the pure components in both structures.

6.4. Conclusions

We have investigated the adsorption behavior of the main components of natural gas in Cu-BTC and IRMOF-1 using Monte Carlo Simulations. We computed adsorption isotherms at 298 K for pure components and mixtures, and analyzed the preferential adsorption sites on these two MOFs. The detailed study of the sitting of the molecules in both structures provided an explanation for the high adsorption capacity of IRMOF-1 and for the high adsorption selectivity towards carbon dioxide of Cu-BTC. On the basis of our observations, IRMOF-1 seems a good material for the storage of the different components of natural gas, whereas Cu-BTC could be a promising material for their separation.

7

Separation of xylene isomers in MIL-47

The separation performance of the metal-organic framework MIL-47 for xylene isomers was studied by Monte Carlo simulations in the grand-canonical ensemble. The experimental adsorption isotherms of xylene isomers in MIL-47 between 343 and 423 K were reproduced by using force fields available in the literature. Mixture isotherms were computed and compared with the mixture isotherms predicted by using pure component adsorption data and the ideal adsorption solution theory. This theory accurately predicts mixture isotherms of xylene isomers in MIL-47. The ideal adsorption solution theory was further employed to calculate the separation factors of xylene isomers in MIL-47. The order of preferential adsorption was found to be ortho > para > meta. The adsorption selectivity was found to increase with pressure, and the results showed a good agreement with the experimental data available. Henry coefficients and low coverage heats of adsorption and adsorption entropies were computed at 543 K showing an excellent agreement with experiments. It was found that the reason for adsorption selectivity is the interaction of CH_3 groups of neighboring molecules at high loadings, mainly for molecules adsorbed on the same wall of the MIL-47 channels.

7.1. Introduction

Xylene isomers are used commercially as organic solvents in the printing, rubber and leather industries[346]. Para-xylene, the isomer with the largest industrial applications, is also used for the production of polyester, as the reactant (terephthalic acid) is obtained by oxidation of para-xylene[347]. Ortho-xylene is largely used in the production of phthalic anhydride, which is an additive used in the plastic industry[348]. Meta-xylene is a precursor of isophthalic acid, which is used as a copolymer in the synthesis of polyethylene terephthalate[349]. To use the different xylene isomers for their particular industrial application, it is necessary to separate them. The separation of xylene isomers is not straightforward, as their physical properties are very similar. Ortho-xylene is the only isomer that can be separated via distillation due to their nearly identical boiling points (o-xylene: 144.5 °C; m-xylene: 139.3 °C; p-xylene: 138.5 °C at 1 atm[350]). Crystallization can be used for the separation of xylene isomers[351,352]. However, the Parex process, based on adsorption in a simulated moving bed, is more frequently used for its larger production rate, better selectivity and lower cost[353].

The Parex process has been extensively studied to increase its performance. Reactors have been modified[354,355], and simulation methods have been employed[356] to optimize its productivity. The effects of different operation parameters, such as the surrounding equipment of the bed[357], switching time[358] or the composition of the desorbents[359] have been extensively studied. The adsorbent used in this process is generally faujasite (FAU-type zeolite)[356], although other adsorbents such as cation-exchanged zeolite A (LTA-type zeolite) are also possible[360]. Other types of materials have proved to be effective in the separation of xylene isomers, such as silicalite[361,362], various polymers, and carbon materials[363,364] or hydrotropes[365]. Recently, it was reported that the metal-organic materials MIL-47 and MIL-53 have large adsorption selectivity for xylene isomers[366-370].

Metal-organic frameworks (MOFs) are crystalline porous materials, composed by metal centers linked by organic molecules[259]. In general, this type of materials have the following properties: pores ranging from a few angstroms to 2-3 nanometers, low density, large surface areas and a large potential for tailor-made design[260]. In its calcined form, MIL-47 consists of vanadium cations associated to six oxygen atoms, forming chains linked by terephthalic acid molecules. The porous structure of MIL-47 consists of 1-D, diamond-shaped straight channels (10.5 Å x 11.0 Å), where the metal centers lay at the vertices and the organic molecule on the walls of the channels. These channels are not interconnected. Framework flexibility in MIL-47 is not as important as in MIL-53[371], another MOF with the same structure as MIL-47 but with a different metal center[34].

Modeling studies of MIL-47 are scarce. The adsorption properties of linear and branched alkanes, and benzene in MIL-47 have been studied by molecular simulation[372]. The adsorption of carbon dioxide has been studied both by molecular simulation and by density functional theory calculations[323]. The self-diffusion coefficients of adsorbed molecules have only been computed for small molecules like methane[373] and hydrogen[374]. Simulation studies on the separation potential of this structure have been performed for nitrogen, methane, and carbon dioxide[375], but we have not found any simulation study on xylene separation in MIL-47. Xylene adsorption has been extensively studied by molecular simulations in faujasite[141,376,377], and to a less extent in silicalite[378].

The objective of this work is to provide molecular insight on the separation mechanism for xylene isomers that takes place in MIL-47. For this purpose we will use molecular simulations that will be compared with available experimental data. It results that we are able to reproduce the experimental pure component adsorption isotherms of xylene in MIL-47. The validity of the Ideal Adsorption Solution Theory is tested for predicting the adsorption isotherms of xylene mixtures in MIL-47. Finally, we study the arrangement of molecules in the MIL-47 pores at high loadings to understand the separation mechanism for xylene isomers that takes place in this material. The force field used in this work has been taken directly from force fields available in the literature. The remainder of this paper is organized as follows: in section 7.2 we present the simulation force fields and methods. We continue in section 7.3 with the results and discussion and in section 7.4 we present our conclusions.

7.2. Simulation details

Grand-canonical Monte Carlo (GCMC) simulations were used to compute the adsorption isotherms of xylene isomers and their mixtures at different temperatures. The Peng-Robinson equation of state[379] was used to relate pressures and fugacities or the pure components. The Lewis and Randall rule was used to calculate partial pressures of xylene mixtures in the gas phase[380]. The Configurational-bias Monte Carlo technique[47] was used to efficiently insert and delete xylene molecules in the system. Henry coefficients, energies, enthalpies, and entropies of adsorption were computed from MC simulations in the NVT ensemble. Detailed information about the methodology can be found elsewhere[97]. The MC simulations were performed in cycles and in each cycle one of the following trial moves was selected at random for each adsorbed molecule: translation, rotation, regrow at a random position, and insertion or deletion of a molecule (only for simulations in the grand-canonical ensemble). More details on the simulation

technique can be found elsewhere[45,52]. For calculating mixture isotherms, we also used trial moves that attempt to change the identity of an adsorbed molecule[94]. Xylene molecules tightly fit in the MIL-47 channels at high loadings. The acceptance probability of the insertion/deletion and identity change Monte Carlo moves is therefore small. For this reason, a large number of simulation cycles are needed both for equilibrating the system and for data production.

Xylenes were modelled using the OPLS force field for pure liquid substituted benzenes[381]. In this model, the carbon and hydrogen atoms forming part of the aromatic ring of the xylene molecules are described explicitly. The CH_3 groups are considered as single interaction centers. The interactions between xylene-xylene isomers and xylene-framework consist of Lennard-Jones and electrostatic interactions.

MIL-47 is modelled as a rigid structure. The crystal structure was obtained from the Cambridge Crystallographic Data Centre, CCDC-166785[26]. The Lennard-Jones dispersive interactions were taken from the DREIDING force field[289], except those for the vanadium atoms that were taken from the UFF force field[290]. The use of a rigid framework is rationalized by the experimental observation that the presence of xylene molecules in MIL-47 does not alter the framework structure to a large extent[366]. Rigid framework structures have been used in previous molecular simulation studies on adsorption and diffusion in MIL-47[372-375,382]. It has been shown that the influence of framework flexibility on the computed adsorption isotherm in zeolites is negligible[56]. Therefore, it is reasonable to expect a similar behavior in other porous materials which do not exhibit a manifest flexibility, as in the case of MIL-47. In the simulations, our system consisted of 16 unit cells of MIL-47 (4 x 2 x 2; a = 6.1879 Å, b = 16.1430 Å, c = 13.9390 Å). Each unit cell contains 72 atoms, of which 4 are vanadium, 20 oxygen, 16 hydrogen and 32 carbon. The carbon and oxygen atoms of the structure are classified according to their bonding environment. C_a carbon atoms are bonded to one hydrogen and other two carbon atoms. C_b carbon atoms are bonded to another three carbon atoms. C_c carbon atoms are bonded to two oxygen atoms. O_a oxygen atoms are linked to two vanadium atoms and O_b to one vanadium and one carbon atom. The framework charges of MIL-47 were taken from literature[372].

The Lennard-Jones interactions between different atoms of the system were obtained using the Lorentz-Berthelot mixing rules. The Lennard-Jones potentials are truncated and shifted at a cutoff distance of 12 Å. Coulombic interactions were computed using the Ewald summation with a relative precision of 10^{-6}. The parameters of the force field are given in Table 7.1

MIL-47			
Atom type	$\varepsilon/k_B/K$	$\sigma/\text{Å}$	q/e
V	8.05	3.144	1.68
O_a	48.19	3.03	-0.6
O_b	48.19	3.03	-0.52
C_a	47.86	3.47	-0.15
C_b	47.86	3.47	0.00
C_c	47.86	3.47	0.56
H	7.65	2.85	0.12
Xylene			
Atom type	$\varepsilon/k_B/K$	$\sigma/\text{Å}$	q/e
C	35.24	3.55	-0.115
H	15.03	2.42	0.115
CH_3	85.51	3.80	0.115

Table 7.1. *Intermolecular Lennard-Jones parameters and partial charges used in this work.*

7.3. Results and discussion

The computed Henry coefficients, and heats of adsorption and entropy of adsorption at zero loading of xylene isomers in MIL-47 at 543 K are summarized in Table 7.2, together with experimental data[368]. The calculated Henry coefficients perfectly match the experimental data, having the same order of preferential adsorption (ortho>para>metha). The adsorption enthalpy of the xylene isomers in MIL-47 is identical within a deviation of less than 1%, revealing that the different isomers interact in a very similar way with the framework pores. The differences in adsorption entropy, although larger, are still too small to raise a definitive conclusion on the influence of steric effects in the adsorption. Nonetheless, the molecules with the lowest entropy of adsorption (in absolute value), and larger Henry coefficients, are the most preferentially adsorbed.

Molecule	K_H (mol/kg/Pa)	Exp.	$-\Delta H$ (kJ/mol)	Exp.	$-\Delta S$ (J/mol/K)
Ortho	$2.70 \cdot 10^{-4}$ (3)	$2.9 \cdot 10^{-4}$	57.70 (4)	59.6 (7)	38.9 (2)
Meta	$1.89 \cdot 10^{-4}$ (2)	$2.1 \cdot 10^{-4}$	57.28 (5)	59.7 (7)	41.1 (2)
Para	$2.31 \cdot 10^{-4}$ (1)	$2.2 \cdot 10^{-4}$	57.70 (2)	61.2 (4)	40.2 (1)

Table 7.2. *Henry coefficients and heats of adsorption and entropies of adsorption at zero loading of xylene isomers in MIL-47 at 543 K. The values between parentheses are the error in the last digit. Experimental values are also given for comparison* [368].
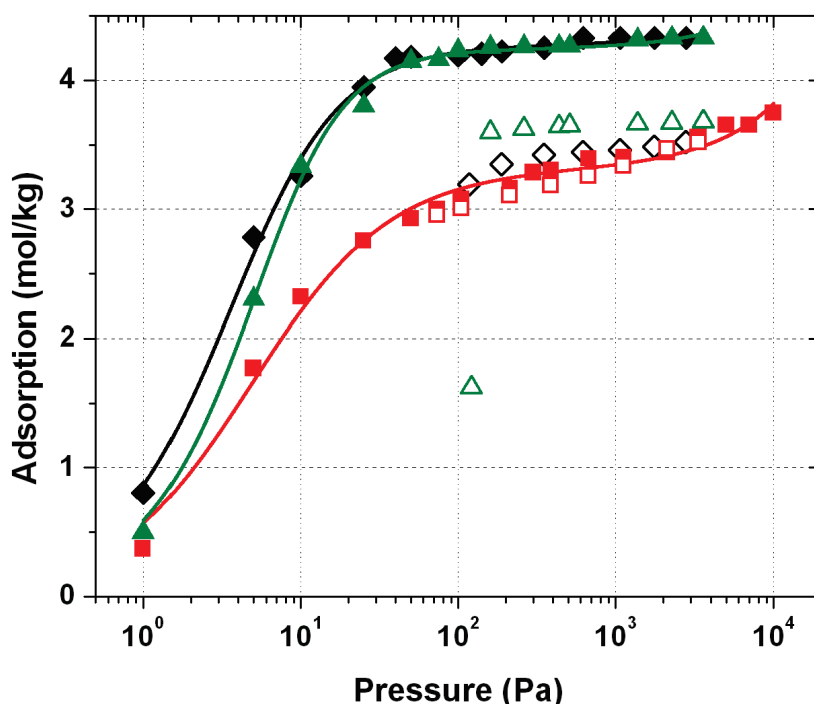

Figure 7.1. *Adsorption isotherms of xylene in MIL-47 at 343 K. Closed symbols, simulation data; open symbols, experimental data* [368]. *Diamonds, ortho-xylene; squares, meta-xylene; triangles, para-xylene. Lines, fitting of the calculated isotherms using the Jensen equation (Eq. 7.1). Error bars are within the symbol size.*

The computed adsorption isotherms of pure ortho, meta and para-xylene at 343 K, 383 K, and 423 K are shown in Figures 7.1, 7.2, and 7.3 respectively, together with available experimental data[368]. At the highest temperature, the calculated isotherm is in very good agreement with the experiment. However, at the lowest temperature (343 K) the calculated isotherm overestimates the loading of ortho and para-xylene, while at the higher temperatures (383 K and 423 K) the loadings of ortho-xylene and meta-xylene are underestimated at low pressures. One possible explanation for this discrepancy may be due to small changes in the framework structure with temperature. The adsorption of xylene molecules does not induce large changes the structure of MIL-47[366], although it has been shown that MIL-47 has some flexibility

upon the adsorption of guest molecules, possibly sufficient to undergo changes in its crystal simmetry[383]. The size of the rhombohedric channels of MIL-47 changes from 12.0 x 7.9 Å in the as-synthesized form to 11.0·10.5 Å after calcination[384]. It is known that ethyl-benzene and other organic molecules induce single crystal transformations in the structure[366,383]. A comparison of experimental and simulation data suggest that at low temperatures, the xylene molecules induce a small contraction of the crystallographic structure, reducing the pore size of MIL-47 and therefore its adsorption capacity. Apparently, this effect is less pronounced for meta-xylene. Note that the saturation loading reached in our simulations was 4 molecules per unit cell (4.33 mol/kg), while experimentally the maximum loading reached was 3.4 molecules per unit cell[368].
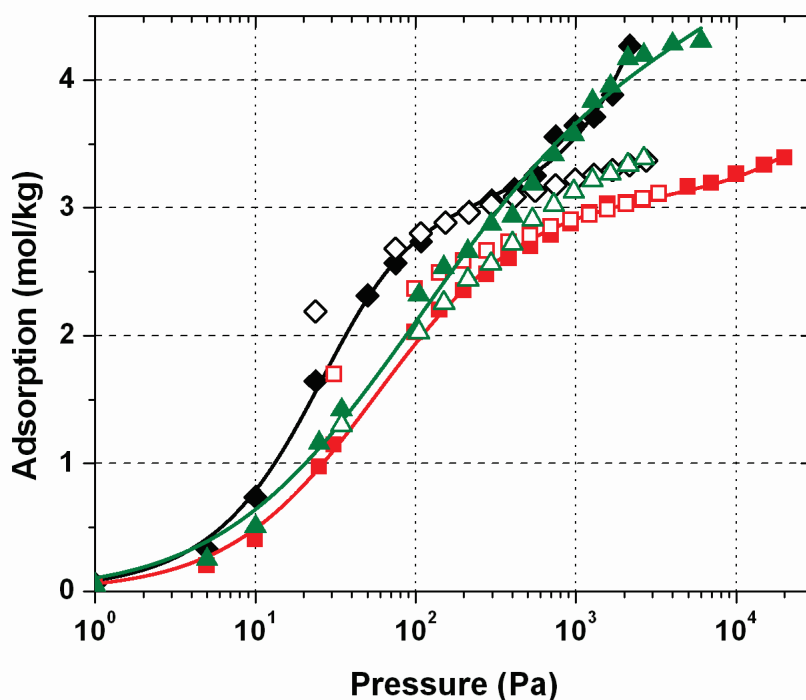

Figure 7.2. *Adsorption isotherms of xylene in MIL-47 at 383 K. Closed symbols, simulation data; open symbols, experimental data [368]. Diamonds, ortho-xylene; squares, meta-xylene; triangles, para-xylene. Lines, fitting of the calculated isotherms using the Jensen equation (Eq. 7.1). Error bars are within the symbol size.*

Figure 7.3. *Adsorption isotherms of xylene in MIL-47 at 423 K. Closed symbols, simulation data; open symbols, experimental data [368]. Diamonds, ortho-xylene; squares, meta-xylene; triangles, para-xylene. Lines, fitting of the calculated isotherms using the Jensen equation (Eq. 7.1). Error bars are within the symbol size.*
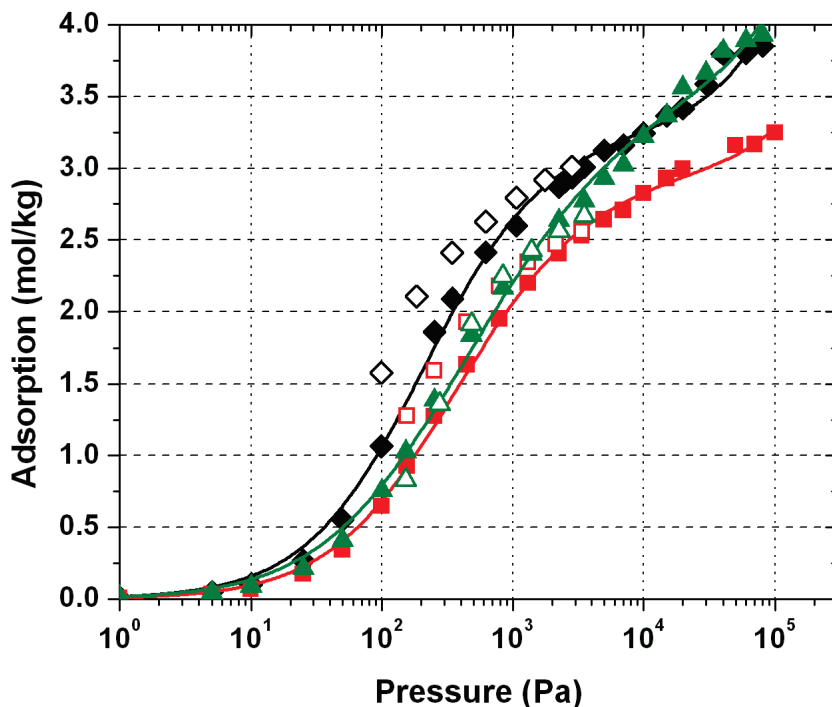
The calculated isotherms were fitted using the isotherm equation of Jensen[385], also plotted as solid lines in Figures 7.1, 7.2, and 7.3:

$$n(P) = KP\left[1 + \left(\frac{KP}{a(1+\kappa P)}\right)^{c}\right]^{1/c} \qquad (7.1)$$

The pure component isotherms are well described with the Jensen isotherm, and their fitting parameters are given in Table 7.3. Using the fit to Eq. (7.1), the Ideal Adsorption Solution Theory[386] (IAST) was used to compute mixture isotherms from the pure component isotherms. The IAST was previously used successfully for calculating the mixture adsorption of carbon dioxide, nitrogen, and methane in MIL-47[131]. The mixture isotherms obtained from IAST were compared with the computed 50/50 binary mixtures of ortho-meta, ortho-para and meta-para xylene, as well as with an equimolar, ternary mixture of ortho, meta and para xylene. These simulations were performed at 343 K, 383 K and 423 K. As an example, in Figures 7.4 and 7.5 we show 50/50 mixture isotherms of ortho and meta-xylene, and a ternary mixture of xylenes respectively at 343 K. The agreement between the IAST and the calculated mixture isotherms was found to be acceptable for every system and temperature considered in this study. The

IAST is therefore a recommendable method to calculate mixture isotherms in this system, as the computation of mixture isotherms of xylene in MIL-47 is very time consuming and subject to large error bars. This is due to the large size of the xylene molecules that leads to a very low acceptance probability of the MC identity moves. Note that experimental measurement of these mixture isotherms can be challenging too, due to slow diffusion and the similarity of the molecules adsorbed.

Our results for the selectivity are compiled in Table 7.4, calculated from the equimolar mixture isotherms obtained by the IAST. The selectivity is defined as[342]:

$$S_{AB} = \frac{x_A}{y_A} \frac{y_B}{x_B} \tag{7.2}$$

where S_{AB} is the selectivity of component A relative to component B, x_A and x_B the mole fractions of component A and B in the adsorbed phase, and y_A and y_B the mole fractions of component A and B in the gas phase. If component A is preferentially adsorbed over B, S_{AB} is larger than 1, and vice versa. As it can be seen from Figures 7.4 and 7.5, the selectivity was found to increase with pressure, reaching its maximum value at saturation loading. This increase of selectivity with pressure agrees with previous experimental results[366,368].
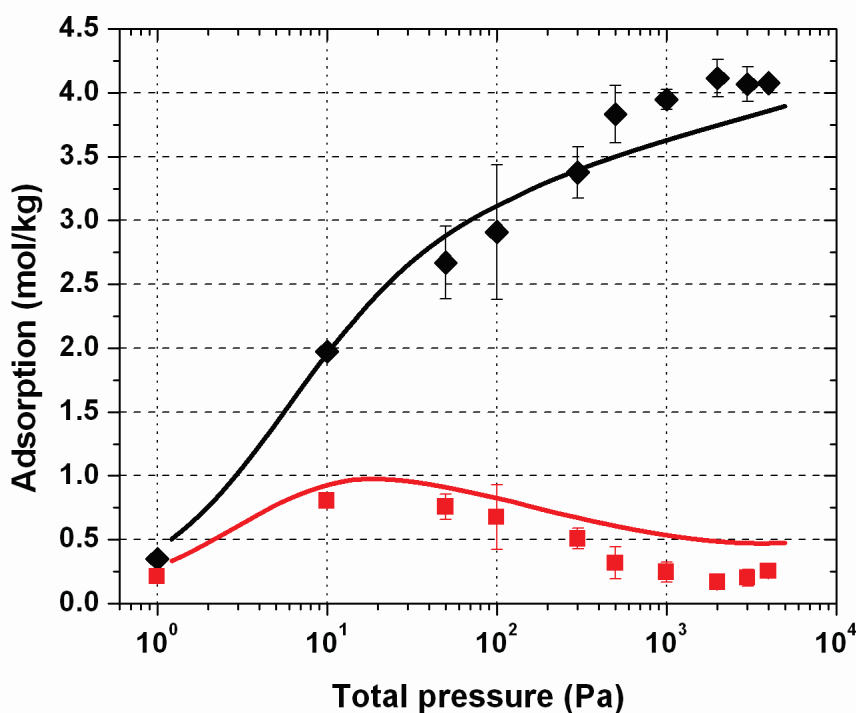

Figure 7.4. *Calculated adsorption isotherm of a 50/50 binary gas mixture of ortho and meta-xylene in MIL-47 at 343 K. Diamonds, ortho-xylene; squares, meta-xylene. Lines, mixture isotherm obtained with IAST.*

	T = 343 K			T = 383 K			T = 423 K		
	ortho	**meta**	**para**	**ortho**	**Meta**	**para**	**ortho**	**meta**	**para**
K (mol/kg/Pa)	0.954	0.700	0.606	$8.47 \cdot 10^{-2}$	$6.17 \cdot 10^{-2}$	0.133	$1.71 \cdot 10^{-2}$	$1.07 \cdot 10^{-2}$	$1.69 \cdot 10^{-2}$
a (mol/kg)	4.269	3.314	4.239	2.968	3.109	4.777	3.257	2.984	3.655
κ (Pa^{-1})	$7.53 \cdot 10^{-6}$	$1.53 \cdot 10^{-5}$	$8.09 \cdot 10^{-6}$	$2.02 \cdot 10^{-4}$	$5.23 \cdot 10^{-6}$	$4.32 \cdot 10^{-6}$	$2.87 \cdot 10^{-6}$	$1.11 \cdot 10^{-6}$	$1.84 \cdot 10^{-6}$
c (-)	1.311	0.976	1.642	1.663	0.910	0.551	0.926	0.816	0.632

Table 7.3. *Fitting parameters of the Jensen equation (Eq. 7.1) for the calculated pure component adsorption isotherms of meta, ortho and para-xylene at 343 K, 383 K, and 423 K.*

	T = 343 K				T = 383 K				T = 423 K			
Mixture	**o-m**	**o-p**	**m-p**	**o-m-p**	**o-m**	**o-p**	**m-p**	**o-m-p**	**o-m**	**o-p**	**m-p**	**o-m-p**
Component 1	o	o	p	o	o	o	p	o	o	o	p	o
Component 2	m	p	m	p	m	p	m	p	m	p	m	p
S$_{om}$	8.2 (1.17)	-	-	8.2	3.5	-	-	3.5	3.2	-	-	3.2
S$_{op}$	-	1.4 (1.01)	-	1.4	-	1.5	-	1.5	-	1.5	-	1.5
S$_{pm}$	-	-	5.7 (2.07)	6.0	-	-	3.0	2.3	-	-	1.9	2.1

Table 7.4. *Adsorption selectivities of xylene mixtures in MIL-47 at 343 K, 383 K and 423 K. Selectivities were calculated from Eq. (7.2) using the equimolar IAST mixture isotherms. The mole fraction of the components adsorbed was calculated from the adsorption at the largest pressure reached by the isotherm. o = ortho-xylene; m = meta-xylene; p = para-xylene. Component 1 is the preferentially adsorbed isomer in the mixture, Component 2 the second. Experimental values obtained from breakthrough experiments are included between parentheses for comparison [368].*

The preferential order of adsorption is ortho, para and meta-xylene. This order is in agreement the computed Henry coefficients (Table 7.2) and with experimental selectivities obtained from batch adsorption, breakthrough curves, and zero coverage loading[366,368]. At the temperatures considered here, the selectivities obtained at high loading are always significantly larger than the ones computed from the Henry coefficients. This indicates that the adsorption selectivity of xylene is caused by packing effects. Interestingly, the experimental para-meta selectivity is either larger or smaller than the ortho-meta depending on the method used to measure it[366,368]. In our study, the ortho-meta selectivity is always larger than the para-meta selectivity. The same result is obtained experimentally when the selectivity is estimated using zero coverage adsorption[368]. We speculate that this difference may be due to diffusion limitations in the experiments. The different selectivities increase with decreasing temperature, except for the ortho-para mixture that keeps constant. For the equimolar ternary mixture, the calculated selectivities are the same as for the binary mixture. Only in the case of the para-meta selectivity there is a small change in selectivity with respect to the binary mixture. The order of magnitude of the selectivities obtained is consistent with the experimental data available[366,368].
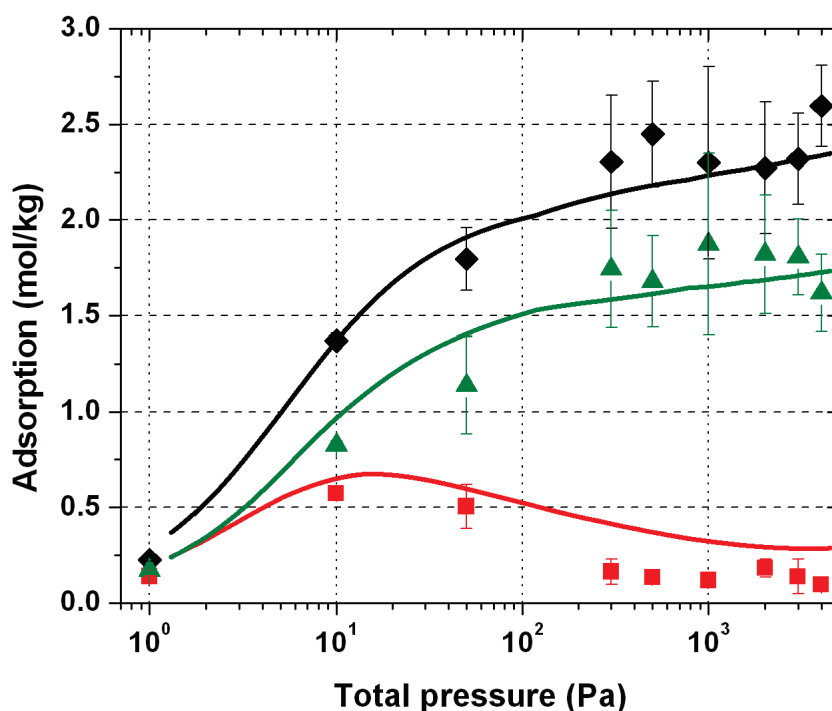

Figure 7.5. *Calculated adsorption isotherm of an equimolar ternary gas mixture of ortho, meta and para-xylene in MIL-47 at 343 K. Diamonds, ortho-xylene; squares, meta-xylene; triangles, para-xylene. Lines, mixture isotherm obtained with IAST.*

The selectivity of xylene isomers in MIL-47 has been attributed to packing effects[366,368]. At high loadings it has been speculated that molecules are adsorbed by pairs, their benzene rings facing each other and approximately parallel to the aromatic rings of the terephthalic acid in the framework. The spatial arrangement of the CH_3 groups of every xylene opposing pair has been presented as the determining factor for preferential adsorption[366,368].

In Figure 7.6 we show snapshots of xylene molecules adsorbed in a MIL-47 channel along the **a** crystallographic direction. The snapshots were obtained from molecular simulations of pure component adsorption at high loading and 423 K. At these conditions, the benzene rings of the xylene molecules are approximately parallel to the aromatic rings of the framework structure. However, at lower loadings we find that the molecules have random orientations in the channel. Similar results were obtained for benzene molecules adsorbed in MIL-47[372]. The difference with the interpretation of the experimental X-ray diffraction data is that at high loading the molecules are not adsorbed by pairs in the channel facing their aromatic rings. This configuration is not energetically favorable due to the electrostatic repulsion between the carbon and hydrogen atoms of facing aromatic rings. In our simulations, xylene molecules do not face the aromatic ring of other guest molecules on the opposite wall of the channel (face-face configuration), but instead the void spaces between them (face-side configuration, see Figure 7.6). This latter arrangement causes that the distances between carbon atoms of one xylene molecule and the hydrogen atoms of the opposite xylene molecules in the channel are minimal, decreasing the electrostatic interaction energy. These two configurations have been previously reported for benzene dimmers, the face-side configuration having lower energy[387]. In simulations of xylene in MIL-47 at low pressures we have also found T configurations, which is the lowest energy configuration for the benzene dimer[387], as well as face-face configurations. The differences between the experimental and the simulation results may be due to the different temperature used in the experimental and simulation studies. The X-ray diffraction data was obtained at ambient temperature, while the lowest temperature studied by simulations was 343 K. It has been previously suggested that the molecular packing is slightly different at room temperature and at temperatures larger than 383 K[368].

At high loading, the aromatic rings of the ortho-xylene molecules adsorbed close to the same channel wall have the same orientation. The angle between the aromatic rings of ortho-xylene and the channel wall is around 25 degrees (Figure 7.6). Ortho-xylene molecules adsorbed on opposite channel walls are close to a T arrangement. This arrangement increases the packing efficiency and reduces the interaction energy between adsorbed xylene molecules. Para-xylene molecules adsorbed on the same channel have the same orientation of their CH_3 groups. Therefore, the packing efficiency of para-xylene is caused by the

arrangement of the CH_3 groups of the xylene molecules adsorbed on the same face of the channel, and to a less extent by the arrangement on the opposite channel wall. In the case of meta-xylene, the disposition of the CH_3 groups of neighbouring molecules does not allow neither a favourable arrangement of the CH_3 groups, nor a T configuration of their aromatic rings. Therefore, the distance between meta-xylene molecules is larger than for the other two isomers and the saturation loading is only reached at higher pressures. This is in agreement with the computed pure component isotherms. We did not distinguish any appreciable different arrangement of molecules at different temperatures, as it was previously suggested[368].

7.4. Conclusions

Both experiments and molecular simulations show a large adsorption selectivity of xylene isomers in MIL-47. Our simulations show that this selectivity is due to differences in the packing of xylene isomers. The Ideal Adsorption Solution Theory is a valuable tool to model the mixture adsorption of xylene isomers in MIL-47. The selectivity factors obtained at low temperatures are larger than the experimental ones (Table 7.4). This may suggest that the experimental selectivity of xylenes in MIL-47 can still be improved. In our simulations we use pure crystals, while real MIL-47 crystals may contain defects that may reduce their separation efficiency. In addition, the saturation loading found in the simulations might be difficult to achieve experimentally.
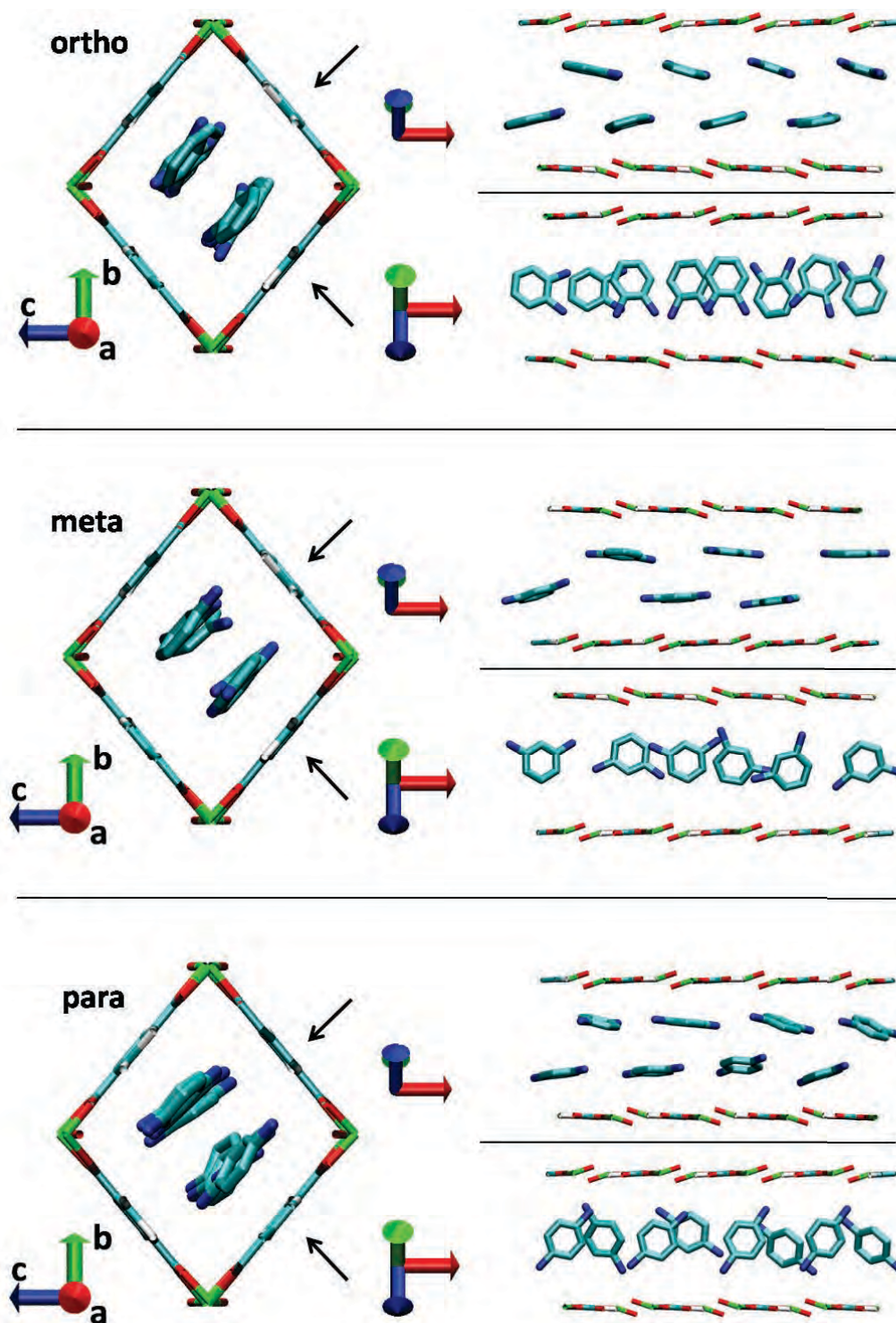
Figure 7.6. *Snapshots of xylene molecules adsorbed in a single channel of MIL-47 at high loading (4 molecules per unit cell for ortho and para, and 3.5 molecules per unit cell for meta) and 343 K, obtained from molecular simulations. For the xylene molecules, the CH3 groups are colored in dark blue, and their hydrogen atoms removed. On the right we show side views of the framework with part of the atoms removed for clarity. The orientation of the side views is indicated by the black arrows.*
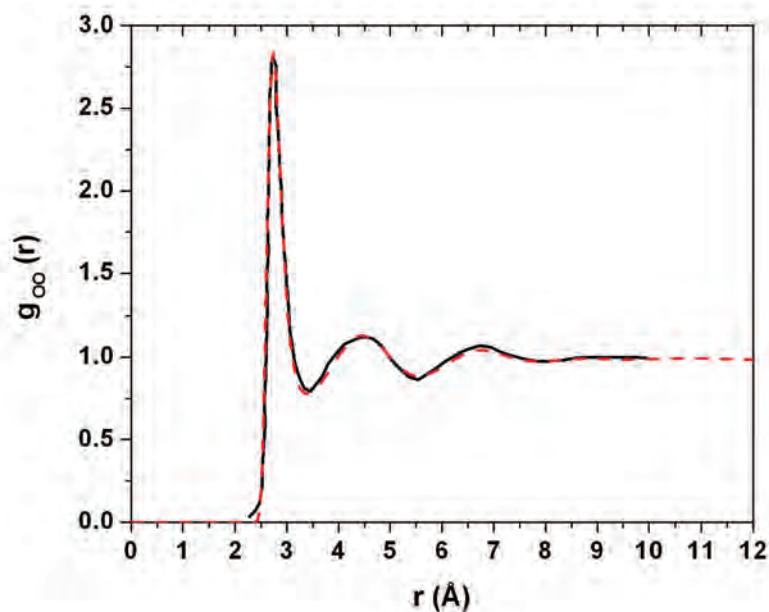
Appendix

Figure A. *Oxygen-oxygen radial distribution function of liquid water at T = 298 K and P = 1 atm, $g_{oo}(r)$, comparing the Tip5pEw potential simulation results (dashed line) with x-ray experimental data (solid line)* [388].
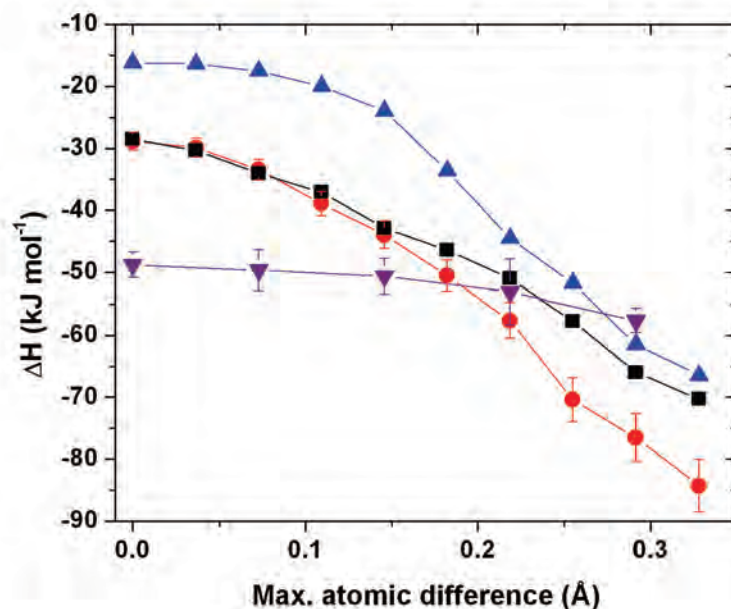

Figure B. *Calculated heats of adsorption for water in test structures of pure siliceous MFI (squares), DDR (circles), LTA (triangles), and the MOF Cu-BTC (triangles down) at 298 K. The maximum difference between the atom positions of the original and the test structures is displayed at the horizontal axis. For each structure, the atoms are progressively displaced independently along a random direction until a random maximum displacement is reached. Random directions and random maximum displacements are generated for each atom.*
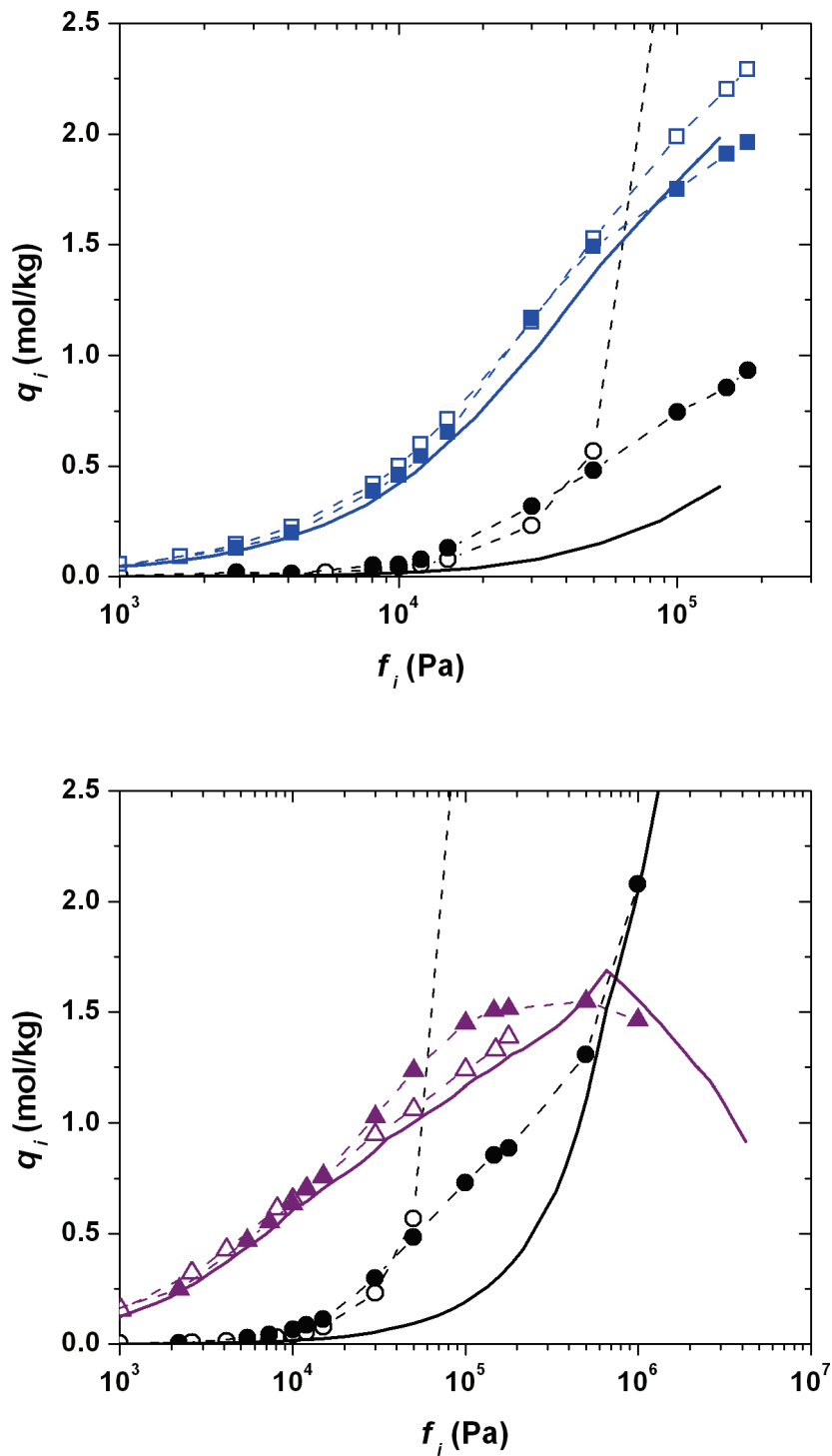
Figure C. *Ideal Adsorption Solution Theory for the adsorption of water/methanol (top) and water/ethanol (bottom) in DDR at 360 K. Water is represented by circles, methanol by squares and ethanol by triangles. Open symbols, pure component adsorption, closed symbols, mixture adsorption. Solid lines, predictions of the Ideal Adsorption Solution Theory. The IAST theory underpredicts the adsorption of water in the mixture at low fugacities.*

Bibliography

[1]   Cronstedt, A. F. *Kongl Vetenskaps Academiens Handlingar Stockholm* **1756**, 120.

[2]   Ferey, G. *Chemical Society Reviews* **2008**, *37*, 191.

[3]   *International Zeolite Association. Database of Zeolite Structures. http://www.iza-structure.org/databases.*

[4]   Tang, L. Q.; Shi, L.; Bonneau, C.; Sun, J. L.; Yue, H. J.; Ojuva, A.; Lee, B. L.; Kritikos, M.; Bell, R. G.; Bacsik, Z.; Mink, J.; Zou, X. D. *Nature Materials* **2008**, *7*, 381.

[5]   Christensen, A. N.; Jensen, T. R.; Norby, P.; Hanson, J. C. *Chemistry of Materials* **1998**, *10*, 1688.

[6]   Peterson, B. K. *Journal of Physical Chemistry B* **1999**, *103*, 3145.

[7]   Zhou, W. Z. *Journal of Materials Chemistry* **2008**, *18*, 5321.

[8]   Ramachandran, C. E.; Chempath, S.; Broadbelt, L. J.; Snurr, R. Q. *Microporous and Mesoporous Materials* **2006**, *90*, 293.

[9]   Baerlocher, C. H.; McCusker, L. B.; Olson, D. H. *Atlas of zeolite framework types*, sixth ed.; Elsevier: London, 2007.

[10]   Altshuler, G. N.; Shkurenko, G. Y. *Bulletin of the Academy of Sciences of the USSR Division of Chemical Science* **1990**, *39*, 1331.

[11]   Anerousis, J. P. *Chemical Engineering* **1976**, *83*, 128.

[12]   Watanabe, Y.; Yamada, H.; Tanaka, J.; Komatsu, Y.; Moriyoshi, Y. *Separation Science and Technology* **2004**, *39*, 2091.

[13]   Santos, J. C.; Cruz, P.; Regala, T.; Magalhaes, F. D.; Mendes, A. *Industrial & Engineering Chemistry Research* **2007**, *46*, 591.

[14]   Reut, S.; Prakash, A. *Fuel Processing Technology* **2006**, *87*, 217.

[15]   Chambellan, A.; Chevreau, T.; Khabtou, S.; Marzin, M.; Lavalley, J. C. *Zeolites* **1992**, *12*, 306.

[16]   Arruebo, M.; Falconer, J. L.; Noble, R. D. *Journal of Membrane Science* **2006**, *269*, 171.

[17]   Takagi, S. *Journal of Nuclear Science and Technology* **1978**, *15*, 213.

[18]   Komaromine, M. K.; Loksa, G.; Csereklye, K. E.; Bardoczyne, E. S.; Kallai, S. *Cereal Research Communications* **2008**, *36*, 1783.

[19]   Shoho, S. K. K. *Patent Number: JP63269934-A* **1988**.

[20]   Tsengas, S. *Patent Number: US7089882-B1* **2006**.

[21]   Dawoud, B.; Amer, E. H.; Gross, D. M. *International Journal of Energy Research* **2007**, *31*, 135.

[22]   Fragoulis, D.; Chaniotakis, E.; Stamatakis, M. G. *Cement and Concrete Research* **1997**, *27*, 889.

[23]   Hoskings, B. F.; Robson, R. *Journal of the American Chemical Society* **1989**, *111*, 5962.

[24]   Hoskings, B. F.; Robson, R. *Journal of the American Chemical Society* **1990**, *112*, 1546.

[25]   Kremer, C.; Torres, J.; Domínguez, S. *Journal of Molecular Structure* **2008**, *879*, 130.

[26]   Cambridge crystallographic database; Cambridge Crystallographic Data Centre. http://www.ccdc.cam.ac.uk/.

[27]   Barea, E.; Navarro, J. A. R.; Salas, J. M.; Masciocchi, N.; Galli, S.; Sironi, A. *Polyhedron* **2003**, *22*, 3051.

[28]   Ferey, G.; Serre, C.; Mellot-Draznieks, C.; Millange, F.; Surble, S.; Dutour, J.; Margiolaki, I. *Angewandte Chemie-International Edition* **2004**, *43*, 6296.

[29]   Ghosh, S. K.; Ribas, J.; Bharadwaj, P. K. *Crystal Growth & Design* **2005**, *5*, 623.

[30]   Greathouse, J. A.; Allendorf, M. D. *Journal of the American Chemical Society* **2006**, *128*, 10678.

[31]   Subramanian, S.; Zaworotko, M. J. *Angewandte Chemie-International Edition* **1995**, *34*, 2127.

[32]   Greathouse, J. A.; Allendorf, M. D. *Journal of the American Chemical Society* **2006**, *128*, 13312.

[33]   Szeto, K. C.; Prestipino, C.; Lamberti, C.; Zecchina, A.; Bordiga, S.; Bjorgen, M.; Tilset, M.; Lillerund, K. P. *Chemistry of Materials* **2007**, *19*, 211.

[34]   Serre, C.; Millange, F.; Thouvenot, C.; Nogues, M.; Marsolier, G.; Louer, D.; Ferey, G. *Journal of the American Chemical Society* **2002**, *124*, 13519.

[35]   Li, H.; Eddaoudi, M.; O'Keeffe, M.; Yaghi, O. M. *Nature* **1999**, *402*, 276.

[36]   Chui, S. S. Y.; Lo, S. M. F.; Charmant, J. P. H.; Orpen, A. G.; Williams, I. D. *Science* **1999**, *283*, 1148.

[37]   Martín-Calvo, A.; García-Pérez, E.; Castillo, J. M.; Calero, S. *Physical Chemistry Chemical Physics* **2008**, *10*, 7085.

[38]   Mueller, U.; Schubert, M.; Teich, F.; Puetter, H.; Schierle-Arndt, K.; Pastre, J. *Journal of Materials Chemistry* **2005**, *16*, 626.

[39]   Xiao, B.; Wheatley, P. S.; Zhao, X. B.; Fletcher, A. J.; Fox, S.; Rossi, A. G.; Megson, I. L.; Bordiga, S.; Regli, L.; Thomas, K. M.; Morris, R. E. *Journal of the American Chemical Society* **2007**, *129*, 1203.

[40]   Sigma-Aldrich. http://www.sigmaaldrich.com/sigma-aldrich/home.html.

[41]   Weiner, P. K.; Kollman, P. A. *Journal of Computational Chemistry* **1981**, *2*, 287.

[42]   Weiner, P. K.; Tainer, J. A.; Getzoff, E. D.; Kollman, P. A. *Abstracts of papers of the American Chemical Society* **1984**, *188*, 32.

[43]   Brooks, B. R.; Bruccoleri, R. E.; Olafson, B. D.; States, D. J.; Swaminathan, S.; Karplus, M. *Journal of Computational Chemistry* **1983**, *4*, 187.

[44]   Dauber-Osguthorpe, P.; Roberts, V. A.; Osguthorpe, D. J.; Wolff, J.; Genest, M.; Hagler, A. T. *Proteins: Structure, Function and Genetics* **1988**, *1998*, 31.

[45]   Calero, S.; Dubbeldam, D.; Krishna, R.; Smit, B.; Vlugt, T. J. H.; Denayer, J. F. M.; Martens, J. A.; Maesen, T. L. M. *Journal of the American Chemical Society* **2004**, *126*, 11377.

[46]   Allen, M. P.; Tildesley, D. J. *Computer Simulations of Liquids*; Clarendon Press: Oxford, 1987.

[47]   Frenkel, D.; Smit, B. *Understanding Molecular Simulation, 2nd ed.*; Academic Press: London, 2002.

[48]   Bourrelli, S.; Llewellyn, P. L.; Serre, C.; Millange, F.; Loiseau, T.; Ferey, G. *Journal of the American Chemical Society* **2005**, *127*, 13519.

[49]   Salles, F.; Ghoufi, A.; Maurin, G.; Bell, R. G.; Mellot-Draznieks, C.; Ferey, G. *Angewandte Chemie-International Edition* **2008**, *47*, 8487.

[50]   Atkins, P. W. *Physical chemistry*, sixth ed.; Oxford University Press: New York, 1998.

[51]   Smit, B. *Journal of Physical Chemistry* **1995**, *99*, 5597.

[52]   Vlugt, T. J. H.; Krishna, R.; Smit, B. *Journal of Physical Chemistry B* **1999**, *103*, 1102.

[53]   Bezus, A. G.; Kiselev, A. V.; Lopatkin, A. A.; Du, P. Q. *Journal of the Chemical Society-Faraday Transactions Ii* **1978**, *74*, 367.

[54]   Kiselev, A. V.; Lopatkin, A. A.; Shulga, A. A. *Zeolites* **1985**, *5*, 261.

[55]   Zimmermann, N. E. R.; Jakobtorweihen, S.; Beerdsen, E.; Smit, B.; Keil, F. J. *Journal of Physical Chemistry C* **2007**, *111*, 17370.

[56]   Vlugt, T. J. H.; Schenk, M. *Journal of Physical Chemistry B* **2002**, *106*, 12757.

[57]   Dubbeldam, D.; Walton, K. S.; Ellis, D. E.; Snurr, R. Q. *Angewandte Chemie-International Edition* **2007**, *46*, 4496.

[58]   Nicholas, J. B.; Hopfinger, A. J.; Trouw, F. R.; Iton, L. E. *Journal of the American Chemical Society* **1991**, *113*, 4792.

[59]   Guillot, B. *Journal of Molecular Liquids* **2002**, *101*, 219.

[60]   Mahoney, M. W.; Jorgensen, W. L. *Journal of Chemical Physics* **2000**, *112*, 8910.

[61]   Stern, H. A.; Rittner, F.; Berne, B. J.; Friesner, R. A. *Journal of Chemical Physics* **2001**, *115*, 2237.

[62]   Bukowski, R.; Szalewicz, K.; Groenenboom, G. C.; van der Avoird, A. *Science* **2007**, *315*, 1249.

[63]   Berendsen, H. J. C.; Postma, J. P. M.; van Gunsteren, W. F.; Hermans, J. *J. In Intermolecular Forces*; Dordrecht, 1981.

[64]   Berendsen, H. J. C.; Grigera, J. R.; Straatsma, T. P. *Journal of Physical Chemistry* **1987**, *91*, 6269.

[65]   Wu, Y. J.; Tepper, H. L.; Voth, G. A. *Journal of Chemical Physics* **2006**, *124*.

[66]   Jorgensen, W. L.; Chandrasekhar, J.; Madura, J. D.; Impey, R. W.; Klein, M. L. *Journal of Chemical Physics* **1983**, *79*, 926.

[67]   Levitt, M.; Hirshberg, M.; Sharon, R.; Laidig, K. E.; Daggett, V. *Journal of Physical Chemistry B* **1997**, *101*, 5051.

[68]   Jorgensen, W. L.; Madura, J. D. *Molecular Physics* **1985**, *56*, 1381.

[69]   Horn, H. W.; Swope, W. C.; Pitera, J. W.; Madura, J. D.; Dick, T. J.; Hura, G. L.; Head-Gordon, T. *Journal of Chemical Physics* **2004**, *120*, 9665.

[70]   Rick, S. W. *Journal of Chemical Physics* **2001**, *114*, 2276.

[71]   Abascal, J. L. F.; Sanz, E.; Fernández, R. G.; Vega, C. *Journal of Chemical Physics* **2005**, *122*, 234511.

[72]   Abascal, J. L. F.; Vega, C. *Journal of Chemical Physics* **2005**, *123*, 234505.

[73]   Stillinger, F. H.; Rahman, A. *Journal of Chemical Physics* **1974**, *60*, 1545.

[74]   Rick, S. *Journal of Chemical Physics* **2004**, *120*, 6085.

[75]   Martin, M. G.; Siepmann, J. I. *Journal of Physical Chemistry B* **1998**, *102*, 2569.

[76]   Martin, M. G.; Siepmann, J. I. *Journal of Physical Chemistry B* **1999**, *103*, 4508.

[77]   Jorgensen, W. L.; Madura, J. D.; Swenson, C. J. *Journal of the American Chemical Society* **1984**, *106*, 6638.

[78]   Harris, J. G.; Yung, K. H. *Journal of Physical Chemistry* **1995**, *99*, 12021.

[79]   Etters, R. D.; Kuchta, B. *Journal of Chemical Physics* **1989**, *90*, 4537.

[80]   Pathria, R. K. *Statistical Mechanics*, Second ed.; Butterworth-Heinemann: Oxford, 1996; Vol. 1.

[81]   Metropolis, N.; Rosenbluth, A. W.; Rosenbluth, M. N.; Teller, A. H.; Teller, E. *Journal of Chemical Physics* **1953**, *21*, 1087.

[82]   Landau, D. P.; Binder, K. *A guide to Monte Carlo simulations in statistical physics*; Cambridge University Press: New York, 2002.

[83]   Norman, G. E.; Filinov, V. S. *High Temperature* **1969**, *7*, 216.

[84]   Siepmann, J. I.; Frenkel, D. *Molecular Physics* **1992**, *75*, 59.

[85]   Frenkel, D.; Mooij, G. C. A. M.; Smit, B. *Journal of Physics - Condensed Matter* **1992**, *4*, 3053.

[86]   de Pablo, J. J.; Laso, M.; Suter, U. W. *Journal of Chemical Physics* **1992**, *96*, 6157.

[87]   Siepmann, J. I. *Computer simulation of biomolecular systems: theoretical and experimental applications*; Escom Science Publisher: Leiden, 1993.

[88]   Valderrama, J. O.; Vargas, D. A. *Applied Thermal Engineering* **2003**, *23*, 1417.

[89]   Wagner, W.; Pruss, A. *Journal of Physical and Chemical Reference Data* **2002**, *31*, 387.

[90]   Martin, M. G.; Frischknecht, A. L. *Molecular Physics* **2006**, *104*, 2439.

[91]   Dodd, L. R.; Boone, T. D.; Theodoru, D. N. *Molecular Physics* **1993**, *78*, 961.

[92]   Pant, P. V. K.; Theodoru, D. N. *Macromolecules* **1995**, *28*, 7224.

[93]   Mavrantzas, V. G.; Boone, T. D.; Zervopoulou, E.; Theodoru, D. N. *Macromolecules* **1999**, *32*, 5072.

[94]   Martin, M. G.; Siepmann, J. I. *Journal of the American Chemical Society* **1997**, *119*, 8921.

[95]   Widom, B. *Journal of Chemical Physics* **1963**, *39*, 2808.

[96]   Vlugt, T. J. H. *Molecular Simulation* **1999**, *23*, 63.

[97]   Vlugt, T. J. H.; García-Pérez, E.; Dubbeldam, D.; Ban, S.; Calero, S. *Journal of Chemical Theory and Computation* **2008**, *4*, 1107.

[98]   Vlugt, T. J. H.; Martin, M. G.; Smit, B.; Siepmann, J. I.; Krishna, R. *Molecular Physics* **1998**, *94*, 727.

[99]   Pauli, W. *Thermodynamics and the kinetic theory of gasses*; Dover: Mineola, NY, 2000; Vol. 3.

[100]   Goldstein, H.; Poole, C. P.; Safko, J. L. *Classical Mechanics*, third ed.; Addison Wesley: Menlo Park, CA, 2001.

[101]   Martyna, G. J.; Tuckerman, M. E.; Tobias, D. J.; Klein, M. L. *Molecular Physics* **1996**, *87*, 1117.

[102]   Andersen, H. C. *Journal of Computational Chemistry* **1983**, *52*, 24.

[103]   Nose, S. *Molecular Physics* **1984**, *52*, 255.

[104]   Nose, S. *Journal of Chemical Physics* **1984**, *81*, 511.

[105]   Hoover, W. G. *Physical Review A* **1986**, *34*, 2499.

[106]   Krishna, R. *Journal of Physical Chemistry C* **2009**, *113*, 19756.

[107]   Lau, K. F.; Alper, H. E.; Thacher, T. S.; Stouch, T. R. *Journal of Physical Chemistry* **1994**, *98*, 8785.

[108]   Patra, M.; Karttunen, M.; Hyvonen, M. T.; Falck, E.; Lindqvist, P.; Vattulainen, I. *Biophysics Journal* **2003**, *84*, 3636.

[109]   Patra, M.; Karttunen, M.; Hyvonen, M. T.; Falck, E.; Vattulainen, I. *Journal of Physical Chemistry B* **2004**, *108*, 4485.

[110]   Steinbach, P. J.; Brooks, B. R. *Journal of Computational Chemistry* **1994**, *15*, 667.

[111]   Ewald, P. P. *Annalen der Physik* **1921**, *64*, 253.

[112]   Fennell, C. J.; Gezelter, J. D. *Journal of Chemical Physics* **2006**, *124*.

[113]   Wolf, D.; Keblinski, P.; Phillpot, S. R.; Eggebrecht, J. *Journal of Chemical Physics* **1999**, *110*, 8254.

[114]   Neumann, M. *Molecular Physics* **1983**, *50*, 841.

[115]   Guisnet, M.; Gilson, J.-P. *Zeolites for cleaner technologies*; Imperial College Press: New York, 2002; Vol. 3.

[116]   Kusic, H.; Bozic, A. L.; Koprivanac, N.; Papic, S. *Dyes and Pigments* **2007**, *74*, 388.

[117]   Rajakovic, V.; Aleksic, G.; Radetic, M.; Rajakovic, L. *Journal of Hazardous Materials* **2007**, *143*, 494.

[118]   Gunay, A.; Arslankaya, E.; Tosun, I. *Journal of Hazardous Materials* **2007**, *146*, 362.

[119]   Hornig, G.; Northcott, K.; Snape, I.; Stevens, G. *Cold Regions Science and Technology* **2008**, *53*, 83.

[120]   Kuleyin, A. *Journal of Hazardous Materials* **2007**, *144*, 307.

[121]   Zadaka, D.; Mishael, Y. G.; Polubesova, T.; Serban, C.; Nir, S. *Applied Clay Science* **2007**, *36*, 174.

[122]   Soyer, E.; Erdim, E.; Tasiyici, S.; Koyuncu, I. *Desalination and Water Treatment* **2009**, *9*, 201.

[123]   Janchen, J.; Bish, D. L.; Mohlmann, D. T. F.; Stach, H. *Icarus* **2006**, *180*, 353.

[124]   Bjorklund, R. B.; Hedlund, J.; Sterte, J.; Arwin, H. *Journal of Physical Chemistry B* **1998**, *102*, 2245.

[125]   Olson, D. H.; Haag, W. O.; Borghard, W. S. *Microporous and Mesoporous Materials* **2000**, *35-6*, 435.

[126]   Kuznetsov, B. V.; Rakhmanova, T. A. *Russian Journal of Physical Chemistry* **2001**, *75*, 933.

[127]   Oumi, Y.; Miyajima, A.; Miyamoto, J.; Sano, T. Binary mixture adsorption of water and ethanol on silicalite. In *Impact of Zeolites and Other Porous Materials on the New Technologies at the Beginning of the New Millennium, Pts a and B*, 2002; Vol. 142; pp 1595.

[128]   Soulard, M.; Patarin, J.; Eroshenko, V.; Regis, R. C. In Proceedings of the 14th International Zeolite Conference, 2004, Cape Town.

[129]   Ball, P. *Nature* **2008**, *452*, 291.

[130]   Kivelson, D.; Tarjus, G. *Journal of Physical Chemistry B* **2001**, *105*, 6620.

[131]   Liu, B.; Smit, B.; Rey, F.; Valencia, S.; Calero, S. *Journal of Physical Chemistry C* **2008**, *112*, 2492.

[132]   García-Pérez, E.; Parra, J. B.; Ania, C. O.; García-Sánchez, A.; van Baten, J. M.; Krishna, R.; Dubbeldam, D.; Calero, S. *Adsorption-Journal of the International Adsorption Society* **2007**, *13*, 469.

[133]   García-Pérez, E.; Torrens, I. M.; Lago, S.; Dubbeldam, D.; Vlugt, T. J. H.; Maesen, T. L. M.; Smit, B.; Krishna, R.; Calero, S. *Applied Surface Science* **2005**, *252*, 716.

[134]   Desbiens, N.; Boutin, A.; Demachy, I. *Journal of Physical Chemistry B* **2005**, *109*, 24071.

[135]   Puibasset, J.; Pellenq, R. J. M. *Journal of Physical Chemistry B* **2008**, *112*, 6390.

[136]   Liem, S. Y.; Popelier, P. L. A.; Leslie, M. *International Journal of Quantum Chemistry* **2004**, *99*, 685.

[137]   Fanourgakis, G. S.; Xantheas, S. S. *Journal of Physical Chemistry A* **2006**, *110*, 4100.

[138]   Paricaud, P.; Predota, M.; Chialvo, A. A.; Cummings, P. T. *Journal of Chemical Physics* **2005**, *122*, Article number 244511.

[139]   Bizjak, A.; Urbi, T.; Vlachy, V.; Dill, K. A. *Acta Chimica Slovenica* **2007**, *54*, 532.

[140]   Tanaka, H. *Journal of Chemical Physics* **2000**, *112*, 799.

[141]   Beauvais, C.; Boutin, A.; Fuchs, A. H. *Adsorption-Journal of the International Adsorption Society* **2005**, *11*, 279.

[142]   Di Lella, A.; Desbiens, N.; Boutin, A.; Demachy, I.; Ungerer, P.; Bellat, J. P.; Fuchs, A. H. *Physical Chemistry Chemical Physics* **2006**, *8*, 5396.

[143]   Trzpit, M.; Soulard, M.; Patarin, J.; Desbiens, N.; Cailliez, F.; Boutin, A.; Demachy, I.; Fuchs, A. H. *Langmuir* **2007**, *23*, 10131.

[144]   Wang, H. J.; Xi, X. K.; Kleinhammes, A.; Wu, Y. *Science* **2008**, *322*, 80.

[145]   Cailliez, F.; Stirnemann, G.; Boutin, A.; Demachy, I.; Fuchs, A. H. *Journal of Physical Chemistry C* **2008**, *112*, 10435.

[146]   Desbiens, N.; Demachy, I.; Fuchs, A. H.; Kirsch-Rodeschini, H.; Soulard, M.; Patarin, J. *Angewandte Chemie-International Edition* **2005**, *44*, 5310.

[147] Pellenq, R. J. M.; Roussel, T.; Puibasset, J. *Adsorption-Journal of the International Adsorption Society* **2008**, *14*, 733.

[148] Halasz, I.; Kim, S.; Marcus, B. *Molecular Physics* **2002**, *100*, 3123.

[149] Yang, J. Z.; Chen, Y.; Zhu, A. M.; Liu, Q. L.; Wu, J. Y. *Journal of Membrane Science* **2008**, *318*, 327.

[150] Boulougouris, G. C.; Economou, I. G.; Theodorou, D. N. *Journal of Physical Chemistry B* **1998**, *102*, 1029.

[151] Guillot, B.; Guissani, Y. *Journal of Chemical Physics* **2001**, *114*, 6720.

[152] Jorgensen, W. L. *Journal of Chemical Physics* **1982**, *77*, 4156.

[153] Jaramillo, E.; Chandross, M. *Journal of Physical Chemistry B* **2004**, *108*, 20155.

[154] Ockwig, N. W.; Cygan, R. T.; Criscenti, L. J.; Nenoff, T. M. *Physical Chemistry Chemical Physics* **2008**, *10*, 800.

[155] *NIST Chemistry Webbook (http://webbook.nist.gov/chemistry).*

[156] Myers, A. L.; Monson, P. A. *Langmuir* **2002**, *18*, 10261.

[157] Martyna, G. J.; Klein, M. L.; Tuckerman, M. *Journal of Chemical Physics* **1992**, *97*, 2635.

[158] Dubbeldam, D.; Calero, S.; Vlugt, T. J. H.; Krishna, R.; Maesen, T. L. M.; Beerdsen, E.; Smit, B. *Physical Review Letters* **2004**, *93*, Article number 088302.

[159] Bougeard, D.; Smirnov, K. S. *Physical Chemistry Chemical Physics* **2007**, *9*, 226.

[160] Price, D. J.; Brooks, C. L. *Journal of Chemical Physics* **2004**, *121*, 10096.

[161] Lamoureux, G.; MacKerell, A. D.; Roux, B. *Journal of Chemical Physics* **2003**, *119*, 5185.

[162] Hess, B.; Saint-Martin, H.; Berendsen, H. J. C. *Journal of Chemical Physics* **2002**, *116*, 9602.

[163] Moise, J. C.; Bellat, J. P.; Methivier, A. *Microporous and Mesoporous Materials* **2001**, *43*, 91.

[164] Boddenberg, B.; Rakhmatkariev, G. U.; Hufnagel, S.; Salimov, Z. *Physical Chemistry Chemical Physics* **2002**, *4*, 4172.

[165] Rychaert, J. P.; A, B. *Faraday Discussions* **1978**, 95.

[166] Dubbeldam, D.; Calero, S.; Vlugt, T. J. H.; Krishna, R.; Maesen, T. L. M.; Smit, B. *Journal of Chemical Physics B* **2004**, *108*, 12301.

[167] Pascual, P.; Ungerer, P.; Tavitian, B.; Pernot, P.; Boutin, A. *Physical Chemistry Chemical Physics* **2003**, *5*, 3684.

[168] Vega, C.; Abascal, J. L. F.; Conde, M. M.; Aragonés, J. L. *Faraday Discussions* **2008**.

[169] Coudert, F. X.; Vuilleumier, R.; Boutin, A. *Chemphyschem* **2006**, *7*, 2464.

[170] Smirnov, K. S.; Bougeard, D. *Chemical Physics* **2003**, *292*, 53.

[171] Halasz, I.; Kim, S.; Marcus, B. *Journal of Physical Chemistry B* **2001**, *105*, 10788.

[172] Olson, D. H.; Kokotailo, G. T.; Lawton, S. L.; Meier, W. M. *Journal of Physical Chemistry* **1981**, *85*, 2238.

[173] van Koningsveld, H.; Vanbekkum, H.; Jansen, J. C. *Acta Crystallographica Section B-Structural Science* **1987**, *43*, 127.

[174] Clark, L. A.; Snurr, R. Q. *Chemical Physic Letters* **1999**, *308*, 155.

[175] Eroshenko, V.; Regis, R. C.; Soulard, M.; Patarin, J. *Journal of the American Chemical Society* **2001**, *123*, 8129.

[176] Zhu, W.; Kapteijn, F.; Moulijn, J. A. *Adsorption-Journal of the International Adsorption Society* **2000**, *6*, 159.

[177] Eder, F. *Thermodynamic siting of alkane adsorption in molecular sieves*; PhD Thesis. University of Twente, The Netherlands: Enschede, 1996.

[178] Smit, B.; Maesen, T. L. M. *Nature* **1995**, *374*, 42.

[179] Nada, H.; van der Eerden, J. *Journal of Chemical Physics* **2003**, *118*, 7401.

[180] van den Bergh, J.; Zhu, W.; Gascon, J.; Moulijn, J. A.; Kapteijn, F. *Journal of Membrane Science* **2008**, *316*, 35.

[181] van den Bergh, J.; Zhu, W.; Groen, J. C.; Kapteijn, F.; Moulijn, J. A.; Yajima, K.; Nakayama, K.; Tomita, T.; Yoshida, S. Natural gas purification with a DDR zeolite membrane; permeation modelling with

Maxwell-Stefan equations. In *Studies in Surface Science and Catalysis*; Xu, R., Gao, Z., Chen, J., Yan, W., Eds.; Elsevier: Amsterdam, The Netherlands, 2007; Vol. 170A; pp 1077.

[182]   van den Bergh, J.; Zhu, W. D.; Kapteijn, F.; Moulijn, J. A.; Yajima, K.; Nakayama, K.; Tomita, T.; Yoshida, S. *Research on Chemical Intermediates* **2008**, *34*, 467.

[183]   Yajima, K.; Nakayama, K.; Niino, M.; Tomita, T.; Yoshida, S. "Dehydratation properties of DDR-type membranes"; Proceedings of the 9th International Conference on Inorganic Membranes, 2006, Lillehammer, Norway.

[184]   Kuhn, J.; Yajima, K.; Tomita, T.; Gross, J.; Kapteijn, F. *Journal of Membrane Science* **2008**, *321*, 344.

[185]   Khajavi, S.; Jansen, J. C.; Kapteijn, F. *Journal of Membrane Science* **2009**, *326*, 153.

[186]   Khajavi, S.; Kapteijn, F.; Jansen, J. C. *Journal of Membrane Science* **2007**, *299*, 63.

[187]   Morigami, Y.; Kondo, M.; Abe, J.; Kita, H.; Okamoto, K. *Separation and Purification Technology* **2001**, *25*, 251.

[188]   Caro, J.; Noack, M. *Microporous and Mesoporous Materials* **2008**, *115*, 215.

[189]   Gies, H. *Journal of Inclusion Phenomena and Macrocyclic Chemistry* **1984**, *2*, 275.

[190]   Kuhn, J.; Gascón, J.; Gross, J.; Kapteijn, F. *Microporous and Mesoporous Materials* **2009**, *120*, 12.

[191]   Stewart, A. *Patent number: GB2193202-A; GB2193202-B* **1988**.

[192]   Ernst, S.; Weitkamp, J. *Chemie Ingenieur Technik* **1991**, *63*, 748.

[193]   Zhu, W.; Kapteijn, F.; Moulijn, J. A.; Jansen, J. C. *Physical Chemistry Chemical Physics* **2000**, *2*, 1773.

[194]   Nakayama, K.; Suzuki, K.; Yoshida, M.; Yajima, K.; Tomita, T.; Kunio, N.; Kenji, S.; Manabu, Y.; Kenji, Y.; Toshihiro, T. *Patent number: WO2003024577-A1* **2003**, 1437172.

[195]   Tomita, T.; Nakayama, K.; Sakai, H. *Microporous and Mesoporous Materials* **2004**, *68*, 71.

[196]   Krishna, R.; van Baten, J. M. *Chemical Physics Letters* **2007**, *446*, 344.

[197]   Zhu, W.; Kapteijn, F.; Moulijn, J. A.; den Exter, M. C.; Jansen, J. C. *Langmuir* **2000**, *16*, 3322.

[198]   den Exter, M. J.; Jansen, J. C.; vanBekkum, H.; Zikanova, A. *Zeolites* **1997**, *19*, 353.

[199]   Krishna, R.; van Baten, J. M.; García-Pérez, E.; Calero, S. *Chemical Physics Letters* **2006**, *429*, 219.

[200]   Himeno, S.; Takenaka, M.; Shimura, S. *Molecular Simulation* **2008**, *34*, 1329.

[201]   Jakobtorweihen, S.; Hansen, N.; Keil, F. J. *Molecular Physics* **2005**, *103*, 471.

[202]   Smit, B.; Maesen, T. L. M. *Chemical Reviews* **2008**, *108*, 4125.

[203]   Demontis, P.; Stara, G.; Suffritti, G. B. *Journal of Physical Chemistry B* **2003**, *107*, 4426.

[204]   Fleys, M.; Thompson, R. W. *Journal of Chemical Theory and Computation* **2005**, *1*, 453.

[205]   Fleys, M.; Thompson, R. W.; MacDonald, J. C. *Journal of Physical Chemistry B* **2004**, *108*, 12197.

[206]   Vigner-Maeder, F.; Auroux, A. *Journal of Physical Chemistry* **1990**, *94*, 316.

[207]   Pelmenschikov, A. G.; Morosi, G.; Gamba, A.; Zecchina, A.; Bordiga, S.; Paukshtis, E. A. *Journal of Physical Chemistry* **1993**, *97*, 11979.

[208]   Hinderer, J.; Keil, F. J. *Chemical Engineering Science* **1996**, *51*, 2667.

[209]   Plant, D. F.; Maurin, G.; Bell, R. G. *Journal of Physical Chemistry B* **2007**, *111*, 2836.

[210]   Gupta, A.; Clark, L. A.; Snurr, R. Q. *Langmuir* **2000**, *16*, 3910.

[211]   Lu, L. H.; Shao, Q.; Huang, L. L.; Lu, X. H. *Fluid Phase Equilibria* **2007**, *261*, 191.

[212]   Takaba, H.; Koyama, A.; Nakao, S. *Journal of Physical Chemistry B* **2000**, *104*, 6353.

[213]   Jia, W.; Murad, S. *Molecular Physics* **2006**, *104*, 3033.

[214]   Furukawa, S.; Goda, K.; Zhang, Y.; Nitta, T. *Journal of Chemical Engineering of Japan* **2004**, *37*, 67.

[215]   Yang, J. Z.; Liu, Q. L.; Wang, H. T. *Journal of Membrane Science* **2007**, *291*, 1.

[216]   Kox, M. H. F.; Stavitski, E.; Groen, J. C.; Pérez-Ramírez, J.; Kapteijn, F.; Weckhuysen, B. M. *Chemistry-a European Journal* **2008**, *14*, 1718.

[217]   Castillo, J. M.; Dubbeldam, D.; Vlugt, T. J. H.; Smit, B.; Calero, S. *Molecular Simulation* **2009**, *35*, 1067.

[218]   Gascón, J.; Blom, W.; van Miltenburg, A.; Ferreira, A.; Berger, R.; Kapteijn, F. *Microporous and Mesoporous Materials* **2008**, *115*, 585.

[219]   Krishna, R.; Wesselingh, J. A. *Chemical Engineering Science* **1997**, *52*, 861.

[220]   Krishna, R. The Maxwell-Stefan formulation of diffusion in zeolites. In *Fluid Transport in Nanoporous Materials*; Conner, W. C., Fraissard, J., Eds., 2006; Vol. 219; pp 211.

[221] Krishna, R.; van Baten, J. M. *Chemical Engineering Science* **2009**, *64*, 3159.

[222] Krishna, R. *International Communications in Heat and Mass Transfer* **2001**, *28*, 337.

[223] Krishna, R.; Paschek, D. *Chemical Engineering Journal* **2002**, *85*, 7.

[224] Krishna, R.; van Baten, J. M. *Industrial & Engineering Chemistry Research* **2006**, *45*, 2084.

[225] Kärger, J.; Ruthven, D. M. *Diffusion in zeolites and other microporous solids*; John Wile & Sons, Inc., 1992.

[226] Kuhn, J.; Stemmer, R.; Kapteijn, F.; Kjelstrup, S.; Gross, J. *Journal of Membrane Science* **2009**, *330*, 388.

[227] Kapteijn, F.; Moulijn, J. A.; Krishna, R. *Chemical Engineering Science* **2000**, *55*, 2923.

[228] Krishna, R.; van Baten, J. M.; García-Pérez, E.; Calero, S. *Industrial & Engineering Chemistry Research* **2007**, *46*, 2974.

[229] Smith, J. M.; van Ness, H. C.; Abbott, M. M. *Introduction to chemical engineering thermodynamics*; McGraw-Hill: New York, 2001.

[230] Gmehling, J.; Onken, U. *Vapor-liquid equilibrium data collection - Aqueous-organic systems*; Dechema: Frankfurt, 1997; Vol. 1.

[231] de Bruijn, F.; Gross, J.; Olujic, Z.; Jansens, P.; Kapteijn, F. *Industrial & Engineering Chemistry Research* **2007**, *46*, 4091.

[232] Kapteijn, F.; Zhu, W.; Moulijn, J. A.; Gardner, T. Q. Zeolite membranes: modeling and application. In *Structured catalysts and reactors*; Cybulski, A., Moulijn, J. A., Eds.; CRC Taylor & Francis: Boca Raton, USA, 2006; pp 700.

[233] Bird, R. B.; Lightfoot, W. E.; Stewart, E. N. *Transport phenomena*; John Wiley & Sons, 2002.

[234] Kjelstrup, S.; Bedeaux, D. *Non-equilibrium thermodynamics of heterogeneus systems*; World Scientific Publishing: Singapore, 2008; Vol. 16.

[235] Dubbeldam, D.; Snurr, R. Q. *Molecular Simulation* **2007**, *33*, 305.

[236] Chen, B.; Potoff, J. J.; Siepmann, J. I. *Journal of Physical Chemistry B* **2001**, *105*, 3093.

[237] Chandler, D. *Journal of Chemical Physics* **1978**, *68*, 2959.

[238] Beerdsen, E.; Smit, B.; Dubbeldam, D. *Physical Review Letters* **2004**, *93*.

[239] Dubbeldam, D.; Beerdsen, E.; Vlugt, T. J. H.; Smit, B. *Journal of Chemical Physics* **2005**, *122*.

[240] Chen, H. B.; Sholl, D. S. *Langmuir* **2006**, *22*, 709.

[241] Gies, H. *Zeitschrift Fur Kristallographie* **1986**, *175*, 93.

[242] Beerdsen, E.; Dubbeldam, D.; Smit, B.; Vlugt, T. J. H.; Calero, S. *Journal of Physical Chemistry B* **2003**, *107*, 12088.

[243] Beerdsen, E.; Smit, B.; Calero, S. *Journal of Physical Chemistry B* **2002**, *106*, 10659.

[244] Calero, S.; Lobato, M. D.; García-Pérez, E.; Mejías, J. A.; Lago, S.; Vlugt, T. J. H.; Maesen, T. L. M.; Smit, B.; Dubbeldam, D. *Journal of Physical Chemistry B* **2006**, *110*, 5838.

[245] den Exter, M. J. *Zeolites*; PhD Thesis. Delft University of Technology, 1996.

[246] Finqueneisel, G.; Zimny, T.; Weber, J. V. *Carbon* **2005**, *43*, 1093.

[247] Wahnstrom, G.; Haug, K.; Metiu, H. *Chemical Physics Letters* **1988**, *148*, 158.

[248] Hedin, N.; DeMartin, G. J.; Roth, W. J.; Strohmaier, K. G.; Reyes, S. C. *Microporous and Mesoporous Materials* **2008**, *109*, 327.

[249] Linders, M. J. G.; van den Broeke, L. J. P.; Kapteijn, F.; Moulijn, J. A.; van Bokhoven, J. *AIChE Journal* **2001**, *47*, 1885.

[250] Okamoto, K.; Kita, H.; Horii, K.; Tanaka, K.; Kondo, M. *Industrial & Engineering Chemistry Research* **2001**, *40*, 163.

[251] Kristof, T.; Csanyi, E.; Rutkai, G.; Merenyi, L. *Molecular Simulation* **2006**, *32*, 869.

[252] Corma, A.; Rey, F.; Rius, J.; Sabater, M. J.; Valencia, S. *Nature* **2004**, *431*, 287.

[253] Himeno, S.; Tomita, T.; Suzuki, K.; Yoshida, S. *Microporous and Mesoporous Materials* **2007**, *98*, 62.

[254] Chen, H. L.; Li, Y. S.; Yang, W. S. *Journal of Membrane Science* **2007**, *296*, 122.

[255]   Demontis, P.; Suffritti, G. B.; Quartieri, S.; Fois, E. S.; Gamba, A. *Journal of Physical Chemistry* **1988**, *92*, 867.

[256]   Hunger, M.; Karger, J.; Pfeifer, H.; Caro, J.; Zibrowius, B.; Bulow, M.; Mostowicz, R. *Journal of the Chemical Society-Faraday Transactions I* **1987**, *83*, 3459.

[257]   Kuhn, J.; Gross, J.; Jansen, J. C.; Jansens, P. J. Investigating mass transport in zeolite pores by tuning the framework polarity. In *Studies in Surface Science and Catalysis: From zeolites to porous MOF materials*; Xu, R., Gao, Z., Chen, J., Yan, W., Eds.; Elsevier: Amsterdam, 2007; Vol. 170A; pp 942.

[258]   Babarao, R.; Hu, Z. Q.; Jiang, J. W.; Chempath, S.; Sandler, S. I. *Langmuir* **2007**, *23*, 659.

[259]   Batten, S. R. *Current Opinion in Solid State & Materials Science* **2001**, *5*, 107.

[260]   Chae, H. K.; Siberio-Perez, D. Y.; Kim, J.; Go, Y.; Eddaoudi, M.; Matzger, A. J.; O'Keeffe, M.; Yaghi, O. M. *Nature* **2004**, *427*, 523.

[261]   Ferey, G. *Chemistry of Materials* **2001**, *13*, 3084.

[262]   Pan, L.; Olson, D. H.; Ciemnolonski, L. R.; Heddy, R.; Li, J. *Angewandte Chemie-International Edition* **2006**, *45*, 616.

[263]   Rao, C. N. R.; Natarajan, S.; Vaidhyanathan, R. *Angewandte Chemie-International Edition* **2004**, *43*, 1466.

[264]   Rowsell, J. L. C.; Yaghi, O. M. *Angewandte Chemie-International Edition* **2005**, *44*, 4670.

[265]   Yang, Q. Y.; Xue, C. Y.; Zhong, C. L.; Chen, J. F. *AIChE Journal* **2007**, *53*, 2832.

[266]   Batten, S. R.; Robson, R. *Angewandte Chemie-International Edition* **1998**, *37*, 1460.

[267]   Carlucci, L.; Ciani, G.; Proserpio, D. M. *Coordination Chemistry Reviews* **2003**, *246*, 247.

[268]   Eddaoudi, M.; Kim, J.; Rosi, N.; Vodak, D.; Wachter, J.; O'Keeffe, M.; Yaghi, O. M. *Science* **2002**, *295*, 469.

[269]   Erxleben, A. *Coordination Chemistry Reviews* **2003**, *246*, 203.

[270]   Gu, J. Z.; Lu, W. G.; Jiang, L.; Zhou, H. C.; Lu, T. B. *Inorganic Chemistry* **2007**, *46*, 5835.

[271]   Michaelides, A.; Skoulika, S.; Bakalbassis, E. G.; Mrozinski, J. *Crystal Growth & Design* **2003**, *3*, 487.

[272]   Zhao, H. K.; Ding, B.; Yang, E. C.; Wang, X. G.; Zhao, X. J. *Zeitschrift Fur Anorganische Und Allgemeine Chemie* **2007**, *633*, 1735.

[273]   Cao, R.; Sun, D. F.; Liang, Y. C.; Hong, M. C.; Tatsumi, K.; Shi, Q. *Inorganic Chemistry* **2002**, *41*, 2087.

[274]   Shi, Q.; Cao, R.; Sun, D. F.; Hong, M. C.; Liang, Y. C. *Polyhedron* **2001**, *20*, 3287.

[275]   Fang, Q. R.; Zhu, G. S.; Xue, M.; Zhang, Q. L.; Sun, J. Y.; Guo, X. D.; Qiu, S. L.; Xu, S. T.; Wang, P.; Wang, D. J.; Wei, Y. *Chemistry-a European Journal* **2006**, *12*, 3754.

[276]   Li, Y.; Yang, R. T. *Langmuir* **2007**, *23*, 12937.

[277]   Lin, X.; Blake, A. J.; Wilson, C.; Sun, X. Z.; Champness, N. R.; George, M. W.; Hubberstey, P.; Mokaya, R.; Schroder, M. *Journal of the American Chemical Society* **2006**, *128*, 10745.

[278]   Kitaura, R.; Kitagawa, S.; Kubota, Y.; Kobayashi, T. C.; Kindo, K.; Mita, Y.; Matsuo, A.; Kobayashi, M.; Chang, H. C.; Ozawa, T. C.; Suzuki, M.; Sakata, M.; Takata, M. *Science* **2002**, *298*, 2358.

[279]   Kondo, A.; Daimaru, T.; Noguchi, H.; Ohba, T.; Kaneko, K.; Kanob, H. *Journal of Colloid and Interface Science* **2007**, *314*, 422.

[280]   Maji, T. K.; Ohba, M.; Kitagawa, S. *Inorganic Chemistry* **2005**, *44*, 9225.

[281]   Wang, Q. M.; Shen, D. M.; Bulow, M.; Lau, M. L.; Deng, S. G.; Fitch, F. R.; Lemcoff, N. O.; Semanscin, J. *Microporous and Mesoporous Materials* **2002**, *55*, 217.

[282]   Zacher, D.; Baunemann, A.; Hermes, S.; Fischer, R. A. *Journal of Materials Chemistry* **2007**, *17*, 2785.

[283]   Panella, B.; Hirscher, M.; Putter, H.; Muller, U. *Advanced Functional Materials* **2006**, *16*, 520.

[284]   Liu, J. C.; Culp, J. T.; Natesakhawat, S.; Bockrath, B. C.; Zande, B.; Sankar, S. G.; Garberoglio, G.; Johnson, J. K. *Journal of Physical Chemistry C* **2007**, *111*, 9305.

[285]   Vishnyakov, A.; Ravikovitch, P. I.; Neimark, A. V.; Bulow, M.; Wang, Q. M. *Nano Letters* **2003**, *3*, 713.

[286]   Wang, S. Y.; Yang, Q. Y.; Zhong, C. L. *Separation and Purification Technology* **2008**, *60*, 30.

[287]   Yang, Q. Y.; Zhong, C. L. *Journal of Physical Chemistry B* **2006**, *110*, 17776.

[288]   Kell, G. S. *Journal of Chemical and Engineering Data* **1975**, *20*, 97.

[289]   Mayo, S. L.; Olafson, B. D.; Goddard, W. A. *Journal of Physical Chemistry* **1990**, *94*, 8897.

[290] Rappe, A. K.; Casewit, C. J.; Colwell, K. S.; Goddard, W. A.; Skiff, W. M. *Journal of the American Chemical Society* **1992**, *114*, 10024.

[291] Prestipino, C.; Regli, L.; Vitillo, J. G.; Bonino, F.; Damin, A.; Lamberti, C.; Zecchina, A.; Solari, P. L.; Kongshaug, K. O.; Bordiga, S. *Chemistry of Materials* **2006**, *18*, 1337.

[292] Frost, H.; Snurr, R. Q., personal communication.

[293] Li, Y.; Tang, R. T. *AIChE Journal* **2008**, *54*, 269.

[294] Dubbeldam, D.; Frost, H.; Walton, K. S.; Snurr, R. Q. *Fluid Phase Equilibria* **2007**, *261*, 152.

[295] Surble, S.; Millange, F.; Serre, C.; Duren, T.; Latroche, M.; Bourrelly, S.; Llewellyn, P. L.; Ferey, G. *Journal of the American Chemical Society* **2006**, *128*, 14889.

[296] Liu, Y.; Brown, C. M.; Neumann, D. A.; Peterson, V. K.; Kepert, C. J. *Journal of Alloys and Compounds* **2007**, *446*, 385.

[297] Peterson, V. K.; Liu, Y.; Brown, C. M.; Kepert, C. J. *Journal of the American Chemical Society* **2006**, *128*, 15578.

[298] Krungleviciute, V.; Lask, K.; Migone, A. D.; Lee, J.-Y.; Li, J. *AIChE Journal* **2008**, *54*, 918.

[299] Kitagawa, S.; Kitaura, R.; Noro, S. *Angewandte Chemie-International Edition* **2004**, *43*, 2334.

[300] Mueller, U.; Schubert, M.; Teich, F.; Puetter, H.; Schierle-Arndt, K.; Pastre, J. *Journal of Materials Chemistry* **2006**, *16*, 626.

[301] Eddaoudi, M.; Kim, J.; Rosi, N.; Vodak, D.; Wachter, J.; O'Keeffe, M.; Yaghi, O. M. *Science* **2002**, *295*, 469.

[302] Yaghi, O. M.; O'Keeffe, M.; Ockwig, N. W.; Chae, H. K.; Eddaoudi, M.; Kim, J. *Nature* **2003**, *423*, 705.

[303] Lee, J. Y.; Olson, D. H.; Pan, L.; Emge, T. J.; Li, J. *Advanced Functional Materials* **2007**, *17*, 1255.

[304] Wang, J. C. F.; Ronnebro, E. C. E. *Trends in Materials and Manufacturing Technologies for Transportation Industries and Powder Metallurgy Research and Development in the Transportation Industry* **2005**, 21.

[305] Schlichte, K.; Kratzke, T.; Kaskel, S. *Microporous and Mesoporous Materials* **2004**, *73*, 81.

[306] Alaerts, L.; Seguin, E.; Poelman, H.; Thibault-Starzyk, F.; Jacobs, P. A.; De Vos, D. E. *Chemistry-a European Journal* **2006**, *12*, 7353.

[307] Ramsahye, N. A.; Maurin, G.; Bourrelly, S.; Llewellyn, P.; Loiseau, T.; Ferey, G. *Physical Chemistry Chemical Physics* **2007**, *9*, 1059.

[308] Walton, K. S.; Millward, A. R.; Dubbeldam, D.; Frost, H.; Low, J. J.; Yaghi, O. M.; Snurr, R. Q. *Journal of the American Chemical Society* **2008**, *130*, 406.

[309] Wang, S. Y. *Energy & Fuels* **2007**, *21*, 953.

[310] Yang, Q. Y.; Zhong, C. L. *Journal of Physical Chemistry B* **2005**, *109*, 11862.

[311] Krungleviciute, V.; Lask, K.; Heroux, L.; Migone, A. D.; Lee, J. Y.; Li, J.; Skoulidas, A. *Langmuir* **2007**, *23*, 3106.

[312] Skoulidas, A. I.; Sholl, D. S. *Journal of Physical Chemistry B* **2005**, *109*, 15760.

[313] Yang, Q. Y.; Zhong, C. L. *Chemphyschem* **2006**, *7*, 1417.

[314] Yang, Q. Y.; Zhong, C. L. *Journal of Physical Chemistry B* **2006**, *110*, 655.

[315] Millward, A. R.; Yaghi, O. M. *Journal of the American Chemical Society* **2005**, *127*, 17998.

[316] Murthy, C. S.; Singer, K.; Klein, M. L.; McDonald, I. R. *Molecular Physics* **1980**, *41*, 1387.

[317] Mellot, C.; Lignieres, J. *Molecular Simulation* **1996**, *18*, 349.

[318] Dubbeldam, D.; Calero, S.; Vlugt, T. J. H.; Krishna, R.; Maesen, T. L. M.; Smit, B. *Journal of Physical Chemistry B* **2004**, *108*, 12301.

[319] Duren, T.; Snurr, R. Q. *Journal of Physical Chemistry B* **2004**, *108*, 15703.

[320] Duren, T.; Sarkisov, L.; Yaghi, O. M.; Snurr, R. Q. *Langmuir* **2004**, *20*, 2683.

[321] Garberoglio, G.; Skoulidas, A. I.; Johnson, J. K. *Journal of Physical Chemistry B* **2005**, *109*, 13094.

[322] Wagener, A.; Schindler, M.; Ruclolphi, F.; Ernst, S. *Chemie Ingenieur Technik* **2007**, *79*, 851.

[323] Ramsahye, N. A.; Maurin, G.; Bourrelly, S.; Llewellyn, P. L.; Serre, C.; Loiseau, T.; Devic, T.; Ferey, G. *Journal of Physical Chemistry C* **2008**, *112*, 514.

[324] Brasseur, G. P.; Orlando, J. J.; Tyndall, G. S. *Atmospheric Chemistry and Global Change* **1999**, 1.

[325] *Sources and control of air polution*; Heinsohn, R. J.; Kabel, R. L., Eds.; Prentice Hall: Upper Saddle River, New Yersey, 1998, pp 696.

[326] Dybtsev, D. N.; Chun, H.; Yoon, S. H.; Kim, D.; Kim, K. *Journal of the American Chemical Society* **2004**, *126*, 32.

[327] Fletcher, A. J.; Cussen, E. J.; Bradshaw, D.; Rosseinsky, M. J.; Thomas, K. M. *Journal of the American Chemical Society* **2004**, *126*, 9750.

[328] Ohmori, O.; Kawano, M.; Fujita, M. *Angewandte Chemie-International Edition* **2005**, *44*, 1962.

[329] Pan, L.; Adams, K. M.; Hernandez, H. E.; Wang, X. T.; Zheng, C.; Hattori, Y.; Kaneko, K. *Journal of the American Chemical Society* **2003**, *125*, 3062.

[330] Rowsell, J. L. C.; Yaghi, O. M. *Microporous and Mesoporous Materials* **2004**, *73*, 3.

[331] Snurr, R. Q.; Hupp, J. T.; Nguyen, S. T. *Aiche Journal* **2004**, *50*, 1090.

[332] Fletcher, A. J.; Thomas, K. M.; Rosseinsky, M. J. *Journal of Solid State Chemistry* **2005**, *178*, 2491.

[333] Eddaoudi, M.; Li, H. L.; Yaghi, O. M. *Journal of the American Chemical Society* **2000**, *122*, 1391.

[334] Eddaoudi, M.; Moler, D. B.; Li, H. L.; Chen, B. L.; Reineke, T. M.; O'Keeffe, M.; Yaghi, O. M. *Accounts of Chemical Research* **2001**, *34*, 319.

[335] Chen, B. L.; Eddaoudi, M.; Hyde, S. T.; O'Keeffe, M.; Yaghi, O. M. *Science* **2001**, *291*, 1021.

[336] Wong-Foy, A. G.; Matzger, A. J.; Yaghi, O. M. *Journal of the American Chemical Society* **2006**, *128*, 3494.

[337] Pan, L.; Liu, H. M.; Lei, X. G.; Huang, X. Y.; Olson, D. H.; Turro, N. J.; Li, J. *Angewandte Chemie-International Edition* **2003**, *42*, 542.

[338] Lee, J. Y.; Pan, L.; Kelly, S. R.; Jagiello, J.; Emge, T. J.; Li, J. *Advanced Materials* **2005**, *17*, 2703.

[339] Walton, K. S.; Millward, A. R.; Dubbeldam, D.; Frost, H.; Low, J. J.; Yaghi, O. M.; Snurr, R. Q. *Journal of the American Chemical Society* **2008**, *130*, 406.

[340] Keskin, S.; Sholl, D. S. *Journal of Physical Chemistry C* **2007**, *111*, 14055.

[341] Zhou, W.; Wu, H.; Hartman, M. R.; Yildirim, T. *Journal of Physical Chemistry C* **2007**, *111*, 16131.

[342] Krishna, R.; Smit, B.; Calero, S. *Chemical Society Reviews* **2002**, *31*, 185.

[343] Rowsell, J. L. C.; Spencer, E. C.; Eckert, J.; Howard, J. A. K.; Yaghi, O. M. *Science* **2005**, *309*, 1350.

[344] Jiang, J. W.; Sandler, S. I. *Langmuir* **2006**, *22*, 5702.

[345] Krishna, R.; Calero, S.; Smit, B. *Chemical Engineering Journal* **2002**, *88*, 81.

[346] Flick, E. W. *Industrial solvents handbook*, 5 ed.; William Andrew: Weswood, New Yersey, 1999.

[347] Scheirs, J.; Long, T. E. *Modern polyesters: chemistry and technology of polyesters and copolyesters*, 1 ed.; John Wiley & Sons, Ltd.: Chichester, West Sussex, 2003.

[348] Thorat, T. S.; Yadav, V. M.; Yadav, G. D. *Applied Catalysis A-General* **1992**, *90*, 73.

[349] Sakellarides, S. L. *Plastics Engineering* **1996**, *52*, 33.

[350] Hammond, P. D.; McArdle, E. H. *Industrial and Engineering Chemistry* **1943**, *35*, 809.

[351] Vicens, J.; Armah, A. E.; Fujii, S.; Tomita, K. I. *Journal of Inclusion Phenomena and Molecular Recognition in Chemistry* **1991**, *10*, 159.

[352] Shiau, L. D.; Wen, C. C.; Lin, B. S. *AIChE Journal* **2008**, *54*, 337.

[353] Broughton, D. B.; Neuzil, R. W.; Pharis, J. M.; Brearley, C. S. *Chemical Engineering Progress* **1970**, *66*, 70.

[354] Minceva, M.; Gomes, P. S.; Meshko, V.; Rodrigues, A. E. *Chemical Engineering* **2008**, *140*, 305.

[355] Jin, W. H.; Wankat, P. C. *Separation Science and Technology* **2007**, *42*, 669.

[356] Kurup, A. S.; Hidajat, K.; Ray, A. K. *Industrial & Engineering Chemistry Research* **2005**, *44*, 5703.

[357] Minceva, M.; Rodrigues, A. E. *Separation Science and Technology* **2003**, *38*, 1463.

[358] Drechsel, B.; Hantsch, W.; Weber, K. *Chemische Technik* **1991**, *43*, 57.

[359] Spindler, H.; Stief, C.; Hantsch, W.; Entner, R. *Chemische Technik* **1990**, *42*, 159.

[360] Roethe, K. P.; Fiedler, K.; Roethe, A.; Suckow, M.; Stach, H.; Spindler, H.; Wittke, H.; Seidel, G.; Ermischer, W.; Roscher, W.; Seidel, R. *Chemische Technik* **1985**, *37*, 107.

[361] Gu, X.; Dong, J.; Nenoff, T. M.; Ozokwelu, D. E. *Journal of Membrane Science* **2006**, *280*, 624.

[362] Guo, G. Q.; Chen, H.; Long, Y. C. *Microporous and Mesoporous Materials* **2000**, *39*, 149.

[363] Mohammadi, T.; Razaeian, M. P. *Separation Science and Technology* **2009**, *44*, 817.

[364] Wu, X.; Yang, Y.; Tu, B.; Webley, P. A.; Zhao, D. *Adsorption* **2009**, *15*, 123.

[365] Ramesh, N.; Jayakumar, C.; Gandhi, N. N. *Chemistry and Engineering Technology* **2009**, *32*, 129.

[366] Alaerts, L.; Kirschhock, C. E. A.; Maes, M.; van der Veen, M. A.; Finsy, V.; Depla, A.; Martens, J. A.; Baron, G. V.; Jacobs, P. A.; Denayer, J. E. M.; De Vos, D. E. *Angewandte Chemie-International Edition* **2007**, *46*, 4293.

[367] Alaerts, L.; Maes, M.; Jacobs, P. A.; Denayer, J. E. M.; De Vos, D. E. *Physical Chemistry Chemical Physics* **2008**, *10*, 2979.

[368] Finsy, V.; Verelst, H.; Alaerts, L.; De Vos, D. E.; Jacobs, P. A.; Baron, G. V.; Denayer, J. E. M. *Journal of the American Chemical Society* **2008**, *130*, 7110.

[369] Finsy, V.; Kirshhock, C. E. A.; Vedts, G.; Maes, M.; Alaerts, L.; De Vos, D. E.; Baron, G. V.; Denayer, J. F. M. *Chemistry - A European Journal* **2009**, *15*, 7724.

[370] Krishna, R.; van Baten, J. M. *Molecular Simulation* **2009**, *35*, 1098.

[371] Dubbeldam, D.; Krishna, R.; Snurr, R. Q. *Journal of Physical Chemistry C* **2009**, *113*, 19317.

[372] Finsy, V.; Calero, S.; García-Pérez, E.; Merkling, P. J.; Vedts, G.; de vos, D. E.; Baron, G. V.; Denayer, J. F. M. *Physical Chemistry Chemical Physics* **2009**, *11*, 3515.

[373] Rosenbach, N.; Jobic, H.; Ghoufi, A.; Salles, F.; Maurin, G.; Bourrelly, S.; Llewellyn, P. L.; Devic, T.; Serre, C.; Ferey, G. *Angewandte Chemie-International Edition* **2008**, *47*, 6611.

[374] Salles, F.; Jobic, H.; Maurin, G.; Koza, M. M.; Llewellyn, P. L.; Devic, T.; Serre, C.; Ferey, G. *Physical Review Letters* **2008**, *100*, 245901.

[375] Liu, B.; Smit, B. *Langmuir* **2009**, *25*, 5918.

[376] Moise, J. C.; Bellat, J. P. *Journal of Physical Chemistry B* **2005**, *109*, 17239.

[377] Lachet, V.; Boutin, A.; Tavitian, B.; Fuchs, A. H. *Langmuir* **1999**, *15*, 8678.

[378] Chempath, S.; Snurr, R. Q.; Low, J. J. *AIChE Journal* **2004**, *50*, 463.

[379] Robinson, D. B.; Peng, D. Y.; Chung, S. Y. K. *Fluid Phase Equilibria* **1985**, *24*, 25.

[380] Kenneth, D. *The principles of chemical equilibrium*, Fourth ed.; Cambridge University Press: Cambridge, 1981.

[381] Jorgensen, W. L.; Nguyen, T. B. *Journal of Computational Chemistry* **1993**, *14*, 195.

[382] Ramsahye, N. A.; Maurin, G.; Bourrelly, S.; Llewellyn, P. L.; Devic, T.; Serre, C.; Loiseau, T.; Ferey, G. *Adsorption* **2007**, *13*, 461.

[383] Wang, X.; Liu, L.; Jacobson, A. J. *Angewandte Chemie-International Edition* **2006**, *45*, 6499.

[384] Barthelet, K.; Marrot, J.; Riou, D.; Ferey, G. *Angewandte Chemie-International Edition* **2002**, *41*, 281.

[385] Jensen, C. R. C.; Seaton, N. A. *Langmuir* **1996**, *12*, 2866.

[386] Myers, A. L.; Prausnitz, J. M. *AIChE Journal* **1965**, *11*, 121.

[387] Jorgensen, W. L.; Severance, D. L. *Journal of the American Chemical Society* **1990**, *112*, 4768.

[388] Hura, G.; Sorenson, J. M.; Glaeser, R. M.; Head-Gordon, T. *Journal of Chemical Physics* **2000**, *113*, 9140.

Summary

The adsorption of water on hydrophobic zeolites such as silicalite and on hydrophilic MOF (metal-organic framework), Cu-BTC, is completely different, as described in chapters 2 and 4. While in hydrophobic materials water adsorption isotherms are very steep and difficult to measure, both experimentally and by simulation, in hydrophilic materials water adsorbs easily and its isotherms are similar to the isotherms of other molecules. The key property to understand these differences is the dipole moment of water. Water molecules prefer to stay in a bulk water phase rather than adsorbing in a microporous material. In bulk liquid water, molecules interact strongly, forming clusters via hydrogen bonds. Inside a hydrophobic zeolite pore, the formation of water clusters is restricted by the geometry of the pores. Only at high pressures water molecules are forced to enter the zeolite pores. When a few water molecules are adsorbed, new molecules adsorb in layers close to the already adsorbed molecules. This is the reason why the adsorption isotherm of water in hydrophobic zeolites is very steep.

The adsorption properties of water in zeolites are difficult to measure both experimentally and by molecular simulations. Experiments are complicated by the fact that water is adsorbed at defects. Therefore, the inflection point in the isotherm of water is very sensitive to defects, as well as to the structural crystallographic positions of the zeolite framework atoms (in addition to pore blockage/collapse etc.). There are only a few water models that are suitably calibrated for studying water adsorption in zeolites. The Tip5pEw model is calibrated using the Ewald summation and reproduces the bulk properties of water properly. Therefore, it is a suitable candidate to describe water in a periodic porous environment, even though there is still much uncertainty in the proper values of the partial charges of the zeolite framework atoms. The dipole moment of water results in behavior that is completely different from other molecules with similar size but without dipole moment, so the partial charge of the zeolite atoms is a critical parameter that has to be chosen carefully. The adsorption of water is also very sensitive to small changes in the precise location of the zeolite atoms. We provided evidence that this sensitivity is directly related to the coupling of the dipole of the water molecules with the electric field induced by the zeolite. Therefore, one has to be cautious when computing the properties of water and highly polar molecules in these hydrophobic structures.

The inclusion of framework flexibility considerably increases the required simulation time, and the error bars of the computed points of the isotherm are much larger than in the case of a rigid structure. It would be desirable to reproduce the experimental isotherm quantitatively, so further refinement of the force field parameters is needed. Fitting these parameters in the case of a flexible framework is quite time consuming, and in the rigid case it resulted to be impossible.

Contrarily to hydrophobic zeolites, water adsorbs easily in the hydrophilic Cu-BTC MOF. Cu-BTC contains pores with open metal centers which interact strongly with water. Therefore, the adsorption isotherm of water in Cu-BTC is not as steep as in the case of zeolites, but linear up to relatively large loadings. Fitting the force field to reproduce the experimental adsorption isotherm was straightforward. It was only necessary to modify one decisive parameter of the interactions, i.e. the charge of the metal center (and the rest of the atom charges are scaled accordingly in order to keep the structure charge neutral). The strong electrostatic interaction of water with the metal centers is also responsible for the special behavior of water in Cu-BTC, compared to other molecules without dipole moment. At low loadings, water is preferentially adsorbed at the metal centers. Most of the molecules studied in Cu-BTC, such as alkanes, nitrogen, and carbon dioxide, prefer to adsorb at the side pockets of the structure. This property may be exploited for the separation of components from water. It is interesting to note that the qualitative behavior of water was the same at all the partial charges assigned to the structure during the study.

Despite all the difficulties that occur when describing the adsorption of polar molecules in hydrophobic porous materials, we still can use suitable force fields to obtain a qualitative description of adsorption. In chapter 3 we studied the separation performance of water and alcohol mixtures in the hydrophobic, pure siliceous zeolite DDR. This is an example of a separation based on differences in diffusion coefficients rather than in adsorption. Adsorption isotherms for water, methanol, and ethanol on all-silica DDR were experimentally measured by single-component vapor-phase adsorption and calculated by GCMC simulations. The measured alcohol adsorption can be described by a single-site Langmuir adsorption isotherm. The Monte Carlo (MC) simulations were able to qualitatively reproduce the adsorption behavior of the experimental isotherms. The adsorption of water is of type II. The water loading is under predicted by the calculations at pressures up to 2.5kPa. The calculated saturation loadings of all the components considered are larger than the experimental values, although they are comparable to saturation loadings on LTA-type zeolites. The molecular models and force field parameters were taken directly from literature without further adjustment. Nevertheless, the order of magnitude and the shape of the pure-component isotherms give a good resemblance of the experimental data.

Mixture adsorption isotherms and diffusivities were calculated and compared with permeation data measured under pervaporation conditions and using specific models. The calculated mixture isotherms show that the loading of both alcohols and water at constant partial fugacity increases as compared to pure-component adsorption. Moreover, the shape of the water isotherm changes from type IV to type I. The decrease in water and ethanol permeance in the mixture as compared to pure-component permeation is not caused by competitive adsorption. The increase in loading in mixture adsorption is significantly

more profound for water than for alcohols, but this does not lead to adsorption selectivity for water at the feed conditions of the pervaporation experiments. Therefore, we studied the diffusion of molecules in DDR to find the influence of the dynamics in the separation of water and alcohols.

The self-diffusivities calculated by Molecular Dynamics (MD) simulations showed that the water diffusivity is at least 1-3 orders of magnitude higher than the diffusivity of the alcohols. Although component fluxes calculated from the simulation data over predict the experimentally observed values by one order of magnitude, the permeate composition corresponds well with experimental data. The selective water transport through DDR-type zeolite membranes can, therefore, be explained by the higher diffusivity of water respect to alcohols in the hydrophobic DDR-type zeolite.

In chapter 5 we studied with more detail the adsorption properties of the MOF Cu-BTC. Cu-BTC consists of two types of cages. One of the cages is commensurate with small molecules and the other is capable of adsorbing larger molecules. This characteristic may induce strong selectivity for mixtures. Understanding separation selectivity requires a proper description of the adsorption behavior of Cu-BTC, which was provided in this chapter. We also described the properties of the structure when as-synthesized water is removed. The observed negative thermal expansion for Cu-BTC has important implications for adsorption, because of the close match between small molecules and the small pockets.

In chapter 6 we investigated the adsorption behavior of the main components of natural gas in Cu-BTC and IRMOF-1 using Monte Carlo Simulations. We computed adsorption isotherms at 298 K for pure components and mixtures, and analyzed the preferential adsorption sites on these two MOFs. The detailed study of the sitting of the molecules in both structures provided an explanation for the high adsorption capacity of IRMOF-1 and for the high adsorption selectivity towards carbon dioxide of Cu-BTC. On the basis of our observations, IRMOF-1 seems a good material for the storage of the different components of natural gas, whereas Cu-BTC could be a promising material for their separation.

In chapter 7 we analyzed the reasons for separation of xylene isomers found experimentally in the MOF MIL-47. Both experiments and molecular simulations show a large adsorption selectivity of xylene isomers in MIL-47. Our simulations show that this selectivity is due to differences in the packing of xylene isomers. The Ideal Adsorption Solution Theory (IAST) correctly described the binary and ternary mixture adsorption isotherms of xylene isomers in MIL-47. The selectivity factors obtained at low temperatures are larger than the experimental ones. This may suggest that the experimental selectivity of xylenes in MIL-47 can still be improved. In our simulations we use pure crystals, while real MIL-47

crystals may contain defects that may reduce their separation efficiency. In addition, the saturation loading found in the simulations might be difficult to achieve experimentally.

Samenvatting

Zoals beschreven in hoofdstukken 2 en 4, is de adsorptie van water in hydrofobe zeolieten verschillend van die in hydrofiele zeolieten. In hydrofobe zeolieten is de vorm van de adsorptie isotherm van water erg stijl. Hierdoor is de isotherm lastig te bepalen, zowel in experimenten als in moleculaire simulaties. In hydrofiele zeolieten wordt water veel gemakkelijker geadsorbeerd en is de vorm van de isotherm minder stijl en vergelijkbaar met die van andere moleculen. Deze verschillen zijn de begrijpen door het dipool moment van water te beschouwen. Water moleculen prefereren een omgeving van andere water moleculen, in plaats van te adsorberen in een microporie. In vloeibaar water hebben water moleculen een sterke interactie met elkaar omdat water moleculen waterstofbruggen vormen. In de porie van een hydrofoob zeoliet wordt de vorming van water clusters beperkt door de geometrie van de porie, zodat water moleculen alleen bij een grote externe druk adsorberen. Indien slechts een klein aantal water moleculen in een porie zijn geadsorbeerd, zullen nieuwe water moleculen bij voorkeur hier in de buurt adsorberen. Dit is de reden waarom de adsorptie isotherm een steile vorm heeft.

De adsorptie isotherm van water in zeolieten is lastig te bepalen, zowel in experimenten als in moleculaire simulaties. Een complicatie hierbij is dat in experimenten water moleculen bij voorkeur zullen adsorberen in de buurt van defecten in het zeoliet. Hierdoor is de inflectie in de adsorptie isotherm van water zeer gevoelig voor defecten, de precieze posities van de atomen van het zeoliet alsmede de mate van "pore blockage/collapse". Slechts een aantal water modellen zijn geschikt om te gebruiken in adsorptie simulaties in zeolieten. Het zogenaamde Tip5pEw model is gekalibreerd met behulp van de Ewald sommatie en dit model kan de eigenschappen van vloeibaar water goed voorspellen. Hierdoor is het geschikt om te gebruiken in adsorptie simulaties, dit ondanks dat er een zekere onzekerheid is betreffende de partiële ladingen die aan de zeoliete atomen dient te worden toegekend. Het dipoolmoment van water resulteert in eigenschappen die volledig verschillend zijn van die van andere moleculen van dezelfde grootte, maar dan zonder dipoolmoment. Hierdoor is het cruciaal om een goede keuze te maken voor de partiële ladingen van de zeolietatomen. De adsorptie van water is ook zeer gevoelig voor kleine veranderingen in de posities van de zeolietatomen. We laten zien dat deze gevoeligheid direct gerelateerd is aan de koppeling van de dipool van watermoleculen met het door het zeoliet geïnduceerde elektrische veld. Hierdoor dient men uiterst voorzichtig te zijn met het interpreteren van adsorptie simulaties van water in zeolieten.

Door het gebruik van een flexibel zeolietrooster stijgt de benodigde rekentijd zeer veel. Dit resulteert in een grotere foutenmarge in de berekende belading van het zeoliet vergeleken met een rigide zeoliet. Het is ook wenselijk om de experimentele adsorptie isotherm van water te reproduceren in de simulaties.

Hiervoor is het noodzakelijk om de "force field" parameters verder te optimaliseren. In het geval van een flexibel zeoliet is dit een zeer tijdrovende zaak. Echter, in het geval van een rigide zeoliet blijkt dit onmogelijk.

In tegenstelling tot hydrofobe zeolieten wordt water gemakkelijk geadsorbeerd in hydrofiele structuren zoals het zogenaamde Cu-BTC "Metal Organic Framework" (MOF). De structuur Cu-BTC bestaat uit poriën met toegankelijke metaalatomen. Deze hebben een sterke interactie met water. Hierdoor is de vorm van de adsorptie isotherm van water in Cu-BTC niet stijl zoals in zeolieten, maar lineair voor relatief hoge beladingen. Hierdoor is het relatief eenvoudig om force field parameters te fitten aan experimentele gegevens. Het blijkt dat het voldoende is om slechts de lading van het metaalatoom van het MOF te veranderen en de andere ladingen mee te schalen zodat de gehele structuur elektrisch neutraal is. De sterke interacties van water met de metaalatomen resulteert in speciaal gedrag van watermoleculen in Cu-BTC, in tegenstelling tot dat van moleculen zonder dipoolmoment. Bij lage belading wordt water bij voorkeur geadsorbeerd in de buurt van de metaalatomen. Dit gedrag was onafhankelijk van de lading van de zeolietatomen. Andere moleculen zoals alkanen, stikstof, koolstofdioxide adsorberen bij de zogenaamde "site pockets" van de Cu-BTC structuur. Dit gegeven kan mogelijk worden gebruikt om water van andere componenten te scheiden.

Ondanks de de genoemde complicaties bij het beschrijven van het adsorptiegedrag van water in hydrofobe materialen is het toch mogelijk om dit gedrag te modelleren met behulp van geschikte force fields. In hoofstuk 3 wordt de scheiding van mengsels van water en alcoholen onderzocht in het hydrofobe zeoliet DDR. Het blijkt dat de scheiding van water en alcoholen wordt veroorzaakt door verschillen in de diffusiecoëfficiënt, en niet door verschillen in adsorptie. Adsorptie isothermen van water, methanol en ethanol zijn experimenteel bepaald door middel van gas-fase adsorptie experimenten alsmede moleculaire simulaties in het groot-canoniek ensemble. De gemeten adsorptie isothermen van alcoholen kunnen nauwkeurig worden geschreven met behulp van een "single site" Langmuir isotherm. Het blijkt dat de Monte Carlo simulaties de adsorptie experimenten goed kunnen beschrijven. De adsorptie van water is van het type II. De berekende water belading voor drukken tot 2.5 kPa is lager dan in de experimenten. De berekende maximale belading is voor alle componenten significant groter dan in de experimenten. Deze berekende maximale beladingen zijn ongeveer even groot als die in zeoliet LTA. De modellen en force field parameters zijn direct verkregen uit de litteratuur zonder enige aanpassing. Desondanks wordt de experimentele adsorptie goed beschreven.

Tevens zijn diffusiecoëfficiënten en mengsel isothermen berekend. Deze zijn gebruikt om een voorspeling te maken voor de uitkomst van permeatie experimenten onder condities van pervaporatie. De mengsel

isothermen laten zien dat de belading van zowel water als alcoholen groter is dan die bij isothermen van enkele componenten, berekend bij dezelfde partiële fugaciteit. Bovendien is in mengsels de isotherm van water van het type IV. De permeatie van water en ethanol in een mengsel is groter dan de permeatie van de zuivere componenten onder gelijke condities. Dit wordt niet veroorzaakt door competatieve adsorptie. De toename in de belading voor mengsels is groter voor water, maar dit leidt niet tot een grote adsorptie selectiviteit van water onder de condities van de voeding van het membraan. Hierdoor is het van belang om de diffusiecoëfficiënten van water en alcoholen in dit zeoliet te berekenen.

Moleculaire dynamica simulaties laten zien dat de zelf-diffusiecoëfficiënt van water 1 tot 3 grootte ordes groter is dan die van alcoholen. Hoewel de voorspelde fluxen van de componenten ongeveer een factor 10 te groot zijn ten opzichte van de experimenten, wordt de samenstelling van het permeaat zeer goed voorspeld. Het selectieve transport van water in DDR zeoliet membranen kan dus worden toegeschreven aan een hoge diffusicoëfficiënt van water ten opzichte van de andere componenten.

In hoofdstuk 5 wordt dieper ingegaan op de adsorptie eigenschappen van kleine moleculen in Cu-BTC. Cu-BTC bevat twee types kooien. Slecht één van deze is ongeveer even groot als typische kleine moleculen. In de andere kooien kunnen grotere moleculen worden geadsorbeerd. Dit gegeven kan resulteren in een grote adsorptieselectiviteit voor mengsels van kleine en grotere moleculen. Het begrijpen van deze selectiviteit vereist een gedetailleerde beschrijving van het adsorptiegedrag van kleine moleculen. Deze uitgebreide beschrijving is terug te vinden in hoofdstuk 5. De waargenomen negatieve thermische uitzettingscoëfficiënt van Cu-BTC heeft mogelijk belangrijke gevolgen voor adsorptie toepassingen. Dit is omdat de selectiviteit zeer sterk afhangt van de grootte van de kooien.

In hoofdstuk 6 wordt het adsorptiegedrag van de belangrijkste componenten in aardgas in Cu-BTC en IRMOF-1 onderzocht met behulp van Monte Carlo simulaties. We hebben bij 298K de adsorptie isothermen van de zuivere componenten, alsmede hun mengsels berekend. Bovendien hebben de de locatie van de geadsorbeerde moleculen geanalyseerd. Een gedetailleerde beschrijving van het adsorptiegedrag van moleculen in beide structuren heeft geresulteerd in in een verklaring voor de grote maximale belading van IRMOF-1, alsmede voor de grote adsorptie selectiviteit van koolstofdioxide in Cu-BTC. Op basis van onze waarnemingen kunnen we concluderen dat IRMOF-1 een geschikt materiaal zou kunnen zijn voor de opslag van de verschillende componenten in aardgas en dat Cu-BTC mogelijk geschikt is voor hun scheiding.

In hoofdstuk 7 laten we zien waarom xyleen isomeren kunnen worden gescheiden door middel van adsorptie in het MOF MIL-47. Zowel experimenten als moleculaire simulaties laten een hoge adsorptie selectiviteit zien van xyleen isomeren in MIL-47. De simulaties laten zien dat dit komt door verschillen in de efficiëntie van de stapeling van de isomeren. De zogenaamde "Ideal Adsorbed Solution Theory" kan isothermen van binaire en ternaire systemen bestaande uit xyleen isomeren goed beschrijven. De berekende selectiviteiten zijn groter dat de experimenteel bepaalde selectiviteiten. Dit suggereert dat het mogelijk zou moeten zijn om de selectiviteit in de experimenten te vergroten. De reden hiervoor is dat we in de simulaties perfecte MIL-47 kristallen beschouwen, dit in tegenstelling tot de experimenten. Imperfecties in de MIL-47 structuur zullen in de regel leiden tot een lagere selectiviteit. De hoge selectiviteit in de simulaties wordt bereikt bij hoge beladingen. Het is de vraag of deze hoge beladingen experimenteel kunnen worden bereikt.

Curriculum vitae

Name:	Juan Manuel Castillo Sanchez
Birth:	10th August 1977 in Puertollano, Spain

Education:

1990-1995	Secondary school
	I.B. Julio Rodriguez, Motril, Spain

1995-2002	Master of Science
	University of Granada, Granada, Spain
	Major Theoretical physics

2006-2010	PhD Research
	University Pablo de Olavide, Sevilla, Spain
	Delft University of Technology, Delft, The Netherlands
	European Center of Atomic and Molecular Computation (CECAM), Lyon, France
	Thesis title Molecular simulation in microporous materials: adsorption, diffusion and separation
	Promotor Prof. dr. ing. J. Gross
	Promotor Prof. dr. S. Calero
	Copromotor Dr. Ir. T.J.H. Vlugt

List of publications

Chapter 2

Castillo, J. M.; Dubbeldam, D.; Vlugt, T. J. H.; Smit, B.; Calero, S. "Evaluation of various water models for simulation of adsorption in hydrophobic zeolites". Molecular Simulations 2009, Vol. 35, 1067-1076

Chapter 3

Kuhn, J.; Castillo, J. M.; Gascón, J.; Calero, S.; Dubbeldam, D.; Vlugt, T. J. H.; Kapteijn, F.; Gross, J. "Adsorption and diffusion of water, methanol and ethanol in all-silica DD3R: experiments and simulation". Journal of Physical Chemistry C 2009, Vol. 113, 14290-14301. Journal of Physical Chemistry C 2010, Vol. 114, 6877-6878.

Chapter 4

Castillo, J. M.; Vlugt, T. J. H.; Calero, S. "Understanding water adsorption in Cu-BTC metal-organic frameworks". Journal of Physical Chemistry C 2008, Vol. 112, 15934-15939

Chapter 5

García-Pérez, E.; Gascón, J.; Morales-Flórez, V.; Castillo, J. M.; Kapteijn, F.; Calero, S. "Identification of adsorption sites in Cu-BTC by experimentation and molecular simulation". Langmuir 2009, Vol. 25, 1725-1731

Chapter 6

Martín-Calvo, A.; García-Pérez, E.; Castillo, J. M.; Calero, S. "Molecular simulations for adsorption and separation of natural gas in IRMOF-1 and Cu-BTC metal-organic frameworks". Physical Chemistry Chemical Physics 2008, Vol. 10, 7085-7091

Chapter 7

Castillo, J. M.; Vlugt, T. J. H.; Calero, S. "Molecular simulation study on the separation of xylene isomers in MIL-47 metal-organic frameworks". Journal of Physical Chemistry C 2009, Vol. 113, 20869-20874

Not included in this thesis

García-Pérez, E.; Parra, J. B.; Ania, C. O.; Dubbeldam, D.; Vlugt, T. J. H.; Castillo, J. M.; Merkling, P. J.; Calero, S. "Unraveling the argon adsorption processes in MFI-type zeolite". Journal of Physical Chemistry C 2008, Vol. 112, 9976-9979

Maesen, T. L. M.; Krishna, R.; van Baten, J. M.; Smit, B.; Calero, S.; Castillo, J. M. "Shape selective n-alkane hydroconversion at exterior zeolite surfaces". Journal of Catalysis 2008, Vol. 256, 95-107

Acknowledgements

First, I would like to thank my promotors, Sofía Calero and Joachim Gross, and my co-promotor, Thijs Vlugt, for their constant support and motivation during the last years in so many different countries. Without them I would have probably resigned after my short stay in the USA. They always gave me good advice and good ideas to solve my problems, and not only at work. They also showed me the importance of being creative. Sofía taught me how to analyze problems using a different perspective. With Thijs I gained a better understanding of simulation methods and science in general. Joachim was always very interested in every project I was involved, and encouraged me at every point to improve my work. I would also like to thank my former promotor, Berend Smit, as he allowed me to start an academic career after several years far from the university.

The collaborators I had in the different projects I was involved have been a vital contribution to this work. I have had the privilege to work with excellent researchers from different countries; all of them recognized experts in their field. Dr. David Dubbeldam was always eager to help giving quick and professional support to the simulation code, detailed information on simulation methods, and valuable comments on the articles we were writing. Prof. Freek Kapijn, Prof. Parra, and Dr. Jelan Kuhn, Dr. Jorge Gascon, Dr. Víctor Morales, and Dr. Ania were an invaluable source of experimental data and knowledge on experimental methodology, which I lacked so much during my work with them. Prof. Krishna, and Dr. Jasper van Baten were very patient finding small errors in the simulation results, and provided valuable advice on diffusion processes. Dr. Theo Maesen served as a link out of the university world, giving advice on the concerns and aims of the chemical engineering industry.

The research group in Sevilla was always a great team to work with, where you could always find help whenever you needed it. I would have needed double the time to complete this thesis without the help of Elena García, Almudena García, Juan José Gutiérrez, Ana Martín, Professor Patrick Merkling, and Dr. Sahid Hamad. I also must thank the rest of the people in Sevilla that always made me feel at home. Although too many to cite them all, I would like to thank specially to Prof. Juan Antonio Anta for his always warm welcome, and Prof. Paula Zaderenko. This thesis is also dedicated to the memory of Dr. José Antonio Mejías, who cheered our lives in Sevilla and who gave us a lesson on courage. He kindly supported me during a short period of time after my return from the USA.

I am also in debt with the research teams at TU Delft, and at the CECAM in Lyon. It was a great and pleasant experience working with such a large group of international students, every one with a different point of view on life and work. I was pleased to work with Shuai Ban, Phillip Schapotschnikow, Xin Liu,

Kirill Glavatskiy, and Sondre Kvalvåg. Special thanks to Sukanya Srisanga, who made my life in Holland much more interesting and exciting; and to Bei Liu, who between other things showed me what being a PhD student meant.